Università degli Studi di Cagliari

PhD DEGREE

Physics

Cycle XXXIV

TITLE OF THE PhD THESIS

The low HI-mass galaxy population in the Fornax galaxy cluster

Scientific and Disciplinary Sector(s)

FIS/05

PhD Student:	Alessandro Loni
Supervisor	Dott. Paolo Serra, Dott. Andrea Possenti, Prof. Luciano Burderi

Final exam. Academic Year 2020/2021
Thesis defence: February 2022 Session

Università degli Studi di Cagliari

Dipartimento di Fisica
Dottorato di Ricerca in Fisica
Ciclo XXXIV

Ph.D. Thesis

The low HI-mass galaxy population in the Fornax galaxy cluster

S.S.D. FIS 05

Candidate
Alessandro Loni

Supervisor
Dott. Paolo Serra
Dott. Andrea Possenti
Prof. Luciano Burderi

PhD Coordinator
Prof. Paolo Ruggerone

Final examination academic year 2020/2021
February 2, 2022

Contents

Chapter 1

Introduction

1.1 Overview of the thesis

The topic of this thesis is the study of galaxy evolution in the Fornax galaxy cluster based on blind interferometric radio data taken with the Australia Telescope Compact Array (ATCA) and the MeerKAT telescope, plus ancillary multi-wavelength data. The ATCA survey of the Fornax cluster consists of observations performed between December 2013 and January 2014. Studies based on these data are presented in Chapt. 2 and Chapt. 3. The MeerKAT Fornax Survey (MFS - Serra et al. 2016) is currently 25% complete and is collecting data with all 64 antennas of the MeerKAT telescope. Although the MFS is still on-going, the currently available data have a sensitivity and a resolution a factor of ~ 10 better than those of the ATCA survey. A study based on these data is presented in Chapt. 4.

Chapt. 2, which is based on Loni et al. (2021), draws a global picture of the cluster. Here, we present the neutral hydrogen properties of Fornax galaxies along with properties of other galaxy components derived from ancillary data. This study provides information on the evolutionary state of Fornax members as well as of the cluster as a whole. Two main points are treated: the comparison between Fornax galaxies and non-cluster galaxies and the time scales which shape the neutral hydrogen content of infalling Fornax members.

In Chapt. 3, we discuss the first attempt to measure the HI mass function (HIMF) of the Fornax cluster using a new Bayesian approach, which includes both HI detections and non-detections in the analysis. This new technique was firstly developed to study the evolution of the HIMF as a function of redshift by Pan et al. (2020). Here, we adapt the code to the case of constant redshift and we apply it to real data for the first time.

The improved resolution and sensitivity of the MFS data with respect to the ATCA Fornax survey provide a spectacular opportunity to study in details individual Fornax members. Hence in Chapt. 4, we present the study of NGC 1436, a low-$M_{\rm HI}$ Fornax galaxy which appears to be evolving from a spiral to a lenticular morphology (Raj et al. 2019). Our MeerKAT data show this galaxy to have a truncated HI-disc. The data set used in this study includes also molecular gas observations carried out with the Atacama

Large Millimeter/submillimeter Array (ALMA) and optical data obtained with the Multi-Unit Spectroscopic Explorer (MUSE) on the ESO Very Large Telescope. The aim of this chapter is to derive the star formation history (SFH) of NGC 1436, which helps us to understand the physical processes behind the optical morphology and the inter-stellar medium (ISM) properties of this galaxy.

In the rest of the current chapter we provide a brief overview on how galaxy evolution depends on environment (Sect. 1.2). Then, we introduce the main environmental processes which can shape the gas content of galaxies (Sect. 1.3). Finally, we introduce our target, Fornax (Sect. 1.4), and the Fornax photometric and spectroscopic catalogue used in much of this thesis (Sect. 1.5).

1.2 Galaxy evolution in dense environments

Studies on the relative abundance of red early-type galaxies and blue late-type galaxies as a function of environment have shown a clear relation between galaxy morphology and local density (Hubble & Humason 1931; Oemler 1974; Dressler 1980). By studying 55 nearby galaxy clusters, Dressler (1980) found that the fraction of elliptical and lenticular (S0) galaxies increases and that of spiral galaxies decreases with increasing local density in all clusters (Fig. 1.1). Based on galaxy morphological classification, the author also showed that most S0s in clusters are not spirals whose gas was removed and thus lost their capability of forming new stars. This suggests that galaxies in clusters were born and grew as ellipticals and S0s due to the long time scales required for a proto-galaxy to collapse. Indeed, the disc formation of a collapsing proto-galaxy would likely be interrupted by the interactions with other forming galaxies, whose encounters become more frequent as the density of the environment increases (Aarseth et al. 1979). In this picture, S0s in clusters have never had the morphology of modern spirals.

However, observations at higher redshift (z∼1) show that: (i) in dense environment the fraction of S0s was smaller in favor of a larger fraction of spirals, while the fraction of more massive systems generally classified as ellipticals is similar with respect to what is observed today; (ii) in the field the fraction of S0s and spirals appear similar from z∼1 to z∼0. These evidences show that: (i) an actual morphological transformation from spirals to S0s happens; (ii) galaxy evolution is faster in denser environments (Dressler & Gunn 1983; Dressler et al. 1997, 1999; Fasano et al. 2000; Diaferio et al. 2001; Postman et al. 2005) and, as a consequence, the relative abundance of red early-type galaxies and blue late-type galaxies changes with time (for a review on the time scales of galaxy evolution, we refer the reader to Cortese et al. 2021.)

More recently, the morphology-density relation has been revisited in light of a more quantitative, objective classification of galaxies based on kinematics. Using the specific angular momentum as defined in Emsellem et al. (2011), Cappellari et al. (2011) found an increment of fast rotators (S0s), a decrement of spirals and a rather constant number of slow rotators (ellipticals) as the density of the local environment increases (Fig. 1.2). Altogether, these studies suggest that physical mechanisms that depend on the local envi-

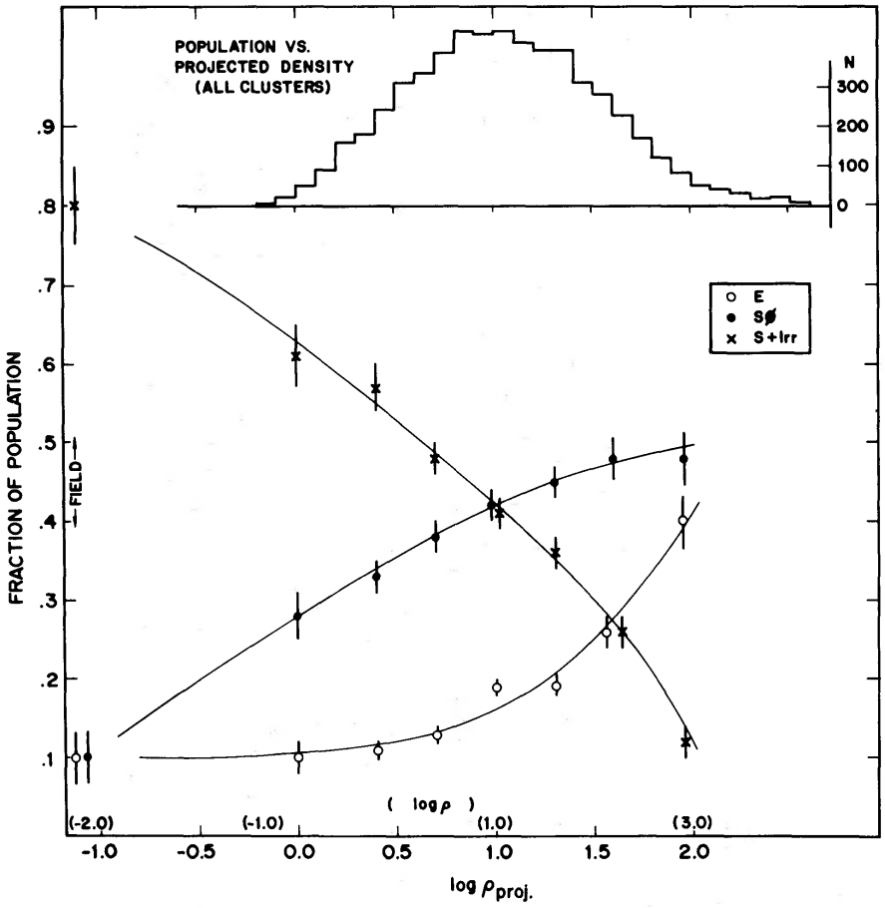

Figure 1.1: The figure from Dressler (1980) shows an increment of the fraction of elliptical (E) and lenticular (S0) cluster galaxies and a decrements of the fraction of spiral (S) and irregular (Irr) cluster galaxies as the density of the local environment increases. The morphological classification of galaxies was based on optical imaging.

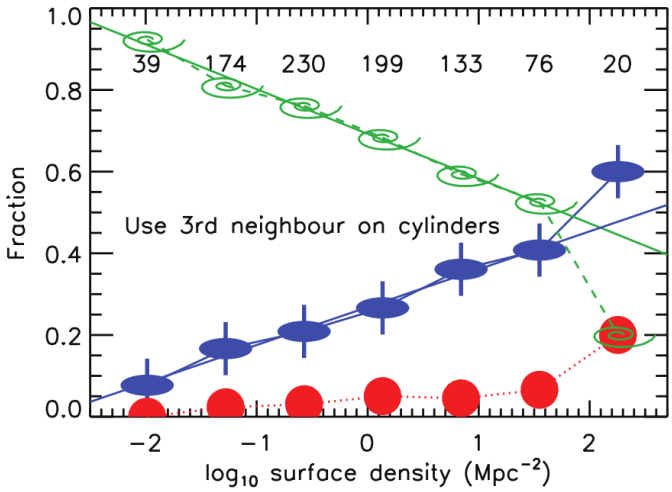

Figure 1.2: The figure from Cappellari et al. (2011) is similar to Fig. 1.1, but here galaxies were classified according to the stellar kinematics. Also in this case, the fraction of spirals decreases (green markers) and the fraction of S0s (blue color - the fast rotators class) increases as the density of the local environment increases. The fraction of elliptical galaxies (red colour – the fast rotators class) is rather constant with respect to the variation of the local environment density.

ronment might be responsible for the optical morphology of a galaxy.

In this context, galaxy clusters are the densest environments where galaxies can form, interact and evolve. They are the largest gravitationally bound systems in the Universe and can host from 100 to 1000 galaxies in a few Mpc^3. They are also characterized by a dense intra-cluster medium (ICM), which is denser and hotter in the center of clusters. In general, the density of the ICM depends on the mass of its host cluster, thus massive galaxy clusters ($M \geq 10^{15}$ $M_\odot$) are charactherized by a denser ICM with respect to less massive systems.

In these conditions, environmental interactions between galaxies, as well as between galaxies and the ICM, are likely to happen. The nature of these interactions can be either hydrodynamical (such as in the case of ram pressure stripping; Gunn & Gott 1972) or gravitational (such as in the case of tidal interactions; Toomre & Toomre 1972). While the density of the ICM is a key factor for hydrodynamical interactions, the number density of galaxies is important for tidal interactions, and depend on the velocity of galaxies (with respect to the ICM or other galaxies, respectively). These interactions (which we will describe in more detail in Sect. 1.3) deplete the cold gas reservoirs of galaxies, affecting their star formation activity and, therefore, their optical morphology– contributing decisively to the transformation of gas-rich, star-forming spirals into gas-poor, quiescent S0s.

Observations show that clusters, too, grow both through mergers and accretion of smaller systems, which include subclusters and galaxy groups (Drinkwater et al. 2001a; Furusho et al. 2001; Paolillo et al. 2002; Takahashi & Yamashita 2003). In particular,

mergers are responsible of the thermal state of clusters by inducing turbulence in the ICM, whose temperature increases. X-ray emission can trace these interactions (Bykov et al. 2015). A cluster which shows signs of recent merging events should shape the cold gas content of in-falling galaxies differently with respect to what a more dynamically evolved (virialized) cluster does (Roberts & Parker 2019).

In less dense environments such as groups of galaxies, which can host an order of magnitude less galaxies with respect to clusters, the density of the intragroup medium (IGM) is lower than that of the ICM. However, there is evidence that, although the gas removal due to gravitational and hydrodynamical interactions is less effective, it can still take place (Hester 2006; Westmeier et al. 2013; Serra et al. 2013; Hess & Wilcots 2013; Catinella et al. 2013; de Blok et al. 2018; Jones et al. 2019; Cortese et al. 2021; Boselli et al. 2021). Furthermore, several galaxies observed in clusters today, entered the main cluster as part of a group of galaxies, where gas removal might have begun. The lower velocity dispersion of the galaxy population means that, in groups, tidal interactions are more likely to happen, making them more effective than ram pressure stripping – the opposite situation than the one in clusters. The lower efficiency of ram pressure stripping in galaxy groups also depends on the lower density of the IGM. However, ram pressure stripping can still occur (e.g., Freeland & Wilcots 2011). The term "pre-processing" is commonly used to refer to both gravitational and hydrodynamical interactions which take place in groups of galaxies falling into clusters (e.g. Boselli & Gavazzi 2006; Bianconi et al. 2018; Kleiner et al. 2021).

In general, the balance between hydrodynamical and gravitational interactions depends on the mass of the host halo (group or cluster) which determines the density of the gas medium (IGM or ICM), on the velocity dispersion of its members, on the number density of galaxies, and also on galaxy properties such as their mass and orbit (Stevens et al. 1999).

Thus, galaxy evolution depends on several factors, and discriminating where and through which processes a galaxy has become red and quenched (i.e., it has stopped forming stars) is not trivial. Typically, a galaxy that is passive now has spent a few billion years in its host halo (e.g., McGee et al. 2009; Han et al. 2018). Therefore, most likely, multiple hydrodynamical and gravitational processes have played a role in shaping the cold gas content and halting the star formation of the galaxy. Furthermore, cold gas can also evaporate or be ejected via internal processes (e.g. heating/ejection by nuclear activity and stellar feedback Croton et al. 2006; De Lucia et al. 2019), making it even more difficult to understand the role played by the environment in the quenching processes.

One of the most powerful tools in the study of galaxy evolution in dense environments is the observation of galaxies' neutral hydrogen through the 21 cm wavelength emission line (HI), which gives us information on the evolutionary state of galaxies as well as a global picture of the cluster. The evolution of galaxies depends on the evolution of their atomic hydrogen reservoir, which is the primary reservoir of fuel for star formation. Since it typically extends to the outskirts of galaxies, HI gas is the first component that is affected by tidal interactions, ram-pressure stripping and mergers. Indeed, cluster galaxies are usually deficient in atomic hydrogen with respect to non-cluster galaxies

(Giovanelli & Haynes 1983; Haynes & Giovanelli 1986; Solanes et al. 2001; Boselli & Gavazzi 2006). HI is, therefore, a crucial observable for understanding galaxy evolution in dense environments (Hughes & Cortese 2009; Chung et al. 2009).

1.3 Environmental interactions shaping the cold gas content of galaxies

In the previous sections we saw that galaxies are not isolated, non-interacting systems. Galaxies are constantly influenced by gravitational and hydrodynamical interactions with other systems or environments. Typically, these interactions can lead a galaxy to become fully quenched, losing its capability of forming new stars. However, there are less frequent cases of rejuvenation, too, which consists in fuelling a quenched galaxy with gas. These processes might cause galaxies to restart their star formation activity (Trager et al. 2000; Yi et al. 2005; Serra et al. 2008; Cortese & Hughes 2009; Thilker et al. 2010).

We also saw that the balance between these types of interactions depends both on galaxy properties – including their orbits – and on environment properties, such as the number density of galaxies and the IGM/ICM density. Therefore, we expect galaxy evolution to proceed differently in different environments. In the rest of the thesis, we will focus on the impact of a low-mass cluster - the Fornax cluster - on the cold gas content of its members. In this section, we review the main processes which are often recalled in the literature for explaining galaxy quenching, although we must keep in mind that more than one process might simultaneously affect the gas content of any given galaxy.

1.3.1 Starvation

The first requirement for a galaxy to not form stars is halting cold gas accretion onto the system, which would otherwise supply material to form new stars. In general, the replenishment of gas in galaxies is a necessary process which has been proposed to explain the constant SFR of late-types for much of the Hubble time. Indeed, the cold gas depletion time, defined as $\tau_{dep} = M_{gas}/SFR$ is roughly a few billion years for both molecular and atomic phases (Boselli et al. 2014b), thus shorter than the Hubble time. As a consequence, if gas accretion had not occurred, today's galaxies would not be forming new stars. In dense environment the hot dense medium plays a role in halting gas accretion in infalling galaxies from their own hot halo – either by removing the hot halo itself, or by preventing it from cooling. In clusters of galaxies, there is evidence that gas accretion is halted when galaxies cross the virial radius for the first time or even before (2-3 $\times$ R_{vir} - Bekki et al. 2002; Bahé et al. 2013; Maier et al. 2016). Finally, when gas accretion is halted in infalling galaxies, star formation can still occur for a certain time if their cold gas reservoirs have not been removed by other environmental interactions. In the literature, the lack of cold gas replenishment and the consequent quenching through exhaustion of the remaining cold gas is referred to as starvation or strangulation (Larson et al. 1980;

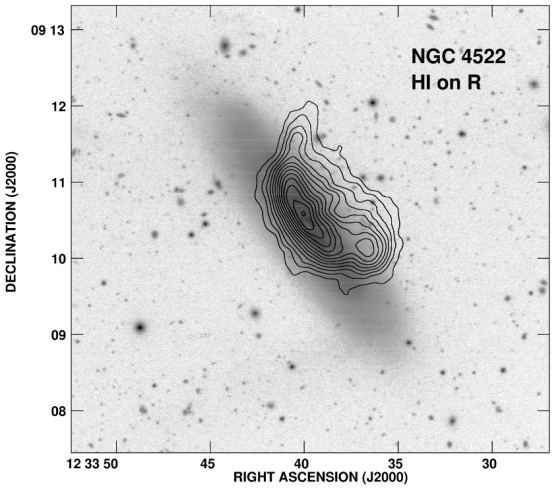

Figure 1.3: This figure from Kenney et al. (2004) shows a Virgo cluster galaxy whose gas is being removed by ram pressure stripping. The HI (black contours) is truncated within the stellar body and partially extraplanar.

Balogh & Morris 2000).

1.3.2 Cold gas stripping

Several mechanisms might be responsible for an active cold gas removal in galaxies. Satellite galaxies might be unable to retain the cold gas at their ourskirts while interacting with the environment. We have already mentioned that, among environmental interactions, hydrodynamical mechanisms can play a role in an active gas removal from galaxies. For example, while a galaxy is moving through its host halo, it feels a pressure exerted by the ICM (Gunn & Gott 1972). This process is called ram pressure stripping, whose conditions for stripping gas depend on the square of the velocity of the galaxy relative to the ICM as well as on the density of the ICM. If this pressure exceeds the gravitational force that binds the ISM to the galaxy, then the gas will be removed. In general, an in-falling galaxy would be on an eccentric orbit along which its velocity and the ICM density change as a function of time and space, respectively. Hence, it is most likely that any in-falling galaxy will experience ram pressure stripping sooner or later. Fig. 1.3 from Kenney et al. (2004) shows the effect of ram pressure stripping on a Virgo galaxy, NGC 4522 whose HI is truncated within the stellar body and partially extraplanar.

Besides gas removal, the leading side of the galaxy along the orbit might actually be compressed causing a temporary enhancement in the SFR (e.g. Vulcani et al. 2018; Ramatsoku et al. 2019) Furthermore the stripped gas on the opposite side may remain bound to the galaxy, fall back and induce a later starburst (Vollmer et al. 2001). Fig. 1.4 from Ramatsoku et al. (2019) shows both the HI emission and SFR surface density obtained by H_α emission in a galaxy which is experiencing ram pressure stripping. The SFR surface density map shows an enhancement of SFR in the western region of the disc which

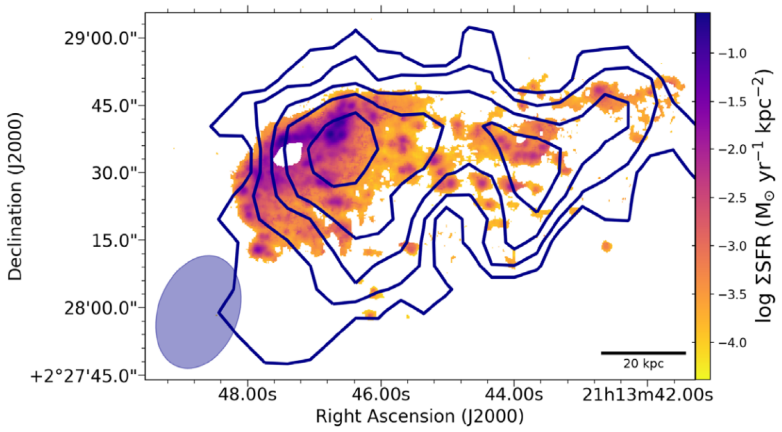

Figure 1.4: This figure from Ramatsoku et al. (2019) shows the SFR surface density map and the HI emission of a galaxy which is experiencing ram pressure. HI contour levels correspond to column densities of 3, 6, 9, ... $\times 10^{19}$ atoms cm^{-2}.

coincides with the location of the bright HI. While the long term effect of environmental interactions is usually the quenching of star formation, these studies show that the actual path to quenching can be complex.

The motion of a galaxy thorough the ICM can also cause viscous stripping, which occurs at the boundary between the ISM and the ICM and consists in the removal of the outer layer of the ISM due to the viscosity momentum transferred with the ICM (Nulsen 1982). Since the time scales and the duration of the mass loss due to ram pressure stripping and viscous stripping are different, they are referred as to instantaneous and continuous stripping, respectively (Roediger & Hensler 2005). In the former, stripping the main galaxy disc happens in a short phase from 20 to 200 Myr, while the latter is a continuous process that in general causes a slow decrease of the disc mass (and radius) with a rate of 1 $M_\odot$/yr (Roediger & Hensler 2005). Viscous stripping is usually accompanied with a thermal evaporation of the ISM caused by the rise of temperature due to heat transfer between the cold ISM ($\leq 10^4$ K) and the hot ICM ($\sim 10^7 - 10^8$ K). In general, the efficiency of ram pressure stripping increases when the ICM (and the ISM) presents turbulent motion (e.g. when a galaxy passes through a dense region with bright X-ray emission - Shin & Ruszkowski 2013; Domainko et al. 2006), thus clusters which underwent a merger are more efficient environments to remove the ISM through hydrodynamical interactions. Furthermore, since low-mass clusters are characterized by a less dense ICM with respect to more massive systems, we expect ram pressure stripping to take longer to remove the cold gas. These environments should allow HI tails to survive longer, possibly providing us with a good opportunity to observe the gas stripping in action.

The nature of the second class of environmental interactions is gravitational. The condition for these processes to strip material is the variation (both temporal and spatial) of the external gravitational potential that the outskirts of disc galaxies feel (Binney & Tremaine 1987). The main difference with hydrodynamical interactions is that the former

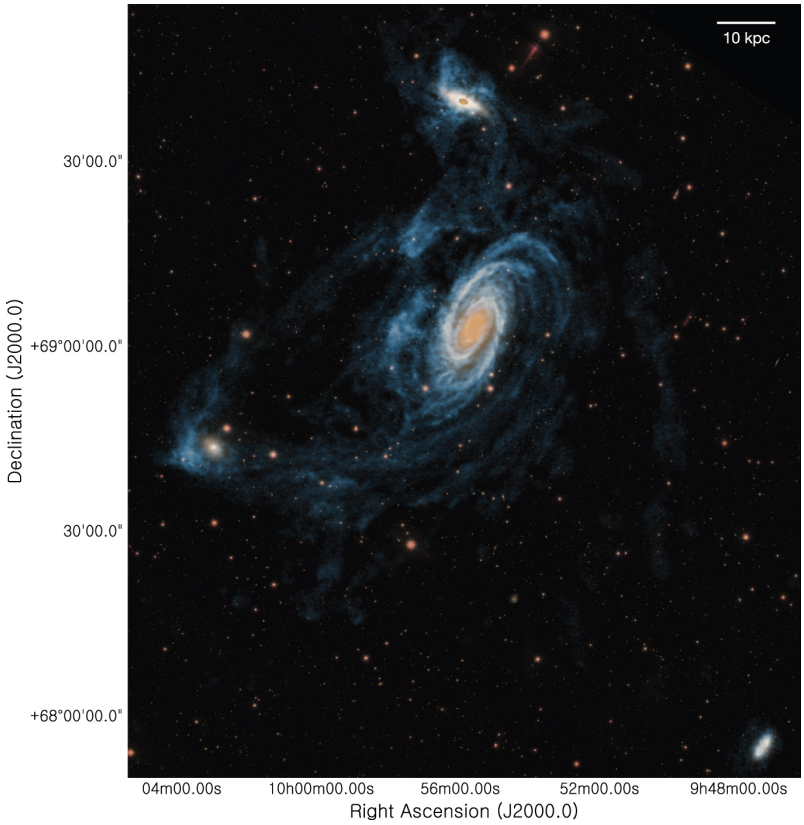

Figure 1.5: The figure from de Blok et al. (2018) shows the perturbed HI distribution (in blue) of the M81 triplet of galaxies by tidal interactions.

only removes gas, while the latter is able to affect both the gas and the stellar component of the disc. Galaxy-galaxy tidal interactions are included in this category of mechanisms. In clusters, the typical velocity of a galaxy is of the order of the velocity dispersion of the cluster, which is larger than the internal velocity dispersion of the galaxy. Therefore, galaxy encounters are high-speed in nature. These encounters can displace the weakly bound material in the disc of galaxies. An example of tidal interactions, though not in a cluster, is shown in Fig. 1.5. Furthermore, the heated ISM becomes less bound and, thus, more susceptible to disruption by further encounters and by tidal interactions with the cluster potential. Multiple high-speed encounters are refereed to as galaxy harassment. The effects of harassment in disc galaxies falling into the cluster was firstly simulated by Farouki & Shapiro (1981). These authors show that the disc of a galaxy can be entirely destroyed by one or two passages through the cluster. Galaxies might also experience a substantial amount of mass loss as the heating pushes stars onto unbound orbits, while the change in the orbits of stars which stay bound to the disc might change the morphology of the disc itself.

Simulations also suggest that harassment is an efficient mechanisms to transform late-type spirals in dwarf galaxies, and ealy-type spirals to elliptical and S0 galaxies (Aguerri

& González-García 2009). Other simulations focused on the HI content of galaxies show that a cluster crossing time is sufficient for low-mass galaxies – and a few pericenter passages for more massive galaxies – in order to deplete the cold gas content of galaxies which experience harassment (Marasco et al. 2016).

1.4 The Fornax galaxy cluster

Fornax is the closest representative of the class of low-mass clusters ($\sim 5 \times 10^{13}$ $M_\odot$ within the virial radius, $R_{\rm vir}$ = 700 kpc; Drinkwater et al. 2001a), located in the southern sky at a distance of 20 Mpc (Blakeslee et al. 2009). This distance makes our target the second closest galaxy cluster to us after the more massive Virgo. Therefore, the study of Fornax is crucial for understating the evolution of galaxies in the context of hierarchical structure formation. One of the aim of this thesis is addressing the question of how galaxy evolution proceeds in the low-mass Fornax cluster, where we expect ram pressure stripping to be less effective than in more massive systems (e.g. the Virgo and the Coma clusters). Indeed, the density of the Fornax ICM and the velocity dispersion are roughly a factor of two lower than those of Virgo, while the number density of galaxies in Fornax is two times higher (see Table 1 in Jordán et al. 2007 and references therein). If, on the one hand, these conditions make ram pressure stripping less effective, on the other hand they would increase the probability of low-speed encounters among Fornax galaxies, and thus of tidal interactions.

Due to its close proximity, Fornax has been extensively imaged and observed at a number of wavelengths by a range of telescopes and instruments. A recent large campaign of optical observations provides images and photometry of Fornax members down to a magnitude of $\sim$28 mag/arcsec^2 (Peletier et al. 2020a). Studies on several single Fornax objects can now rely on high-quality integral-field spectroscopic data (Sarzi et al. 2018), which are powerful tools to study the star formation history (SFH) and kinematics of galaxies (Pinna et al. 2019a,b), and to understand the interplay between galaxies and the cluster environment. Furthermore, a recent collection of spectroscopic observations provides velocities for numerous Fornax galaxies within $R_{\rm vir}$ (Maddox et al. 2019 – see Sect. 1.5 for further details).

Fornax was also observed in radio wavelengths which has enabled the study of the cold gas content of Fornax members (Zabel et al. 2019; Loni et al. 2021, Chapt. 2 in this thesis) leading to the conclusion that galaxies in the cluster center are gas poor. Currently, the MeerKAT Fornax Survey is still ongoing and will provide the most sensitive 1-2 GHz data of the cluster to date (Serra et al. 2016). A more complete introduction to previous radio observations of the Fornax cluster is provided in Chapt. 2.

X-ray observations of the Fornax cluster reveal that the peak of the X-ray emission coincides with the central dominant galaxy, NGC 1399 (Paolillo et al. 2002). Furthermore, the X-ray data show asymmetries in the ICM (Scharf et al. 2005; Su et al. 2017), whose origin is due to a minor merger and multiple encounters that involved NGC 1399 and NGC 1404 (Sheardown et al. 2018). The latter is an elliptical galaxy $\sim$60 kpc away

from NGC 1399. Recent studies on the magnetic field of Fornax corroborate the finding of sloshing in the ICM (Anderson et al. 2021). The cluster center also shows evidence of asymmetries in temperature and metallicity distributions. Murakami et al. (2011) found that 71 kpc north of the center, the ICM has a lower temperature and higher Fe abundance with respect to south (93-143 kpc), probably do to the recent dynamical evolution of Fornax.

Although, in general, Fornax shows a more dynamically evolved state than Virgo (Grillmair et al. 1994; Jordán et al. 2007), its growth is not over at all. The Fornax region includes two main substructures (Drinkwater et al. 2001a). The first is the cluster itself centred on NGC 1399, whose interaction with NGC 1404 is revealed by the perturbed ICM distribution. Here, three well defined groups of galaxies with different light and colour distributions, kinematics, and stellar populations were found by combining the Fornax Deep Survey imaging (Iodice et al. 2019b) with Fornax 3D spectroscopy (Iodice et al. 2019a) in the two-dimensional projected phase space: the core, the north-south clump and the infalling galaxies (see Fig. 7 in Iodice et al. 2019a). The core is still dominated by NGC 1399, which is one of only two slow-rotators inside the virial radius (NGC 1427 is the other one, located on the east side of the cluster). The NS-clump is located in the high-density region of the cluster (within $0.4R_{\rm vir} \sim 0.3$ Mpc in projection), where the X-ray emission is still bright. It hosts the reddest and most metal-rich galaxies, all of them fast-rotating early-type galaxies. The bulk of the gravitational interactions between Fornax galaxies as well as most of the intra-cluster baryons (i.e. diffuse light, globular clusters and planetary nebulae Cantiello et al. 2018; Spiniello et al. 2018; Iodice et al. 2019b) are found in this NS clump, where galaxy growth is still ongoing through the accretion of mass onto galaxies' outer regions (Spavone et al. 2020). The third group of objects in the cluster includes the infalling galaxies, which are distributed nearly symmetrically around the core in the low-density region outside $\sim 0.4R_{\rm vir} \sim 0.3$ Mpc in projection. The majority of these galaxies are late-types with ongoing star formation. Most of them exhibit signs of interaction with the environment and/or minor mergers in the form of tidal tails and disturbed molecular and atomic gas (Zabel et al. 2019; Raj et al. 2019; Loni et al. 2021). Previous work had also shown that numerous dwarf galaxies are currently falling into the centre of the cluster (Drinkwater et al. 2001b; Schröder et al. 2001; Waugh et al. 2002). Recently, the population of Fornax dwarf galaxies has been inspected by Venhola et al. (2018) with $\sim 3\times$ deeper data than Ferguson (1989b). These authors classified 564 galaxies as dwarfs ($M_{r'} > -18.5$ mag), providing new data to study the evolution of galaxies in the Fornax cluster. Venhola et al. (2019) show a radial variation of the fraction of early-type dwarfs, which increases towards the center of the cluster, suggesting that the cluster environment is responsible for transforming the morphology of its members.

Finally, the other major structure in the Fornax volume is the infalling group centred on NGC 1316 (Fornax A), located ~ 1.5 Mpc south-west of the cluster center. The central galaxy is a peculiar lenticular formed through a 1:10 merger 2 Gyr ago (Schweizer 1980; Horellou et al. 2001; Iodice et al. 2017b; Serra et al. 2019). The group hosts mostly blue, gas-rich, star-forming galaxies with various levels of HI asymmetries and gas deficiencies, likely caused by on-going interactions. Such interactions are demonstrated by the

abundant intra-group neutral and ionised gas detected with HI and Hα imaging (Kleiner et al. 2021). Whether this group is currently interacting with the large-scale Fornax cluster environment is currently an open question.

In this thesis we focus our attention on the central part of Fornax (R< $R_{\rm vir}$).

1.5 Photometric and spectroscopic Fornax catalogues

In the rest of the thesis, we need exhaustive spectroscopic and photometric catalogues which includes Fornax members within the central Fornax cluster region (rougly 1× $R_{\rm vir}$). In this section we present our work on cleaning published catalogues from duplicates and cross-matching photometric and spectroscopic catalogues, and we present a first characterization of galaxy properties based on their photometry and position in phase-space.

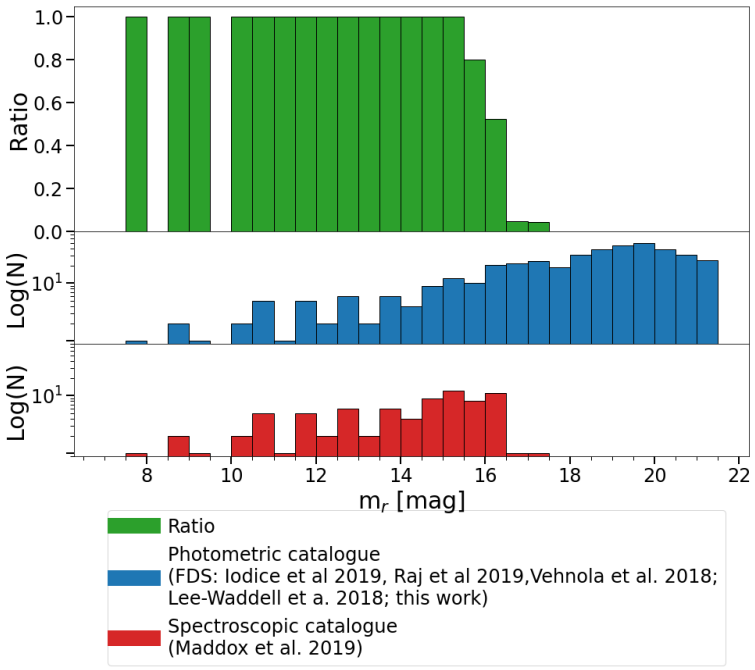

Figure 1.6: Comparison between the joint photometric catalogue and the cleaned spectroscopic catalogue. The top histogram indicates the level of completeness of the spectroscopic catalogue against the joint photometric one in each magnitude bin.

We inspected and compared the spectroscopic catalogue of Maddox et al. (2019) with a photometric catalogue obtained joining all the photometric catalogues published from the Fornax Deep Survey (FDS) collaboration where we further add the photometry of NGC 1427A whose photometry was measured in Lee-Waddell et al. (2018). The former is a compilation of several spectroscopic surveys, which also includes foreground and background sources with respect to the Fornax cluster and Fornax compact stellar systems (e.g. globular clusters). It also includes duplicates. Thus, we firstly made sure

to take all sources within the Fornax velocity range applying a velocity cut from 600 to 3000 $\mathrm{km\,s^{-1}}$(Drinkwater et al. 2001a). Then we removed compact stellar systems (CSSs, which are not expected to host interstellar matter, hence HI) identified by the following flags in Maddox et al. (2019): GS (Globular System), GC (Globular Cluster), GCC (Globular Cluster Candidate), KnownCSS (Known Compact Stellar System), NewCSS (New Compact Stellar System). Furthermore, we also removed all sources smaller than 2 arcsec (190 pc at the distance of Fornax) based on size measurements by Venhola et al. (2018; see below), since they fall into the classification of CSS (even though they had no CSS flag in Maddox et al. 2019). The final spectroscopic catalogue consists of 81 unique Fornax galaxies, some of which are however present multiple times in the catalogue. We removed duplicates as follows: we collected sources within a matching radius of 1 arcmin in subgroups of objects. Then, using optical FDS images we verified whether or not objects in the same subgroup were part of the same extended Fornax source. If so, we applied two criteria to decide which spectroscopic measurement to keep and reject the others. The first criterion was that of keeping the closest optical velocity to that measured (and converted in optical convention) with the ATCA telescope (we will show these measurements in Chapt. 2). Whenever this comparison was not possible due to lack of HI detections, we applied a second criterion: since almost all spectroscopic surveys included in Maddox et al. (2019) have a resolution (fibre aperture) of 2 arcsec, we kept the closest spectroscopical measurements to the center of the source. The final result of these steps is a spectroscopic catalogue of 81 unique galaxies with no duplicates.

The joint photometric catalogue includes Fornax early-type galaxies (ETGs) from Iodice et al. (2019a), late-type galaxies (LTGs) from Raj et al. (2019) and dwarf galaxies from Venhola et al. (2018). Since some of the objects were included in more than one FDS catalogue (e.g. the dwarf catalogue of Venhola et al. 2018 includes some LTGs in Raj et al. 2019), we made sure to have a photometric catalogue without duplicates. Also in this case, any time we found duplicates, we inspected FDS images. In general, although LTGs magnitudes are slightly brighter with respect to those of the duplicate galaxies found in the dwarf catalogue, they agree within the uncertainties.

While the Fornax membership of ETGs and LTGs is well known, the same is not true for the dwarf galaxies, many of which do not have a redshift. Venhola et al. (2018) used four different criteria to establish whether a dwarf is a Fornax galaxy or not: a color cut, a surface brightness cut, a visual inspection of the image and a concentration parameter cut. The color cut criterion is based on the comparison between the magnitude of galaxies which belong to Fornax according to their redshift with the magnitude of galaxies with no redshift. The surface brightness cut relies on the fact that the surface brightness of cluster galaxies decreases with decreasing total flux while that of distant galaxies should stay constant (Binggeli et al. 1984). Furthermore, non cluster galaxies are likely to have some sort of structure (e.g. bars, spiral arms) and they are homogeneously distributed around the center of the cluster independently of the distance. Whenever the evaluation of structures was hard to decide between elliptical background galaxies and dwarf Fornax members, they performed the concentration parameter cut. The concentration parameter takes into account the ratio between the radii which contain the 80% and 20% of the

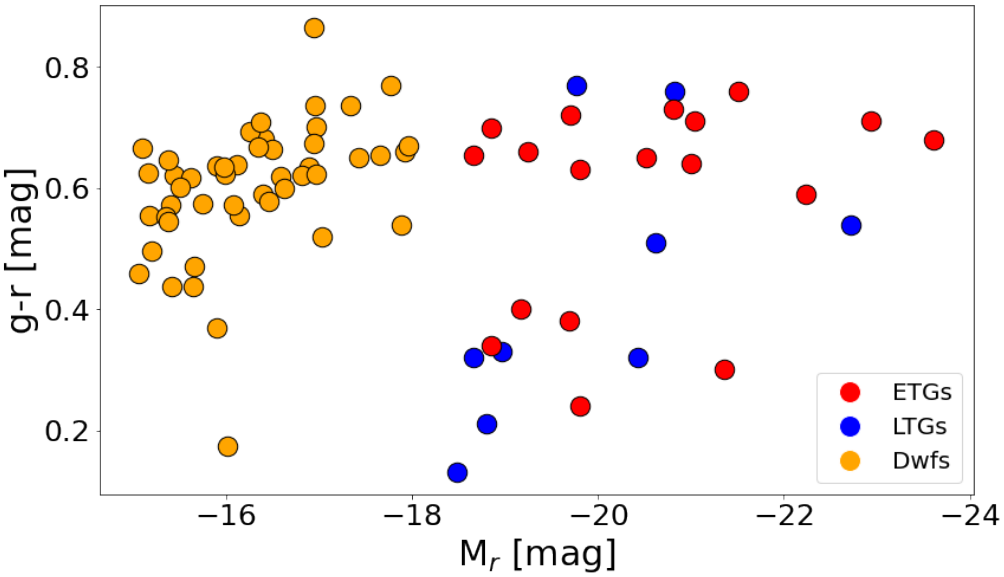

Figure 1.7: Colour-magnitude diagram of the final Fornax photometric and spectroscopic catalogue (Table 1.1), which includes 79 galaxies with photometry from Venhola et al. (2018), Iodice et al. (2019a), Raj et al. (2019), Lee-Waddell et al. (2018), this work, and redshift from the compilation in Maddox et al. (2019). See text for details on how this final catalogue was assembled.

light of a galaxy. Early-type galaxies have a higher concentration parameter than dwarf galaxies. Among Fornax members with redshift measurements, it is worth noting that Venhola et al. (2018) included all galaxies within the velocity range 745-2241 $\mathrm{km\,s^{-1}}$, while we had previously selected galaxies within 600-3000 $\mathrm{km\,s^{-1}}$ from the spectroscopic catalogue. Thus, we cross matched the background galaxy catalogue (provided by Venhola et al. 2018) with our spectroscopic catalogue (see above) in the velocity ranges 600-745 $\mathrm{km\,s^{-1}}$ and 2241-3000 $\mathrm{km\,s^{-1}}$. The match resulted in two objects that are actually included both in the dwarf Fornax catalogue and that of background galaxies, thus we did not need to add any further objects in the photometric Fornax catalogue. This is most likely due to the uncertainty on the redshift of these galaxies, which might make them both Fornax and background galaxies given the lower and upper velocity limits adopted by Venhola et al. (2018). Finally, the authors performed a self-completeness check, testing the source finding algorithm after introducing artificial objects within the data. They estimated an efficiency of 50% when searching for galaxies with m_r = 21 mag, while the efficiency increases as the magnitude of galaxies decreases.

Having taken all aforementioned steps to clean the spectroscopic and photometric catalogues, we searched for a match between objects in the cleaned spectroscopic catalogue with objects included in the cleaned photometric one. All but six objects in the former catalogue were also included in the latter. We inspected FDS images at the position of the six objects with a spectroscipic but not a photometric measurement and we realized that

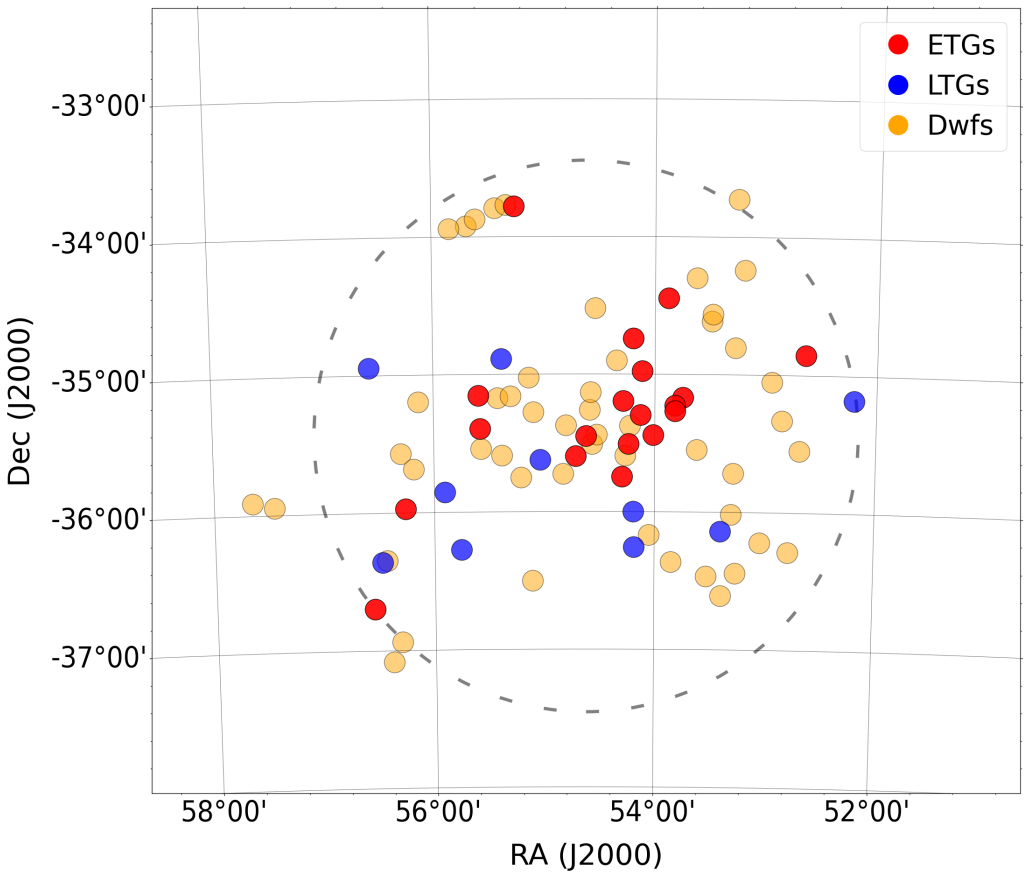

Figure 1.8: Distribution of all spectroscopically confirmed Fornax members (Table 1.1) on the sky. We adopted the same color coding as in Fig. 1.7. The dashed gray circle shows $R_{\rm vir}$ and is centred on the brightest elliptical of Fornax: NGC 1399.

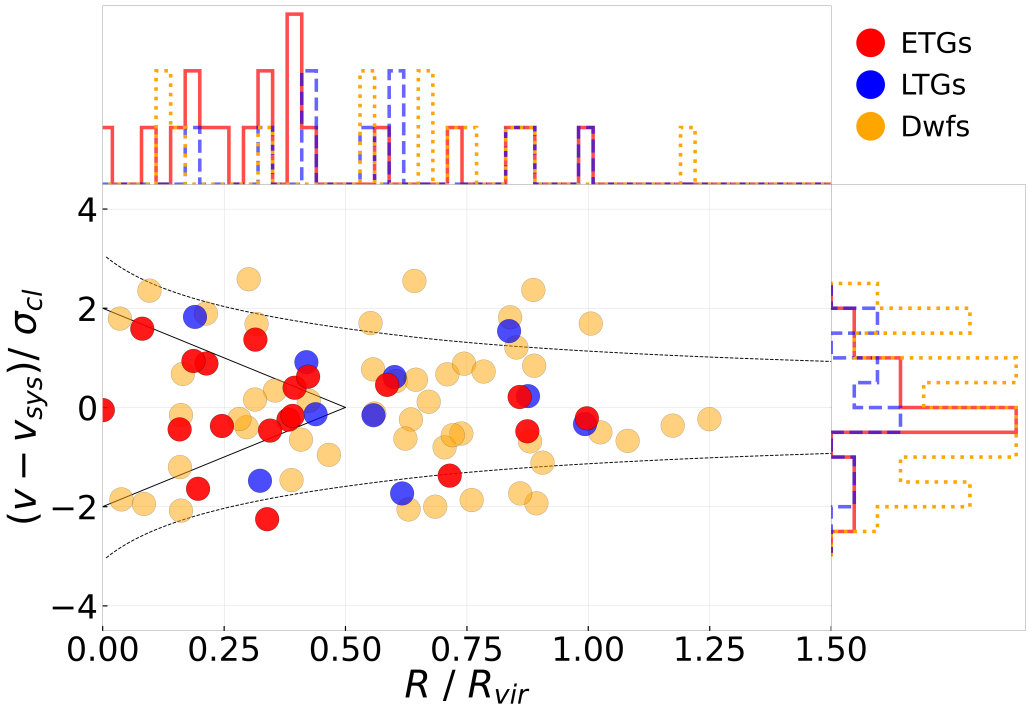

Figure 1.9: Phase space diagram of the spectroscopically confirmed Fornax members. Here we used the same color coding as in Fig. 1.8.

these are extended (larger than 2 arcsec) objects, and this should be included in our final catalogue. Proceeding as in Iodice et al. (2019a), we estimated their total magnitude in *r*-band. Following this, we could straightforwardly associate a magnitude to each of the 81 objects with a redshift.

Fig. 1.6 shows the ratio between the number of galaxies with both redshift and magnitude measurements and the number of galaxies with just photometry but no redshift, as a function of apparent magnitude. All bins with m_r brighter than 16.5 mag have a completeness higher that 50%. Thus we decided to build a spectroscopic catalogue with all objects with magnitude lower than m_r =16.5 mag, which includes 79 galaxies. Information on the photometry and velocity of Fornax galaxy members which have both measurements are provided in Table 1.1. The total completeness of the catalogue is ~85%. We made the choice to classify all galaxies with $m_r > 13.5$ mag as dwarf galaxies. While visual inspection was also used to further classify the morphology of brighter dwarfs and brighter galaxies whose photometry was measured in this work into the class of ETG and LTG galaxies.

In Fig. 1.7 we show the color-magnitude diagram which shows a segregation between dwarf, LTGs and ETG galaxies. Focusing on the y axes, LTGs also show bluer colors as expected.

In Fig. 1.8 we show the 2D distribution of all galaxies included in Table 1.1. Within 0.5 $R_{\rm vir}$ we find the 73% of all ETGs, 40% of all LTGs and 38% of all dwarfs. Thus, the

majority of the spectroscopically confirmed Fornax members in the center of the cluster are ETGs. In the figure, the aforementioned NS clump stands out clearly as an elongated concentration of ETGs just east of NGC 1399.

The additional kinematic information is provided in Fig. 1.9. Here, we show the projected phase-space diagram. We used a cluster systemic velocity of $v_{\rm sys} = 1442$ km s^{-1}and a cluster velocity dispersion of $\sigma_{\rm cl} = 318$ km s^{-1}(Maddox et al. 2019). We proceed as in Jaffé et al. (2015) to draw caustic curves. We set $M_{\rm vir} = 5 \times 10^{13}M_\odot$, $R_{\rm vir} = 700$ kpc (Drinkwater et al. 2001a) and a cluster concentration parameter equal to 6 (Navarro et al. 1996; the exact value of this parameter does not change the result significantly). The inner triangle shows the virialized area where it is most likely to find old members of the Fornax cluster (Rhee et al. 2017). Within this area, we find 52% of all ETGs, 11% of all LTGs, 20% of all dwarfs. The top histogram in the projected phase-space diagram shows the distribution of galaxies as a function of the distance from the center of the cluster (where we can draw similar results mentioned above while commenting on Fig. 1.8). The right histograms shows that the velocity distribution of ETGs and dwarfs peak at the systemic velocity of the cluster.

We make use of the final Fornax catalogue in Table 1.1 to study the distribution of HI detections relative to that of all other cluster members in Chapt. 2, and to include HI non-detections in the analysis of Fornax' HIMF in Chapt. 3.

Name	RA [h:m:s]	Dec [d:m:s]	$m_r[mag]$	$e_r[mag]$	$m_g[mag]$	$e_g[mag]$	Velocity [km/s]
FCC143	03:34:59.10	-35:10:10.00	12.6600	0.030000	13.3600	0.020000	1364.0
FCC147	03:35:16.80	-35:13:34.00	10.5000	0.010000	11.1400	0.010000	1294.0
FCC148	03:35:16.80	-35:15:56.00	11.7000	0.010000	12.3300	0.010000	726.6
FCC153	03:35:30.90	-34:26:45.01	11.7000	0.030000	11.9400	0.020000	1587.1
FCC161	03:36:04.00	-35:26:30.00	10.4700	0.010000	11.1800	0.010000	1324.0
FCC167	03:36:27.50	-34:58:31.00	9.2700	0.020000	9.8600	0.010000	1877.0
FCC170	03:36:31.60	-35:17:43.00	10.9900	0.010000	11.6400	0.010000	1724.0
FCC177	03:36:47.40	-34:44:17.00	11.8000	0.010000	12.5200	0.010000	1568.8
FCC184	03:36:56.90	-35:30:24.00	10.0000	0.040000	10.7600	0.010000	1302.0
FCC190	03:37:08.90	-35:11:37.00	12.2600	0.010000	12.9200	0.010000	1740.0
FCC193	03:37:11.70	-35:44:40.01	10.6900	0.020000	11.4200	0.010000	921.0
FCC213	03:38:29.20	-35:27:01.99	7.8900	0.090000	8.5700	0.090000	1425.0
FCC219	03:38:52.10	-35:35:37.99	8.5700	0.040000	9.2800	0.080000	1947.0
FCC276	03:42:19.20	-35:23:36.00	10.1500	0.020000	10.4500	0.060000	1388.0
FCC277	03:42:22.60	-35:09:10.01	12.3400	0.020000	12.7400	0.010000	1640.0
FCC301	03:45:03.50	-35:58:17.00	12.6500	0.010000	12.9900	0.050000	1005.0
FCC310	03:46:13.70	-36:41:43.01	11.8100	0.040000	12.1900	0.050000	1373.0
FCC083	03:30:34.98	-34:51:14.19	10.8400	-	-	-	1510.0
FDS4_DWARF001	03:41:03.60	-33:46:44.76	12.8435	0.086590	13.4974	0.101726	1290.0
FCC121	03:33:36.40	-36:08:25.00	8.7900	0.030000	9.3300	0.040000	1638.0
FCC176	03:36:45.00	-36:15:22.00	11.7400	0.010000	12.5100	0.010000	1399.0
FCC179	03:36:46.30	-35:59:57.99	10.6800	0.010000	11.4400	0.010000	972.1
FCC263	03:41:32.60	-34:53:16.99	12.7000	0.020000	12.9100	0.050000	1732.6
FCC285	03:43:02.20	-36:16:24.01	13.0200	0.030000	13.1500	0.020000	891.0
FCC290	03:43:37.10	-35:51:13.00	11.0800	0.010000	11.4000	0.010000	1392.0
FCC308	03:45:54.70	-36:21:25.00	12.5400	0.010000	12.8700	0.010000	1515.0
FCC312	03:46:18.90	-34:56:37.00	10.8900	0.090000	11.4000	0.020000	1932.0
FCC235	03:40:09.20	-35:37:23.00	12.8500	-	13.1700	-	2023.0
FCC067	03:28:48.72	-35:10:41.34	13.0200	-	-	-	1336.0
FCC090	03:31:08.10	-36:17:19.00	13.6200	0.030000	14.1600	0.020000	1827.0
FCC182	03:36:54.30	-35:22:23.00	13.5800	0.010000	14.2400	0.010000	1657.0
FDS15_DWARF107	03:33:07.06	-34:48:20.16	14.4746	0.136908	14.9939	0.155594	1365.0
FDS16_DWARF081	03:33:09.19	-35:43:05.16	16.0964	0.197405	16.5335	0.219851	1686.3
FDS4_DWARF053	03:41:45.41	-33:47:29.40	15.3627	0.140364	15.9172	0.160912	828.0
FDS6_DWARF176	03:45:12.29	-35:34:15.24	15.4917	0.226263	15.6647	0.236115	806.0
FDS7_DWARF310	03:45:45.38	-36:20:45.96	15.6050	0.108310	15.9744	0.118630	891.0
FDS10_DWARF014	03:37:23.33	-34:54:00.36	16.0722	0.164491	16.6933	0.191691	1315.4
FDS10_DWARF189	03:38:09.17	-34:31:07.68	14.6089	0.129557	15.2431	0.151467	1138.3
FDS11_DWARF069	03:40:50.40	-35:44:54.60	15.0978	0.120180	15.7794	0.142156	1368.0
FDS11_DWARF079	03:39:19.70	-35:43:28.92	15.4275	0.163722	15.9997	0.188509	781.0
FDS11_DWARF155	03:37:04.54	-35:35:24.36	15.2505	0.131069	15.9441	0.155495	1059.4
FDS11_DWARF204	03:38:16.66	-35:30:27.72	16.3438	0.151762	16.9681	0.176996	2012.3
FDS11_DWARF235	03:38:06.55	-35:26:23.64	14.1693	0.105080	14.9055	0.125978	853.6
FDS11_DWARF283	03:39:13.32	-35:22:17.04	14.5402	0.127615	15.2405	0.151647	824.0
FDS11_DWARF327	03:40:23.52	-35:16:35.76	16.1018	0.174497	16.6736	0.200896	2044.9
FDS11_DWARF339	03:38:21.48	-35:15:34.92	15.3976	0.097648	16.0360	0.114281	2191.6
FDS11_DWARF396	03:38:19.25	-35:07:44.76	14.9245	0.106346	15.5430	0.123852	1393.6
FDS11_DWARF458	03:40:33.84	-35:01:22.44	15.0140	0.135684	15.6781	0.159803	2265.0
FDS12_DWARF194	03:40:27.00	-36:29:56.04	15.6069	0.140934	16.2427	0.164834	1404.0
FDS12_DWARF367	03:36:12.86	-36:09:59.40	15.5136	0.125372	16.1361	0.146153	1485.0
FDS14_DWARF073	03:33:03.60	-33:43:29.28	16.1310	0.170201	16.7770	0.199565	1283.0
FDS15_DWARF209	03:33:57.34	-34:36:43.20	16.4459	0.156912	16.9053	0.175716	1242.6
FDS15_DWARF232	03:33:56.18	-34:33:42.48	16.3285	0.107483	16.8837	0.123238	2254.0
FDS15_DWARF384	03:34:30.82	-34:17:50.64	14.6853	0.126086	15.3058	0.146913	1186.3
FDS15_DWARF417	03:32:47.69	-34:14:19.32	14.0861	0.091484	14.7360	0.107370	2020.2
FDS16_DWARF159	03:34:29.47	-35:32:47.40	13.7403	0.109556	14.5104	0.132445	1236.0
FDS16_DWARF417	03:31:47.64	-35:03:05.04	14.5493	0.142756	15.2866	0.171193	1655.3
FDS17_DWARF110	03:33:34.18	-36:36:20.16	15.8469	0.188124	16.3181	0.211282	849.0
FDS17_DWARF161	03:34:07.03	-36:27:57.60	16.3026	0.141509	16.7993	0.159930	1479.0
FDS17_DWARF167	03:33:03.31	-36:26:35.16	16.4133	0.199712	17.0784	0.235271	1275.0
FDS17_DWARF188	03:35:24.07	-36:21:49.68	14.8830	0.087517	15.4826	0.101450	1983.0
FDS17_DWARF265	03:32:10.56	-36:13:10.56	15.8666	0.153290	16.3044	0.170749	1723.0

FDS17_DWARF325	03:33:12.74	-36:01:02.64	15.1395	0.142643	15.8480	0.169848	1611.0
FDS20_DWARF138	03:30:46.20	-35:33:00.36	15.1049	0.161236	15.6954	0.186485	1672.8
FDS2_DWARF000	03:50:36.72	-35:54:33.84	13.5423	0.094510	14.2127	0.111483	1367.0
FDS2_DWARF002	03:49:49.01	-35:56:44.52	14.5670	0.117219	15.4330	0.145098	1326.0
FDS4_DWARF000	03:42:45.55	-33:55:12.36	13.8524	0.093898	14.5075	0.110345	1225.0
FDS4_DWARF002	03:43:22.66	-33:56:19.68	14.5661	0.123577	15.2404	0.145911	1088.0
FDS4_DWARF030	03:42:27.22	-33:52:14.88	16.1498	0.122973	16.7031	0.140933	2196.0
FDS4_DWARF061	03:41:21.19	-33:46:09.84	15.0469	0.147177	15.6251	0.169710	1710.0
FDS6_DWARF098	03:44:44.42	-35:41:01.32	15.8915	0.113795	16.5082	0.132467	1620.0
FDS6_DWARF170	03:41:31.75	-35:35:22.56	16.0028	0.143830	16.6041	0.166797	1977.3
FDS6_DWARF208	03:42:17.26	-35:32:26.52	15.7625	0.147669	16.3364	0.170097	976.9
FDS6_DWARF414	03:44:32.83	-35:11:45.24	15.5321	0.127403	16.1677	0.149000	789.0
FDS6_DWARF455	03:41:41.33	-35:10:13.08	15.1591	0.094543	15.8280	0.111481	1551.0
FDS6_DWARF462	03:41:12.86	-35:09:31.32	16.1330	0.205774	16.6774	0.235311	1493.0
FDS7_DWARF001	03:45:14.09	-36:56:12.12	14.5409	0.121881	15.1640	0.142104	1980.0
FCC305	03:45:33.80	-37:04:58.01	14.1700	-	-	-	1228.0
FCC095	03:31:24.86	-35:19:51.80	13.6800	-	-	-	1265.0

Table 1.1: Table of confirmed spectroscopic members with $m_r < 16.5$ mag. The total completeness of the catalogue is $\sim 85\%$. All galaxies with $m_r > 13.5$ mag are classified as dwarfs. The further classification between ETGs and LTGs is based on morphology. The first column (name) shows ETGs with red color, LTGs in blue and dwarf galaxies in orange. The photometry of these galaxies was measured in Iodice et al. (2019a), Raj et al. (2019), Venhola et al. (2018), Lee-Waddell et al. (2018). Photometry of four galaxies was measured in this work. Velocity measurements are from Maddox et al. (2019).

Chapter 2

The ATCA survey of the Fornax galaxy cluster

Based on Loni et al. (2021)

2.1 Introduction

This chapter is based on recent published results (Loni et al. 2021). The aim of this work is to study galaxy evolution in the Fornax cluster through the analysis of the neutral hydrogen emission (HI). For a proper introduction of our target, see Sect. 1.4. In this section, we summarize some important points which make Fornax an ideal target to study galaxy evolution. As mentioned in Chapt. 1, galaxy evolution proceeds faster in dense environment due to environmental interactions (Dressler & Gunn 1983; Dressler et al. 1997, 1999; Fasano et al. 2000; Diaferio et al. 2001; Postman et al. 2005). Indeed, a cluster galaxy can interact with other galaxies or the intra cluster medium (ICM). These interactions, whose nature can be both hydrodynamical and gravitational (e.g. tidal interactions and ram pressure stripping, Gunn & Gott 1972; Toomre & Toomre 1972), deplete the cold gas content of galaxies and, since it is the fuel for star formation, they affect the ability of a galaxy to form new stars (see Sect. 1.3 for a brief introduction to the role of environmental interaction in gas removal and in quenching galaxies). Therefore, in general, galaxy evolution in dense environments depends on the number density of galaxies, the velocity dispersion of galaxies and the density of the ICM.

Fornax is at a distance of 20 Mpc with a mass of $5{\times}10^{13}$ $M_{\odot}$ within the virial radius $R_{\rm vir}$ = 700 kpc (Drinkwater et al. 2001a). Thus, Fornax is the closest representative of the class of the low-mass galaxy cluster with a mass an order of magnitude lower than the closer (16 Mpc, Fouqué et al. 2001) and more massive Virgo cluster. Differences between Fornax and Virgo concern also the number density of galaxy, the velocity dispersion of their members and the ICM density. On the one hand, the density of the Fornax ICM and the velocity dispersion of Fornax members are $\sim 2\times$ lower than those of Virgo. On the other hand, the number density of galaxy is $\sim 2\times$ higher in Fornax (Jordán et al. 2007).

As a consequence, the balance between hydrodynamical and gravitation interactions in Fornax is not the same as in Virgo. For example, since ram pressure stripping depends on the squared velocity of a galaxy with respect to the ICM and on the density of the ICM, it should be $\sim 10\times$ less effective in Fornax than in Virgo. On the contrary, low-speed encounters between galaxies which cause tidal interactions are expected to be more frequent in Fornax.

The best tracer for environmental interactions is HI because it extends to the very outskirts of galaxies (in isolated galaxies the HI radius is $\sim 1.5\times$ the optical one) and thus is the first component that is affected by tidal interactions, ram-pressure stripping and mergers. Therefore, observation of galaxies' HI gives us information on the evolutionary state of galaxies (e.g., Hughes & Cortese 2009; Chung et al. 2009) as well as a global picture of the cluster. Indeed, cluster galaxies are usually deficient in atomic hydrogen with respect to non-cluster galaxies (Giovanelli & Haynes 1983; Haynes & Giovanelli 1986; Boselli & Gavazzi 2006).

Fornax HI content was inspected in previous works typically though single-dish observations. Here, we list these studies and summarize their findings. Bureau et al. (1996) used the Parkes radio telescope to measure the amount of atomic hydrogen in 21 undisturbed galaxies with morphologies S0/a or later, located within 6 deg from NGC 1399 and with $cz \leq 2520$ km s^{-1}. The eight galaxies within $R_{\rm vir}$ did not show any peculiar value in the $M_{\rm HI}/I-$band infrared luminosity ratio with respect to the rest of the sample. The same ratio evaluated for Ursa Major galaxies, a lower density environment than Fornax, led them to conclude that the observed Fornax galaxies are not HI deficient.

The first blind HI survey of Fornax was carried out by Barnes et al. (1997), also with the Parkes telescope. They detected HI in eight galaxies within an area of 8×8 deg^2. Of those, two galaxies are within the cluster $R_{\rm vir}$: ESO 358G-063 and NGC 1365. Thanks to the survey sensitivity, they excluded the existence of a significant population of optically undetected HI clouds with HI mass greater than 10^8 M$_\odot$.

The number of HI detections within the Fornax central region increased with the targeted survey by Schröder et al. (2001). They found HI in 37 out of 66 galaxies. Of those, 14 are within $R_{\rm vir}$, while the rest lies within 5 deg from the centre of the cluster. They found a lack of HI in the cluster centre, and measured the HI deficiency parameter to be 0.38 ± 0.09 (as defined in Solanes et al. 1996). This shows a modest HI depletion in Fornax (usually, galaxies with HI deficiency parameter > 0.3 are considered to be HI deficient, e.g. Dressler 1986; Solanes et al. 2001). Furthermore, the $M_{\rm HI}-$to$-$blue light ratio of Fornax galaxies - mean value (0.68 ± 0.15) M$_\odot$/L$_\odot$ - is a factor 1.7 lower than in the field. They also showed that the velocity dispersion of the sample of HI deficient galaxies is lower than that of the remaining HI detected galaxies. This difference in velocity dispersion agrees with the deficient galaxies having more radial orbits (as shown in Dressler 1986), which makes them good candidates for ram-pressure stripping (as discussed in Solanes et al. 2001).

Waugh et al. (2002) presented a blind survey of Fornax based on the HI Parkes All Sky Survey (HIPASS − Barnes et al. 2001) data with a $M_{\rm HI}$ limit of 1.4×10^8 M$_\odot$. They detected 110 galaxies within an area of $\sim$620 deg^2 around the cluster. Of those, nine HI

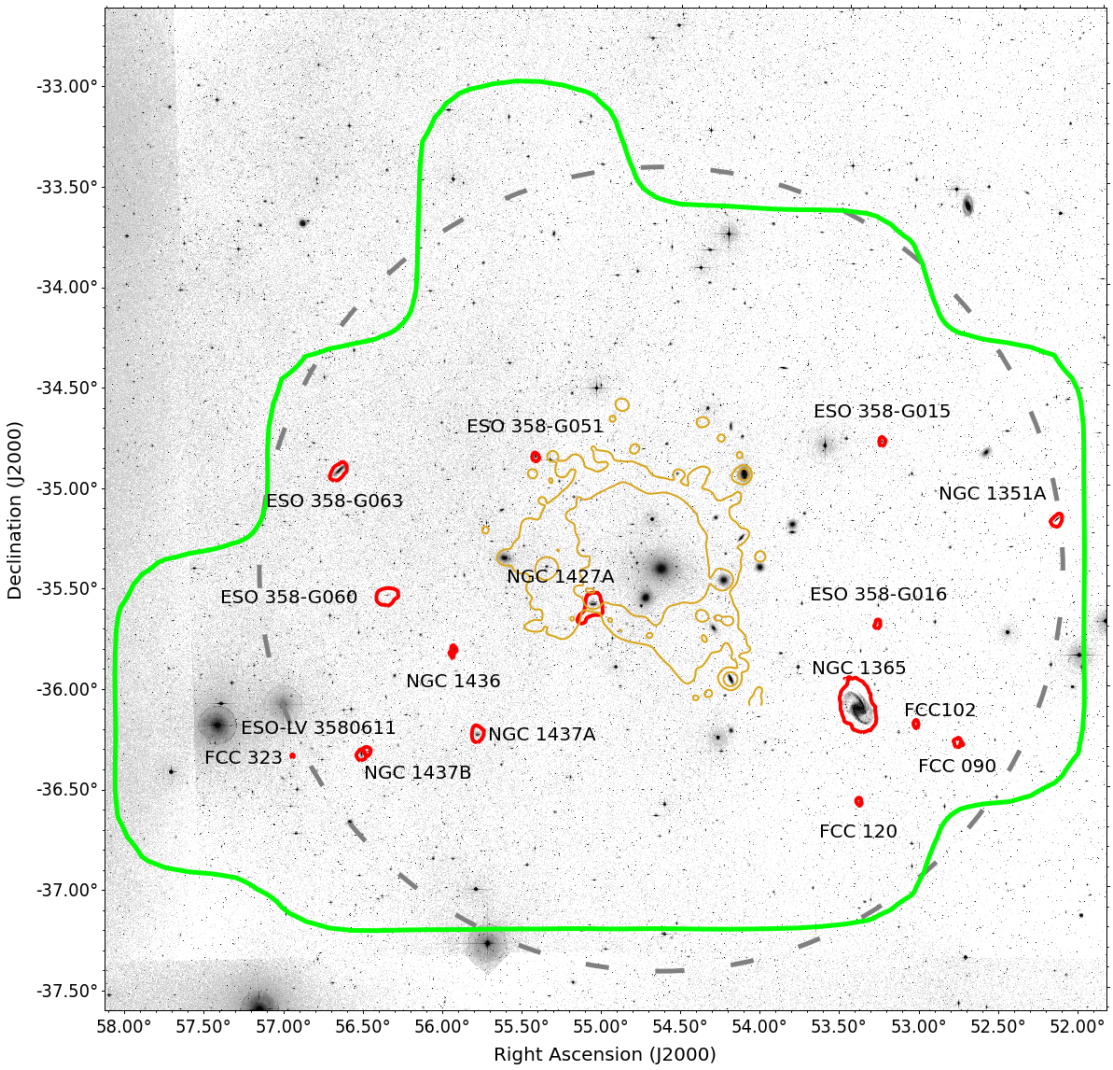

Figure 2.1: Layout and detections of our ATCA HI survey. The green outline includes the 15-deg^2 region where the average noise is 2.8 mJy beam^{-1} (see section 2.2). The red contours represent the lowest reliable HI column density – 3σ over 25 km s^{-1} – of our 16 detections. The grey dashed circle is $R_{\rm vir}$. The background optical image comes from the Digital Sky Survey (blue band). The yellow contours show the X-ray emission in the Fornax cluster detected with XMM-Newton (Frank et al. 2013) and convolved with a 3 arcmin FWHM gaussian kernel. These contours are spaced by a factor of 2, with the lowest level at 3.7 counts deg^{-2} s^{-1}.

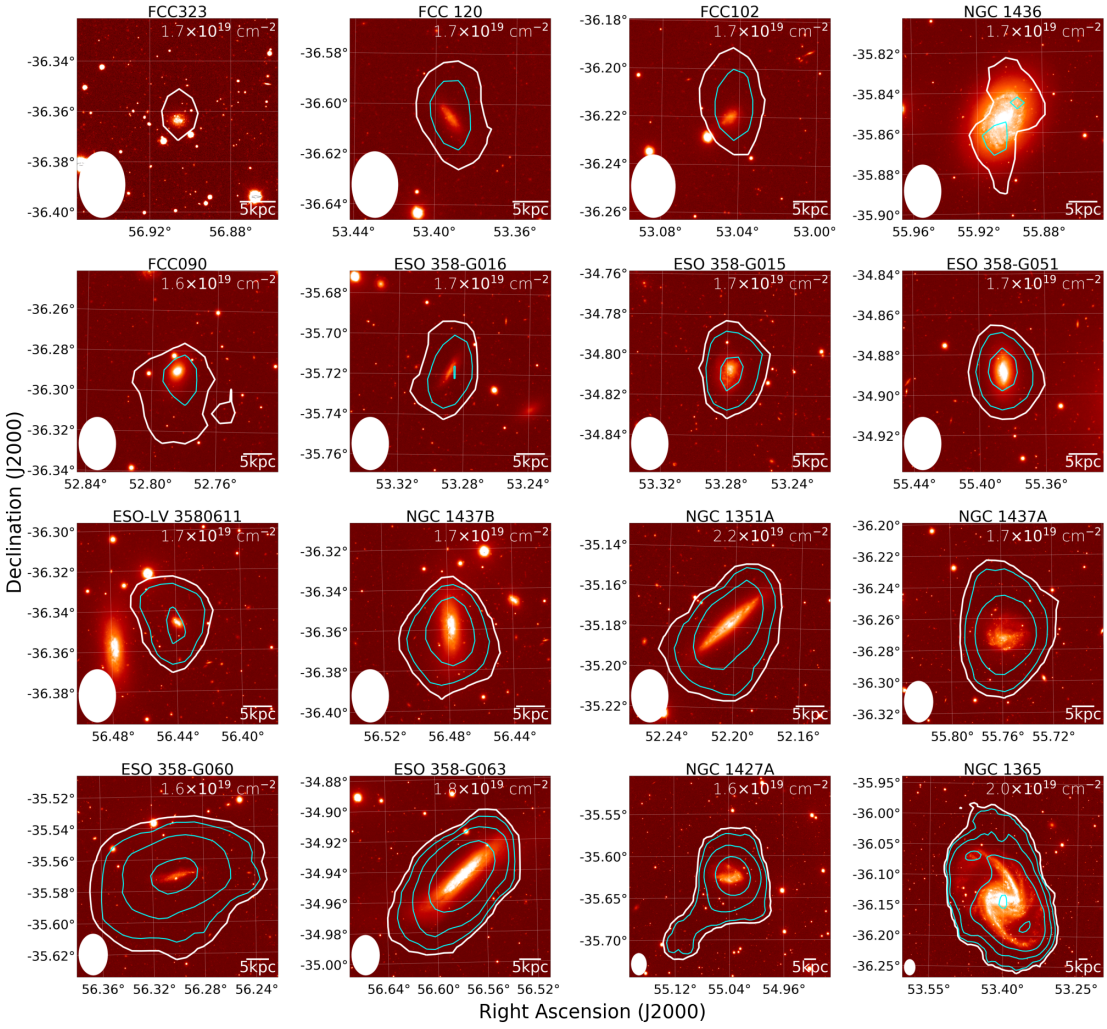

Figure 2.2: ATCA HI contours overlaid on an optical image for all our HI detections, sorted according to increasing HI mass. The *g*-band optical images come from the Fornax Deep Survey (Iodice et al. 2016; Venhola et al. 2018; Peletier et al. 2020b) for all galaxies except FCC 323, whose *g*-band optical image comes from the DESI Legacy Imaging Surveys, DR8 release, (Dey et al. 2019). In each panel we show the 3σ column density sensitivity - values reported in the top right corner - with white colour, while cyan contours represent steps of 3^n from it (n = 0, 1, 2, ...). We show the PSF on the bottom-left corner of each panel, and a 5 kpc scale bar in the bottom-right corner.

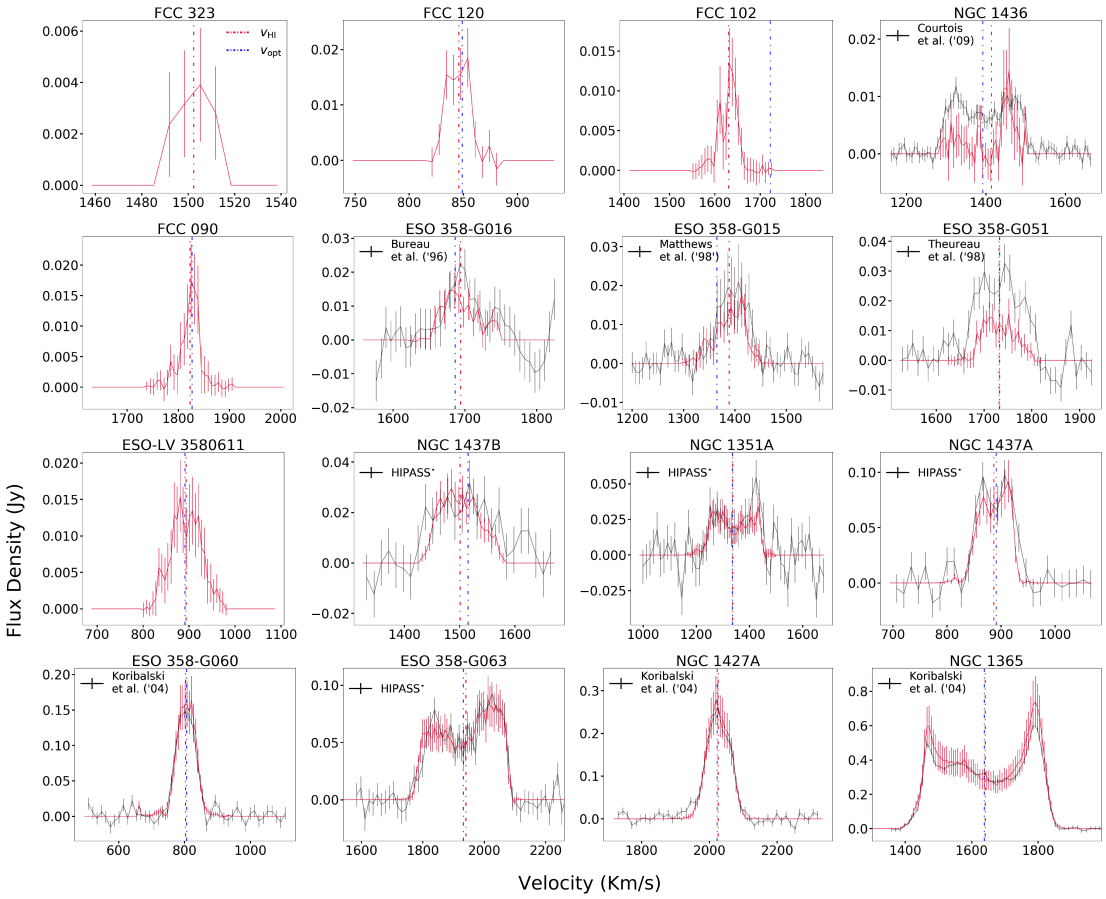

Figure 2.3: Integrated HI spectra of our Fornax HI detections (in red) sorted according to increasing HI mass as in Fig. 2.2. We compare our spectra to spectra from the literature (shown in black; see top-left corner for details). We also show the barycentric velocity obtained from our HI spectra (vertical red line) and from optical spectra (vertical blue line; Maddox et al. 2019).

detections are within $R_{\rm vir}$. The authors confirmed a HI depletion in the HI detections (all late types) near the centre of the cluster, and suggested that HI-rich galaxies detected in the outer parts of the cluster are infalling towards the cluster for the first time. HI detections are arranged in a large scale sheet-like structure with a negative velocity gradient from south-east to north-west.

Waugh (2005) presented the result of the deepest blind HI survey of the cluster so far: the Basketweave survey of Fornax carried out with the Parkes telescope. This survey used a new scanning technique, which improved the sampling and the noise level compared to HIPASS. HI was detected in 53 galaxies within 100 deg^2 down to a detection limit of 10^8 M$_\odot$. Of those, 15 were new detections, which confirmed the results of Waugh et al. (2002). In addition, the author presented higher resolution HI observations (2 arcmin, 3.3 km s^{-1}) of 28 individual Fornax galaxies carried out with the Australia Telescope Compact Array (ATCA). Of those, six are within $R_{\rm vir}$. Within this region, ESO LV-3580611 was marked as having an intriguing HI morphology with an elongation to the north-east of the system. As suggested in Schröder et al. (2001), also Waugh (2005) pointed out that this galaxy may be moving towards us.

The only other Fornax galaxy within $R_{\rm vir}$ with resolved HI imaging is NGC 1365 (van der Hulst et al. 1983; Jorsater & van Moorsel 1995). The latter study observed an elongated HI distribution to the west of the system. They suggested that it may be caused by the interaction with the ICM.

All previous blind HI surveys of Fornax were carried out with the Parkes telescope. Their angular resolution of 15 arcmin was insufficient to study the HI morphology of the detected galaxies, which is a powerful tracer of environmental effects. Better angular resolution was achieved with the interferometric observation of a few selected galaxies in Fornax (see references above), but those observations covered only a small portion of the cluster volume. Here we present the first, blind, interferometric HI survey of the Fornax cluster.

Our survey was carried out with the ATCA and covers an area of 15 deg^2 centred on NGC 1399 with a spatial and velocity resolution of $67'' \times 95''$($\sim 6 \times 9$ kpc at a distance of 20 Mpc) and 6.6 km s^{-1}, respectively. The average column density sensitivity within the survey area is $2{\times}10^{19}$ cm^{-2} (3σ over 25 km s^{-1}) and the $M_{\rm HI}$ sensitivity is $2{\times}10^7$ M$_\odot$ (3σ over 100 km s^{-1}). Initially, a case study by Lee-Waddell et al. (2018) revealed the tidal origin of NGC 1427A using spatially resolved HI images from a subregion of our ATCA mosaic. In Sect.2.2 we describe observations and data reduction. In Sect.2.3 we present the HI detections, their HI images and spectra. We also compare their HI mass, H_2 mass and SFR relative to non-cluster control samples, and compare their spatial and velocity distribution with those of the general Fornax population. In Sect. 2.4 we discuss our results, which we then summarise in Sect.2.5. We include supplementary material on each galaxy in Appendix A.

2.2 ATCA observations and data reduction

Our blind Fornax survey covers an area of 15 deg^2 (defined at a sensitivity level 3 × higher than in the best region of the HI cube), spanning from the centre of the cluster to a distance slightly further than $R_{\rm vir}$. The observations were carried out with the ATCA in the 750B configuration, from December 2013 to January 2014 (project code C2894)[1]. The cluster was observed for 336 hrs using 756 different pointings with a spacing of 8.6 arcmin (1/4 of the primary beam FWHM at 1.4 GHz)

The 64 MHz bandwidth, centred at 1396 MHz, was divided into 2048 channels, providing a velocity resolution of 6.6 km s^{-1}. We reduced the data using the `MIRIAD` software (Sault et al. 1995). PKS B1934-638 and PKS 0332-403 were chosen as the bandpass calibrator and the phase calibrator, respectively. The latter was observed at 1.5 hr intervals between on-source scans. We flagged strong radio frequency interference based on Stokes V visibilities. After flagging and calibration we further processed a restricted frequency range 1407.2 MHz - 1419.6 (which corresponds to the velocity range of 166 - 2783 km s^{-1}), which includes all spectroscopically confirmed Fornax galaxies (Maddox et al. 2019). Within this range we used the `UVLIN` task of `MIRIAD` to fit and subtract continuum emission using 2nd-order polynomials.

We obtained the dirty cube with the `INVERT` task using natural weights to maximise surface-brightness sensitivity. We used `MOSMEM` and `RESTOR` to clean and restore HI emission, respectively. The restoring Gaussian PSF has a major and minor axis FWHM of 95 and 67 arcsec, respectively, and a position angle of 0.4 deg. The root mean square (RMS) noise level of the final cube goes down to 2.0 mJy beam^{-1} in the most sensitive region. Within the survey area the RMS noise is ≤ 6.0 mJy beam^{-1} and, on average, 2.8 mJy beam^{-1}. This corresponds to a 3σ HI column density sensitivity of $N_{\rm HI} \sim 2{\times}10^{19}$ cm^{-2} assuming a line width of 25 km s^{-1} and a 3σ $M_{\rm HI}$ sensitivity of $\sim 2{\times}10^7$ M$_\odot$ over a linewidth of 100 km s^{-1}. We searched for HI sources with the SoFiA source-finding package (Serra et al. 2015) within the survey footprint (see the green outline in Fig. 2.1). By smoothing and clipping, we convolve the input cube with a set of kernels and detect emission above 3.5σ of the local noise level of each kernel. Reliable detections are identified based on the reliability algorithm presented in Serra et al. (2012), which assumes that true sources have positive total flux and that the noise is symmetric around 0. For one faint source, NGC 1436, visual inspection was necessary to improve the SoFiA detection mask used to estimate galaxy parameters. Lastly, our final list of HI detections includes a faint source which did not pass the reliability test, but which we consider a genuine detection given its spatial correspondence with the known optical source FCC 323.

[1] Data available on `https://atoa.atnf.csiro.au/query.jsp`

2.3 HI detections in the Fornax cluster

2.3.1 HI detection properties

We detect HI in the 16 galaxies listed in Table 2.1. Of these, three are new HI detections: FCC 090, FCC 102, FCC 323. The last is the only galaxy with no previous redshift measurement. In Fig. 2.1 we show the location of our HI detections on the sky and in Fig. 2.2 we show the HI morphology of each galaxy. In these figures, red and white contours, respectively, represent the lowest reliable HI column density contour, defined as 3 times the local RMS assuming a typical HI linewidth of ∼25 $\mathrm{km\,s^{-1}}$ (see Table 2.1 and top-right corner of each panel in Fig. 2.2).

Fig. 2.3 shows the integrated ATCA HI spectra of our 16 detections. We calculated the error bars by summing in quadrature the statistical uncertainty – derived from the local RMS (Table 2.1) and the number of independent pixels detected in each channel – and the flux-scale uncertainty. We find the latter to be ±20% based on the flux ratio calculated for a sample of selected bright point sources between our radio continuum image and the Northern VLA Sky Survey (Condon et al. 1998).

We compare our spectra to those obtained from previous observations. In particular, we use HIPASS spectra from the BGC catalogue (Koribalski et al. 2004) or HIPASS data reprocessed by us. Since HIPASS data do not show any emission at the position of NGC 1436 and ESO 358-G016, we used Green Bank Telescope data (GBT - Courtois et al. 2009) and Parkes data (Bureau et al. 1996) as comparison, respectively. On the other hand, HIPASS spectra of ESO 358-G015 and ESO 358-G051 are noisy, so we used comparison spectra from Matthews et al. (1998) and Theureau et al. (1998), respectively, based on Nanacy data. Furthermore the literature spectra of ESO 358-G015 and ESO 358-G016 were rebinned to our ATCA channel-width. For consistency, we calculated the uncertainties in the comparison spectra by combining the noise in the spectrum and the flux-scale uncertainty of each survey, except for ESO 358-G016 for which the flux-scale uncertainty was not provided. For this galaxy, the error bars are shown as the RMS of the spectrum. In each panel of Fig. 2.3 we also show the velocity v_{opt} derived from optical spectroscopy (Maddox et al. 2019) and the barycentric HI velocity v_{HI} derived from our ATCA spectra.

We estimated the HI mass (M_{HI}) of our detections from the integrated HI flux using Eq. 50 in Meyer et al. (2017) and adopting the same distance of 20 Mpc for all galaxies (Mould et al. 2000). The uncertainty on M_{HI} is obtained from the error bars of the spectrum (Fig. 2.3). We report HI fluxes and masses in Table 2.1. Our HI fluxes agree with those in the literature within 1σ for nine out of 13 galaxies, and within 2σ for 11 of them. The two cases with a discrepancy larger than 2.5σ are NGC 1436 and ESO 358-G051. The comparison spectrum for NGC 1436 comes from GBT data (Courtois et al. 2009) and shows that we are most likely missing HI flux from the blue-shifted part of the system. For this galaxy, the total HI flux recovered by ATCA is lower than the GBT flux by 2.5σ (corresponding to a factor of 2.8). The reason of this discrepancy arises from a combination of low S/N and the presence, in at least some of the blue-shifted channels, of artefacts

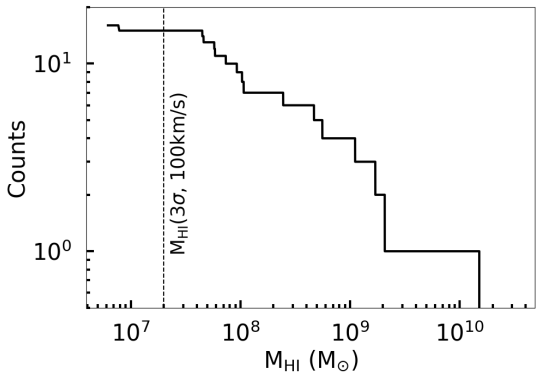

Figure 2.4: Cumulative histogram of the ATCA HI masses of our Fornax sample.

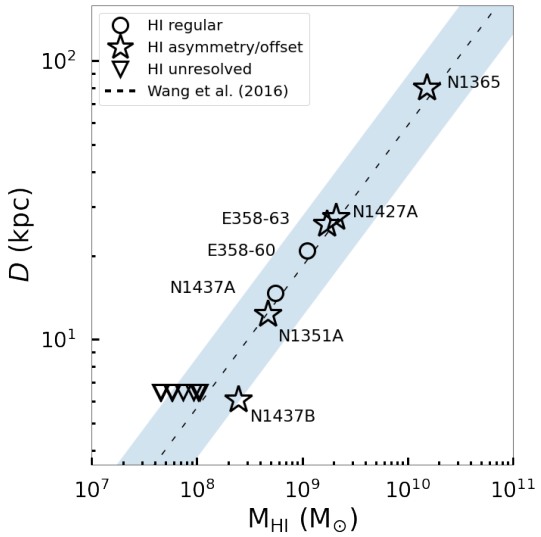

Figure 2.5: HI disc size as a function of ATCA $M_{\rm HI}$ for our resolved HI detections. Dashed line and the blue shaded area show the scaling relation and 3σ scatter respectively in (Wang et al. 2016).

in this part of the ATCA cube. The case of ESO 358-G051 is less clear since the ATCA cube does not show any obvious artefacts and the galaxy well detected. However the total HI flux recovered by ATCA is lower than the Nancay flux by 3σ. Based on the current data it is possible that some of the emission is spread over multiple ATCA beams and therefore is too weak to be detected. Future MeerKAT data will clarify this issue Serra et al. (2016). Finally, the HI mass of FCC 323 is below the typical sensitivity of our data quoted in Sec. 2.2 because of the narrow linewidth as well as the low value of the local noise (Table 2.1). Our detections cover about three of magnitude in $M_{\rm HI}$, from FCC 323 ($M_{\rm HI} = 8 \times 10^6$ M$_\odot$) to NGC 1365 ($M_{\rm HI} = 1.5 \times 10^{10}$ M$_\odot$). Fig. 2.4 shows the cumulative histogram of the HI masses of our sample.

Due to the improved resolution of ATCA over a single dish, we detected, in half of the sample, a variety of HI morphologies (see Fig. 2.2) including offsets between optical and HI centres, truncated discs, asymmetries and HI tails, which we describe in this section and in Appendix A, following the same order in which galaxies are shown in Fig. 2.2 (from the lowest to the highest HI mass): the HI distribution in FCC 102 is offset with respect to the optical centre towards the north. We also notice a large difference between $v_{\rm opt}$ and $v_{\rm HI}$, $\sim$100 km s^{-1}. However, this is consistent with the large uncertainty on $v_{\rm opt}$ given that the latter was measured from absorption lines for this galaxy (Natasha Maddox, priv. comm.); the HI peak of FCC 090 corresponds to the optical centre but the HI distribution has an elongation to the south; HI in ESO-LV 3580611 (FCC 306) is more extended to the north although there is no offset between optical and HI centre (Waugh

2005); the HI morphology of NGC 1437B (FCC 308) is asymmetric and more extended to the south; HI in NGC 1351A (FCC 067) shows an elongation towards the south; the HI of ESO 358-G063 (FCC 312) is more extended to the east side of the disc and the HI contours appear to be compressed on the west side; in NGC 1427A (FCC 235), we detected a HI tail which points to the south-east, away from the cluster centre, consistent with the tidal origin of this galaxy discussed in Lee-Waddell et al. (2018); the HI distribution in NGC 1365 (FCC 121) is extended to the north and appears to be compressed in the south-west part of the disc (see also Jorsater & van Moorsel 1995). We mark these HI disturbed galaxies with star markers in all subsequent figures.

The remaining half of the galaxies are either unresolved (or nearly so) and centred on the stellar body, or do not show noticeable asymmetries. One of them hosts a HI disc unusually truncated within the stellar disc, NGC 1436. This case will be discussed in detail in later sections as well as in Chapt. 4 of this thesis.

A final case worth commenting on is FCC 120. This galaxy has been detected with Parkes and the spectrum in Schröder et al. (2001) shows an evident double horn profile that is $\sim$100 km s^{-1} wide, while we detect a single-peak profile (within the uncertainties - see Fig. 2.3). Careful visual inspection of our HI cube did not reveal any HI emission missing from our SoFiA detection mask. The regular HI morphology of this galaxy in Fig. 2.2 and the good agreement between $v_{\rm HI}$ and $v_{\rm opt}$ in Fig. 2.3 suggest that our HI characterisation of this galaxy is correct. Future, deeper data from the Meerkat Fornax survey may confirm this (Serra et al. 2016).

We estimated the HI size for all our resolved HI detections using the method of Wang et al. 2016 from the HI intensity maps of our galaxies. We considered a galaxy resolved if its surface brightness profile deviates from the shape of the point-spread function. We measured the HI diameter where the surface density is 1 M$_\odot$ pc^{-2} and is then deconvolved with the HI beam. In Fig. 2.5 we show that both disturbed and regular galaxies follow the HI size-mass scaling relation of Wang et al. (2016) within the 3σ scatter. This can be understood as asymmetric HI features usually have a low surface brightness and do not significantly contribute to the total $M_{\rm HI}$ of galaxies. In Fig.2.5 we also show the HI unresolved galaxies. The upper limit on their size were set equal to the ATCA beam minor axis.

2.3.2 $M_{\rm HI}$ to $M_\star$ ratio

Given the abundant (albeit subtle) HI asymmetries and offsets in our Fornax sample, which might be tracing environmental interactions within or on their way to the Fornax cluster (whether with other galaxies, the large-scale potential or the intergalactic medium), we study the amount of HI in these galaxies in search of signs of HI depletion. In order to do so, we evaluated the ratio between $M_{\rm HI}$ and stellar mass ($M_\star$) for each galaxy in our sample. The $M_\star$ values are derived using the WISE W1 (3.4 μm) in−band luminosity, W1−W2 colour and the prescription given by Cluver et al. (2014), with the custom photometry further defined in Jarrett et al. (2019), and assuming a common distance of 20 Mpc for all galaxies. We show the distribution of our sample on the $M_{\rm HI}/M_\star$−vs−$M_\star$

plane in Fig. 2.6.

We compare galaxies in Fornax with a sample consisting of void galaxies from the Void Galaxy Survey (VGS - Kreckel et al. 2012) and field galaxies from the Herschel Reference Survey (HRS - Boselli et al. 2014a). We also used the xGASS $M_\star$-$M_{\rm HI}/M_\star$ scaling relation, which shows the weighted median of $\log_{10}(M_{\rm HI}/M_\star)$ as a function of $M_\star$. This was obtained from 1177 galaxies selected only by stellar mass ($M_\star$ = 10^9–$10^{11.5}$ $M_\odot$) and redshift (0.01 < z < 0.05; Catinella et al. 2018). In Fig. 2.6 we extrapolate the xGASS trend down to 10^7 $M_\odot$ (black dashed line) and show that it is consistent with the non-cluster sample of galaxies.

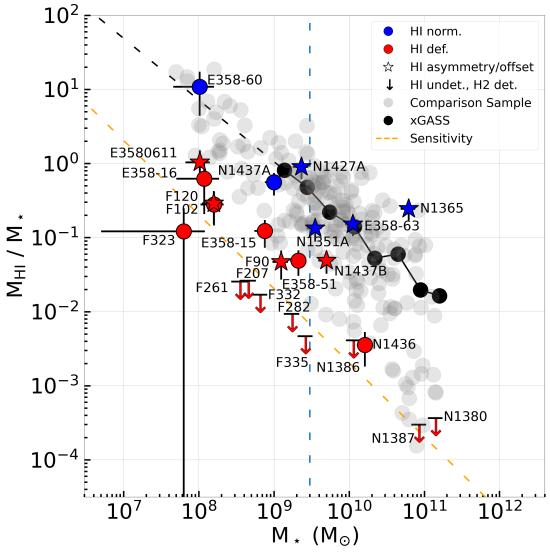

Figure 2.6: $M_{\rm HI}$ to $M_\star$ ratio as a function of $M_\star$. Fornax galaxies (red+blue markers) are compared with non-cluster galaxies from VSG+HRS (grey circles). Red and blue colours show Fornax HI deficient and normal galaxies, respectively. We show Fornax galaxies with a distorted HI morphology with star-shaped markers (see Sect- 2.3). We show with a black solid line the xGASS scaling relation. The black dashed line is the linear extrapolation of this trend for $M_\star < 1.4 \times 10^9 M_\odot$. The orange dashed line shows the ATCA average sensitivity evaluated as 3×2.8 mJy beam^{-1} with a linewidth of 100 km s^{-1}. The vertical dashed line at 3×10^9 $M_\odot$ separates low- from high-mass galaxies.

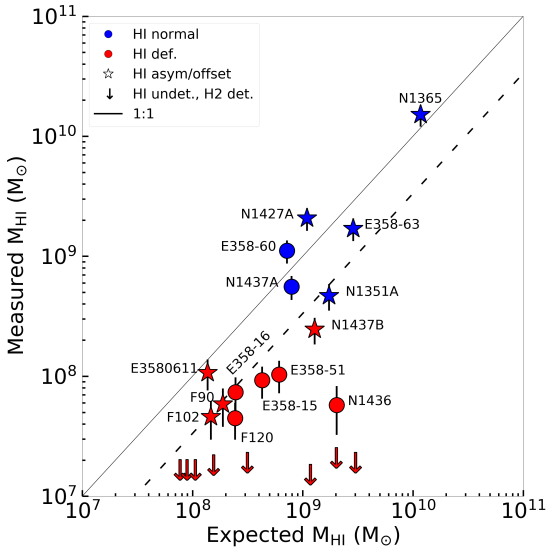

Figure 2.7: Expected $M_{\rm HI}$ versus measured $M_{\rm HI}$. The former were evaluated with the Haynes & Giovanelli's (1984) method with the coefficient summarised by Boselli & Gavazzi (2009). The latter are the ATCA $M_{\rm HI}$ calculated as described in Sect.2.3.1. The dashed line, a factor of 3 below the 1:1 relation, shows the typical threshold below which galaxies are considered deficient.

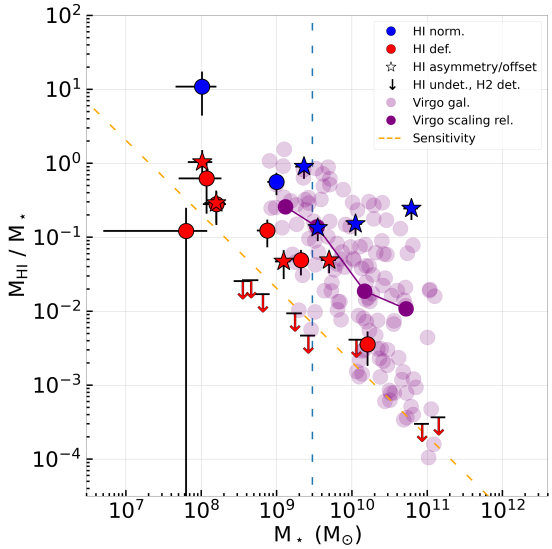

Figure 2.8: We compare Fornax galaxies (same colour coding of Fig.2.6) with Virgo cluster galaxies from HRS (light purple circles). Dark purple circles show the average scaling relation obtained from Virgo cluster galaxies (Cortese et al. 2011)

Our sample of Fornax HI detections appears to be systematically offset with respect to our VGS+HRS comparison sample and to the xGASS scaling relation. A two-sample Kolmogorov–Smirnov test on the distribution of offsets from the xGASS scaling relation rejects the null hypothesis that Fornax and VGS+HRS galaxies are drawn from the same parent sample (p-value = 0.004, KS statistic = 0.43). Indeed, ten out of 16 Fornax galaxies are below or at the lower edge of the distribution of non-cluster galaxies. Their offset from the xGASS scaling relation is larger than the RMS deviation of VGS+HRS galaxies from it, thus indicating HI deficiency. For illustrative purposes we henceforth label these HI deficient galaxies in red colours in Fig. 6 and in all other upcoming figures in this chapter.

HI deficiencies measured from plots like our Fig. 2.6 should be taken with caution because of the large $M_{\rm HI}$ scatter at at fixed $M_\star$ (e.g. Maddox et al. 2015). This scatter is to first order driven by Hubble type or, equivalently, by galaxy properties that correlate with Hubble type, such as the star formation rate (SFR). For this reason, in Sect. 2.3.3 we further analyse how the HI deficiency at fixed $M_\star$ relates to the H_2 and SFR of these galaxies. Furthermore, in the present section we estimate HI deficiencies as proposed by Haynes & Giovanelli (1984) and recently revisited by Jones et al. (2018a), where the measured $M_{\rm HI}$ is compared with an expected $M_{\rm HI}$ calculated based on galaxies' optical size and Hubble type. For this purpose, we use the coefficients summarised by Boselli & Gavazzi (2009) and originally given in Haynes & Giovanelli (1984), Solanes et al. (1996), Boselli & Gavazzi (2009), and adopt the optical sizes and Hubble types listed in Table 2.1 for our galaxies. Fig. 2.7 shows the comparison between the expected and the measured $M_{\rm HI}$. The dashed line, a factor of 3 below the 1:1 relation, is the typical threshold below which

galaxies are considered HI deficient using the Haynes & Giovanelli's (1984) method (e.g. Cortese et al. 2011). Also in this case, Fornax galaxies appear offset towards lower HI masses and there is a good match between galaxies labelled as HI deficient based on our Fig. 2.6 and those below the dashed line in Fig. 2.7.

From these figures, we see that not all galaxies with a disturbed HI morphology are HI deficient. Thus, HI morphological disturbances, whatever their exact nature (e.g. tidal or hydrodynamical, which is difficult to establish with the current data), allow us to identify cases of environmental interactions before a significant fraction of the cold interstellar medium is removed. Combining HI morphological information and $M_{\rm HI}$-$M_\star$ ratio may reveal likely new members of the cluster (we come back to this point in Sect.2.4).

Fornax galaxies with a disturbed HI morphology cover the full $M_\star$ range. However, we measure a stronger HI depletion for low mass galaxies: the average offset from the xGASS scaling relation in Fig. 2.6 is −0.86 dex and −0.33 dex for $M_\star$ below and above $3{\times}10^9$, respectively. We show the threshold of $3{\times}10^9$ $M_\odot$ with a vertical dashed blue line in Fig. 2.6.

We already mentioned the problematic detection of NGC 1436. Although we are probably missing some flux, it remains a deficient galaxy even if we estimate the HI mass from the GBT flux (Table 2.1) with a $\log_{10}(M_{\rm HI}/M_\star) = -2.0$ and an offset from the xGASS scaling relation of −0.93 dex.

Fig. 2.6 shows also eight galaxies where we did not detect HI emission but H_2 was detected with with the Atacama Large Millimeter/submillimeter Array (ALMA) (Zabel et al. 2019). For these galaxies we calculated the $M_{\rm HI}$ upper limit as 3× the local noise (Table 2.1) of the cube and assuming the CO line width of these galaxies estimated by the PV diagrams in Zabel et al. (2019). Some of these galaxies appear to have too little HI given the molecular gas content and star formation rate, as we discuss in following sections. We show the optical morphology of these galaxies in Appendix B.

Finally, Fig. 2.8 shows the comparison between Fornax and Virgo galaxies (from HRS - Boselli et al. 2014a) belonging to Virgo clouds A, B, N, E and S (as defined by Gavazzi et al. 1999) with $10^9 \lesssim M_\star \lesssim 10^{11}$ $M_\odot$. Here we show the Virgo cluster galaxies and the average scaling relation obtained from them in the same $M_\star$ range (Cortese et al. 2011). Since Virgo is populated by HI poor galaxies with respect to field galaxies (Davies & Lewis 1973; Chamaraux et al. 1980; Cayatte et al. 1994; Hughes & Cortese 2009; Chung et al. 2009), this scaling relation is shifted towards lower gas fractions with respect to xGASS (Fig. 2.6). Although Fornax and Virgo galaxies experience different cluster environments, the distribution of Fornax galaxies cover the whole range of $M_{\rm HI}/M_\star$ of Virgo galaxies, reaching the same level of HI deficiency.

2.3.3 Linking HI properties with H_2 and SFR

The ratio between molecular and atomic gas mass ($M_{\rm H_2}/M_{\rm HI}$) can be useful to identify anomalous galaxies where, for example, only the atomic phase is affected by the environment or HI is not efficiently converted to H_2. We thus compared the atomic and molecular gas reservoirs of our detections (see Fig. 2.9). For this purpose, we used H_2 masses from

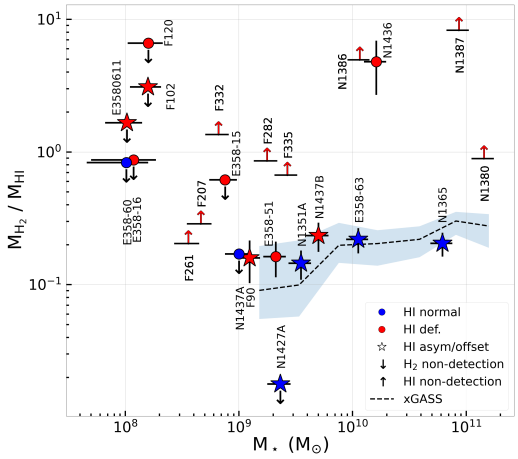

Figure 2.9: M_{H_2}/M_{HI} as a function of $M_\star$. We use the same colour coding as Fig. 2.6. Blue shadow shows $1\times\sigma$ scatter from the xGASS weighted average of $\log_{10}(M_{H_2}/M_{HI})$. We show upper limits with downward arrows. We show lower limits with upward arrows.

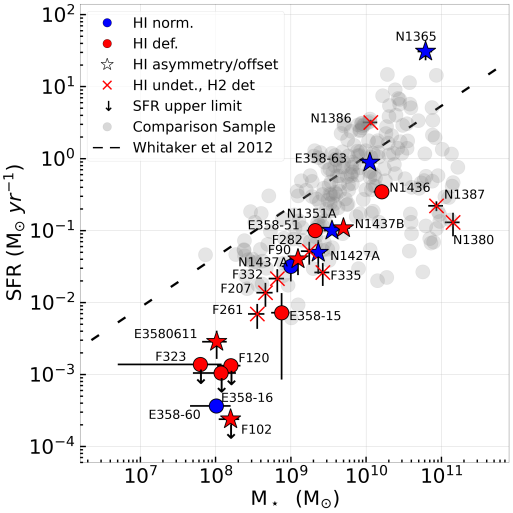

Figure 2.10: SFR as a function of $M_\star$. We use the same colour coding as Fig. 2.6. We show upper limits in SFR with downward arrows. The dashed black line represents the SFR scaling relation in (Whitaker et al. 2012).

Zabel et al. (2019) for all our HI detections except for FCC 323 (no molecular gas data available). We also include in this analysis the eight galaxies detected with ALMA (Zabel et al. 2019) that are not detected in HI (upper limits in Fig. 2.6 and Fig. 2.8; see Sec. 2.3.2). We also scaled the molecular upper limit from Zabel et al. (2019) to be consistent with a line width of 100 km s^{-1}. As a comparison, we used the xGASS $M_\star$-M_{H_2}/M_{HI} scaling relation in Catinella et al. (2018), which describes the typical M_{H_2}/M_{HI} ratio as a function of $M_\star$ at $z = 0$.

For $M_\star$>10^9 M$_\odot$, 55% of all HI detected galaxies are also H_2 detected, while this fraction drops to zero for $M_\star$<10^9 M$_\odot$ (likely because the lower metallicity of these objects makes CO progressively harder to detect). In the rest of this section we therefore focus on the higher $M_\star$ range. Here, we see that about half of the galaxies are consistent with the xGASS sample, while most of the remaining galaxies are above the xGASS scaling (see Fig. 2.9). In particular, galaxies with a distorted HI morphology are compatible with the xGASS trend with the exception of NGC 1427A whose lack of molecular gas is puzzling (see Zabel et al. 2019). Although this galaxy has a normal (and large) HI mass for its stellar mass, no molecular gas was detected with ALMA. The agreement with the scaling relation holds also for NGC 1437B, which is the only HI deficient galaxy with a distorted morphology in this range of $M_\star$.

The detection with the highest M_{H_2}/M_{HI} ratio is NGC 1436. Although we might be

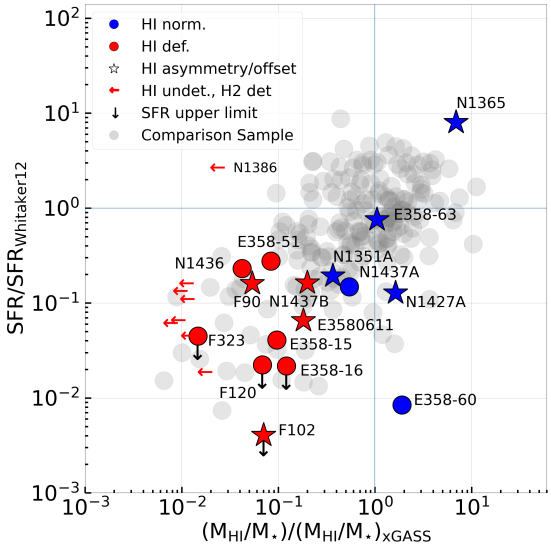

Figure 2.11: SFR deviation from the Whitaker et al. (2012) scaling relation (Fig. 2.10) plotted against the $M_{\rm HI}/M_\star$ deviation from the xGASS scaling relation (Fig. 2.6). We use the same colour coding as Fig. 2.6. We show upper limits in $M_{\rm HI}$ with leftward arrows. The horizontal blue line represents no deviation from the SFR scaling relation, while the vertical blue line represents no deviation from the $M_\star$-$M_{\rm HI}/M_\star$ scaling relation.

missing HI flux (Sect. 2.3.2), this mass ratio remains high even if we use the $M_{\rm HI}$ value estimated from the GBT flux (with a $M_{\rm H_2}/M_{\rm HI}$ = 1.7). Other three galaxies, NGC 1386, NGC 1387 and NGC 1380, may be even more peculiar as the lower limit on their $M_{\rm H_2}/M_{\rm HI}$ ratio is already an order of magnitude above the xGASS scaling relation. High $M_{\rm H_2}/M_{\rm HI}$ ratios have also been measured in Virgo galaxies (Cortese et al. 2016).

Given the broad distribution of $M_{\rm H_2}/M_{\rm HI}$ ratio in Fornax, we further investigate whether their star formation rate follows standard scaling with $M_\star$ and $M_{\rm HI}$. In particular, we are interested in understanding whether the general offset of Fornax galaxies towards low $M_{\rm HI}/M_\star$ ratios in Fig. 2.6 is associated with a decrease of SFR at fixed $M_\star$.

We start by comparing Fornax galaxies with the same sample of non-cluster galaxies used in Sect. 2.3.2. SFR of both samples of Fornax galaxies and non-cluster galaxies are evaluated using eq. 2 in Boquien et al. (2016). We set the scaling coefficient for the infrared 24 μm band (W4) equal to 6.17. We adopted the calibration factor for near UV 231 nm band (NUV) to be $\log_{10}$C = -43.17 (Kennicutt & Evans 2012). NUV fluxes come from (Cortese et al. 2012) and IRSA catalogues (Leroy et al. 2019). The former catalogue does not include all our HI detections, thus we used the latter to get the NUV flux from Fornax HI galaxies. W4 was obtained using custom software optimised for performing aperture photometry on resolved galaxies (Jarrett et al. 2013; Cluver et al. 2014; Jarrett et al. 2019). Then, we removed the contribution from the evolved stellar populations using the method of Helou et al. (2004) which consists of scaling and subtracting the W1 light (a proxy of evolved stellar population) from W4 as described in Cluver et al.

(2017). For a fraction of galaxies, NUV and W4 fluxes were not available (3/212 non-cluster galaxies; 11/24 Fornax galaxies). In these cases, we calculate the SFR from the W3 (12μm) luminosity – with stellar emission subtracted (as for W4)– and the TIR-to-MIR relation using eq. 4 in Cluver et al. (2017), where $L_{12\ \mu m}$ is the continuum-subtracted spectral ($\nu \times L_\nu$) luminosity. Our conclusions below do not change if we calculate SFR from WISE data alone.

Fig. 2.10 shows that the majority of the Fornax galaxies have a SFR below the values predicted by the scaling relation of Whitaker et al. (2012). Furthermore, the difference between the SFR of Fornax galaxies and that predicted from Whitaker et al. (2012) increases towards lower $M_\star$. That is, the SFR-$M_\star$ relation in Fornax is steeper than that of non-cluster galaxies. This might indicate a stronger SFR decrease in low-mass galaxies, similar to what observed for their HI reservoirs (as discussed in Sect. 2.3.2) and their H_2 reservoirs (Zabel et al. 2019). Also when compared to the HRS+VGS comparison sample, Fornax galaxies appear to be offset towards lower SFR values, mirroring the results in Fig. 2.6.

Among the four galaxies with the highest M_{H_2}/M_{HI} ratio in Fig. 2.9, NGC 1386 is the only one with a higher SFR than expected. This is likely due to the presence of an AGN (Rodríguez-Ardila et al. 2017) which affects the SFR measurement. The other two HI undetected galaxies, NGC 1380 and NGC 1387, reside at the lower edge of the comparison sample. We notice that NGC 1380 is also highly H_2 deficient in Zabel et al. (2019).

In Fig. 2.11 we investigate whether, in Fornax, the low SFR (at fixed $M_\star$; Fig. 2.10) can be related to the HI deficiency (Fig. 2.6). This figure plots the SFR and $M_{HI}/M_\star$ deviations from the respective scaling relations (Fig. 2.10 and Fig. 2.6) against one another. We find that Fornax galaxies mostly populate the area of the plot of HI deficient galaxies with low SFR, following the trend of non-cluster galaxies in the comparison sample. That is, in Fornax, a decrease in M_{HI} is accompanied by a decrease in SFR just like in non-cluster galaxies. In Sec. 2.4 we present an interpretation of this result.

On top of this general trend we see a few outliers. The most evident ones are ESO 358-G060 and the HI undetected NGC 1386. While the high SFR in NGC 1386 might be an artefact caused by the presence of an AGN, the case of ESO 358-G060 is more complicated. We carefully inspected this galaxy's WISE images and no SFR from W3/W4 with old stellar population subtraction was detectable. Therefore, we calculated its SFR the from NUV flux alone using eq. 12 in Kennicutt & Evans (2012). Although ESO 358-G060 is HI rich, its SFR is lower than that any galaxy of the comparison sample with a similar $M_\star$. It is worth noting the cases of NGC 1436 which lies at the upper edge of the comparison sample of HI deficient galaxy (bottom-left quadrant of Fig. 2.11) and NGC 1427A which shows a low SFR although its large HI reservoir. All these cases will be discussed in Sect. 2.4.

2.3.4 HI properties as a function of 3D location in Fornax cluster

In this section we compare the distribution of our HI detections and that of the general population of Fornax galaxies. Thus, we made use of the cleaned spectroscopic catalogue we obtained in Sect. 1.5. It includes 81 spectroscopically confirmed Fornax members. We extracted these 81 objects by removing duplicates and compact stellar system (which are not expected to host any HI) from the catalogue of Maddox et al. (2019), which is a recent compilation of spectroscopic observations undertaken within the Fornax region. We evaluated a completeness of our cleaned catalogue higher than 50% in each magnitude bin below $m_r < 16.5$ mag (see Fig. 1.6) by a cross-match with the joint photometric catalogues whose photometry was measured by the Fornax Deep Survey (Venhola et al. 2018; Iodice et al. 2019a; Raj et al. 2019), Lee-Waddell et al. 2018, and some unpublished one was measured in this work. The total completeness of the catalogue is ∼85%.

Fig. 2.12 shows the comparison between the 2D distribution of our Fornax HI detections with that of all spectroscopic Fornax members (Maddox et al. 2019) included within our survey footprint. Keeping in mind that the area of the sky that we observed is not symmetric, most of the galaxies in our sample are located south of the centre of the cluster, while only four out of 16 detections are located north of it.

Almost all our HI detections (88% of the sample) are located farther than 0.5 $R_{\rm vir}$ in projection (the only exceptions being NGC 1427A at 0.2 $R_{\rm vir}$, and ESO 358-G051 at 0.4 $R_{\rm vir}$). In contrast, only 52% of all Fornax galaxies in our footprint are outside 0.5 $R_{\rm vir}$.

The same effect, with the addition of the kinematical information, can be seen in the projected phase-space diagram shown in Fig. 2.13. We used a cluster systemic velocity of $v_{\rm sys} = 1442$ km s^{-1} and a cluster velocity dispersion of $\sigma_{\rm cl} = 318$ km s^{-1} (Maddox et al. 2019). In order to draw caustic curves we proceeded as in Jaffé et al. (2015) using $M_{\rm vir} = 5{\times}10^{13}$ M$_\odot$, $R_{\rm vir} = 700$ kpc (Drinkwater et al. 2001a) and a cluster halo concentration parameter equal to 6 (Navarro et al. 1996; the exact value of this parameter does not change the result significantly). The inner triangle shows the virialised area where it is more likely to find old members of the Fornax cluster (Rhee et al. 2017). From the right histogram in Fig. 2.13, we see that the spectroscopic Fornax members have a peak at the cluster systemic velocity, while velocities of our HI detections cover all velocity range without any preferred velocity. Thus, both Fig. 2.12 and Fig. 2.13 show that the HI galaxy sample does not follow the distribution of spectroscopic galaxies (we refer the reader to Fig. 1.8 and Fig. 1.9 for the detailed 2D distribution and projected phase-space diagram of ETGs, Iodice et al. 2019a, LTGs, Raj et al. 2019, dwarfs, Venhola et al. 2018 and galaxies whose photometry was measured in this work).

In Fig. 2.13, we also see that 11 out of 16 galaxies are within the escape velocity boundary in projection (black lines). It is worth noting that the HI deficient galaxies FCC 120 and ESO-LV 3580611 are located outside the caustic curves. Among HI disturbed galaxies, six out of eight are redshifted with respect to the recessional velocity of the cluster.

Both Fig. 2.12 and Fig. 2.13 show that some galaxies in our sample are not just close

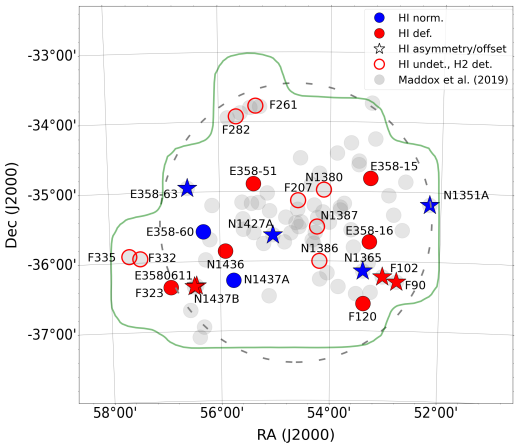

Figure 2.12: Distribution of our Fornax HI detections on the sky (blue and red markers) compared to that of all Fornax galaxies in our footprint (grey circles; Maddox et al. 2019). The green and gray contours are the same as Fig. 2.1.

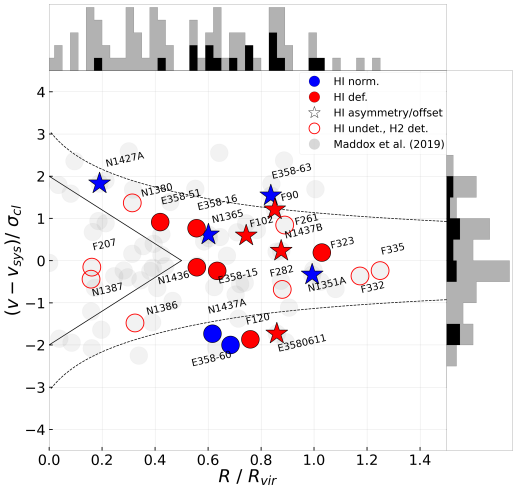

Figure 2.13: Phase space diagram of the Fornax cluster. Here, we used the same colour coding as Fig. 2.12. We show the caustic curves of the cluster with black dashed lines. Histograms: black and gray colours represent HI detected galaxies and all Fornax members, respectively. The area within the black triangle shows the virialised area of the cluster

by one another on the sky but also in velocity. The clearest case is that of NGC 1365 and its three neighbours: FCC 102, FCC 090 and ESO 358-G016. They are all within a region of 250 kpc and a velocity range of 200 km s^{-1}. These galaxies might be part of a substructure which is accreting onto the cluster (as suggested by Drinkwater et al. 2001a). In addition, most galaxies in this substructure exhibit indications of ongoing interactions with one another and/or with the intergalactic medium. Both HI elongations in FCC 102 and NGC 1365 point in projection to the north, while HI in FCC 090 is elongated towards the south. FCC 090, FCC 102 and NGC 1365 form a triplet of galaxies which lies along a line that points towards the centre of the cluster. ESO 358-G016 has a regular HI distribution and it lies in projection to the north of NGC 1365. All but NGC 1365 are HI deficient galaxies. The existence of a sub-group centred on NGC 1365 is also consistent with the large scale structure around Fornax (the Fornax-Eridanus supercluster), which is mainly made by several groups of galaxies that are assembling to form the cluster along the filament (Nasonova et al. 2011).

On the east of the cluster centre, we also see that FCC 323 and NGC 1437B are near each other on the sky in projection (∼120 kpc apart), as well as in velocity (∼10 km s^{-1}

difference). The unresolved HI morphology of FCC 323 does not reveal, at this time, whether there is an ongoing interaction between those galaxies. We mark it as a potential subgroup.

Another intriguing galaxy is ESO 358-G060. Among the galaxies with $M_\star \leq 10^9$ $M_\odot$ it is the only one with a normal HI content compared to non-cluster galaxies (see Fig. 2.6), and it shows no evidence of on-going interactions with the Fornax environment (see Fig. 2.2). Given its position just outside the caustic curves in Fig. 2.13, we discuss in Sect. 2.4 whether it might not have entered the cluster yet. Another, similar case is NGC 1437A. It is a HI rich galaxy which shows a quite regular HI morphology. It is also just outside the caustic curves in Fig. 2.13. However, unlike the undisturbed ESO 358-G060, the optical appearance of NGC 1437A is peculiar, similar to that of NGC 1427A, since they both exhibit an arrow shaped optical morphology as pointed out in Raj et al. (2019). The MeerKAT Fornax Survey (Serra et al. 2016) will deliver a higher resolution HI image of this object and will be able to reveal any HI asymmetries that might be hidden by projection effects within the ATCA beam.

2.4 Discussion

The population of HI detected Fornax galaxies exhibits several interesting features. Despite the limited resolution of our data, half of all detections reveal HI asymmetries and offsets relative to the stellar body (Fig. 2.2). Furthermore, the HI sample as a whole is gas-poorer and is forming stars at a lower rate than samples of non−cluster galaxies in the same $M_\star$ range (Fig. 2.6 and Fig. 2.10), and half of the galaxies with $M_\star > 10^9$ $M_\odot$ have an anomalous M_{H_2}/M_{HI} ratio. Finally, the HI detections are distributed in a noticeably different way with respect to the majority of cluster galaxies both on the sky and in projected phase space (Fig. 2.12 and Fig. 2.13). This body of evidence suggests that the Fornax environment is influencing the evolution of these galaxies, which may be the most recent arrivals in the cluster. In particular, the difference between the 3D distribution of HI detected galaxies compared with that of spectroscopically confirmed Fornax members, indicates that HI is a crucial observable to test the volume of the cluster where HI rich galaxies become HI deficient, before a complete HI removal in the inner part of the cluster.

An outstanding question is how long it takes for a galaxy to lose its HI – the dominant component of the interstellar medium – as it falls into a cluster. In the case of Fornax we can gain some insight through a joint analysis of Fig. 2.11 and Fig. 2.13. If we assume that HI is being actively removed from within galaxies in Fornax (as suggested by the frequently disturbed HI morphologies - see Fig. 2.2), the lack of HI detections in the virialised region of Fig. 2.13 implies that HI removal happens on a time scale $\tau_{HI,loss}$ shorter than the cluster's crossing time: $\tau_{HI,loss} \leq \tau_{cross} \sim R_{vir}/\sigma_{cl} \sim 2$ Gyr (see Sect. 2.3.4; this τ_{cross} is similar to that estimated from simulations, 1.2 ± 0.5 Gyr independent of cluster mass; Rhee et al. 2017). Hence, we expect that our 16 detections will have lost most of their HI by the time they reach the pericentre.

On the other hand, Fig. 2.11 suggests that, so far, HI has been lost slowly in our HI detections (having been removed and/or consumed, and not replenished). In that figure, our Fornax HI detections are distributed along the same correlation defined by non-cluster galaxies. Thus, for those Fornax galaxies, the SFR has so far had sufficient time to respond to a variation in HI mass – just like outside clusters. Since the transition from HI to new stars happens through the intermediate phase of H_2, this 'equilibrium' between HI and SFR implies that H_2 is depleted faster than HI is lost in galaxies currently at the cluster's outskirts, giving the entire cycle of HI-to-H_2-to-SFR enough time to 'see' the varying HI content. Thus, while for Fornax as whole $\tau_{\rm HI,loss} \leq \tau_{\rm cross} \sim 2$ Gyr (see above), for our HI detections in the outer regions of Fornax $\tau_{\rm HI,loss}$ has so far been $\geq \tau_{\rm H_2,depl} \sim$ 1-2 Gyr (Bigiel et al. 2008). (The H_2 depletion time $\tau_{\rm H_2,depl}$ is only marginally shorter in Fornax, in particular at its outskirts, and anyway with large variations from galaxy to galaxy; Zabel et al. 2020.)

It is likely that, further inside Fornax, HI is removed faster than what we estimated above for galaxies at the cluster's outskirts. Indeed, simulations indicate that for a galaxy within 0.5 $R_{\rm vir}$, $\tau_{\rm HI,loss} < 0.5$ Gyr (Marasco et al. 2016). Such a rapid HI removal may not leave sufficient time for the SFR to 'track' the decrease in HI mass in Fig. 2.11, resulting in galaxies moving to the left of the non-cluster sample. A confirmation of this effect may come from the eight H_2-detected galaxies (most of them H_2-deficient; Zabel et al. 2019) where HI has already been removed at least down to the ATCA $M_{\rm HI}$ sensitivity (left-pointing arrows in Fig. 2.11), and possibly by some HI detections closer to the cluster centre (e.g. NGC 1436). Indeed, these galaxies occupy a region to the left of the comparison sample, showing that their SFR is still significant despite their low HI content. For these galaxies, HI is likely to have been removed faster than H_2 is depleted: $\tau_{\rm HI,loss} \leq \tau_{\rm H_2,depl}$. This conclusion is supported by the anomalously high $M_{\rm H_2}/M_{\rm HI}$ ratio of these galaxies in Fig. 2.9 (in the $M_\star$ range where we have a reliable comparison).

Within the picture discussed above, HI-detected galaxies in the outer regions of Fornax are thus first infallers, which are starting to interact with the Fornax environment and will lose most of their HI by the time they reach the pericentre. Even at the current early stage of infall, they already show a relatively large diversity in HI morphology (Fig. 2.2) and mass (Fig. 2.6). More specifically, we found two morphologically undisturbed HI rich galaxies (12% of the HI detections); four morphologically disturbed HI rich galaxies (25% of the HI detections); four morphologically disturbed HI deficient galaxies (25% of the HI detections); six morphologically undisturbed - within the ATCA resolution - HI deficient galaxies (38% of the HI detections).

The morphologically undisturbed HI-rich galaxies are ESO 358-G060 and NGC 1437A. They both reside outside the caustic curves in projection (Fig. 2.13) and, given their low $M_\star$, they should be easily perturbed by the Fornax environment. Thus, we speculate that they are recent Fornax members which have not yet had enough time to be significantly affected by the cluster. One possible caveat is the low resolution of our images, which may hide HI disturbances in particular in the case of the optically peculiar galaxy NGC 1437A. Another possibility is that they are outside the cluster volume or in a region with lower ICM density. ESO 358-G060 is also an outlier in Fig. 2.11, where the

relatively high $M_{\rm HI}/M_\star$ does not correspond to a high SFR. In this galaxy no SFR was detectable from WISE W3/W4 bands (after subtracting the old stellar population light), and the NUV contribution to star formation is low. Several physical processes might account for the low SFR with respect to the large HI reservoir: for example, an inefficient HI to H_2 conversion due to a small amount of dust, a large angular momentum which prevents the HI from collapsing, and/or an HI external origin (e.g. see Geréb et al. 2016, 2018).

The morphologically disturbed HI-rich galaxies are ESO 358-G063, NGC 1351A, NGC 1427A, NGC 1365. We discuss the last galaxy when we focus our attention on the HI detected subgroup of interacting galaxies. ESO 358-G063 and NGC 1351A, are both disc galaxies north of NGC 1399. They are both quite isolated from all other Fornax Galaxies in RA, Dec and velocity in projection (see Fig. 2.12 and Fig. 2.13). Thus, their slightly HI disturbed morphologies described in Sect.2.3 might be due to the interaction with the ICM of the Fornax cluster. Furthermore, the agreement of $M_{\rm H_2}/M_{\rm HI}$ of ESO 358-G063 and NGC 1351A with the xGASS scaling relation in Fig. 2.9 suggests that they are recent Fornax members, thus the cluster environment has not had enough time to significantly deplete their HI reservoirs. The last morphologically disturbed HI rich galaxy is NGC 1427A. This is the galaxy with the second-highest HI mass in our sample of Fornax HI detections. In Fig. 2.12 and Fig. 2.13, we see that NGC 1427A is the closest HI detected galaxy to the centre of the cluster in projection, but it has also the highest velocity. Thus, it may be a new Fornax member which is infalling from the foreground. As already mentioned, Lee-Waddell et al. (2018) studied the origin of the HI tail using the same data we present here. They concluded that, unlike previously suggestions, ram-pressure is unlikely to be the main process shaping the galaxy's optical appearance. Instead, NGC 1427A is most likely a recent merger remnant, thus shaped by tidal forces. The recent merger might be the cause of the low molecular column density and/or its low metallicity, resulting currently undetected by ALMA (Zabel et al. 2019; it is the upper limit with the highest $M_\star$ in Fig. 2.9). NGC 1427A is also the second HI rich outlier with low SFR in Fig. 2.11. The HI-to-H_2 conversion might be inefficient to have a SFR consistent with its $M_{\rm HI}/M_\star$ ratio.

The only HI deficient and morphologically disturbed galaxies which do not belong to the NGC 1365 subgroup are: ESO-LV 3580611 and NGC 1437B. They are very close to one another on the sky but have significantly different velocities. The former is outside the caustic curve in projection (Fig. 2.13), which supports the hypothesis of an new infalling Fornax member made by Schröder et al. (2001). The latter has a velocity similar to the recessional velocity of the cluster. HI and molecular morphologies (the latter detected by Zabel et al. 2019) are elongated in the same direction. This suggests that both gas phases are experiencing the same environmental interaction. Raj et al. 2019 detected a tidal tail in NGC 1437B, which may be due to a recent fly-by of another galaxy. As mentioned in Sect.2.3.4, although the evidence is not strong, NGC 1437B might be part of a subgroup of interacting galaxies which includes FCC 323. Thus, FCC 323 might be the fly-by galaxy that NGC 1437B has interacted with.

It is difficult to comment on the morphologically undisturbed HI deficient galaxies, since their symmetric HI distribution may be a consequence of the ATCA resolution.

However, a very peculiar case is the truncated HI disc of NGC 1436. It is the closest spiral galaxy to the centre of the cluster detected in HI. Raj et al. (2019) observed an ongoing morphological transition into lenticular: the spiral structure is found only in its inner region, while the outer disc has the smooth appearance typically found in S0 galaxies.

The inner part of NGC 1436 appears regular also in H_2, and the galaxy is just moderately H_2 deficient (Zabel et al. 2019). It is also the only galaxy detected both in HI and H_2 which shows a high M_{H_2}/M_{HI} ratio in Fig. 2.9. These results and the evidence of morphological distortions only in the outer part of the galaxy suggest that this galaxy may have gone through a quick interaction with the cluster environment, which did not affect the inner spiral structure yet. This idea is corroborated by the fact that NGC 1436 lies on the upper edge on the comparison sample in Fig. 2.11, which means that despite its HI deficiency it is still forming stars at a significant rate. In Chapt. 4 of this thesis we study this galaxy in more detail.

Finally, we focus on the NGC 1365 subgroup. We discussed all the HI morphologies and the 3D distribution of the subgroup members in Sect.2.3.1 and Sect.2.3.4, respectively. As mentioned earlier, NGC 1365 is the only HI rich galaxy of the subgroup (Fig. 2.6) with a M_{HI} at least two orders of magnitude larger than the other members. The HI distribution both in NGC 1365 and in FCC 102 is elongated to the north, while it is elongated to the south in FCC 090. ESO 358-G016 is the only galaxy with a regular HI morphology. It is also the only galaxy located north of NGC 1365. We propose two scenarios in order to explain the properties of the subgroup and its members: the former is a case of interaction between galaxies and the cluster environment which is responsible of the high $M_{HI}/M_\star$ ratio of the low mass members. In contrast, due to to its deep gravitational potential, NGC 1365 has been able to retain its HI, although some of it has been perturbed. The latter scenario we propose, it is a case of preprocessing in a group of galaxies where the local environment of the subgroup was able to affect the $M_{HI}/M_\star$ ratio of the low mass members before the group began to interact with the cluster environment.

In general, although we found a large variety of HI properties in our sample of HI detections, we detected an overall trend towards HI disturbances and deficiency in Fornax. Fig. 2.6 makes evident an already evolved state of Fornax HI galaxies where ∼2/3 of the galaxies are HI deficient. Fig. 2.6 also shows that the Fornax environment is more effective in altering the gas content of galaxies with $M_\star < 3 \times 10^9$ $M_\odot$ (see Sect.2.3.2).

Zabel et al. (2019) presented a similar study, where they compare Fornax and field galaxies based on their molecular gas properties. They found some molecular deficiency in all their detections except NGC 1365. However, galaxies with $M_\star < 3{\times}10^9$ $M_\odot$ are both more H_2-deficient and morphologically disturbed with respect to more massive galaxies, whose molecular gas morphology is always regular. We do not observe such a clear difference in HI. Indeed, we observe disturbed HI morphologies across our entire $M_\star$ range, confirming that atomic hydrogen is the best tracer of early interactions. Despite this difference between HI and H_2 morphologies, we also note some similarities between our results and those in Zabel et al. (2019). Indeed, the mass range of molecular disturbed galaxies is also characterised by a stronger HI depletion. Conversely, the HI depletion

is weaker in the mass range in which galaxies show regular molecular-gas morphologies ($M_\star > 3{\times}10^9$ M$_\odot$; Sect.2.3.2). Thus, both gas phases show that the Fornax environment is more effective in altering the gas content of low-mass galaxies compared to high-mass galaxies.

Finally, our results are in agreement with the FDS and the Fornax 3D survey (F3D) results (Iodice et al. 2019a,b). Indeed, almost all galaxies with a disturbed HI morphology are of late type and belong to the group of the infalling galaxies in (Iodice et al. 2019a), which are symmetrically distributed around the cluster's central region. These galaxies have active star formation and are located in the low-density region of the cluster, where the X-ray emission is faint or absent. Our results show that they are interacting with the cluster environment. Deeper into the cluster, the lack of HI detections is consistent with the result that this region is dominated by evolved early-type galaxies. Some of these galaxies have been able to retain part of their H_2 reservoirs (Zabel et al. 2019), but not their HI.

2.5 Summary

The blind ATCA HI survey of the Fornax galaxy cluster covers a field of 15 deg^2 out to a distance of $\sim R_{\rm vir}$ from the cluster centre. It has a spatial and velocity resolution of $67'' \times 95''$and 6.6 km s^{-1}, respectively, and a 3σ $N_{\rm HI}$ and $M_{\rm HI}$ sensitivity of $\sim 2 \times 10^{19}$cm^{-2} and $\sim 2 \times 10^7$M$_\odot$, respectively. The survey revealed HI emission from 16 Fornax galaxies covering a mass range of about three orders of magnitude, from 8×10^6 to 1.5×10^{10} M$_\odot$. These galaxies exhibit a variety of disturbances of the HI morphology, including asymmetries, tails, offsets between HI and optical centres and a case of a truncated HI disc (Fig. 2.2). This suggests environmental interactions within or on their way to Fornax (whether with other galaxies, the large-scale potential or the intergalactic medium), supported by the offset of Fornax galaxies towards low $M_{\rm HI}/M_\star$ ratios with respect to the xGASS $M_\star$-$M_{\rm HI}/M_\star$ scaling relation (Fig. 2.6), and resulting in HI deficiencies similar to those observed in the Virgo cluster (Fig. 2.8). The HI sample of Fornax galaxies is also forming stars at a lower rate than samples of non-cluster galaxies at fixed $M_\star$ (Fig. 2.10). This deficit of SFR is consistent with the deficit of HI when compared to non-cluster galaxies (Fig. 2.11).

Our 16 detections reside outside the virialised region of the cluster – where the distribution of the general population of Fornax galaxies is clustered (see also Sect. 1.5) – both on the sky and in the projected phase space diagram (Fig. 2.12 and Fig. 2.13). This result implies that HI is lost down to the ATCA sensitivity within a crossing time ($\tau_{\rm HI,loss} \leq \tau_{\rm cross} \sim 2$ Gyr), and that our HI detections are recent arrivals in the cluster. They still reside at the outskirts of Fornax, where their HI and SFR properties suggest that HI has so far been lost on a time scale longer than the H_2 depletion time ($\tau_{\rm HI,loss} \geq \tau_{\rm H_2,depl} \sim 1{-}2$ Gyr). In the cluster's central regions HI removal is likely to proceed faster ($\tau_{\rm HI,loss} < \tau_{\rm H_2,depl}$). This is supported by the relatively high SFR of HI-undetected, H_2-detected galaxies and by the anomalously high $M_{\rm H_2}/M_{\rm HI}$ ratios of galaxies

in those regions (Fig. 2.9, Fig. 2.12 and Fig. 2.13). These are galaxies where SFR is likely to be proceeding relatively unperturbed after rapid removal of the HI.

This picture is enriched by the new detection of the NGC 1365 subgroup – where both pre-processing and early interaction with the cluster environment are plausible scenarios to account for the HI properties of its members – and by the detection of several galaxies with peculiar ISM properties, such as some HI-rich but H_2-poor and low-SFR galaxies (NGC 1427A, ESO 358-G060). The future MeerKAT Fornax Survey (Serra et al. 2016) will observe this cluster with a better resolution and sensitivity than those of our ATCA survey, enabling a further step forward in the study of the evolution of Fornax galaxies.

Name	FCC	RA (J2000) (hh:mm:ss.ss)	Dec (J2000) (dd:mm:ss.ss)	v_{opt} $(\frac{km}{s})$	v_{HI} $(\frac{km}{s})$	Flux $(\frac{Jykm}{s})$	M_{HI} $(10^8 M\odot)$	$M_\star$ $(10^8 M_\odot)$	RMS $(\frac{mJy}{beam})$	Flux (literature) $(\frac{Jykm}{s})$	Morph.	D_{25}(B) (arcsec)	Notes
ESO 358-G015	113	03:33:06.85	-34:48:29.19	1365	1389	1.0±0.2	0.9±0.2	8±2	2.4	1.4±0.2*	Scd	72.10	HI def.
ESO 358-G016	115	03:33:09.19	-35:43:06.69	1686	1694	0.8±0.2	0.7±0.2	1.2±0.2	2.5	1.2±0.5△	Im	48.42	HI def.; N1365 s.group
ESO 358-G051	263	03:41:32.59	-34:53:17.99	1733	1731	1.1±0.2	1.0±0.2	21±5	2.5	2.8±0.4◦	Scd	92.90	HI def.
ESO 358-G060	302	03:45:12.14	-35:34:15.26	806	803	12±2	11±2	1.0±0.6	2.4	10.6±0.6▼	Scd	104.30	
ESO 358-G063	312	03:46:19.00	-34:56:36.80	1932	1940	18±4	17±3	110±30	2.6	18.7±0.9▲	Scd	280.60	HI dist;
ESO-LV 358-0611	306	03:45:45.39	-36:20:47.50	891	894	1.1±0.2	1.1±0.2	1.0±0.4	2.4	2.7±0.7▽	Im	31.99	HI def.; HI dist;
FCC 090	090	03:31:08.26	-36:17:24.50	1827	1823	0.6±0.2	0.6±0.1	13 ±3	2.3	#	E	62.80	HI def.; HI dist; N1365 s.group
FCC 102	102	03:32:10.73	-36:13:14.91	1722	1631	0.5±0.1	0.5±0.1	1.6±0.5	2.5	#	Im	33.50	HI def.,HI dist; N1365 s.group
FCC 120	120	03:33:34.22	-36:36:21.29	849	846	0.5±0.1	0.4±0.1	1.6±0.5	2.4	1.9±0.9▽	Im	48.13	HI def.
FCC 207	207	03:38:19.27	-35:07:44.69	1393	#	<0.1	<0.1	5 ± 1	2.3	#	E	36.65	HI undet.
FCC 261	261	03:41:21.52	-33:46:09.19	1710	#	<0.1	<0.1	3.6 ± 0.9	2.3	#	E	39.75	HI undet.
FCC 282	282	03:42:45.31	-33:55:13.80	1225	#	<0.2	<0.2	18 ± 4	2.5	#	E	54.39	HI undet.
FCC 323	323	03:47:37.52	-36:21:46.83	#	1502	0.08±0.03	0.08±0.03	0.6 ± 0.6	2.4	#	E	#	HI def.
FCC 332	332	03:49:49.02	-35:56:44.09	1326	#	<0.1	<0.1	7 ± 2	2.3	#	E	43.90	HI undet.
FCC 335	335	03:50:36.73	-35:54:33.59	1367	#	<0.1	<0.1	27 ± 6	2.6	#	E	80.90	HI undet.
NGC 1351A	067	03:28:48.72	-35:10:41.30	1336	1337	5±1	5±1	35±8	3.2	6.1±0.9▲	Sc	161.50	HI dist;
NGC 1365	121	03:33:36.37	-36:08:25.44	1638	1641	160±30	150±30	600±100	2.8	146±3▼	Sb	673.20	HI dist.; N1365 s.group
NGC 1380	167	03:36:27.59	-34:58:34.41	1877	#	<0.6	<0.5	1400 ± 300	2.6	#	S0a	287.20	HI undet.
NGC 1386	179	03:36:46.18	-35:59:57.86	972	#	<0.5	<0.5	120 ± 30	2.9	#	Sa	203.30	HI undet.
NGC 1387	184	03:36:57.06	-35:30:23.90	1302	#	<0.3	<0.3	900 ± 200	2.1	#	E	169.10	HI undet.
NGC 1427A	235	03:40:09.30	-35:37:27.99	2023	2026	22±4	21±4	23±5	2.3	22.5±0.8▼	Im	140.70	HI dist;
NGC 1436	290	03:43:37.08	-35:51:10.90	1392	1414	0.6±0.2	0.6±0.2	160±40	2.5	1.7±0.2◦	Sc	177.10	HI def.; truncated HI disc
NGC 1437A	285	03:43:02.19	-36:16:24.14	891	887	6±1	6±1	10±3	2.4	7±1▲	Scd	111.70	
NGC 1437B	308	03:45:54.85	-36:21:25.09	1515	1501	2.6±0.5	2.4±0.5	50 ±10	2.5	3.2±0.6▲	Scd	157.80	HI def.; HI dist;

Table 2.1: We report parameters on the HI detected galaxies. RA and Dec coordinates correspond to the optical centres from NED. Errors on the total HI fluxes are evaluated as described in Sect.2.3. 'Flux (literature)' shows the total fluxes measured from other surveys as follows: ⋄ Courtois et al. (2009); △ Bureau et al. (1996); ∗ Matthews et al. (1998); ◦ Theureau et al. (1998); ▽ Schröder et al. (2001); ▼ Koribalski et al. (2004); ▲ HIPASS data reprocessed by us. The total flux uncertainty of the comparison spectra are calculated as described in Sect. 2.3 combining the noise in the spectrum and the flux-scale uncertainty of each survey except for ESO 358-G016 for which the flux-scale uncertainty was not provided. For this galaxy we show the uncertainty on the total flux given in Bureau et al. (1996). Columns 'Morph.' and 'D_{25}(B)' show the optical morphology and the optical size of our galaxies used in Sect. 2.3.2 to evaluate the expected HI content of our galaxies with the Haynes & Giovanelli's (1984) method. D_{25}(B) is the optical isophotal diameter measured at 25 mag/arcsec^2 in B-band; we collected these values from NED for 17 out of 24 galaxies. Almost all of the optical diameters comes from RC3 catalogue (de Vaucouleurs et al. 1991), two out of 15 are from Lauberts & Valentijn (1989). We estimated D_{25}(B) for all the remaining galaxies except for FCC 323 as follows: from the optical multi-component decomposition made by Su et al. (2021), we scaled the r-band radial profile to B-band. In order to do this, we previously converted g-r from Venhola et al. (2019) to obtain B-r using the intermediate conversion formula g-r to B-g (Lupton 2005). In column 'Notes': HI def, HI dist, N 1365 s.group stand for HI deficient, HI morphologically disturbed galaxy, and galaxy included in the NGC 1365 subgroup, respectively.

Chapter 3

The HI mass function of the Fornax galaxy cluster

3.1 Introduction to the HIMF

The idea of measuring the HIMF, which defines the number of galaxies per unit of volume as a function of $M_{\rm HI}$, was firstly introduced by Briggs (1990) as a tool for evaluating the completeness of optical catalogues against 21-cm HI surveys. Optical catalogues might suffer of bias towards bright galaxies, while blind HI surveys might in theory detect HI emission from faint optical objects which are HI rich, for example low surface brightness galaxies (LSB - e.g. Schombert et al. 1992; de Blok et al. 1996). From the original purpose, since its shape tells us how HI in the local Universe is distributed, the HIMF has been crucial to constrain theories of cosmology and galaxy evolution (e.g. Vogelsberger et al. 2014; Lu et al. 2014; Crain et al. 2015). Many factors contribute to making the stellar and HI mass functions at least partly independent of one another and, therefore, both are important for a comparison to models. First of all, galaxies with the same stellar mass show a large scatter in their HI content (Maddox et al. 2015). Secondly, free floating HI clouds with no optical counterpart might also contribute to the HIMF. And, finally, especially in dense environment, the opposite scenario of having bright galaxies with no HI - at least down to the sensitivity of observations - is common (e.g. Haynes & Giovanelli 1986). Generally, having an optical counterpart to cross-match HI objects is important to gain deeper insights into the processes governing the evolution of galaxies (Durbala et al. 2020).

In recent years, large blind HI surveys have collected data which were used to estimate the HIMF of the local universe. Specifically, HIPASS with the Parkes telescope (Zwaan et al. 2005) and ALFALFA with the Arecibo telescope (Jones et al. 2018b) have measured the HIMF, which can be parameterized well as a Schechter function:

$$\phi(M_{\rm HI}) = \frac{dn}{d\log_{10}(M_{\rm HI})\,dV} = \ln(10)\phi_*\left(\frac{M_{\rm HI}}{M_*}\right)^{\alpha+1}\exp\left(-\frac{M_{\rm HI}}{M_*}\right) \tag{3.1}$$

where dn is the number of galaxies within a $d\log_{10}(M_{\rm HI})$ bin and a volume dV. ϕ_* is a

normalization factor, M_* is the knee above which the number of HI rich galaxies decreases exponentially, and α describes the power-law trend at the low-mass end of the HIMF. As an example, we show in Fig. 3.1 three HIMFs with the same normalization factor, the same knee but different α. Focusing our attention on the low-mass end of the HIMF, we see that when α assumes values lower than -1, we obtain a steep HIMF with an increasing number of objects with lower $M_{\rm HI}$. When $\alpha = -1$, the number of objects stays constant (flat HIMF), while this number decreases when α is higher than -1, which is the case of a falling HIMF.

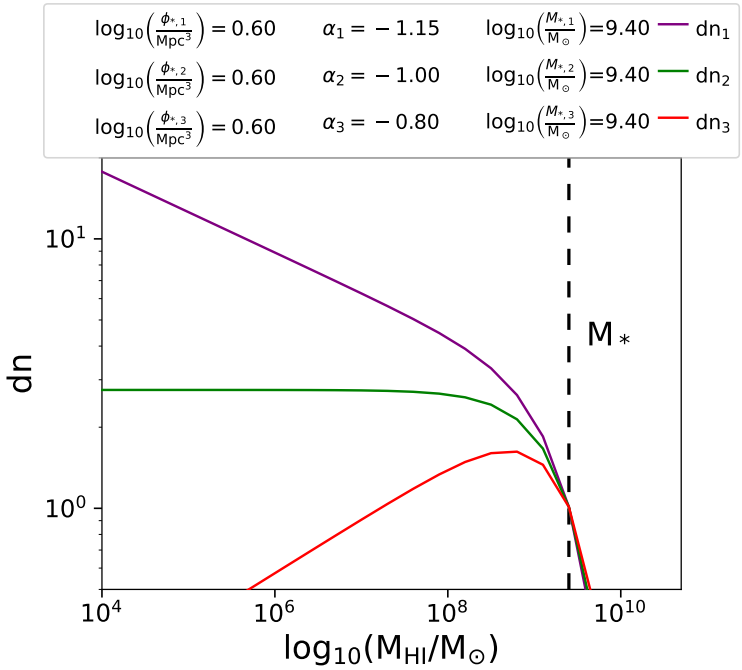

Figure 3.1: The figure shows a steep (purple), falling (red) and flat (green) HIMF with the same normalization factor ϕ_*, and the same knee, M_* (black dashed line).

HIPASS and ALFALFA observed different parts of the sky with different sensitivities. The former covered the entire Southern sky below declination +2° (21341 deg^2), while the latter observed a smaller portion of the sky (~6900 deg^2) with a higher sensitivity and angular resolution (according to Jones et al. 2018b, the maximum volume over which ALFALFA can probe the low-mass slope of the HIMF is about four times larger than what was probed by HIPASS). The different sky coverage, sensitivity and resolution should be taken into account while interpreting the different HIMF parameters measured by HIPASS and ALFALFA. The former measured $\alpha = -1.37 \pm 0.03$ and $\log_{10}(M_*/{\rm M}_\odot) = 9.86 \pm 0.03$, while the latter found an α value of -1.25 ± 0.02 and $\log_{10}(M_*/{\rm M}_\odot)$ of 9.94 ± 0.01.

As mentioned in the previous chapters, the HI content varies with environment. Therefore, we might expect to measure a HIMF with a different shape if we select sample of galaxies in voids, walls, groups or clusters of galaxies. For example, in dense environment HI removal is more effective in low-mass galaxies than more massive systems and,

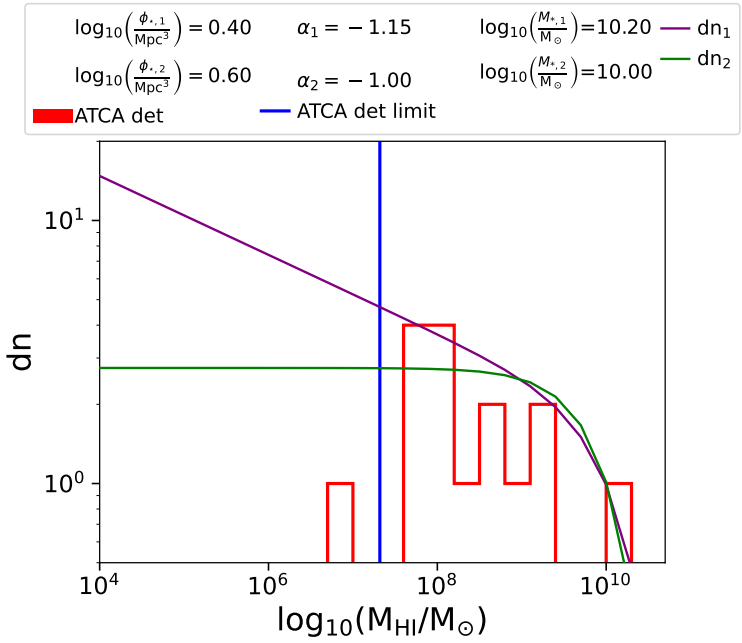

Figure 3.2: The figure shows the comparison between two different HIMFs which predict a distribution of HI masses consistent with that observed from the ATCA HI survey of the Fornax galaxy cluster (Loni et al. 2021). The figure also shows that one of the ATCA detection is below the nominal detection limit. However, Loni et al. (2021) argued that this was a real detection due to the correspondence between HI emission (measured in consecutive spectral channels) and a know Fornax member, FCC 323. This result was further confirmed by more sensitive data (Serra et al. 2016).

in general, HI rich galaxies are less abundant than in less dense environments. Thus, in clusters, α might be more positive and M_* smaller – although the latter might be difficult to constrain given the general lack of HI. Increasing the sensitivity of our HI surveys is important to detect a significant number of HI deficient galaxies and thus measure the slope of the low-mass end of the HIMF.

Several studies show a dependency of the low-mass end of the HIMF with environment, finding a flatter or even falling trend in denser environments (e.g., Gavazzi et al. 2005; Springob et al. 2005; Kovac et al. 2005; Pisano et al. 2011; Said et al. 2019; Jones et al. 2020). It's interesting to note the agreement between the falling optically-selected HIMF of the Virgo cluster measured by Gavazzi et al. (2005) and that obtained by blind HI observations by Davies et al. (2004). Gavazzi et al. (2005) argued that this correspondence suggests that free-floating HI clouds do not significantly contribute to the HIMF and, since they did not survey HI in early-type galaxies, the slope of the HIMF is mainly driven by late-type galaxies. In less dense environment, Moorman et al. (2014) show that the HIMF measured from a sample of void and walls dwarf galaxies - less affected by HI removal - shows an increasing number of objects with low $M_{\rm HI}$ (i.e., $\alpha < -1$).

It is also worth noting that there is an apparent disagreement on the dependency of the low-mass end slope with environment based on HIPASS and ALFALFA data. Specifically, HIPASS found a steeper HIMF in high-density environments (Zwaan et al. 2005), while ALFALFA found a flatter HIMF (Jones et al. 2018b). However, due to the lack of optical surveys covering the same portion of the sky observed by HIPASS, Zwaan et al. (2005) defined high-density environments according with the density of HIPASS HI detections, while ALFALFA relied on optical observations. The different definition of high-density environment, which might be opposite in the most extreme case of galaxy clusters where we have no HI emission in the densest central part of these systems, makes the comparison of the HIPASS and ALFALFA results difficult. Finally, Jones et al. (2018b) compared the HIMF in the ALFALFA spring sky (dominated by the Virgo cluster) with that in the fall sky (dominated by a local void). Analysing the Fall sky, they found a steepening of the low-mass end, which they argue is due to the gas-rich filaments connected to Virgo. These authors also confirmed the limited constraints on M_* using a small volume as that of the Virgo cluster. Indeed, systems like Virgo simply do not contain a sufficient number of HI-rich galaxies to constrain M_*.

In general, these studies are extremely important to test cold dark matter models of galaxy evolution (e.g. Press & Schechter 1974) and to constrain the role of physical processes that add or remove HI from galaxies (e.g., Gunn & Gott 1972; Toomre & Toomre 1972; Sheen et al. 2012; Oh et al. 2018).

Our goal here is to study the HIMF of the Fornax cluster. Fig. 3.2 shows that the limited number of HI detections in our ATCA HI survey of Fornax is well fitted by different HIMFs owing to a degeneracy between α and M_* for small and/or shallow samples. Thus, it is impossible to conclude whether the low-mass end of the HIMF of the low-mass Fornax cluster might be described by a flat, steep or even falling trend. In other words, we cannot easily compare the impact of the Fornax environment in shaping the HI content of galaxies with that of other, denser environments (Gavazzi et al. 2005; Springob et al. 2005; Kovac et al. 2005; Pisano et al. 2011; Said et al. 2019; Jones et al. 2018b). Fig. 3.2 does not however consider the many ATCA HI-non detections (64 of the 79 galaxies included in our catalogue in Table 1.1) which might host HI below the ATCA detection limit (blue vertical line) and thus might contain information about the shape of the HIMF. In this chapter we attempt to include the many ATCA HI non-detections in the study of the Fornax HIMF using a new Bayesian method developed by Pan et al. (2020).

In this chapter we modify the original code of Pan et al. (2020) in order to measure the HIMF of the Fornax cluster using both ATCA HI-detections and ATCA HI non-detections. This is the first attempt to use this method on real data to characterise the HIMF of a cluster. This strategy aims to estimate the main parameters α and M_* (the only parameters with environmental physical meaning, since ϕ_* in environmental HIMFs is arbitrary - Jones et al. 2016), from the measurements of integrated HI fluxes at the position and velocity of HI detected and non-detected galaxies. In fact, given the large uncertainty on the value of M_* derived from a small volume as that of a cluster, we will mainly focus our attention on measuring α.

The chapter is organized as follows: in Sect.3.2 and Sect. 3.3 we introduce the method

of Pan et al. (2020) to infer the best-fitting HIMF parameters using this new approach. In Sect. 3.4 we show the supporting tools our code relies on to estimate the best-fitting HIMF parameters. In Sect.3.5, we show all steps we made and results we obtain to test our code on artificial datasets. Finally, we show the first results of the measured HIMF of Fornax using a Schechter function in Sect. 3.6. Hence, we draw some conclusions in Sect. 3.7.

3.2 Bayesian HIMF below the nominal noise threshold

The knowledge of the position and redshift of HI non-detected galaxies has been used to estimate the average $M_{\rm HI}$ in galaxies, including the signal hidden in the noise. This technique, known as HI stacking, consists in co-adding de-redshifted spectra at the known location of non-detected galaxies in order to improve the S/N. As mentioned, stacking measures just the average HI content of galaxies in the stack (Delhaize et al. 2013; Rhee et al. 2018) but does not provide any information on the distribution of HI masses. In a different context, new techniques based on a maximum-likelihood approach (Mitchell-Wynne et al. 2014; Zwart et al. 2015) were used to model the source counts of faint radio continuum sources below the nominal detection threshold. Pan et al. (2020) extended this technique to determine the HIMF directly from the HI-line flux distribution constructed from extracting integrated fluxes across an appropriate number of spectral channels at the redshift and position of galaxies in simulated HI cubes. This technique, applied to real data, can therefore provide more information than just the average HI mass measured with traditional stacking. In this chapter we modify and apply this technique to our ATCA Fornax HI data.

3.3 Formalism

We indicate with f_m the HI fluxes from which we measure HI masses using Eq. 50 in Meyer et al. (2017). These measurements consists of the sum of the intrinsic flux from the source, f, plus the contribution from the noise, f_n, which can be positive or negative: $f_m = f + f_n$. Following the same approach used by Pan et al. (2020), we assume that the number of sources in a given patch of sky follows a Poissonian distribution, thus the probability of finding $n_{\rm i}$ objects within the observed portion of sky and the i-th flux bin $[f_{m_i}, f_{m_i} + \Delta f_m]$ is:

$$P_i\left(n_i \middle| \frac{dn}{df}(\alpha,\ M_*\ ...)\right) = \frac{\lambda_i^{n_i} e^{-\lambda_i}}{n_i!} \tag{3.2}$$

where dn/df is related to the definition of HIMF (see first identity in Eq. 3.1). Thus, dn counts the number of HI galaxies in the observed sky within a given (infinitesimal) flux bin df, and depends on the HIMF paramenters α, M_* etc. Although these dependencies make clear the relation between dn/df and the shape of the HIMF, for brevity they will be omitted from now on. λ_i in Eq. 3.2 is the theoretically expected number of HI sources in

the i-th bin. In real observation we must take into account how λ_i is affected by the noise in the data. We can express this as the convolution of dn/df with the noise:

$$\lambda_i = \int_{f_{min}}^{f_{max}} df \frac{dn}{df} \int_{f_{m_i}}^{f_{m_i}+\Delta f_{m_i}} df_m P_n(f_m - f) \tag{3.3}$$

where $\mathrm{P}_n(f_n)$ is the distribution of the noise f_n, while f_{min} and f_{max} define the integration interval. In the case of Gaussian noise, Eq. 3.3 assumes the following form:

$$\begin{aligned} \lambda_i = \int_{f_{min}}^{f_{max}} df \frac{dn}{df} \int_{f_{m_i}}^{f_{m_i}+\Delta f_{m_i}} df_m \frac{1}{\mathrm{RMS}\sqrt{2\pi}} \exp\left(-\frac{(f_m - f)^2}{2\,\mathrm{RMS}^2}\right) = \\ \int_{f_{min}}^{f_{max}} df \frac{dn}{df} \frac{1}{2}\left[erf\left(\frac{f_{m_i} - f}{\sqrt{2}\,\mathrm{RMS}}\right) - erf\left(\frac{f_{m_i} + \Delta f_{m_i} - f}{\sqrt{2}\,\mathrm{RMS}}\right)\right] \end{aligned} \tag{3.4}$$

where $\mathrm{RMS} = \sqrt{N_{chan}}\sigma_{chan}dv$, and N_{chan} is the number of channels over the flux-density profile of the HI line for each galaxy, σ_{chan} is the RMS per channel, and dv is the channel width. Assuming that the number of sources in different flux bins are independent, the likelihood for all flux bins is:

$$\mathcal{L} = \prod_{i=bin} P\left(n_i \middle| \frac{dn}{df}\right). \tag{3.5}$$

Finally, we are ready to evaluate the (posterior) probability of having a HIMF with a certain shape given the total number of N objects through the Bayesian' inference:

$$P\left(\frac{dn}{df}\middle| N\right) = \mathcal{L} \cdot P\left(\frac{dn}{df}\right). \tag{3.6}$$

The prior probability, which is the last term in the above equation, expresses our a priori knowledge on the shape of the HIMF, hence on its parameters. Furthermore, since we do not compare different models, Eq. 3.6 does not include the evidence term.

3.4 Supporting tools

While developing our code, we made used of the same tools used in Pan et al. (2020). Specifically, we used the Bayesian Blocks method by Scargle et al. (2013) to determine suitable flux bins, and MULINEST[1], a Bayesian inference tool (Feroz et al. 2009; Buchner et al. 2014) based on a nested sampling technique (Skilling 2004), to evaluate Eq. 3.6.

The Bayesian Blocks method allows varying bin (block) widths in order to be robust to statistical fluctuations and is ideal for distributions of fluxes from astrophysical sources. Instead of an arbitrary a priori binning, it produces a binning that adapts itself to the data, where the optimal segmentation of the data is obtained with blocks where the data are

[1] `https://johannesbuchner.github.io/PyMultiNest/`

statistically consistent with a constant flux. Thus it produces narrow bins where the data are denser and wider where they are more diffuse. The parameter p0 in equation (11) in Scargle et al. (2013) allows to determine how many bins are generated. In general, a small p0 will be more robust to statistical fluctuations in the data, however it might result in a overly coarse binning. The optimal value of p0 is typically determined empirically.

Once we have a distribution of fluxes useful to evaluate Eq.3.6, MULTINEST samples the prior parameter space through a nested sampling technique and produces the posterior samples providing the marginalized likelihood and the best-fitting value of all parameters with associated error estimate. Finally, we chose to adopt the median of the posterior samples as the best estimate of each parameter.

3.5 Testing of the Bayesian method

Before applying our code to the ATCA Fornax HI data we tested it by taking an input HIMF and verifying that the code is able to recover it within the errors. We started by fixing the input values of the HIMF parameters α, ϕ_* and M_* in Eq. 3.1 as well as the minimum and maximum allowed HI mass $M_{\rm min}$ and $M_{\rm max}$. This sets the number of galaxies in each mass bin between $M_{\rm min}$ and $M_{\rm max}$. Supposing that the predicted (integer) number of galaxies in the i-th bin is $\rm n_i$, we generated $\rm n_i$ random $M_{\rm HI}$ values assuming a uniform probability function between the $M_{\rm HI}$ bin edges. We repeated this step for each bin, thus obtaining a catalogue of HI mass values between $M_{\rm min}$ and $M_{\rm max}$ and following the input HIMF. Since the Bayesian part of the code evaluates the distribution of fluxes plus noise, we converted our simulated $M_{\rm HI}$ values to fluxes using Eq. 50 in Meyer et al. (2017) and adopting the same distance of 20 Mpc for all galaxies (Mould et al. 2000) (the adopted distance and the adopted flux-mass conversion is the same as in Chapt. 2). These fluxes represent f, i.e., the intrinsic flux from sources in the sky. Finally, we added Gaussian noise to simulate realistic fluxes, f_m, which we binned with the Bayesian Block method. We used MULTINEST to obtain the best parameter fits.

Since, the aim of this part is to test how reliable our code is, we made a series of experiments with different input parameter values. They were chosen to simulate different input HIMFs which have a steep, falling or flat trend in the power-law part of the mass function, as well as different M_* and ϕ_* values. Finally, we verified whether our code is able to measure the input parameters comparing them with the best fit parameters obtained with MULTINEST.

The next subsections show the results of two sets of experiments. The former has input HIMFs which have 50 galaxies above $M_*/2$. The latter is a more similar case to that of our ATCA survey of Fornax, with 15 galaxies above the 3σ detection limit of $2{\times}10^7$ $\rm M_\odot$ (calculated assuming a linewidth of 100 $\rm km\,s^{-1}$). In both cases, we set RMS to be consistent with the ATCA noise level. Thus, we set $\sigma_{\rm chan}$ = 2.8 mJy beam^{-1} and dv = 6.6 $\rm km\,s^{-1}$. Then, we set the number of channels to be $N_{\rm chan}$ = 15, under the assumption that in low-mass galaxies (the larger population in a cluster where HI is efficiently removed) the linewidth is $\sim$100 $\rm km\,s^{-1}$.

Parameter	Prior probability distribution
$\log_{10}\left(\frac{\phi_*}{\mathrm{Mpc}^{-3}}\right)$	Uniform ∈ [-3, 6]
$\log_{10}\left(\frac{M_*}{\mathrm{M}_\odot}\right)$	Uniform ∈ [8, 11]
α	Uniform ∈ [-2, 0]
$\log_{10}\left(\frac{M_{\mathrm{min}}}{\mathrm{M}_\odot}\right)$	Uniform ∈ [0, 7]
$\log_{10}\left(\frac{M_{\mathrm{max}}}{\mathrm{M}_\odot}\right)$	Uniform ∈ [9, 14]

Table 3.1: Prior parameter ranges used in all experiments with 50 galaxies above $\mathrm{M}_\star/2$ and 15 galaxies above the ATCA detection limit while testing a Schecther function (Eq. 3.1).

In Table. 3.1 we show the uniform priors used to sample the prior parameter space. M_{min} and M_{max} correspond to the conversion of f_{min} and f_{max} which define the integration interval in Eq. 3.3.

3.5.1 Fifty galaxies above $M_*/2$

We performed 25 experiments which have the only constrain of having 50 galaxies above $\mathrm{M}_\star/2$. Fig. 3.3 shows the input parameters used for testing each shape of HIMF: steep ($\alpha < -1$), falling ($\alpha > -1$) and flat ($\alpha = -1$). We note that ϕ_* is not a free parameter, but is determined by our requirement of having 50 galaxies above $\mathrm{M}_\star/2$. We further set $\log_{10}(M_{\mathrm{min}}/\mathrm{M}_\odot)$ and $\log_{10}(M_{\mathrm{max}}/\mathrm{M}_\odot)$ to 4 and 12.5.

In the rest of the section, we show the procedure and results obtained for three representative HIMFs, one for each shape. Each subsequent figure will have three panels. The left and right panels of the first row refer to the case of the steep and falling HIMFs, respectively, while the bottom panel refers to the flat HIMF. In Appendix C we provide results of all 25 experiments.

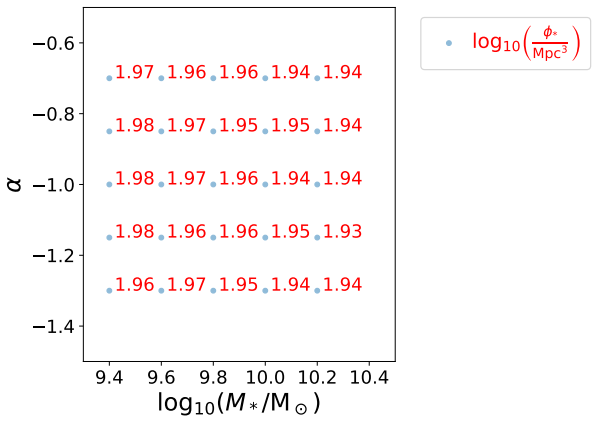

Figure 3.3: Set of parameters used in experiments with 50 galaxies above $M_\star/2$. Results of all experiments are reported in Appendix C.

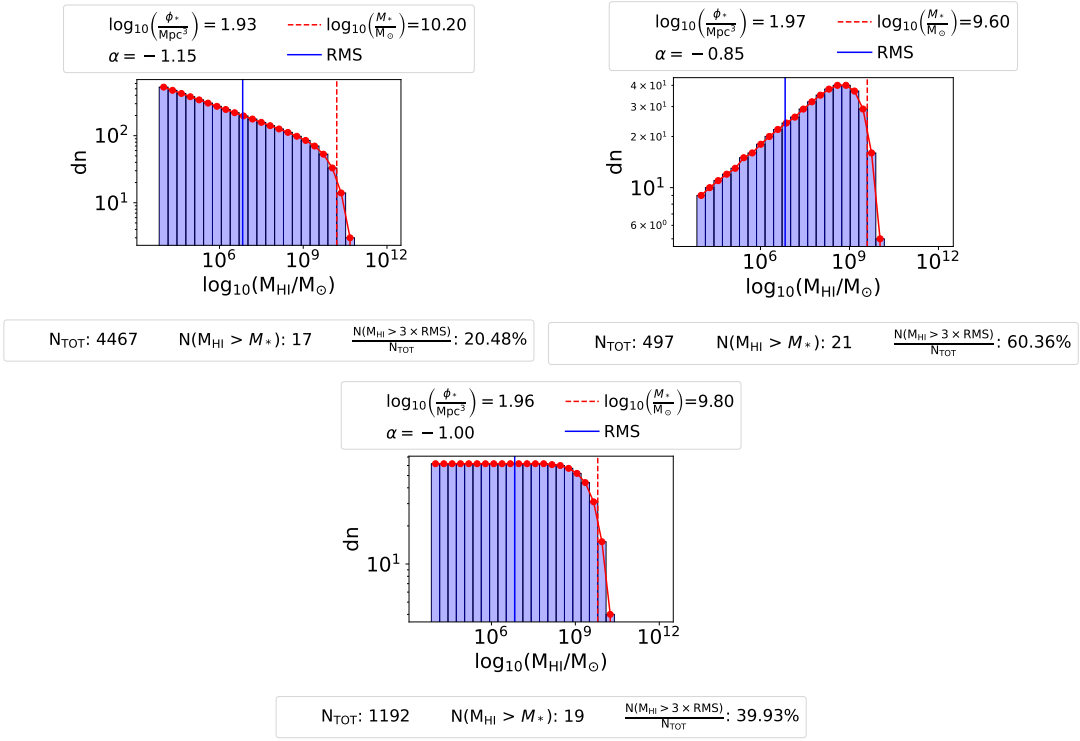

Figure 3.4: Number of galaxies in each $M_{\rm HI}$ bin for the case of a steep (top left), falling (top right), and flat (bottom) input HIMF with 50 galaxies above $M_*/2$. In each panel, the top legend shows the input parameters set in Eq. 3.1, while the bottom panel indicates the total number of objects (N_{TOT}), the number of HI galaxies above M_* ($N(M_{\rm HI} > M_*)$), and the ratio of galaxies above the ATCA detection limit and the total number of objects ($N(M_{\rm HI} > 3\times$ RMS$)/N_{TOT}$) generated from the input HIMF.

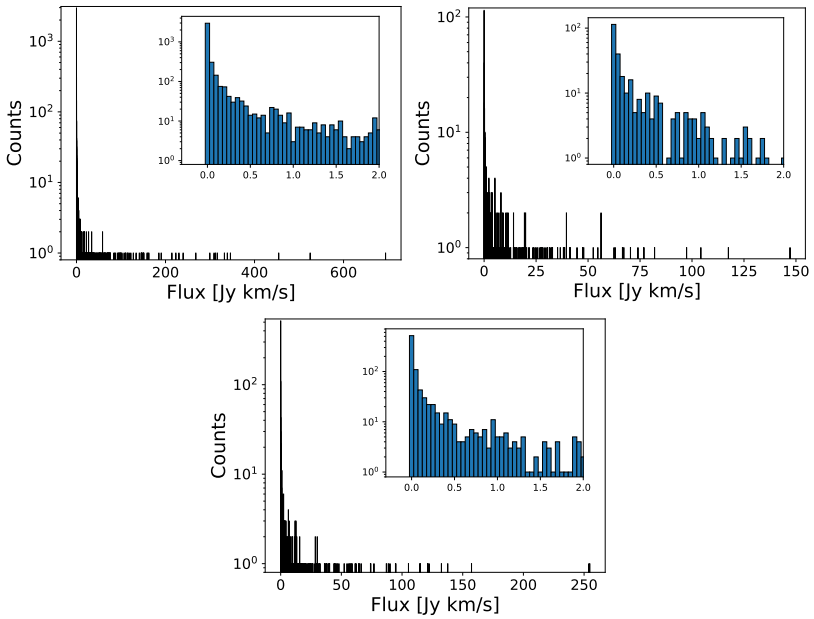

Figure 3.5: Panels are ordered as in Fig. 3.4. Each panel shows the f flux histogram before including noise. A zoom around 0 Jy km s^{-1}shows that there are no negative fluxes.

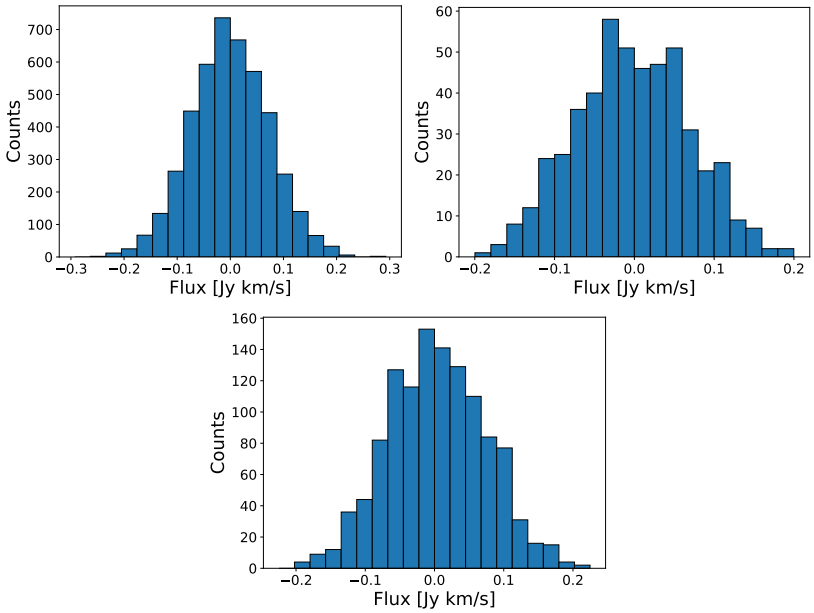

Figure 3.6: Panels are ordered as in Fig. 3.4. Each panel shows the random Gaussian noise generated for the corresponding experiment.

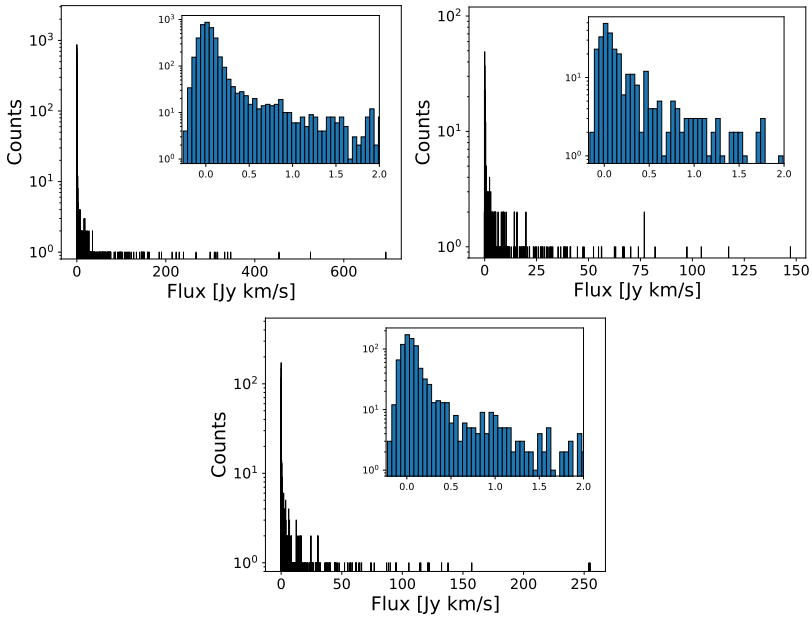

Figure 3.7: Panels are ordered as in Fig. 3.4. Each panel show the f_m flux histogram which results from the sum of Gaussian noise (Fig. 3.6) on top of f (Fig. 3.5). A zoom around 0 Jy km s^{-1}shows that now there are negative fluxes.

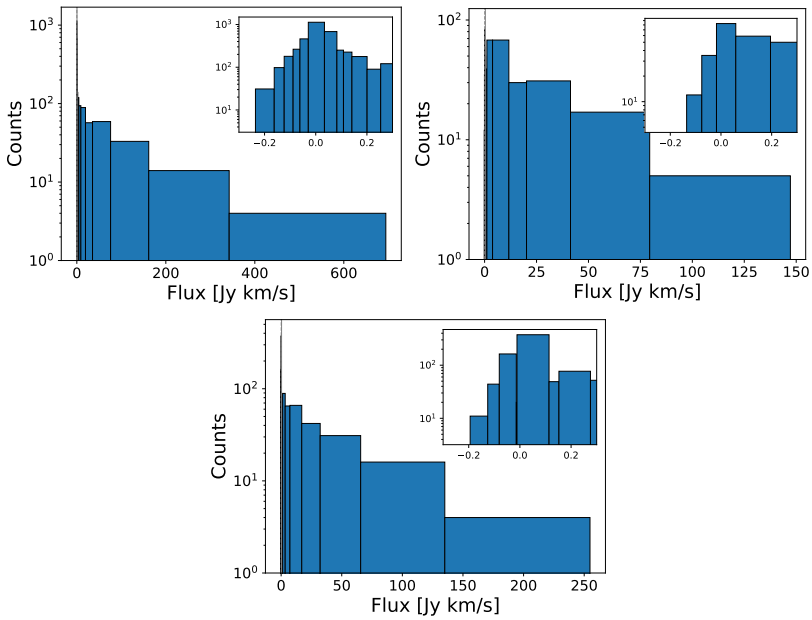

Figure 3.8: Panels are ordered as in Fig. 3.4. Each panel consists in a rebin of f_m (Fig. 3.7), using the Bayesian Block method (Scargle et al. 2013). A zoom around 0 Jy km s^{-1}is shown on the top right of each panel.

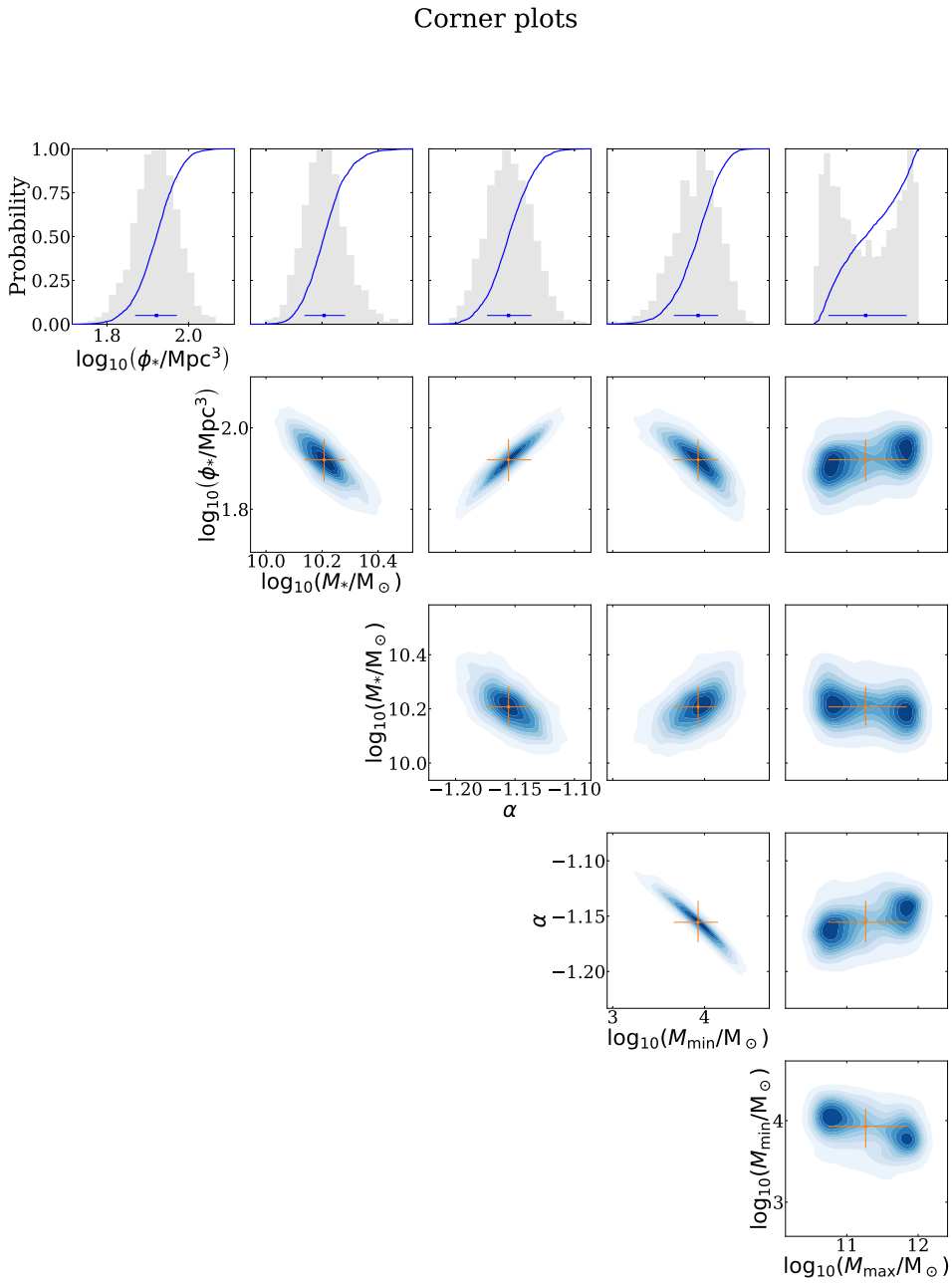

Figure 3.9: Corner plots corresponding to the experiment with a steep HIMF (top left panel Fig. 3.4), with 50 galaxies above $M_\star/2$. Top histograms show the marginal posterior probability densities. The blue curves are the cumulative distribution (integrating over the grey histograms from left to right). The best-fitting parameters are shown by the blue dots (in histograms) and orange dots (in all other panels which show the correlation among parameters) with 1σ error bars.

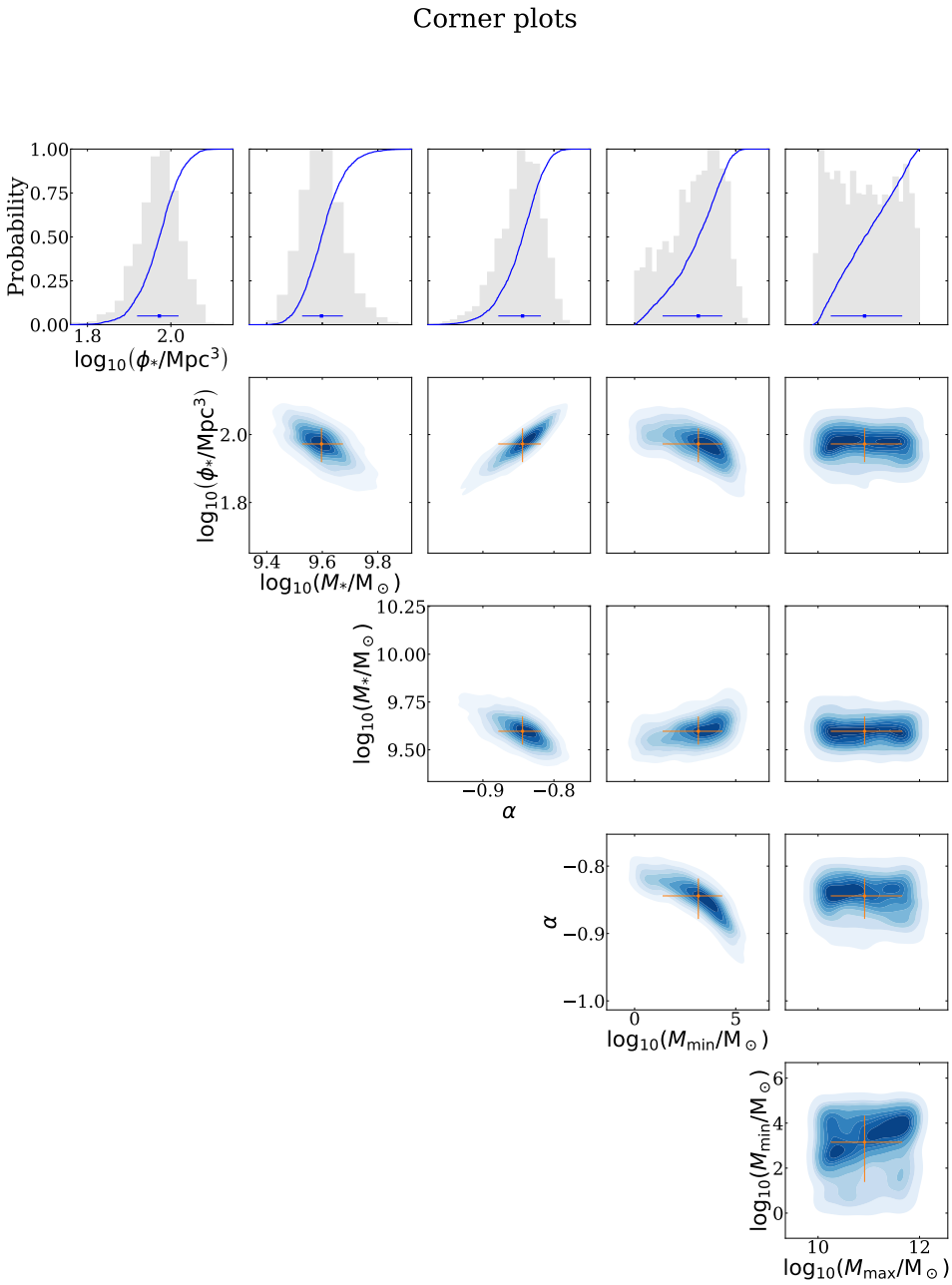

Figure 3.10: Corner plots corresponding to the experiment with a falling HIMF (top right panel Fig. 3.4), with 50 galaxies above $M_\star/2$. Please, refer to Fig. 3.9 for further details.

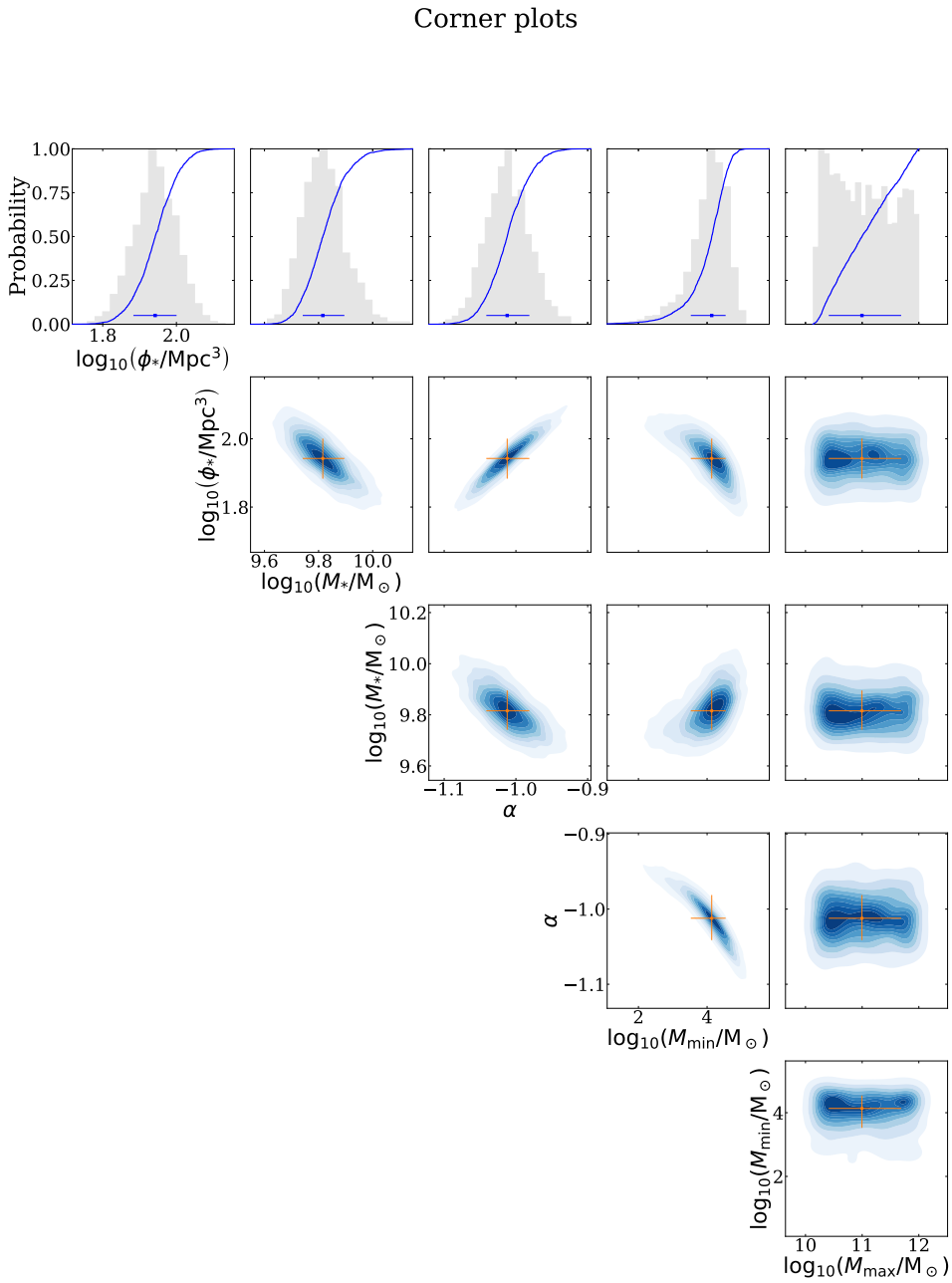

Figure 3.11: Corner plots corresponding to the experiment with a flat HIMF (bottom panel Fig. 3.4), with 50 galaxies above $M_\star/2$. Please, refer to Fig. 3.9 for further details.

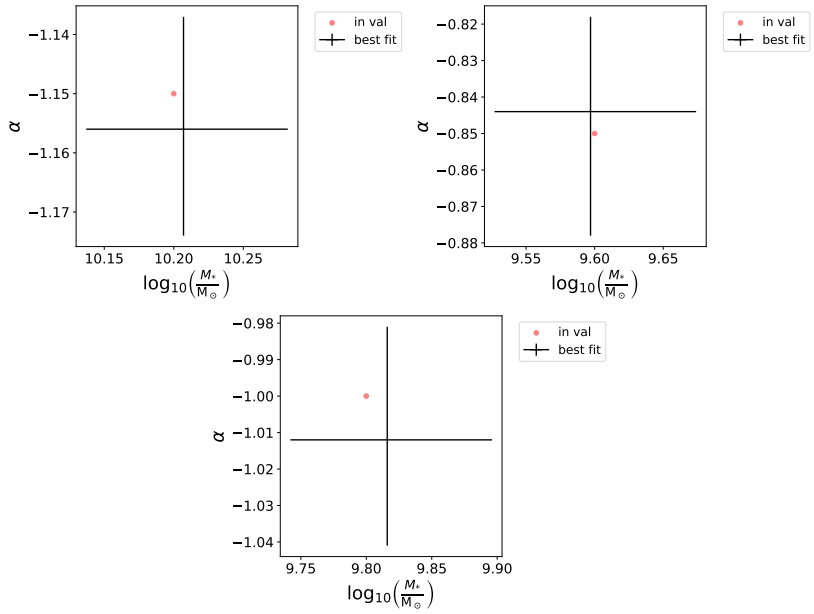

Figure 3.12: Panels are ordered as in Fig. 3.4. Each panel shows the comparison between the input parameter values (in red) used for generating the initial distribution of $M_{\rm HI}$ (Fig. 3.4) and correpsonding best-fitting parameter values and error bars obtained with our code.

Fig. 3.4 shows the input number of galaxies in each $M_{\rm HI}$ bin where the bottom panel of each plot specifies the total number of galaxies, the number of objects above the knee, and the ratio between galaxies above the ATCA detection limit, 3× RMS over 100 km s^{-1}, and the total number of objects. The upper legend shows the input HIMF parameters of the experiment. As mentioned in the previous section, we used these numbers for generating an integer number of random $M_{\rm HI}$ values in each bin. Then, we converted the $M_{\rm HI}$ values to fluxes which represent the intrinsic fluxes from the sources in the sky which are distributed as shown in Fig. 3.5. Finally we added Gaussian noise (Fig. 3.6) obtaining a realistic distribution of fluxes for an ATCA like survey (Fig. 3.7). These fluxes were then re-binned using the Bayesian Blocks method with a p0=0.5 (Fig. 3.8). We also note that using different values of p0 does not change our results.

Fig.s 3.9, 3.10 and 3.11 are corner plots of each experiment which show how the prior parameter space was sampled by MULTINEST. Before discussing whether the Bayesian method returns the correct HIMF values, it is worth discussing how the output parameters are correlated with one another. In general, all parameters show a weak (if any) correlation with $M_{\rm max}$. Instead, we see that the slope α varies with $M_{\rm min}$. More precisely, α increases as $M_{\rm min}$ decreases. This trend becomes flatter as $M_{\rm min}$ decreases in experiments where α defines a falling HIMF. Indeed, although $M_{\rm min}$ was sampled all the way down to 1 $M_\odot$, a falling HIMF might no have objects below a certain $M_{\rm HI} > 1$ $M_\odot$, thus the trend becomes flatter, meaning that the same slope might be fine for different values of $M_{\rm min}$. The other

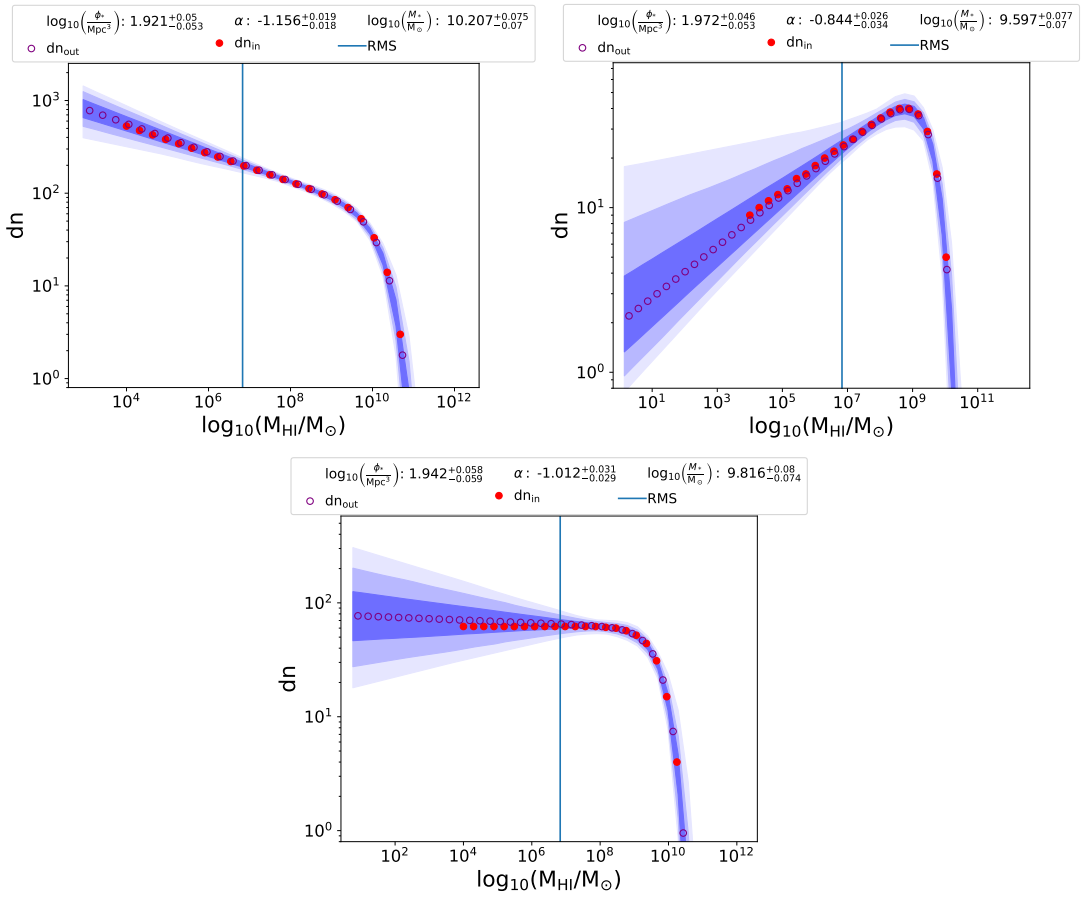

Figure 3.13: Panels are ordered as Fig. 3.4. Each panel shows the comparison between the predicted number of objects in each $M_{\rm HI}$ bin from the input HIMF (so that from the input parameters set in Eq. 3.1 - see top legend Fig. 3.4) and the predicted number of objects from the output HIMF where we set as the value of parameters in Eq. 3.1 equal to the best parameter fit obtained with our code (see Fig. 3.12)

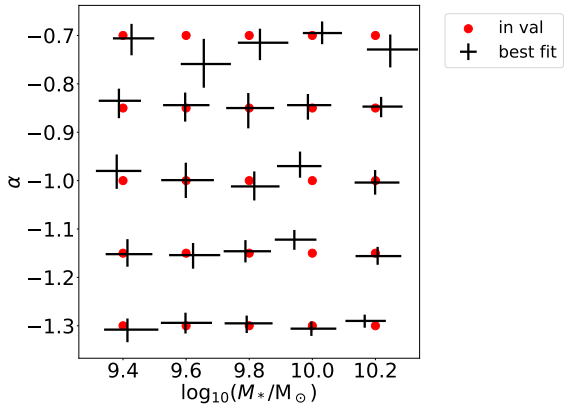

Figure 3.14: Comparison between the input parameter values (in red) used for generating the initial distribution of $M_{\rm HI}$ and the best-fitting parameter values obtained with our code for all 25 experiments with 50 galaxies above $M_\star/2$. Results of all experiments are also reported in Appendix C.

main parameter, which define the total number of objects is ϕ_* and indeed we observe a similar correlation between this parameter and $M_{\rm min}$. It is also worth commenting the correlation between α and ϕ_*. A larger α defines a HIMF with a lower number of objects in the low-mass end. The code tries to sample the posterior parameter space in a way useful to preserve the total number of sources and it therefore shifts upwards the HIMF by making ϕ_* larger. Finally, there is a degeneracy between M_* and α consistent with what shown in Fig. 3.2, whereby a higher M_* can give a similarly good fit if α becomes lower.

Thus, we observe that all parameters which tune the total number of objects (α and ϕ_*) and the one which defines how many objects are above the RMS are well correlated with one another. The code samples the posterior parameter space in a reasonable way to preserve the total number of objects it estimates (including those below the noise threshold).

A visual comparison between the input values for $\log_{10}(M_*)$ and α with the best fit obtained with our code is shown in Fig. 3.12. Black crosses show 1σ uncertainty (see also top legend in Fig. 3.13). In these three experiments the predicted values are consistent with the input values within uncertainties. Finally we show in Fig. 3.13 the comparisons between the number of objects in each $M_{\rm HI}$ bin from the input HIMFs with that from the best-fitting HIMFs. The blue shades represents 1, 2, 3σ of all sampled HIMFs by MULTINEST. Fig. 3.14 shows a comparison between the input values for $\log_{10}(M_*)$ and α with the best fit for all 25 experiments (see also Appendix C). The clear conclusion is that our code is successful at recovering the input HIMF parameters within the error bars for cases like the ones presented in this section. In particular, the agreement between input and output α (the low-mass-end slope of the HIMF and the main focus of this work) is excellent. Below we see to what extent this conclusion holds in cases more similar to the one of our ATCA Fornax HI dataset.

3.5.2 Sixteen galaxies above the ATCA detection limit

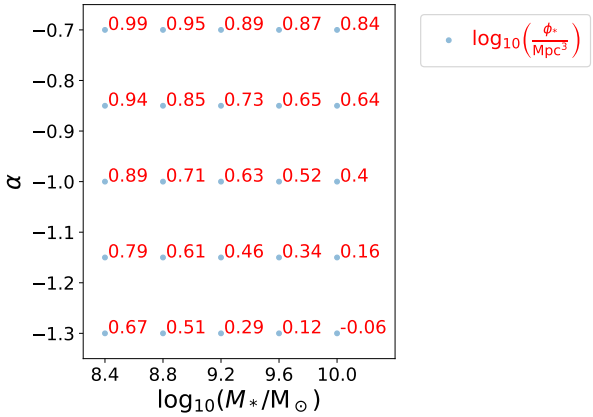

Figure 3.15: Set of parameters used in experiments with 15 galaxies above the ATCA detection limit. Results of all experiments are reported in Appendix C.

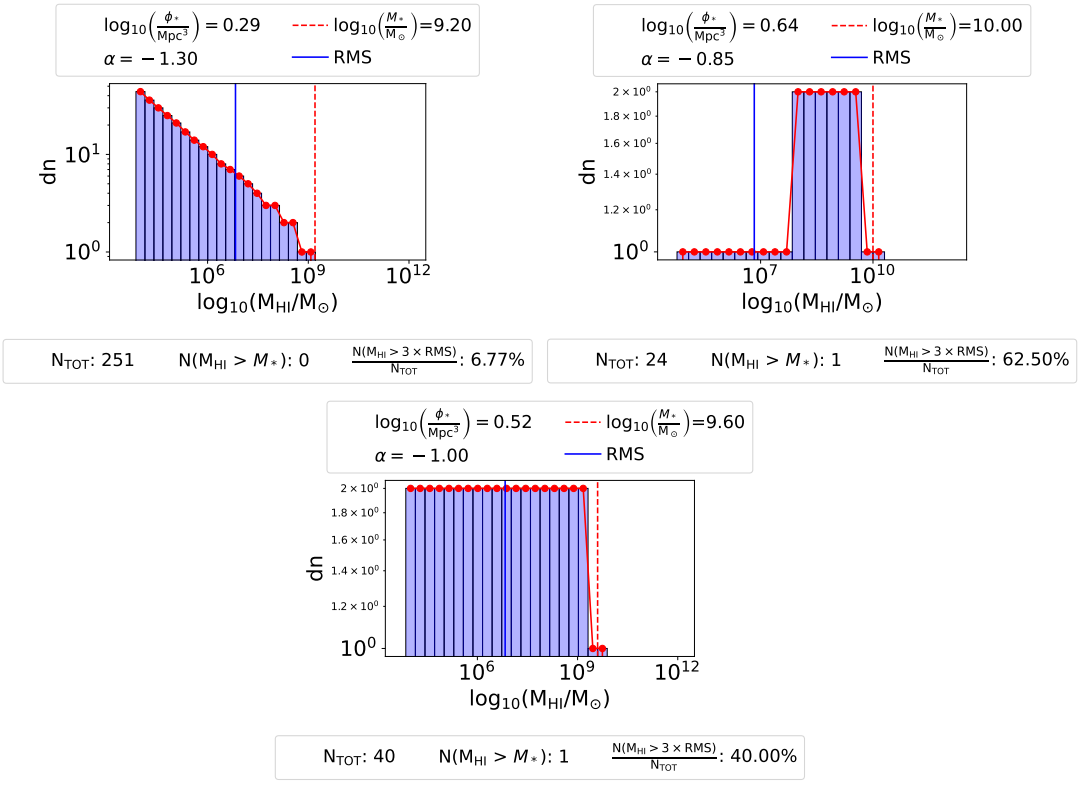

Figure 3.16: Similar to Fig. 3.4 for the case of three experiments with the only constrain of having 15 objects above the ATCA detection limit.

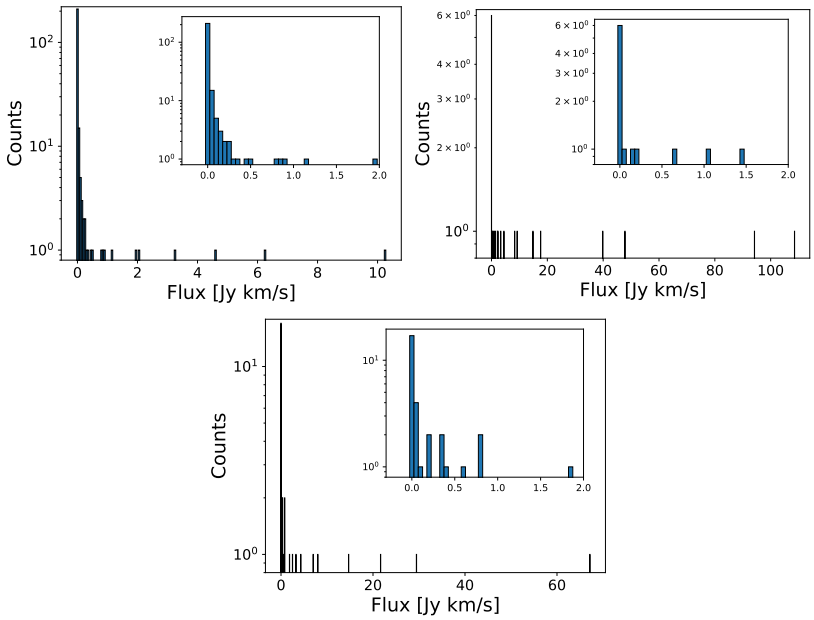

Figure 3.17: Similar to Fig. 3.5 for the case of three experiments with the only constrain of having 15 objects above the ATCA detection limit. A zoom around 0 Jy km s^{-1}shows that there are no negative fluxes.

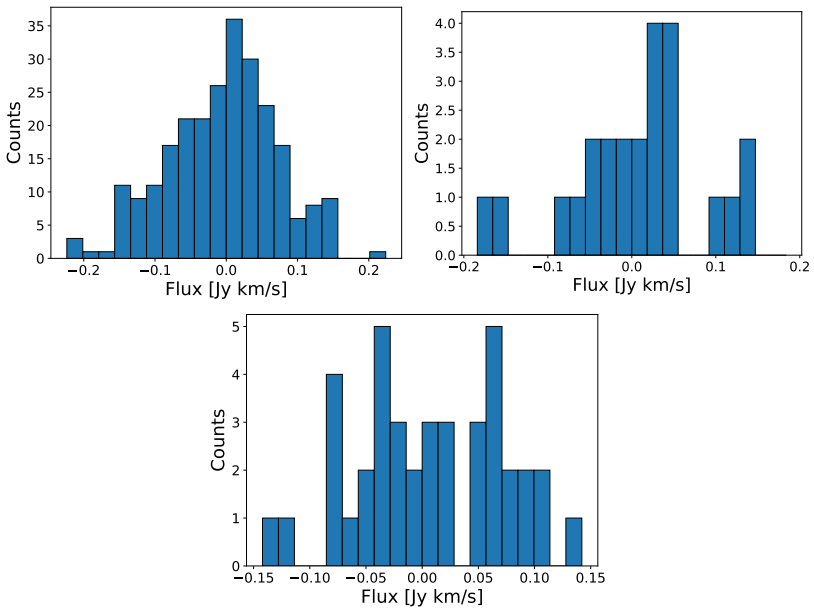

Figure 3.18: Similar to Fig. 3.6 for the case of three experiments with the only constrain of having 15 objects above the ATCA detection limit.

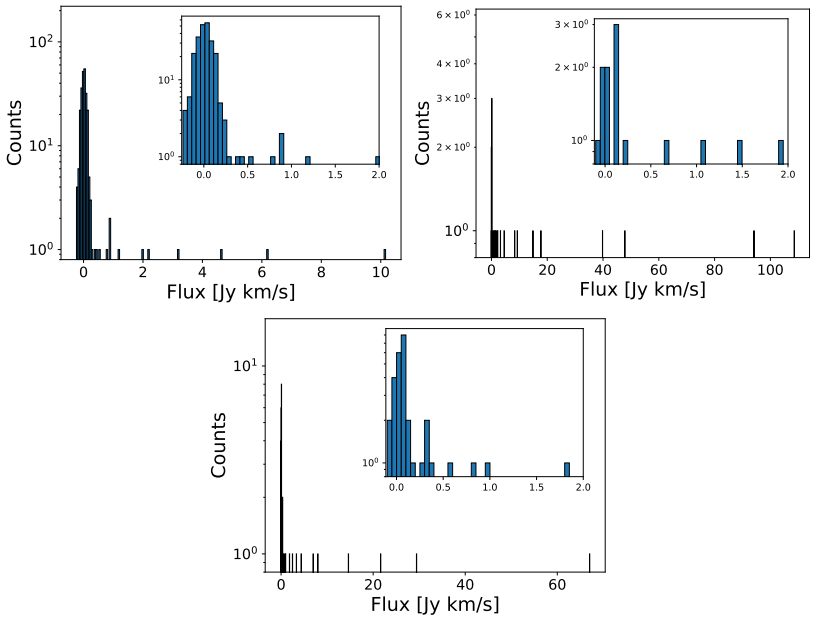

Figure 3.19: Similar to Fig. 3.7 for the case of three experiments with the only constrain of having 15 objects above the ATCA detection limit. A zoom around 0 Jy km s^{-1}shows that now there are negative fluxes.

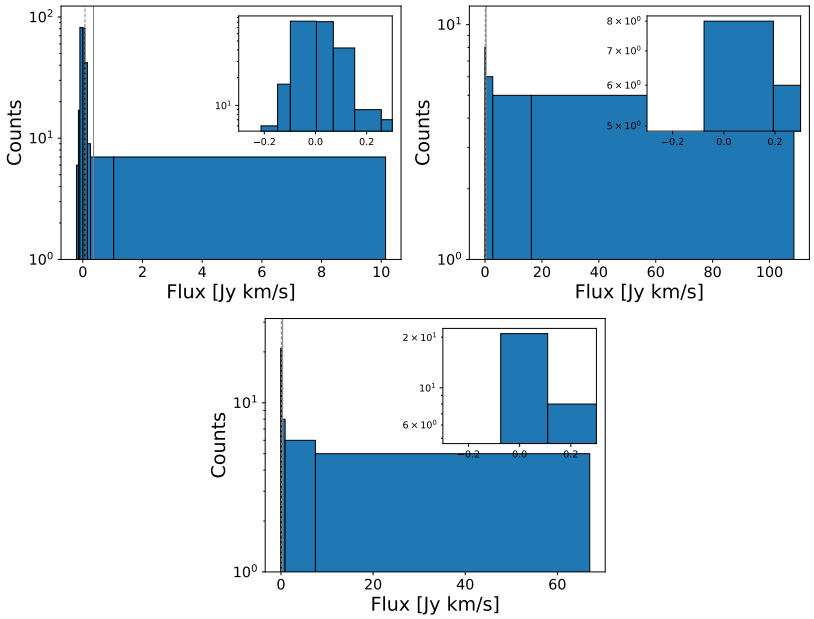

Figure 3.20: Similar to Fig. 3.8 for the case of three experiments with the only constrain of having 15 objects above the ATCA detection limit.

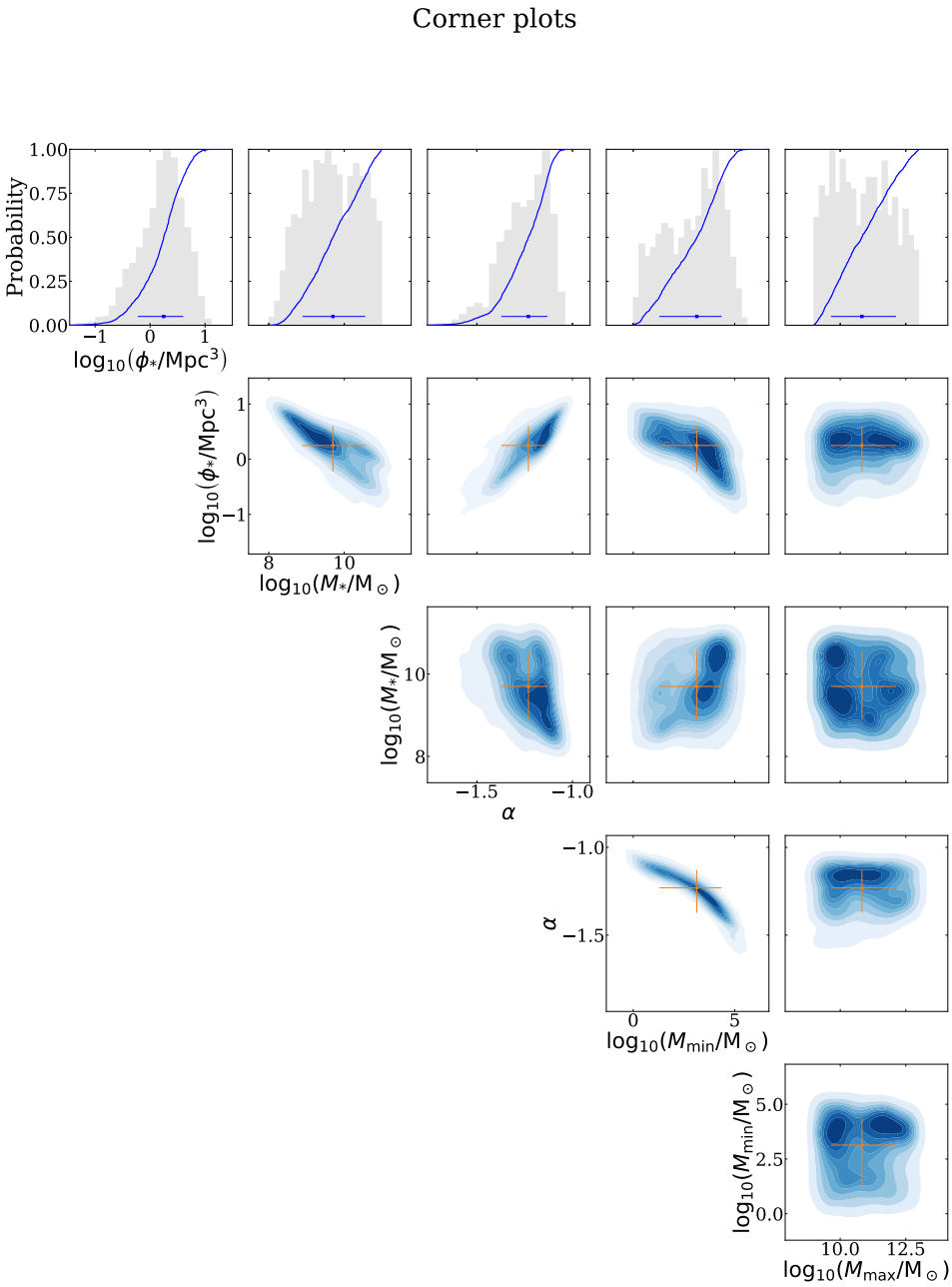

Figure 3.21: Corner plots corresponding to the experiment with a steep HIMF (top left panel Fig. 3.16), which predicts 15 galaxies above the ATCA detection limit. Please, refer to Fig. 3.9 for further details.

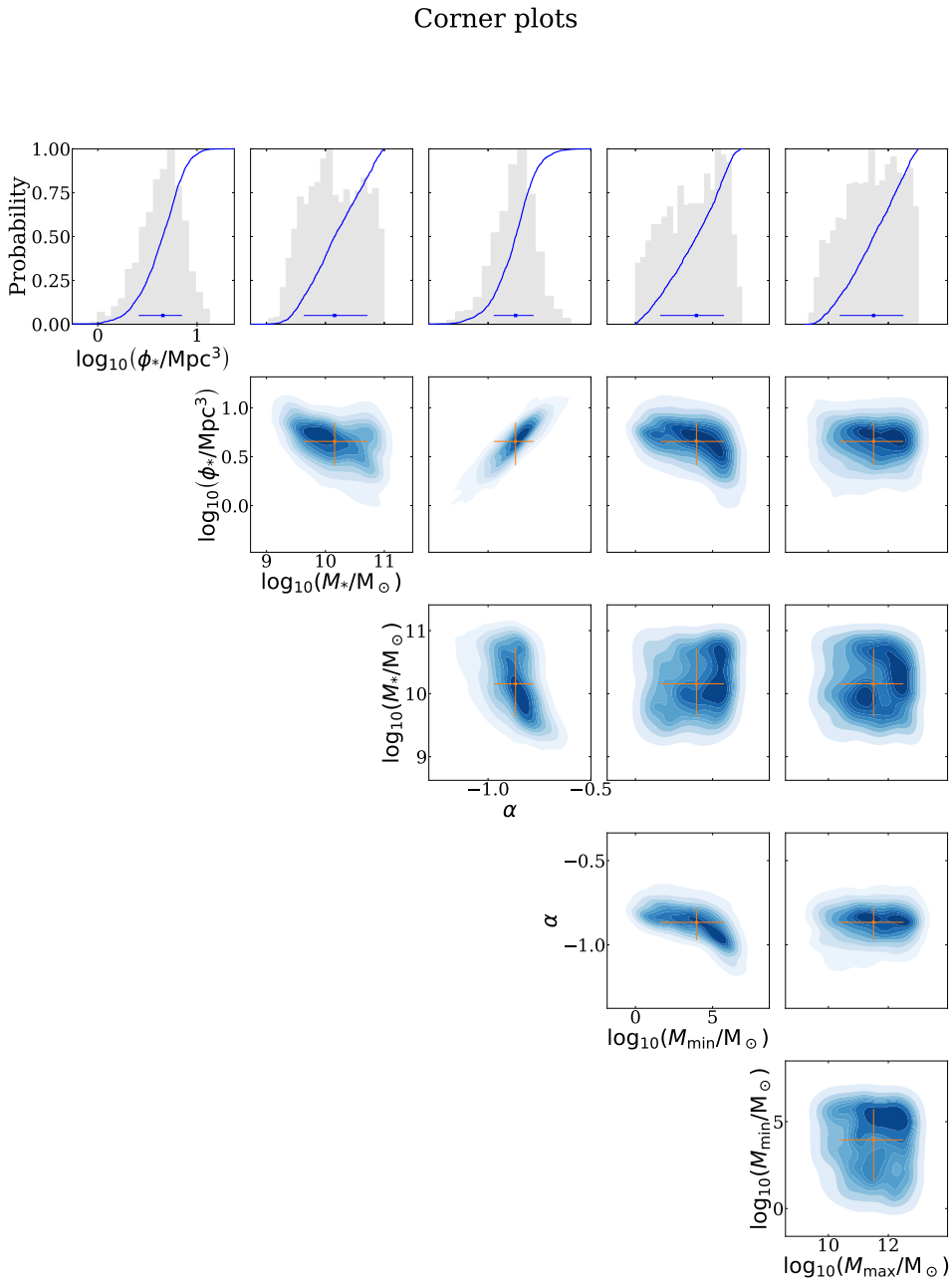

Figure 3.22: Corner plots corresponding to the experiment with a falling HIMF (top right panel Fig. 3.16), which predicts 15 galaxies above the ATCA detection limit. Please, refer to Fig. 3.9 for further details.

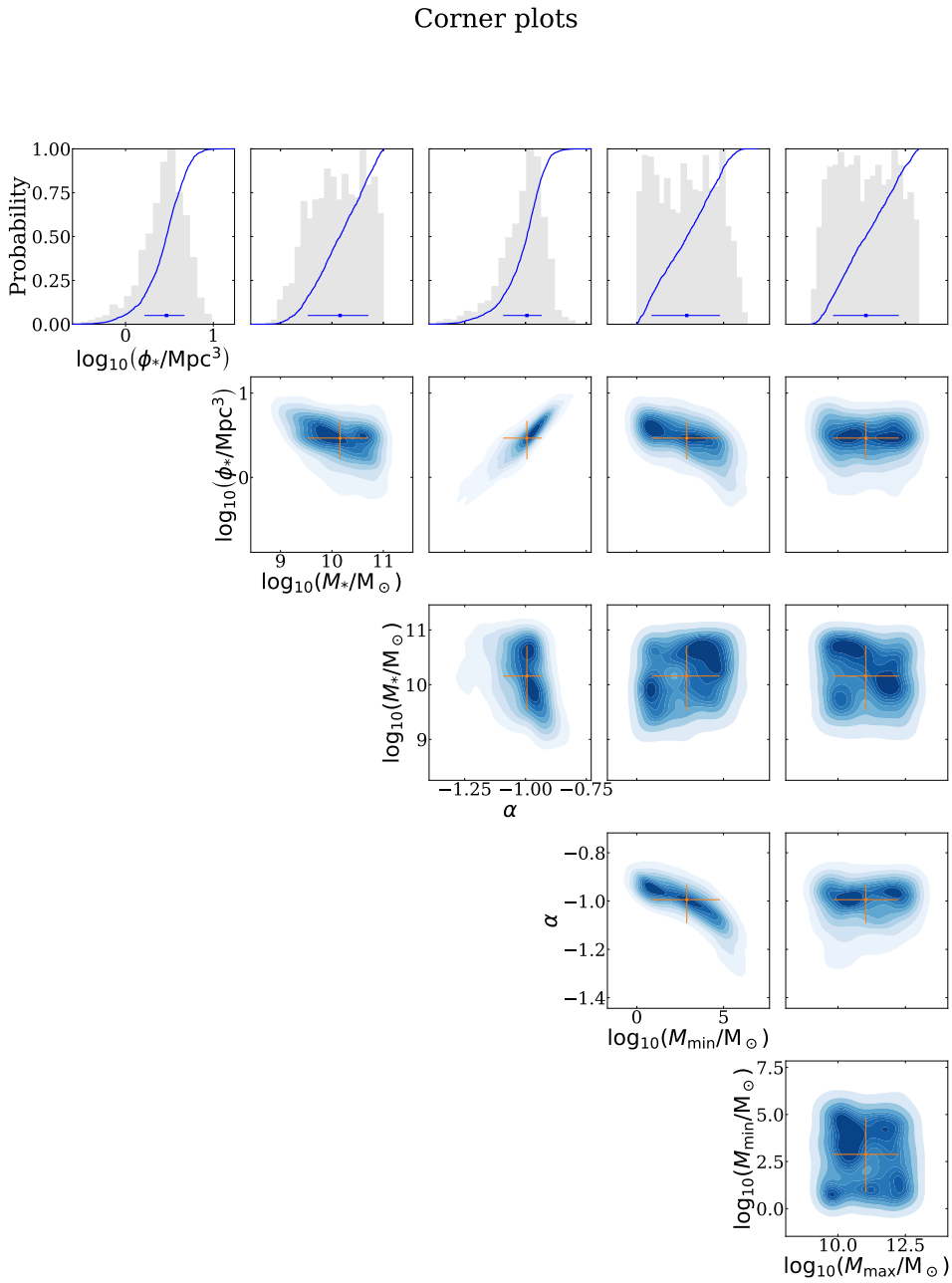

Figure 3.23: Corner plots corresponding to the experiment with a flat HIMF (bottom panel Fig. 3.16), which predicts 15 galaxies above the ATCA detection limit. Please, refer to Fig. 3.9 for further details.

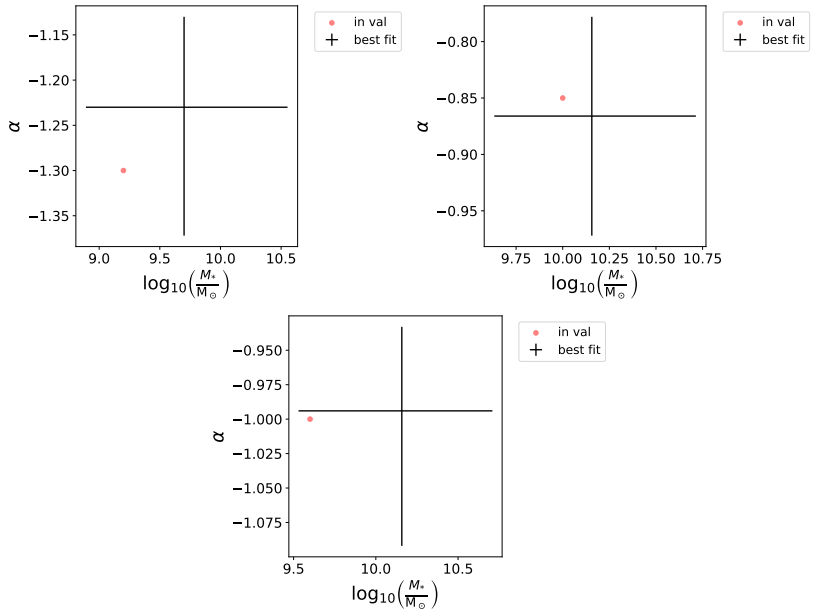

Figure 3.24: Similar to Fig. 3.12 for the case of three experiments with the only constrain of having 15 objects above the ATCA detection limit.

We performed 25 experiments which have the only constrain of having the same number of direct HI detections as in our ATCA survey (Chapt. 2) – that is, 15 galaxies above $M_{\rm HI} = 2{\times}10^7$ M$_\odot$ (in our data we have 16 detections but one is formally below the 3 σ detection limit). Due to discretisation and binning effects in some experiments the actual number of objects above the ATCA detection limit might vary by one or two with respect to the requested number. For similar reasons, these experiments do not always have objects above M_*. Similarly to Sect. 3.5.1, in the rest of the section we show the procedure and results we obtained for the case of steep, falling and flat HIMF. We also adopt the same convention of Sect. 3.5.1 to present the figures in the current subsection. While using the Bayesian Block method for binning our input fluxes, we set p0 = 0.8 (Fig. 3.20). Also in this case, a different value of p0 does not change our results. As mentioned before, it is worth noting that not all our experiments have objects above M_* (e.g. see top left panel in Fig. 3.16). Similarly, some experiments with a falling slope have a lower total number of objects with respect to the number of confirmed Fornax members included in our cleaned spectroscopic catalogue (which are 64 below m$_r$=16.5 mag; Sect. 1.5), plus the 16 ATCA HI detections (see Chapt. 2; Loni et al. 2021). Fig.s 3.21, 3.22 and 3.23 show corner plots which refer to the steep, falling and flat experiments in Fig 3.16, respectively. Corner plots show the same correlations among parameters as for the experiments with 50 galaxies above M$_\star$/2. In general, the best-fitting parameter values agree with the input values within 1σ (see Fig. 3.24 and Fig. 3.25), although we must notice larger uncertainties of each parameters with respect to these obtained in the set of experiment with 50 galaxies above M$_\star$/2 (see Fig. 3.12 and 3.14 for a comparison).

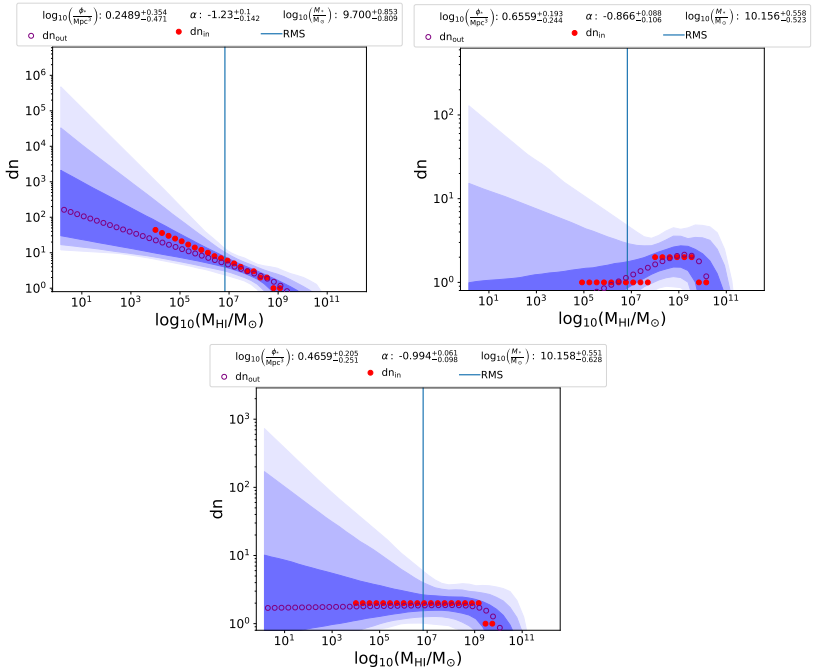

Figure 3.25: Similar to Fig. 3.13 for the case of three experiments with the only constrain of having 15 objects above the ATCA detection limit.

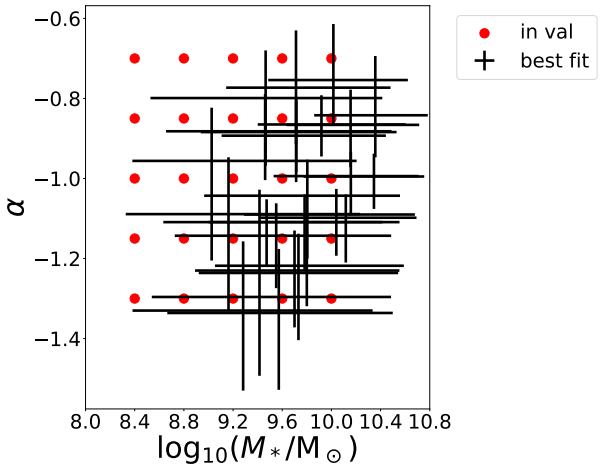

Figure 3.26: Similar to Fig. 3.14 for set of experiments with 15 galaxies above the ATCA detection limit. Results of all experiments are also reported in Appendix C.

More in detail, we find that some HIMF parameters can be estimated more reliably than others. For example, M_* is poorly constrained and typically overestimated in these experiments (Fig. 3.26). As mentioned in Sect. 3.3, such poor constraints on M_* are expected when the number of HI-rich galaxies is low. However, the parameter at the core

of our scientific investigation, i.e., the slope α of the low-mass end of the HIMF, can still be determined reliably.

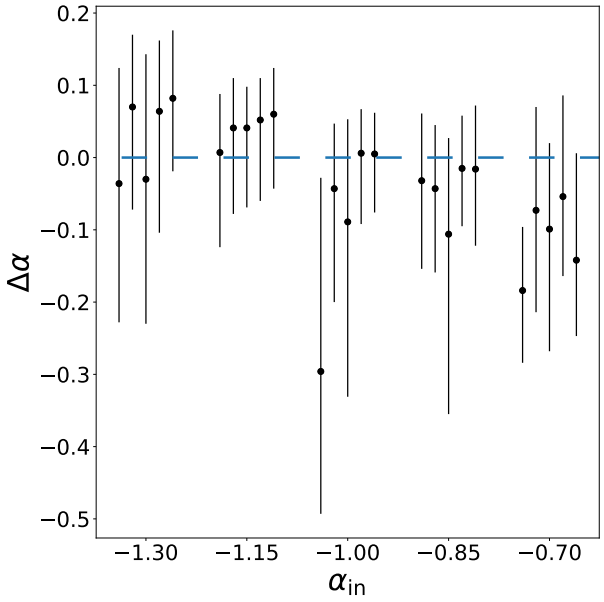

Figure 3.27: Comparison between $\alpha_{\rm in}$ and the best-fitting α for the set of experiment with 15 objects above the ATCA detection limit. On the y-axis, we plot the difference between best-fitting α and $\alpha_{\rm in}$. For presentation purpose, the values of $\alpha_{\rm in}$ are slightly displaced from the real value in order to separate the different experiments with the same $\alpha_{\rm in}$.

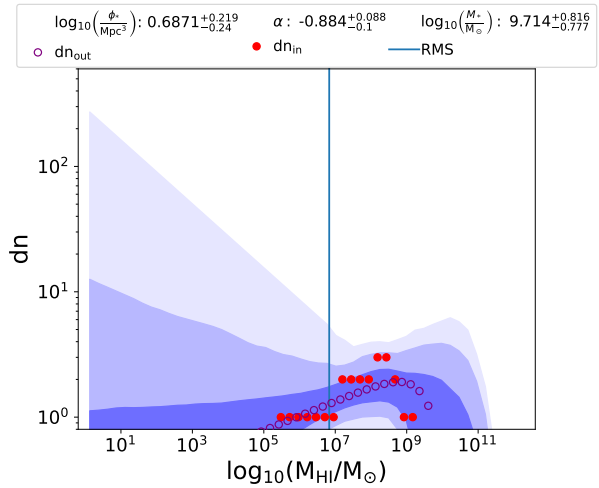

Figure 3.28: The figure shows the predicted number of galaxies in each HI mass bin from the best fitting HIMF compared and the input HIMF for the case where the discrepancy between the best-fitting α and the input one is larger.

Fig. 3.27 shows the comparison between $\alpha_{\rm in}$ and the best-fitting values of this parameter. In all experiments but two, the best-fitting values agrees with the input values within 1 σ. In the two remaining cases within 2 σ. The typical uncertainty is 0.13. In Fig. 3.28 we show the comparison between the number of galaxies in each HI-mass bin from the best-fitting HIMF compared and the input HIMF in the case where discrepancy between the best-fitting α and the input one is the largest. In general, 1σ shade follows the input HIMF.

Based on these results we conclude that, while we wait for more sensitive HI blind surveys of Fornax (e.g., the MeerKAT Fornax Survey; Serra et al. 2016), it is worth applying our method to the ATCA data currently in hand in order to start constraining the shape of the low-mass HIMF in this cluster. By construction, our conclusions will hold as long as the underlying distribution of HI masses follows a Schechter function. We will come back to this point in the next Section.

3.6 Results: the Schechter HIMF of the Fornax cluster

Although the results obtained in the set of experiments with 15 galaxies above the ATCA detection limit (see Sect. 3.5.2) have large uncertainties, they predict HIMF parameters which agree with the input parameters within 1σ, and just in a few cases within 2σ. In particular, the low-mass-end slope of the HIMF, which is our main science interest, can be estimated reliably (albeit with significant error bars). Hence, we are ready to use our code on real data.

We make use of the Fornax spectroscopic catalogue introduced in Sect. 1.5 for extracting spectra at the position of the HI non-detections in the ATCA cube. As shown in Fig. 1.6, the catalogue has a completeness higher than 50% in all bins with a magnitude lower than m_r = 16.5 mag, and 85% overall. Therefore, we decided to measure the integrated HI flux of all spectroscopically confirmed Fornax members brighter than that limit. This choice ignores possibly free-floating HI clouds that recent blind HI surveys are able to detect (e.g. Kleiner et al. 2021). In general, as mentioned in Sect. 3.1, any HIMF study based on optical catalogues would suffer of the same "blindness".

The integrated flux of 64 HI non-detections was measured using a linewidth of 100 $\rm km\,s^{-1}$- which correspond to roughly 15 independent channels in the ATCA data cube - centered at the optical velocity converted to the radio convention[2]. All but one ATCA HI detections were also included in the spectroscopic catalogue, thus we do not extract spectra at these positions. For these 15 galaxies plus FCC 323 (whose redshift was measured for the first time in Loni et al. 2021), we used the HI fluxes obtained in Chapt. 2. Fig. 3.29 shows an example of a spectrum – not yet corrected for the beam – where we have no detected HI emission.

[2]When analysing radio data, where all channels across a spectrum have the same width in frequency, it is customary to convert frequency to velocity using the convention $v_{radio} = c\,(1 - \nu/\nu_0)$, where ν and ν_0 are the observed and rest-frame frequency, respectively. This is different from the velocity convention commonly used at optical wavelengths, $v_{optical} = c\,(\nu_0/\nu - 1)$.

At the position of the HI non-detected galaxies, any real HI emission present below the noise level has obviously not been deconvolved with the dirty ATCA beam. Therefore, unlike for real detections where the sum of pixel values is divided by the integral of the restoring Gaussian beam in order to measure the integrated flux, in this case we divide by the integral of the dirty beam. The `MIRIAD` task used to get the dirty beam at the position of each HI non detection in the ATCA mosaic cube is `MOSPSF`. We extracted each spectrum using an aperture of 1.5×1 arcmin, which is the size of the restoring beam.

Finally, we build a catalogue with all these fluxes plus the flux of our 16 ATCA HI detections, which we refer to as the *on* catalogue. We also build a control, *off* catalogue where the fluxes of the ATCA HI detections are still included, but where the HI flux of the non-detections is measured 800 $\mathrm{km\,s^{-1}}$ away from the optical velocity. Basically, the *off* catalogue includes 64 measurements of pure noise plus the flux of all 16 ATCA HI-detections. We will show that the *off* catalogue serves as a critical comparison to correctly interpret our results based on the *on* catalogue. We show later in this section that our results obtained from both catalogues do not depend on the linewidth we used to measure the integrated fluxes.

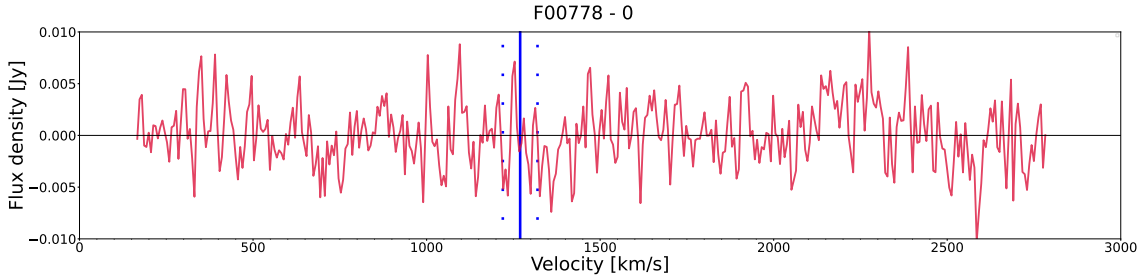

Figure 3.29: The figure shows an example of a (ATCA dirty beam corrected) spectrum extracted from the ATCA cube (see Chapt. 2) at the position of a HI non-detected source. We show the optical velocity of the source previously converted to radio convention with a vertical blue line. The spectral windows within which we measured the integrated flux is enclosed within the dotted blue lines.

We adopt the same prior ranges used in both set of experiments in Sect. 3.5 (see Table 3.1) and p0 = 0.8 while using the Bayesian block as in Sect. 3.5.2. We then run our Bayesian code on the *on* and *off* catalogues. In the rest of the section, the left and right panel of each figure refer to results obtained with the *on* and *off* catalogue, respectively.

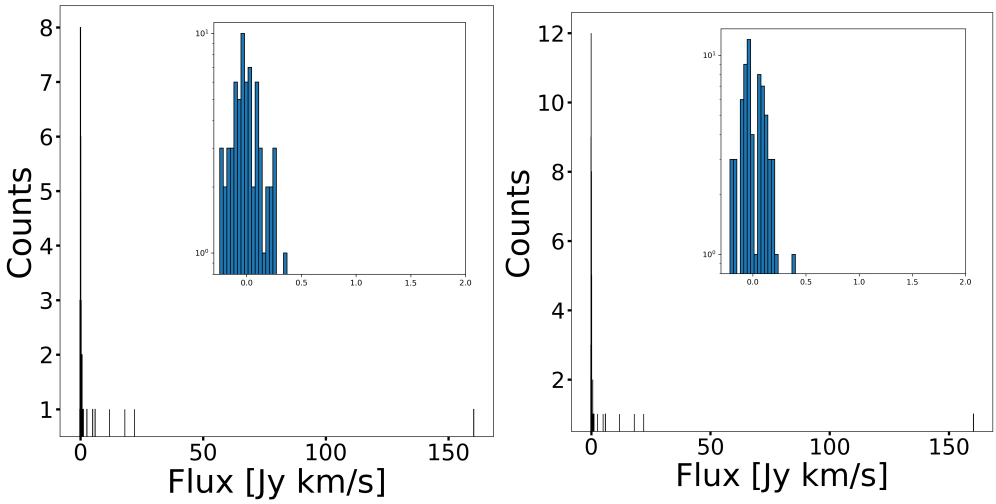

Figure 3.30: We show the histogram of fluxes obtained with the *on* (left) and *off* (right) catalogues. Each inner panel shows a zoom around 0 Jy km s^{-1}, where integrated fluxes of HI non-detections are denser.

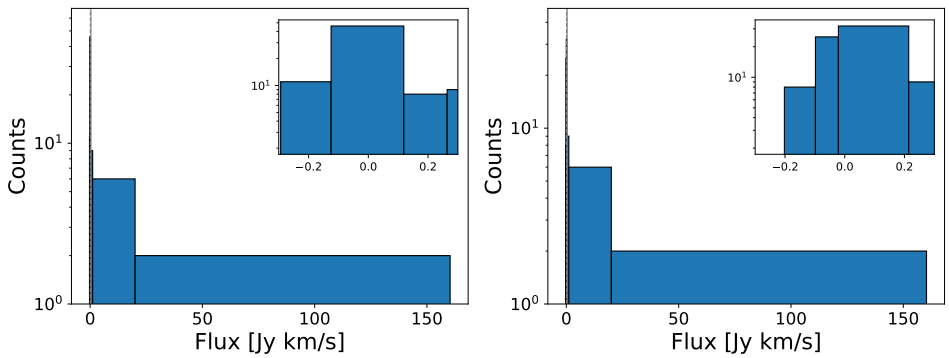

Figure 3.31: We show the binning of fluxes included in the *on* (left) and *off* (right) catalogues obtained with the Bayesian block (Scargle et al. 2013) using a p0 = 0.8. A zoom around 0 Jy km s^{-1}on the top right of each panel shows the width of bins closer to the ATCA detection limit.

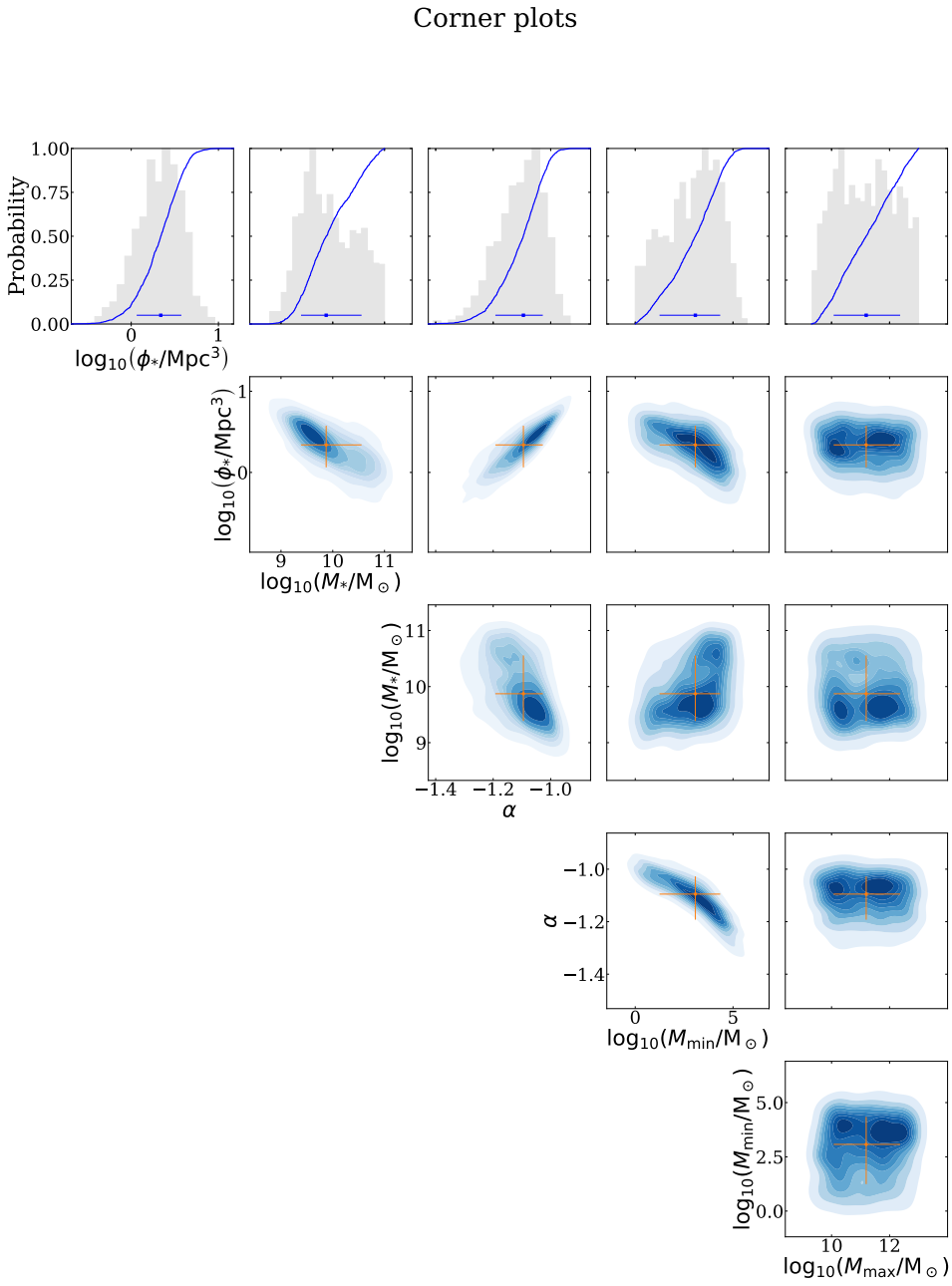

Figure 3.32: Corner plots showing how the parameter space was sampled in the case of the *on* catalogue. Please, refer to Fig. 3.9 for further details.

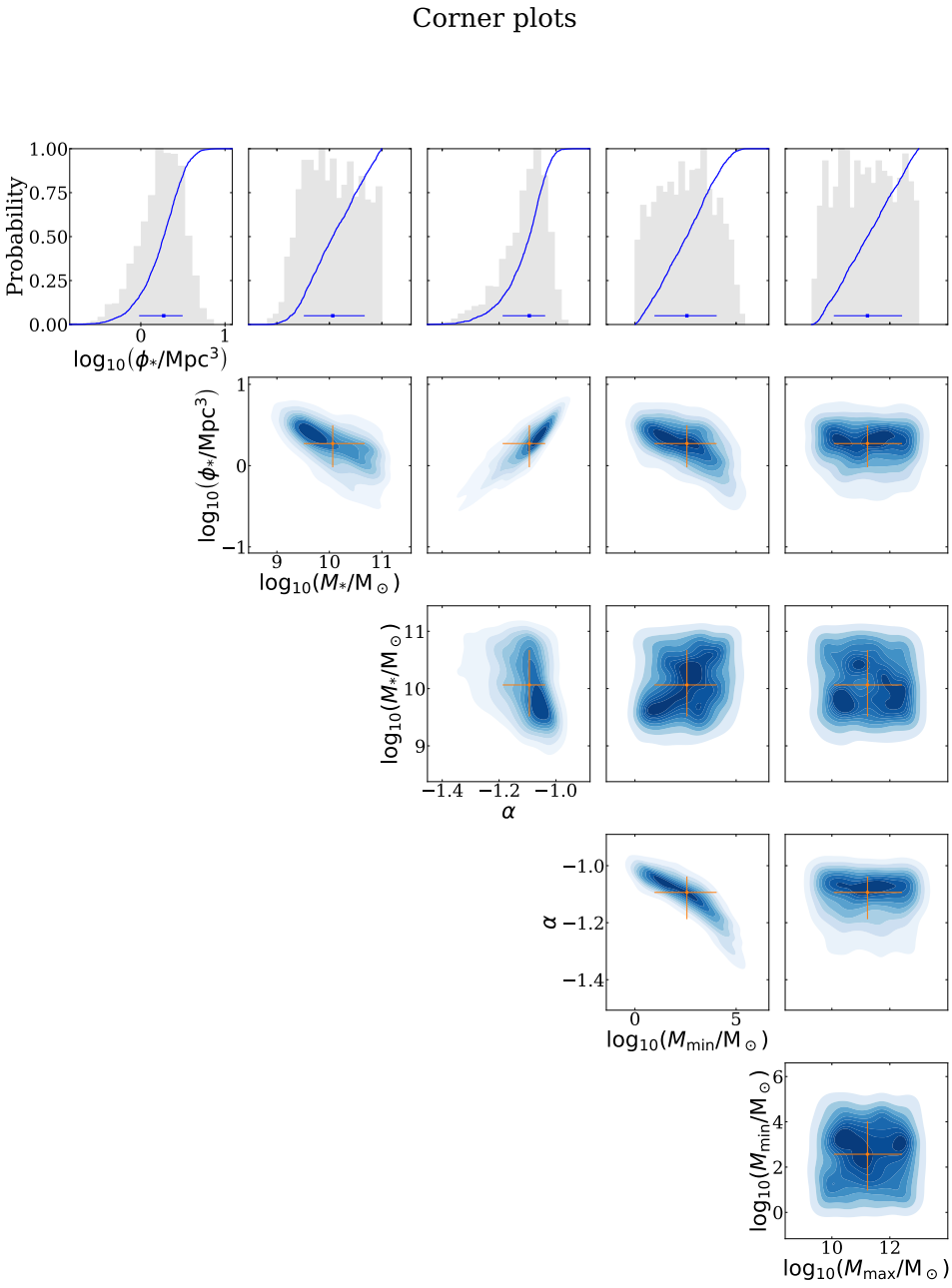

Figure 3.33: Corner plots showing how the parameter space was sampled in the case of the *off* catalogue. Please, refer to Fig. 3.9 for further details.

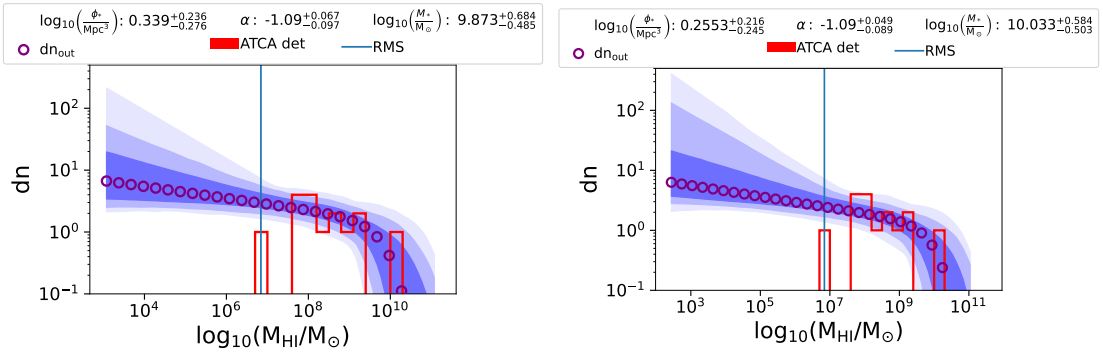

Figure 3.34: The figure shows the number of objects predicted in each mass bin by the HIMFs measured using the *on* (left) and *off* (right) catalogues. Integrated fluxes of HI non-detections are measured using a linewidth of 100 $\mathrm{km\,s^{-1}}$

Fig. 3.30 shows the flux distributions obtained using the *on* (left panel) and *off* (right panel) catalogues, respectively, while Fig. 3.31 shows how the fluxes are re-binned using the Bayesian Block method. Fig.s 3.32 and 3.33, do not show any significant difference between how the parameter spaces of priors were sampled in the case of the *on* and *off* catalogues, respectively.

The left panel in Fig. 3.34 shows the best-fitting parameters obtained from the *on* catalogue, which are $\log_{10}\left(\frac{\phi_*}{\mathrm{Mpc}^3}\right) = 0.339^{+0.236}_{-0.276}$, $\alpha = -1.09^{+0.067}_{-0.097}$ and $\log_{10}\left(\frac{M_*}{\mathrm{M}_\odot}\right) = 9.873^{+0.684}_{-0.485}$. As we mentioned in Sect. 3.1 and Sect. 3.5.2, since the main interesting parameter which can be reliably estimated in a small cosmic volume as that of a cluster is α, in what follows we limit our analysis to this parameter. Comparing the best-fitting α value with those obtained by both HIPASS ($\alpha = -1.37 \pm 0.03$) and ALFALFA (-1.25 ± 0.02), which observed larger volumes, we see that the Schechter HIMF of optically selected galaxies in Fornax (m_r <16.5 mag) is marginally flatter. This result seems to be consistent with what expected. Indeed, dense environments would efficiently remove HI from infalling low-mass galaxies, affecting the low-mass end of the HIMF. Flattening in this part of the HIMF was also observed in other dense environments (e.g. Springob et al. 2005; Kovac et al. 2005; Pisano et al. 2011; Said et al. 2019).

Our results on a flat slope of the low-mass end of the HIMF in Fornax is thus consistent with the expectation and previous literature on HI in clusters. However, we stress that the result was obtained under the *assumption* that the distribution of HI masses follows a Schechter function also below the noise level. What would happen if this were not the case? Our analysis of the *off* sample is meant to provide an answer to this question. By construction, the *off* catalogue does not follow a Schechter function, but is characterised by a (possibly Schechter-like) HIMF down to the ATCA detection limit, plus a large number of objects with zero HI flux. Surprisingly, when running our Bayesian code on the *off* catalogue our result is consistent with the best-fitting parameters we obtain for the *on* catalogue (see Fig. 3.34). Indeed, the best fit parameters of the *on* and *off* catalogues agree within the uncertainties. Fig. 3.35 shows that this agreement happens also when

using a larger linewidth to measure the integrated HI fluxes.

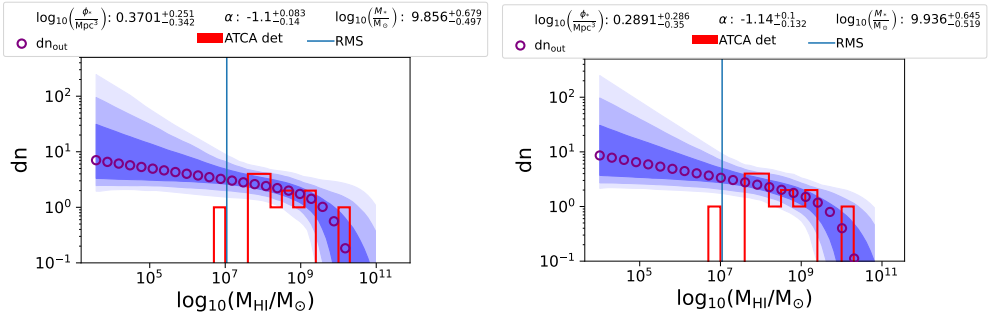

Figure 3.35: The figure shows the number of objects predicted in each mass bin by the HIMFs measured using the *on*-(left) and *off*-(right) catalogues. Integrated fluxes of HI non-detections are measured using a linewidth of 250 $\mathrm{km\,s^{-1}}$.

In summary, our method applied to our Fornax sample of HI detections and non-detections measures a flat Schechter HIMF with a slope $\alpha = -1.09^{+0.065}_{-0.097}$ in agreement with other HIMF measured in dense environment. However, we found an identical results within the uncertainties, $\alpha = -1.09^{+0.049}_{-0.089}$, using the control *off* catalogue. Since the latter does not follow a Schechter function by construction, it is likely that also the *on* catalogue does not follow a Schecthter function. To be more precise, we cannot establish whether the *on* sample follows a Schechter function, but the nearly identical results returned by our code for the *on* and *off* samples suggest that, most likely, it does not. In other words, it is possible that most of the HI undetected galaxies in Fornax have a mass well below the detection threshold, thus indistinguishable from zero (like in the *off* catalogue). This suggests that, in Fornax, we have a small number of HI rich galaxies that approximately follow a Schechter function (at least those detected with the ATCA telescope - see Fig. 3.30), and a large number of galaxies which host a HI mass well below the ATCA detection limit ($\sim 2 \times 10^7 \mathrm{M}_{\odot}$). We would thus be detecting a catastrophic fall of the HIMF below an HI mass of the order of $1 \times 10^7 \mathrm{M}_{\odot}$ in Fornax.

Although this might appear an unexpected result, standard stacking of about 470 spectra extracted at the position of HI-non detected galaxies within the virialized area of the Coma cluster show that there is no hidden signal within the noise (Healy et al. 2021). This suggests that, in clusters, the HIMF might not follow a Schechter function down to arbitrarily low M_{HI} values, but instead drop quickly to zero towards low M_{HI} (in the case of the Coma dataset, the HI mass detection limit was $1 \times 10^8 \mathrm{M}_{\odot}$). We made a similar test by performing a standard stacking of our 64 Fornax spectra to verify whether real signal was hidden in the noise. Before co-adding all spectra, we shifted them in order to have all sources centered at 0 $\mathrm{km\,s^{-1}}$. We also weighted each spectrum with the inverse of the squared RMS. The latter was measured across all HI free channels (in other words, across channels where HI emission is not supposed to be). Finally, we co-added these weighted spectra and divided for the sum of the weights (as in Fabello et al. 2011). Fig. 3.36 shows

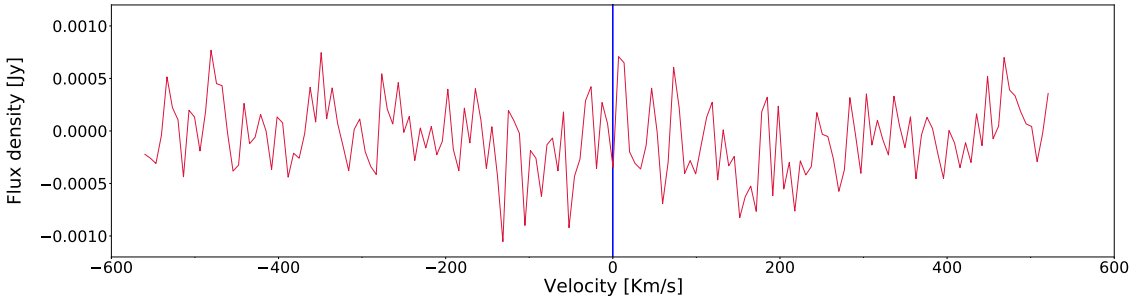

Figure 3.36: The figure shows the stacked spectrum obtained with the overlapping channels of 64 (dirty beam corrected) weighted spectra extracted at the position of HI non-detected Fornax galaxies with a magnitude lower than 16.5. We shifted each spectrum to have the velocity of the source centered at 0 $\mathrm{km\,s^{-1}}$. Each spectrum was also weighted with $1/\mathrm{RMS}^2$, where we measured the RMS across HI free channels. The stack of the weighted spectra was normalised by the sum of all weights.

that there is no signal above the noise around 0 $\mathrm{km\,s^{-1}}$. Thus, we are justified to think that also the Fornax HIMF might not follow a Schechter function at all M_{HI} values, and anyway that the HIMF drops fast below $M_{\mathrm{HI}} \sim 1 \times 10^7 \mathrm{M}_\odot$. This might be a result of the several gas removal and exhaustion mechanisms described in Chapt. 1.

3.7 Conclusion and future perspective

We adopted a new Bayesian approach to measure the parameters of a Schechter-like HIMF in the Fornax galaxy cluster below the nominal noise threshold with the goal of measuring the slope α of the low-mass end of the mass function. The main assumptions behind this method are that: (*i*) the distribution of sources in the sky is Poissonian; (*ii*) the number of sources within a certain M_{HI} bin is convolved with the noise distribution (Eq. 3.3).

Before applying this method to real data, we tested our code with 2 sets of 25 experiments, both with a Schechter HIMF (Eq. 3.1). In the former we put 50 galaxies above $M_*/2$ to firmly establish that the code works in an ideal situation, when many galaxies are detected and the total sample (both detections and non-detections) used to derive the HIMF is large. In the latter, we used 15 galaxies above the ATCA detection limit to simulate the more challenging case of the ATCA HI survey of the Fornax cluster (Loni et al. 2021). In both cases the best-fitting slope α was consistent with that of the input HIMF (see Fig. 3.14 and Fig. 3.26). Despite the larger uncertainties obtained with the ATCA-like set of experiments with respect to that with 50 galaxies above $M_*/2$, we were still able to estimate the slope of the input HIMF within an average uncertainty of ±0.13.

Following these tests we moved to real data. We used the Fornax spectroscopic catalogue (see Chapt. 1.5 and Sect. 3.6) to extract the spectra of all 64 confirmed Fornax members brighter than $\mathrm{m}_r = 16.5$ mag. We measured the integrated HI flux at the position and velocity of ATCA HI non-detected galaxies in the spectroscopic catalogue using

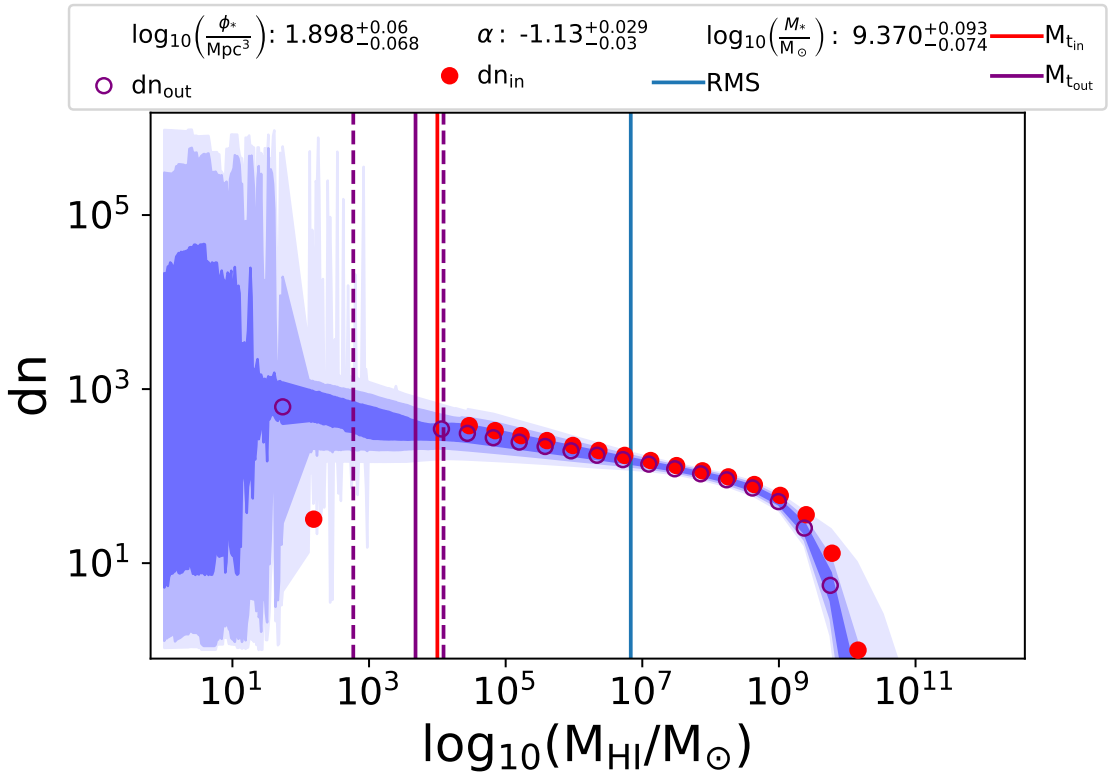

Figure 3.37: Similar to Fig. 3.13 for the case of experiments with the only constrain of having 50 galaxies above $M_\star/2$ assuming a Schechter+δ HIMF. In this experiment we used an input slope α of -1.15, a charachteristic mass $\log_{10}(M_*/M_\odot)$ of 9.40 and a normalization factor $\log_{10}(\phi_*/Mpc^3)$ of 1.87. The blue shades represent 1, 2, 3σ of all sampled HIMFs by MULTINEST. The red circles show the number of objects in each M_{HI} bin of the input HIMF. The red vertical line shows where the input HIMF is truncated ($M_{t_{in}}$). Below this threshold, the red circle shows the position of the δ. Purple open circles show the predicted number of objects from the output Schechter+δ HIMF. The solid vertical purple line shows the best-fitting value of M_t, whose 1 σ uncertainties are shown with dashed vertical purple lines. The open purple circle below the best-fitting value of M_t shows the position of the output δ.

a linewidth of 100 $\mathrm{km\,s^{-1}}$. These fluxes plus the fluxes of our ATCA HI-detections (we measure the latter as described in Chapt. 2) form the *on* catalogue which we used for our analysis. We also made a control *off* catalogue which includes 64 measurements of pure noise and fluxes of our 16 ATCA detections.

We found a flat slope, $\alpha = -1.09\pm^{+0.067}_{-0.097}$, in the Schechter HIMF of the Fornax cluster which is flatter than those measured in larger volume of the local Universe by HIPASS ($\alpha = -1.37 \pm 0.03$, Zwaan et al. 2005) and ALFALFA ($\alpha = -1.25 \pm 0.02$, Jones et al. 2018b). Although this result is consistent with our expectation – due to HI removal in cluster galaxies through environmental interactions – we found an identical slope using the control *off* catalogue which, by construction, does not follow a Schechter function. This suggests that also the *on* catalogue, i.e., our sample of galaxies in Fornax cluster, does not follow a Schechter HIMF below the ATCA detection of 10^7 $\mathrm{M_\odot}$. Rather, it rapidly drops to zero below this limit. This interpretation is supported by recent findings of no signal hidden in the noise by stacking about 470 spectra extracted at the position of HI non-detected galaxies in the Coma cluster (Healy et al. 2021). Therefore, we might be discovering that a general property of galaxy clusters is a sudden drop of the HIMF below a certain $M_{\rm HI}$ threshold, which so far we found to be of $\sim 10^7 \mathrm{M}_\odot$ in the case of the low-mass Fornax cluster and $\sim 10^8 \mathrm{M}_\odot$ in the case of more massive clusters like Coma.

If the above conclusion is correct, a better formalism to study the distribution of HI masses in clusters including the HI non-detections would be one where the HIMF is described by a Schechter function down to a limiting HI mass, plus a delta function with much lower HI mass (possibly zero). We have already begun to test a modified code which assumes the modified Schecther+δ function, and promising results were obtained for the case of 50 galaxies above $M_*/2$. The code was able to fit well α, M_* and $M_{\rm t}$, which is the $M_{\rm HI}$ where the Schechter function is truncated, and thus below which the distribution of HI objects does not follow a Schechter function (see Fig. 3.37). In future work we will test this modified code against a case more similar to that of our ATCA data (as in Sect. 3.5.2) and, eventually, apply it to the ATCA data themselves.

Chapter 4

Morphological transformation in Fornax: the case of NGC 1436

4.1 Introduction

Galaxy morphology depends on galaxy evolution and thus on the physical processes which galaxies go through during their life. Observations at redshift $z = 0$ show us the end-products of all these processes, and thus it is not trivial to understand exactly what a given morphology tells us about the history of a galaxy.

Due to environmental interactions, galaxy evolution is faster in dense environments, resulting in significant morphological transformations and, in a faster quenching of galaxies (Dressler & Gunn 1983; Dressler et al. 1997, 1999; Fasano et al. 2000; Diaferio et al. 2001; Postman et al. 2005).

In the last decades, lenticular galaxies (S0s) in clusters, which show a discky structure but old stellar populations, have received significant attention. Indeed these galaxies appear to be the result of the evolution of star-forming spiral galaxies observed at redshift $z \sim 0.5$ in clusters (e.g. Dressler et al. 1997). The question of how this transformation proceeds has been debated and still stands. Many physical processes, whose nature can be either hydrodynamical (affecting gas alone) or gravitational (affecting also the stellar component of galaxies), have been invoked (see Chapt. 1 for an introduction on these interactions). In general, more than one process might be necessary to quickly halt the star formation activity. The first requirement is to stop cold gas accretion onto galaxies, which would otherwise supply material to form new stars. Then, a faster quenching might happen if the cold gas reservoir is actively removed through environmental interactions. For example, ram-pressure and turbolent/viscous stripping can cause the rapid truncation of star formation (e.g., Quilis et al. 2000). Additionally, repeated tidal interactions promote the further evolution into ealy-type morphologies, causing a gradual increase of the buldge-to-disc light (Moore et al. 1996).

Furthermore, although mergers between galaxies are not frequent in clusters at redshift $z = 0$ (Gottlöber et al. 2001), they can occur between members of groups of galaxies,

which are then said to be experiencing pre-processing before falling into the main cluster. Thus, the S0s that we observe in local clusters might be the result of mergers which took place in an in-falling group of galaxies (Poggianti et al. 1999; Hinz et al. 2003; Cortese et al. 2006).

It is worth noting that each of these processes leaves a footprint on different galaxy components. Indeed, a galaxy whose gas accretion is halted, would progressively lose its ability to form stars. This process, commonly referred to as "starvation", might cause a color gradient which is opposite to that observed in isolated galaxies (Boselli et al. 2006), as young stars might only be found in the inner part of galaxies. A further active cold gas removal through environmental interactions affects their outskirts accelerating the outside-in morphological transformation.

Of course, a galaxy can experience both starvation and cold gas removal. The balance between these interactions is one of the elements which determine the morphology of galaxies that we observe today and how much time was necessary to halt star formation in these systems. Therefore, understanding the causes of quenching and morphological transformation requires not only the study of the star-forming disc of cluster galaxies but also an actual comparison between the the star-forming disc and the quiescent, gas-poor outer regions.

A key point to understand the physical processes a galaxy experienced is the study of the cold gas disc which typically extends at the outskirts of galaxies. Especially HI discs can be $\sim 1.5\times$ larger than the stellar disc, and due to a weaker gravitational potential, HI at larger distance is less bound to the system. Thus it is the first galaxy component which feels environmental interactions. By studying the distribution and kinematics of the cold gas, one can gain information on which kind of interaction a galaxy experienced recently. For example, ram-pressure stripping causes highly asymmetric perturbation in the cold gas distribution of a galaxy, producing HI tails which trail along the orbit of the galaxy. While the footprint of tidal interactions in the cold gas distribution and possibly in the stellar disc, is more symmetric. Indeed, these interactions in general cause two long streams of material in opposite directions (although they can have very different sizes). However, both a galaxy which experienced starvation and a galaxy which experienced gas removal in a sufficiently remote time, would nowadays show show a highly symmetric cold gas distribution. How can we understand whether the gas was used up or removed?

The main difference between starvation and starvation plus active gas removal concerns different quenching timescales. Although in the literature there are several definition of quenching timescale (we refer the reader to Cortese et al. 2021, where these definitions are discussed), starvation implies longer time scales for a galaxy to halt its star formation (rougly 4 Gyr Boselli et al. 2014b) with respect to the shorter (of the order of a few hundreds of Myr) time scales due to active gas removal. Thus, if the study of cold gas distribution and kinematics can help us understand the cause of relatively recent gas removal, the analysis of the stellar populations and, thus, of the star formation history (SFH) of a galaxy are crucial to distinguish between slow (starvation-like) and fast (stripping-like) quenching.

With this in mind, in this chapter we study the cold gas morphology and kinematics,

and the SFH of one particular galaxy in Fornax: NGC 1436.

Why is this galaxy so intriguing? NGC 1436 is located $\sim 0.5 \times R_{\rm vir} = 350$ kpc away from the center (Fig. 2.12) and it has a systemic velocity similar to the recessional velocity of Fornax (Fig. 2.13) (Loni et al. 2021 and Chapt. 2). By the study of the surface brightness profile of NGC 1436 and according to the radius where a break in the surface brightness occurs, Raj et al. (2019) divided the galactic disc in two parts: an inner and an outer disc. The clumpy, inner disc shows a tightly wound spiral structure with abundant dust (giving it an overall red colour) and numerous blue star-forming regions, while the outer disc appears featureless (no dust, spiral arms, or star forming regions). Thus, they argued that NGC 1436 is moving from a spiral to a lenticual morphology outside-in and, therefore, we have the exquisite opportunity to study a galaxy which is most likely evolving from a spiral to an S0 morphology. Iodice et al. (2019a) drew similar conclusions with the additional observation of a settled, inner ionised-gas disc that co-rotates with the stars, and with their finding that this gas is ionised by young stars, implying ongoing star formation in the inner disc. This result is further supported by the molecular emission, which was only detected within the inner disc (Zabel et al. 2020) and shows a similar kinematics as that of stars and Hα.

The idea of a morphological transformation of NGC 1436 is also supported by the truncated HI disc, which seems to extend just as far out as the inner star-forming disc (Loni et al. 2021; Chapt 2). However, caution must be taken while interpreting those ATCA HI observations. Indeed, Loni et al. (2021) highlighted some problems in recovering the total HI flux from this galaxy, and the low signal-to-noise ratio means that the HI morphology is not well constrained (Chapt 2). In this chapter, we will show new HI data from MeerKAT which confirm the existence of a truncated HI disc.

In Fig. 4.1, we show the optical image of this galaxy, where the spiral structure is visible in the inner star-forming disc. This structure is extended out to a star-forming radius $R_{\rm SF} = 6.8$ kpc. The spiral pattern disappears further out. In Fig. 4.1 we also show the ellipse corresponding to a surface brightness of 25 mag/arcsec^2 in B-band, which has semi-major axis $R_{25} = 8.6$ kpc. In this work we study the causes of the outside-in morphological transformation which is evident both from the lack of HI and spiral structure in the outer, quiescent disc of NGC 1436. We address the question of whether these causes are linked to gas stripping or just starvation and, therefore, we investigate the role played by the Fornax cluster environment in shaping the morphology of NGC 1436. In order to discriminate which environmental interaction is most likely responsible for it, we study the star-forming and quiescent disc of NGC 1436. We derive the star formation history of these two regions and thus, we measure the speed of SF quenching at different locations within the galaxy. The comparison between these SFHs should allow us to discriminate between a starvation or ram-pressure evolutionary scenario which has led to the current morphology of this a galaxy.

In this chapter we use data from the MeerKAT telescope to inspect the HI emission of the galaxy with a sensitivity of at least a factor of 10 better than that of the ATCA blind HI survey of the Fornax cluster (Loni et al. 2021). We then compare the HI distribution and kinematics with that of H_2 using data from the Atacama Large Millimeter/submillimeter

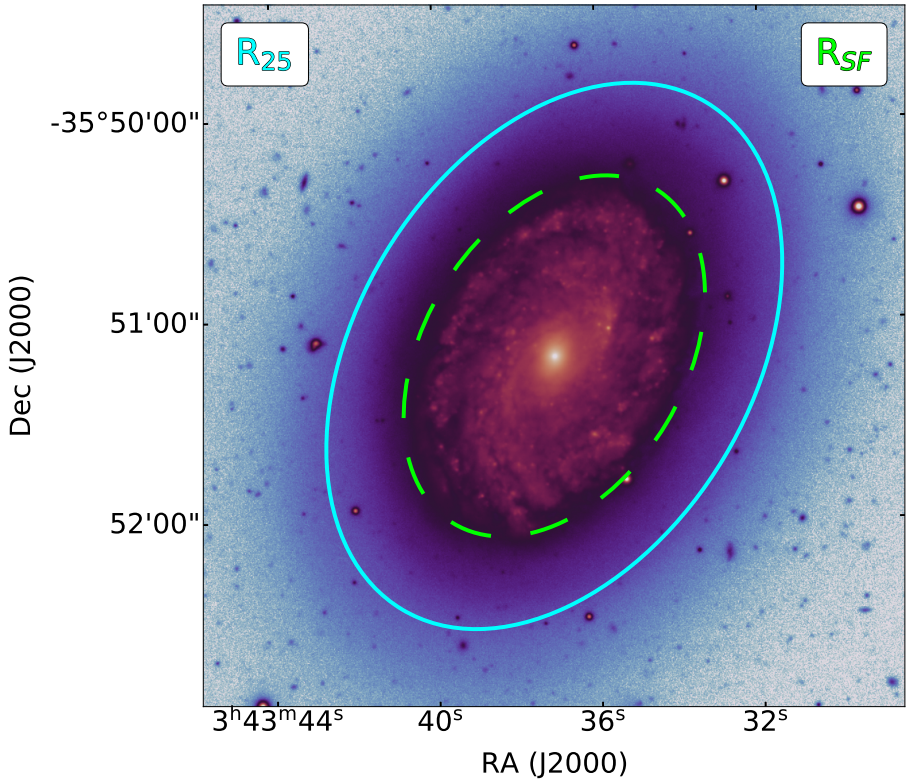

Figure 4.1: The figure shows the FDS optical image in $g-$band of NGC 1436 (Peletier et al. 2020b) where the star-forming disc is within $R_{\rm SF}$ = 59 arcsec (the dashed lime line), while the quiescent disc is further out of it. In the figure we also show R_{25} = 88.5 arcsec (solid cyan line), which indicates the isophotal radius measured at 25 mag/arcsec^2 in B-band (de Vaucouleurs et al. 1991).

Array (ALMA) (Zabel et al. 2019). This should establish whether the cold gas disc is well settled or not, and thus whether NGC 1436 is currently in a state of slow evolution. Finally, using data from the Multi-Unit Spectroscopic Explorer (MUSE) on the ESO Very Large Telescope we measure and compare the SFH of the inner star-forming disc with that of the outer quiescent disc. By performing this analyses, should then be clear in which epochs the galaxy might have experienced environmental interactions, whose strength is measured by smooth or sharp variations in the SFH.

We must remember that NGC 1436 is a Fornax member and it is not the only lenticular in the cluster. The SFH of three more S0s – which do not host any HI according to results of the blind ATCA HI survey of the Fornax cluster (Loni et al. 2021 and Chapt. 2)– , FCC 170, FCC 153 and FCC 177, were derived by Pinna et al. (2019b,a). As expected, these authors found that the stellar mass growth of lower-mass galaxies is delayed compared to that of higher-mass galaxies. Indeed, younger stars (2 Gyr old) were observed in FCC 177, which has the lowest mass, while the most massive S0 of the sample, FCC 170, only hosts old stars mainly formed in two epochs, 10 and 14 Gyr ago. FCC 170 is in

the high-density region of Fornax (see Fig. 4.2 and Fig. 1.8), where tidal interactions are supposed to be the main mechanism of stripping (Iodice et al. 2017a). Furthermore, FCC 170 might have also belonged to an in-falling subgroup of galaxies, where pre-processing might have begun to shape the morphology of the galaxy (Iodice et al. 2019b). By studying the spatial distribution of metallicity, Pinna et al. (2019b) proposed that the the oldest stars (14 Gyr old) were formed in situ in a short time, probably accelerated by the pre-processing occuring in the in-falling subgroup. The youngest stellar population (10 Gyr old), which show a different chemistry, might be the result of a minor merger. Cold gas removal was then proposed as the cause of the global quenching of the galaxy.

The remaining two S0s, FCC 153 and FCC 177 are located outside the densest region of the cluster (see Fig. 4.2 and Fig. 1.8). Pinna et al. (2019a) found a distinction in age in their outer and inner discs. Both outer discs are older than the inner ones. These authors proposed an evolutionary scenario similar to FCC 170, where gas accretion – which explains the different stellar population found in the inner and outer discs – happened before the cluster velocity dispersion became to high to make mergers unlikely (1-1.5 Gyr Bournaud et al. 2009). Furthermore, since the local environment of these galaxies is not as extreme as that of FCC 170, a milder impact of the Fornax environment and a potential lack of pre-procesing might have allowed FCC 153 and FCC 177 to form stars in more recent epochs.

Once we discriminate which physical process is responsible for the SFH and the current morphology of NGC 1436, the comparison with the evolutionary scenario of the three aforementioned S0s can help understand whether Fornax has a favorite channel to transform spirals into S0s.

The chapter is organized as follows: in Sect 4.2, Sect 4.3 and Sect 4.4 we present MeerKAT, ALMA and MUSE observations, respectively. In Sect. 4.5 we study the distribution and kinematics of HI and H_2. In Sect. 4.6 we describe MUSE data analysis and the SFH of the quiescent and star-forming disc of NGC 1436. In Sect. 4.7 we discuss the most likely evolutionary scenario which explains both the distribution and kinematics of the cold gas disc and the SFH of the quiescent and star-forming disc of NGC 1436.

4.2 MeerKAT observations

The MeerKAT Fornax Survey (Serra et al. 2016), which is currently on-going, has begun to collect data of the central part of the cluster in October 2020 using all 64 available antennas. In this chapter we use data from 24 mosicked pointings. Each pointing was observed for 2×5 h between October 2020 and February 2021 with the 32k zoom mode of the SKARAB correlator, which samples a 107 MHz band from 1337 to 1444 MHz with 32,768 channels, each with a width of 3.265 kHz. We used a subset of these data which consists of 12000 rebinned channels with a width of 6.53 kHz (1.38 $\mathrm{km\,s^{-1}}$ for HI at $z = 0$) that cover a velocity range from 216 to 4347 $\mathrm{km\,s^{-1}}$. We used the Container-

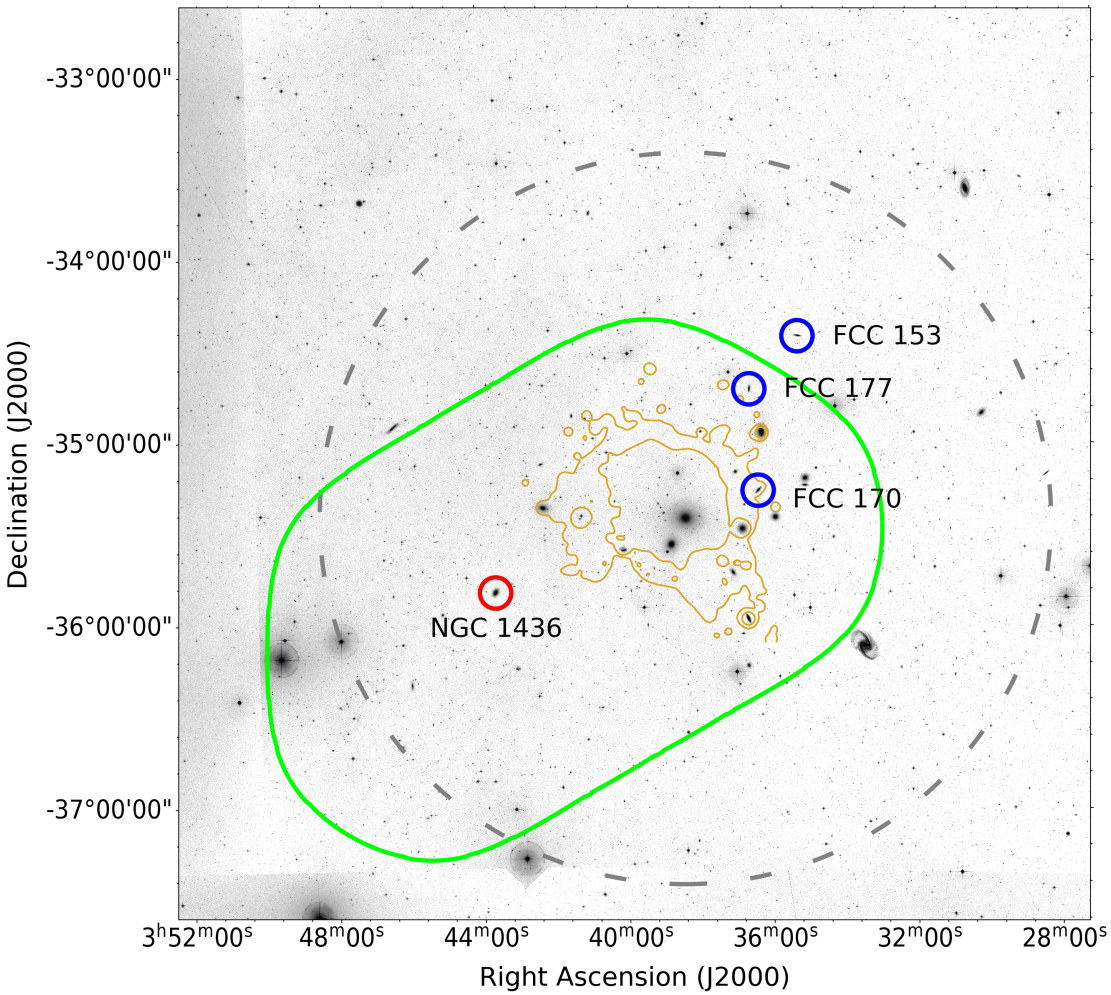

Figure 4.2: Layout of 24 pointings of the MeerKAT Fornax survey. The green outline includes the region where the average noise is 0.29 mJy beam^{-1}. The grey dashed circle is $R_{\rm vir}$. The background optical image comes from the Digital Sky Survey (blue band). The yellow contours show the X-ray emission in the Fornax cluster detected with XMM-Newton (Frank et al. 2013) and convolved with a 3 arcmin FWHM gaussian kernel. These contours are spaced by a factor of 2, with the lowest level at 3.7 counts deg^{-2} s^{-1}. The position of NGC 1436 that we show with a red circle, is outside the X-ray emission and within the lower noise region of the MeerKAT data cube. We also show the position of three S0s galaxies whose SFHs was studied in (Pinna et al. 2019a,b) with blue circle. One of them, FCC 170 is within the X-ray emission in projection.

ized Automated Radio Astronomy Calibration (CARACal) pipeline[1] to reduce the data. Here, we summarize the main steps to obtain the final HI data cube. We observed PKS B1934-638 or 0408-658 as the primary calibrator (depending on which one was visible) and J0440-4333 as the secondary calibrator. The latter was observed for 2 min every ∼1 h between on-source scans. We flagged strong radio frequency interference (RFI) based on Stokes Q visibilities. After flagging, we used CARACal's *crosscal worker* to derive and then apply, delay, bandpass and gain calibration to the data. At this point, we flagged RFI in the cross-calibrated target visibilities based on Stokes Q. Then we used CARACal's *selfcal worker* to perform a self calibration of the data (phase only; solution interval 2 minutes). This step also provides us a model of the continuum emission. Since, we are interested in spectral line emission, we subtracted the continuum emission in two steps. The former subtracts the continuum model obtained with *selfcal* from the visibilities, while the latter performs a subtraction of a polynomial fit to the continuum in the visibility plane in four spectral sub-windows using *UVLIN* (this strategy ensures to have a good polynomial fits even if oscillations in the beseline are present). Then, we performed a first blind cleaning of the HI cubes using CARACal's *line worker* and a second cleaning which made use of masks provided by the Source Finding Application (SoFiA; Serra et al. 2015; Westmeier et al. 2021)[2]. The same worker also restores clean components with the restoring beam. Finally, we mosaicked these 24 pointing. We made HI cubes at different resolutions of which we use two in this work. The former has a resolution of 67×65 arcsec^2, a noise level of 0.29 mJy beam^{-1} and a 3σ HI column density sensitivity of $N_{\rm HI} \sim 1.28 \times 10^{18}$ atoms/cm^{-2}. The latter has a resolution of 12×9.5 arcsec^2, a noise level of 0.28 mJy beam^{-1} and a 3σ HI column density sensitivity of $N_{\rm HI} \sim 4.50 \times 10^{19}$ atoms/cm^{-2}. In both cases the column density sensitivity is calculated assuming a linewidth of 25 km s^{-1}. In Fig. 4.2 we show the footprint of these 24 pointings, which covers the central part of the cluster and extends to the south-east. NGC 1436 is located in the lower noise part of the mosaic.

4.3 ALMA observations

The ALMA data used in this thesis are those presented in Zabel et al. (2021). They consist of a combination of data in Zabel et al. (2019) and data from the ALMA archive (project ID: 2017.1.00129.S, PI: Kana Morokuma).

As part of the ALMA Fornax Cluster Survey (Zabel et al. 2019), the ^{12}CO(1−0) emission from NGC 1436 was observed with a single pointing using the ALMA telescope in the C36-1 configuration (12 m), which is characterized by a primary beam of ∼ 55 arcsec at ∼ 115GHz. The spectral window to target the ^{12}CO(1−0) rotational line was centred at 114.547 GHz with a bandwidths of 1.875 GHz wide covered by 3840 channels.

[1]The CARACal pipeline is available at the following link `https://caracal.readthedocs.io/en/latest/`

[2]Two version of SoFiA are available at the following links `https://github.com/SoFiA-Admin/SoFiA`, `https://github.com/SoFiA-Admin/SoFiA-2/`

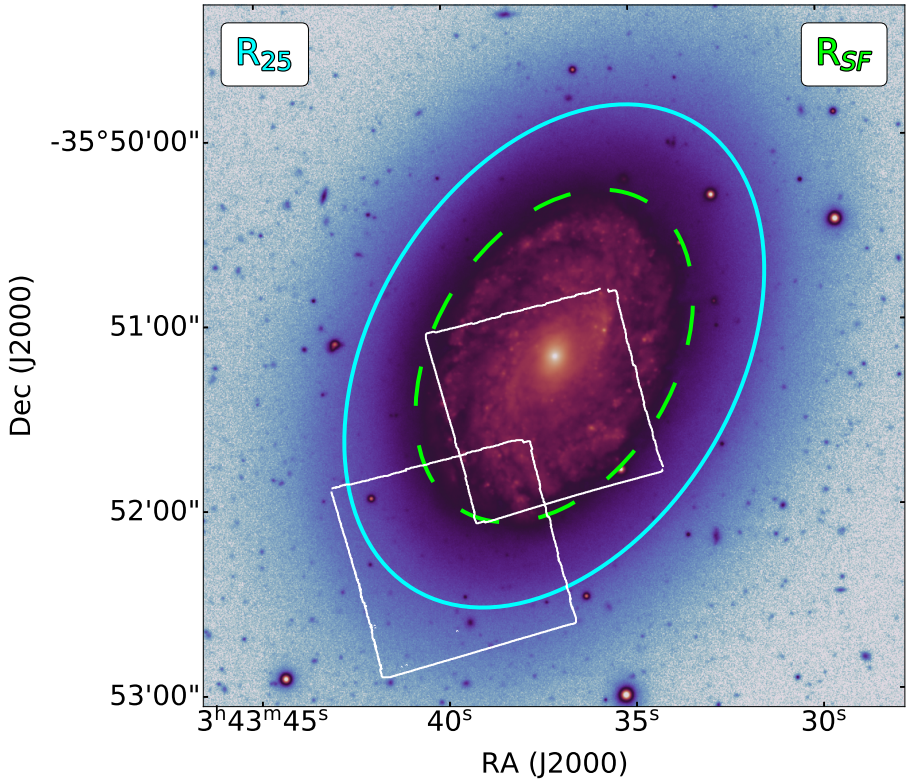

Figure 4.3: Similar to Fig. 4.1. Here, we show the two dedicated MUSE pointings on the star-forming and quiescent disc observed as part of the Fornax 3D survey (F3D; Sarzi et al. 2018).

The spectral windows of the remaining band 3 observations were centered at 113.001, 100.939, 102.544 GHZ with bandwidths of 2 GHz divided in 128 channels.

The archival data were obtained using the Morita Array (the reader finds details on the survey in Morokuma-Matsui et al. 2019) in 2017 November 30. Its primary beam is $\sim$ 90 arcsec at $\sim$ 115 GHz. The spectral window covering the ^{12}CO(1−0) was centred on 114.756 GHz, with a bandwidth of 1.875 GHz, covering 3840 channels.

The data reduction of both datasets was performed by Zabel et al. (2021) using the Common Astronomy Software Applications package (CASA, version 5.1.1 − McMullin et al. 2007). The two datasets were combined using the task `concat` and cleaned interactively using the task `tclean` (Högbom 1974). The final data cube was obtained using a Briggs weighting scheme (Briggs 1995) with a robust parameter of 0.5. The velocity resolution is 10 km s^{-1}and the synthesized beam size is 2.68×2.06 arcsec. The sensitivity reached is ∼2.046 mJy beam^{-1}.

4.4 MUSE observations

The integral field spectroscopic data used in this work (program ID: 296.B−5054(A)[3]) were collected as part of the Fornax 3D survey (F3D; Sarzi et al. 2018), using the Multi Unit Spectroscopic Explorer (MUSE) on the UT 4 at the Very Large Telescope (VLT) (Bacon et al. 2010) in the Wide-Field Extended mode. This ensures high-quality 3D spectroscopy with: (*i*) a spatial sampling of 0.2"×0.2" in a field of view 1'×1' large; (*ii*) a wavelenght range of 4650-9300 Å with a nominal spectral resolution of 2.5 Å at FWHM at 7000 Å and a spectral samplig of 1.25 Å/pixel. However, due to a combinations of different slightly offset exposures taken at different position angles, the average spectral resolution is 2.8 Å at FHWM.

The observations of NGC 1436 were carried out in August 2016, January 2017 and July 2017. Two MUSE pointings, which do not cover the whole galaxy, were dedicated to observing the star-forming and the quiescent disc of NGC 1436, respectively (Fig. 4.3). Each pointing was observed 4 times with an exposure time of 900 s for each. As for the majority of F3D targets, dedicated sky exposures of 3 min were taken within each observing block for the evaluation of the sky background.

The MUSE pipeline version 1.6.2 (201 2012; Weilbacher et al. 2016) was used by Sarzi et al. (2018) to reduce the data under the ESOREFLEX environment (Freudling et al. 2013). This procedure includes a set of bias and overscan subtraction, internal flat fielding (to correct the pixel-to-pixel response variation), wavelength calibration, determination of the line spread function, illumination correction with twilight flats (to account for large-scale variation of the illumination of the detectors), and illumination correction with lamp flats (to correct for edge effects between the integral−field units). The sky subtraction was performed in two steps: (*i*) by fitting and subtracting a sky model spectrum on each spaxel of the field of view; (*ii*) by using Zurich Atmospheric Purge algorithm (ZAP; Soto et al. 2016) which is useful to reduce residual sky contamination.

4.5 Morphology and kinematics of the multi-phase gas disc

As mentioned in Sect. 4.1, previous results on the HI emission in NGC 1436 (Loni et al. 2021, see also Chapt. 2) are not exhaustive and have a large discrepancy with single dish data from Courtois et al. (2009). Here, we address the question of whether NGC 1436 has a truncated HI disc or not. We extracted sub-cubes from the two MeerKAT mosaics at different resolution and sensitivity. The former has a resolution of 65×67 arcsec^2 with a 3σ HI column density sensitivity of $N_{\rm HI} \sim 1.28 \times 10^{18}$ atoms/cm^{-2} (hereafter, low-resolution cube). The latter has a resolution of 12×9.5 arcsec^2 with a 3σ HI column density sensitivity of $N_{\rm HI} \sim 4.50 \times 10^{19}$ atoms/cm^{-2} (hereafter, high-resolution cube). In both cases, the sensitivity is calculated assuming a linewidth of 25 km s^{-1}(see also

[3] http://archive.eso.org/eso/eso_archive_main.html

Sect. 4.2). In theory, the high-resolution cube allows us to gain information both on the HI morphology and kinematics, while the low resolution cube with better sensitivity should recover more flux than the former cube.

By using the Smooth + Clip (S+C) finder in SoFiA, we search for HI emission in both high- and low-resolution MeerKAT cubes. This procedure involves interactively smoothing the input cube with a set of kernels with different size. After smoothing the cube, the noise is evaluated and voxels with absolute value above a user-defined threshold are added to a source detection mask. We set the detection threshold to be $3.5 \times$ the local noise. Then we use a friends-of-friends algorithm to merge pixels into objects if they are adjacent along at least one of the three axes of the cube and reject all detected objects with a size smaller than 5 spatial pixels or 5 channels. We further evaluated the reliability of these detections using the reliability algorithm presented in Serra et al. (2012), which assumes that true sources have positive flux while the noise is symmetric around 0. In general, even using other settings in the S+C algorithm (e.g. size of merging radii) on both high and low-resolution cube, SoFiA detected only one reliable HI source, which is clearly associated with NGC 1436.

Fig. 4.4 shows both mom0 maps, while the bottom panel shows the comparison between contours of the low-resolution mom0 map (green) and those obtained by convolving the high-resolution mom0 map to the same resolution of the lower one (purple). Here we can see that the match between these contours is excellent, meaning that spatial distribution of the HI flux recovered from the high-resolution image is the same as the one from the low-resolution image. That is, NGC 1436 does not host any diffuse, low-column density HI in excess of the HI detected at high resolution. This implies that the HI disc is sharply truncated and does not extend beyond the inner, star-forming disc of NGC 1436. Furthermore, the center of the galaxy shows a strong HI depression. Finally, none of the HI cubes shows any sign of the presence of distortions, asymmetries or tails at low column density. Since the data are extremely sensitive, we can confidently rule out any recent disturbance to the gas disc.

The agreement between the low- and high-resolution views of HI in NGC 1436 is also evident in Fig. 4.5, where we compare the spectra extracted from these cubes. Here, the uncertainties on the total HI fluxes shown in the legend are calculated by summing in quadrature the statistical uncertainties – derived from the local RMS measured by SoFiA and the number of independent pixels detected in each channel. We also show the HI spectrum extracted from single dish data (GBT - Courtois et al. 2009) as a comparison (see Sect. 2.3).

Having established that the high-resolution cube was able to recover the same total HI flux measured from more sensitive data, we can study the HI kinematics at high resolution being confident that we are not missing any information. Therefore, in the rest of this section we show results obtained from the analysis of the high-resolution data.

Fig. 4.6 shows the moment-1 velocity field, and thus the kinematics of the HI within the lowest reliable HI contour shown in the top right-panel of Fig. 4.4. Here, we see that the HI disc is regularly rotating. Furthermore, judging from the appearance of the velocity field, we can already see that the rotation curve is rising in the inner half of the HI disc,

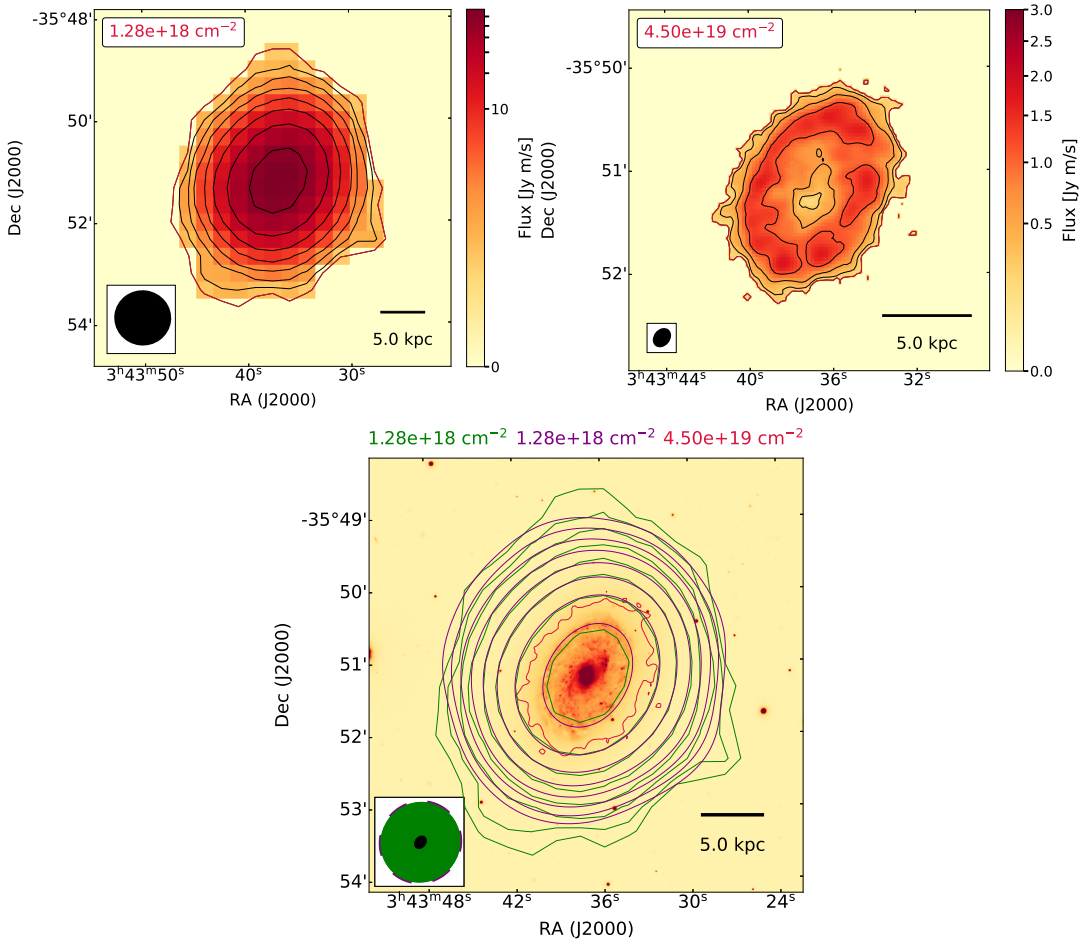

Figure 4.4: Top panels show the mom0 maps of the low-resolution cube (left) and the high-resolution cube (right). On the top left of each panel, we show values of the 3σ column density sensitivity, which represent the outer red contour. Black contours represent steps of 2^n from it (n = 0, 1, 2, ...). We show the PSF on the bottom-left corner of each panel, and a 5 kpc scale bar in the bottom-right corner. The bottom panel shows a further comparison between the previous mom0 maps. Green contours are the same of the low-resolution mom0 map. In red, we show the lowest reliable contour of the 10 arcsec mom0, while in purple contours obtained by convolving the 10 arcsec mom0 to the same resolution of the 60 arcsec mom0. Steps between contours are the same of before. Values with the same colors on the top of the image, represent their 3σ column density sensitivity of the respective mom0 map. Green and black PSFs are the same of the 60 and 10 arcsec cube, respectively. In purple the PSF of the convolved MeerKAT cube at a resolution of 60 arcsec.

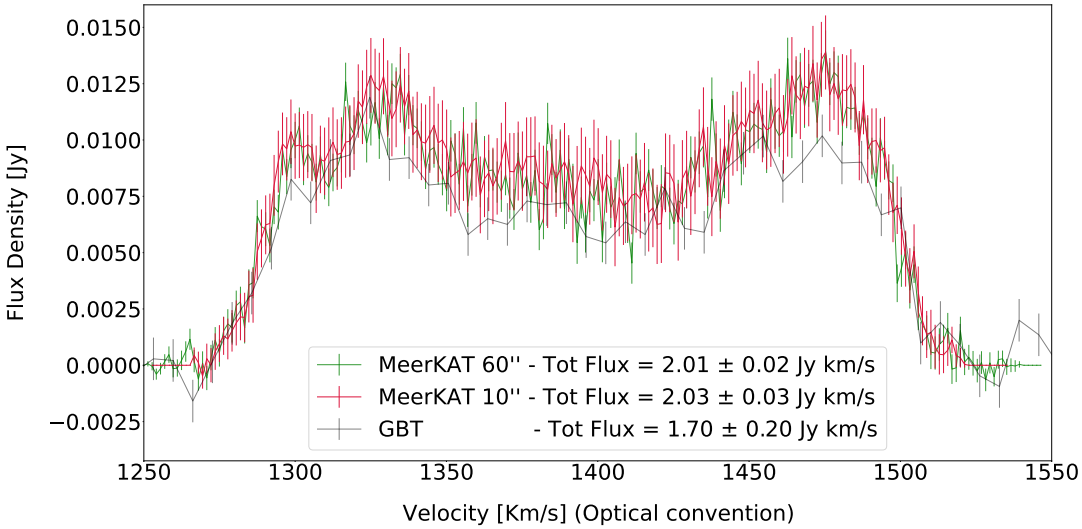

Figure 4.5: The figure shows spectra extracted from the 10 arcsec (red), 60 arcsec (green) MeerKAT cubes, and from single dish data (GBT Courtois et al. 2009 - black), respectively. Legend shows total fluxes obtained from these data.

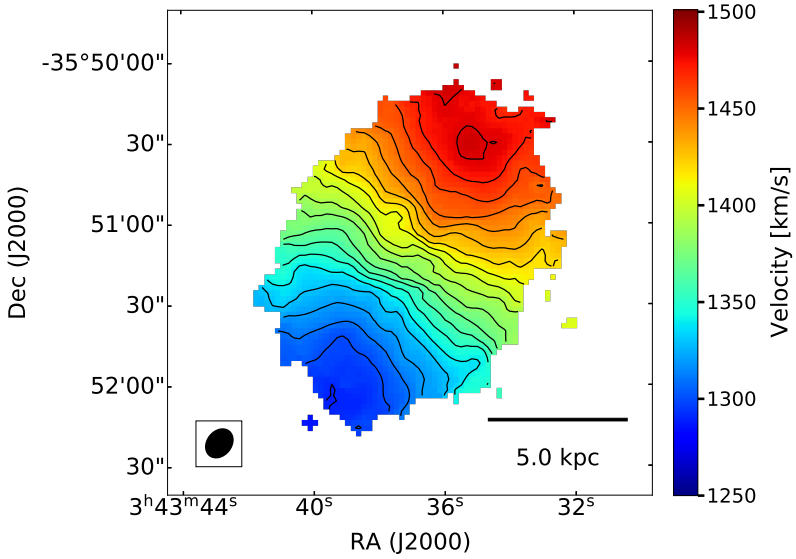

Figure 4.6: The figure shows the mom1 maps obtained by the 10 arcsec MeerKAT cube. In particular it shows the HI kinematics within the lowest reliable HI contour shown in the top-right panel of Fig. 4.4.We show the PSF on the bottom-left corner, and a 5 kpc scale bar in the bottom-right corner.

and flattens further out. Also, there is a slight PA warp at the edge of the disc, which is visible as an anticlockwise rotation of the outer isovelocity contours.

We also show the channel maps of the high resolution cube rebinned in velocity to 23 $\mathrm{km\,s^{-1}}$ channels for presentation purpose (Fig. 4.7). In the two middle rows, we can see how the rotating HI has a depression in the center of the galaxy similarly to that observed in the mom0 map in the top-right panel in Fig. 4.4.

Although the resolutions are not the same, we can compare HI and H_2 in NGC 1436. The latter was studied by Zabel et al. (2019) and also described in this thesis (see Sect. 4.3). We are interested in understanding how the H_2 is distributed and how it is rotating with respect to the HI. Fig. 4.8 shows the high-resolution MeerKAT mom0 map where we overlaid H_2 contours. Here, we can see that H_2 follows the HI ring and that there is no H_2 in the center of the galaxy.

We also compare the kinematics of these two cold gas phases in Fig. 4.9 and in Fig. 4.10, where we see that HI and H_2 are co-rotating. This final comparison establishes with no doubt that the cold gas disc of NGC 1436 is well settled.

In the rest of this section we show results obtained by fitting the HI kinematics of the high-resolution cube with the Tilted Ring Fitting Code[4] (TiRiFiC - Józsa et al. 2012). This allows us to measure the HI surface brightness profile and to find the best-fitting values for geometric parameters (e.g. inclination, position angle) and the rotation curve. The required input for TiRiFiC consists of a first guess of the inclination and position angle of the galaxy, its systemic velocity and central coordinates. Furthermore a measure of the RMS of the input cube is needed. TiRiFiC models the galaxy in rings and sub-rings, where the model parameters are fitted to best reproduce the HI geometry and kinematics in the data (further details in Józsa et al. 2007). We performed several runs of TiRiFiC. For the first run, we set our first guess on the rotation velocity equal to 130 $\mathrm{km\,s^{-1}}$, the inclination equal to 48 deg, the position angle equal to 33 deg and the systemic velocity equal to 1390 $\mathrm{km\,s^{-1}}$. These first guesses are based on visual inspection of moment images, channel maps and position-veloxity diagrams. In each subsequent run we adjusted the input parameter values to improve the quality of the model. In general, we used as input the output of the previous run. We made two main experiments. In the former, we model our galaxy with a flat disc (i.e., we forced TiRiFiC to fit a unique value for PA and inclination across all rings). In the latter, we forced TiRiFiC to fit flat rotation curve, but allowed the disc to not be flat. Between these two experiments, we obtained better results modelling our galaxy with a flat disc. Therefore, we further improve the output flat disc model by using an advanced feature of TiRiFiC, which allows us to fit and interpolate some model parameters in groups of model rings rather than for each ring independently. Eventually, we chose the model that better follows the distribution and kinematics of the observed HI based on visual inspection.

In Fig. 4.11 we show a channel-map similar to Fig. 4.7, where we have also re-binned the TiRiFiC model in order to show a comparison between data and model. We show the

[4]The software is available at the following link `https://gigjozsa.github.io/tirific/index.html`

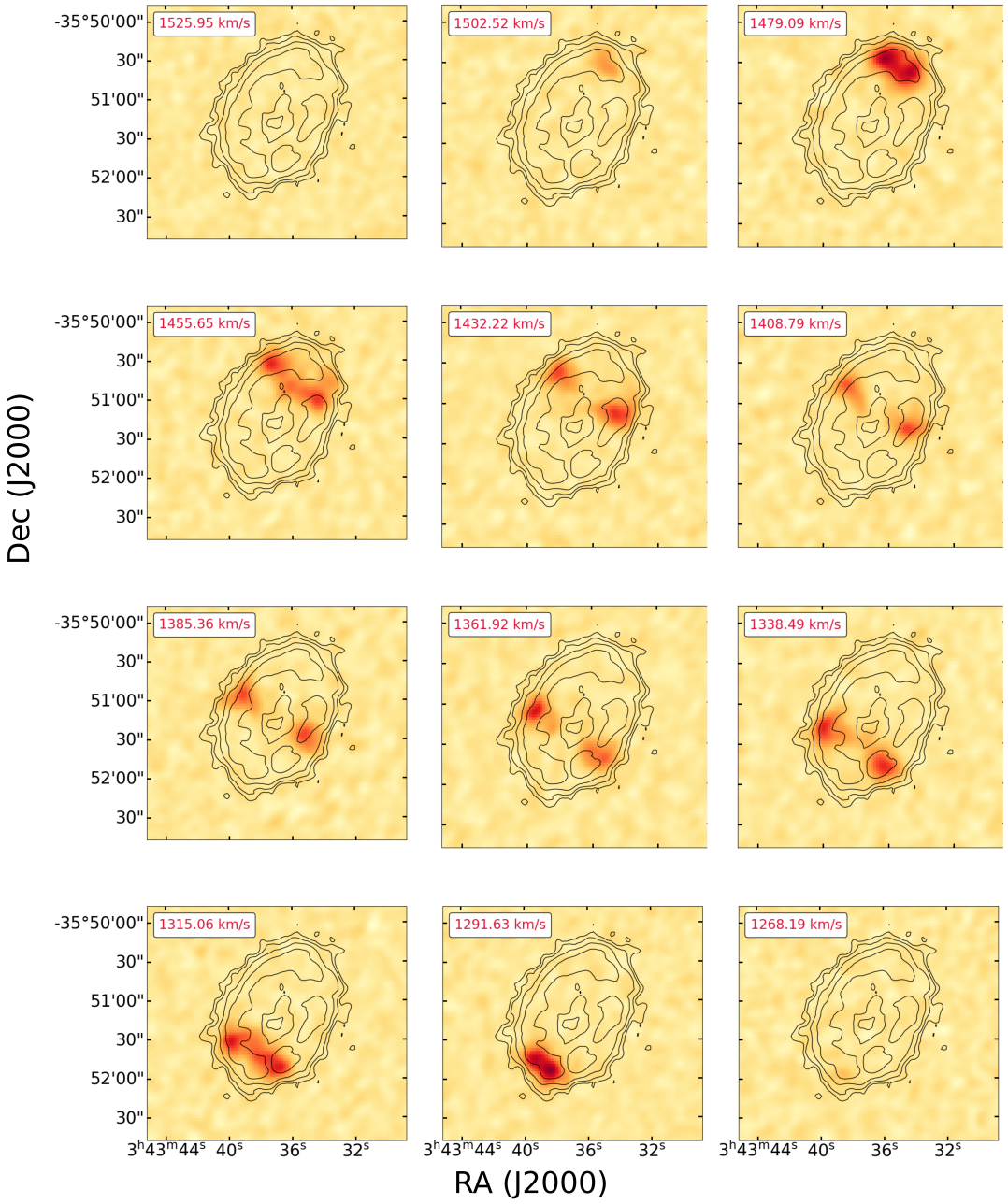

Figure 4.7: The figure shows a channel-map obtained from the 10 arcsec cube, which was previously rebinned to have velocity resolution of 23 $\mathrm{km\,s^{-1}}$(the original resolution is 1.38 $\mathrm{km\,s^{-1}}$). Black contours are the same of the top-right panel in Fig. 4.4.

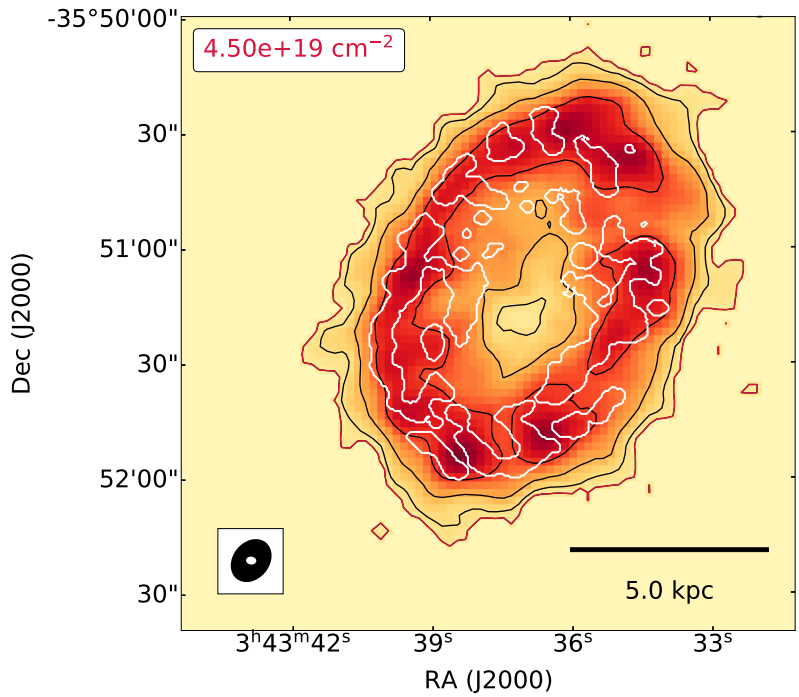

Figure 4.8: The figure shows the MeerKAT 10 arcsec mom0 (same contours as these shown in the top-right panel of Fig. 4.4) where we overlaid the H_2 mom0 map contours (white - Zabel et al. 2019). Both MeerKAT and ALMA PSF are shown on the bottom-left of the figure. ALMA PSF (white) is within the MeerKAT PSF (black).

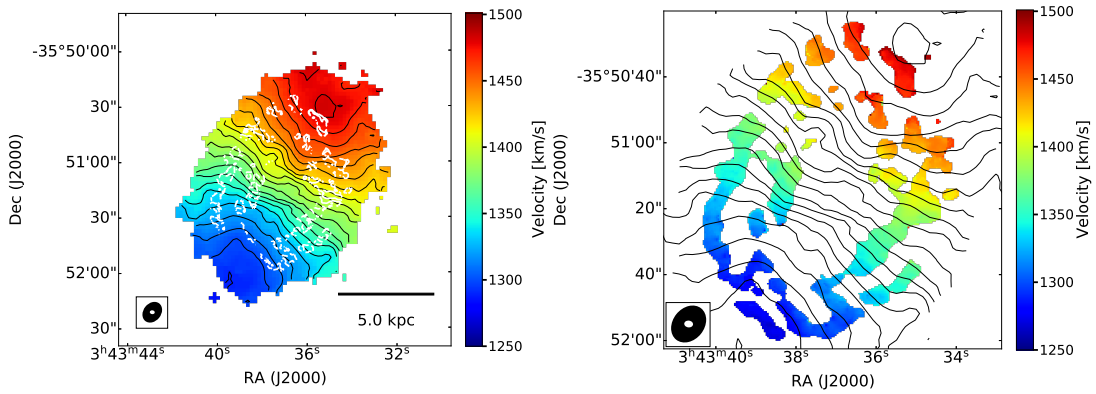

Figure 4.9: The figure shows the comparison between the HI kinematics (left - same as Fig. 4.6) and that of H_2 (right). White contours in the figure on the left are the same of Fig. 4.8, which represents the distribution of H_2 within the HI disc. On the right, we overlaid the HI velocity contours (same contours on the left panel). On the bottom-left of each panels, we show MeerKAT (black) and ALMA (white) PSF.

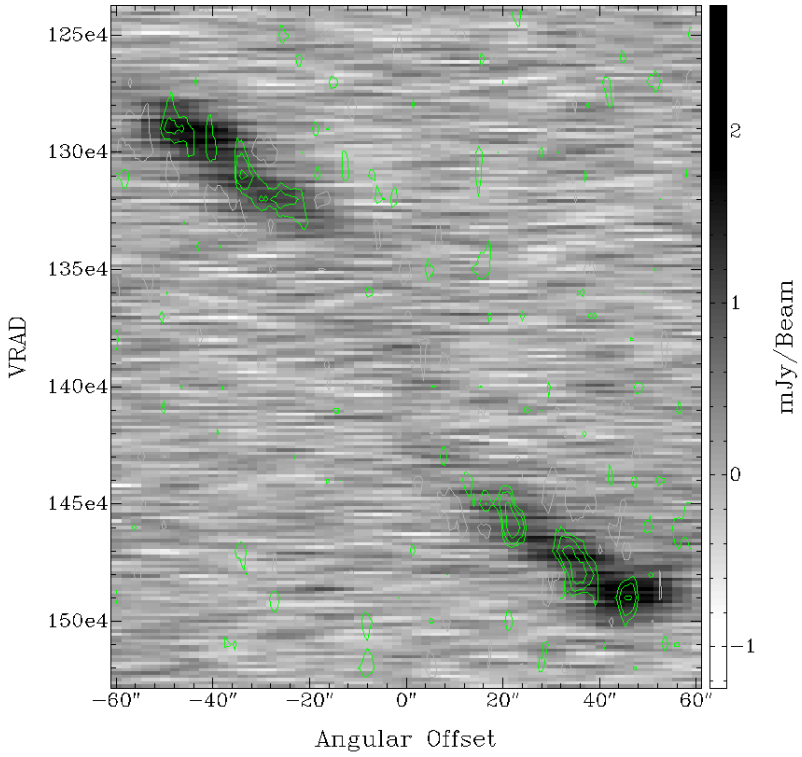

Figure 4.10: PV-diagram of the HI emission of NGC 1436 (measured from the high-resolution cube) where we overlay contours of the H_2 PV-diagram (Zabel et al. 2020). Green contours increase with a step of 2 shows the positive H_2 emission, while the gray contour is set at the same (negative) level of the first green contour.

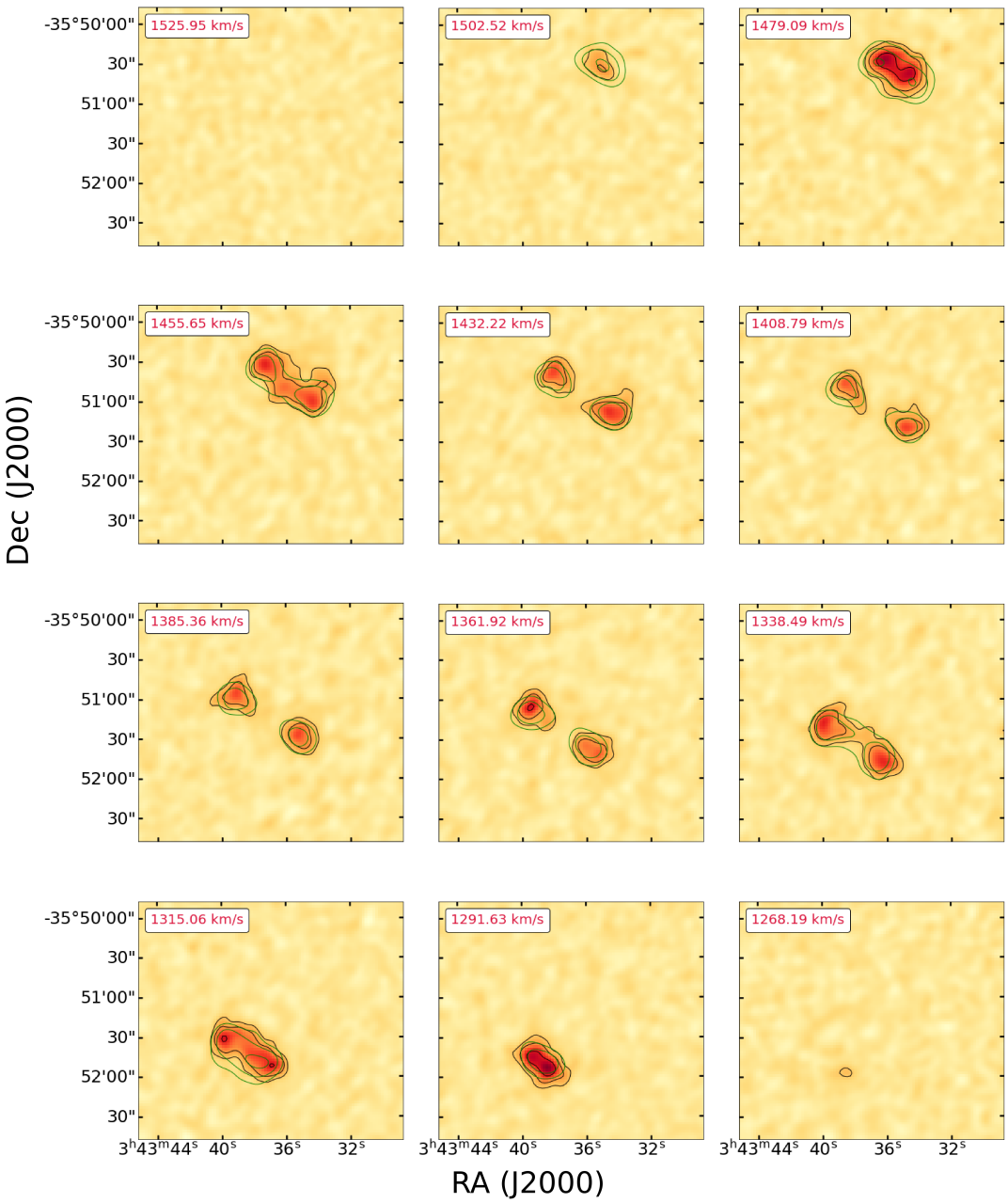

Figure 4.11: This figure shows the channel-map of re-binned MeerKAT data (black - same data used in Fig. 4.7) and TiRiFiC re-binned model (green) at the same velocity resolution (black contours). Contours are set at the same level of ~3× the noise of the re-binned MeerKAT data, with subsequent contours increasing at each step by 2^n (n=1,2,3 ..).

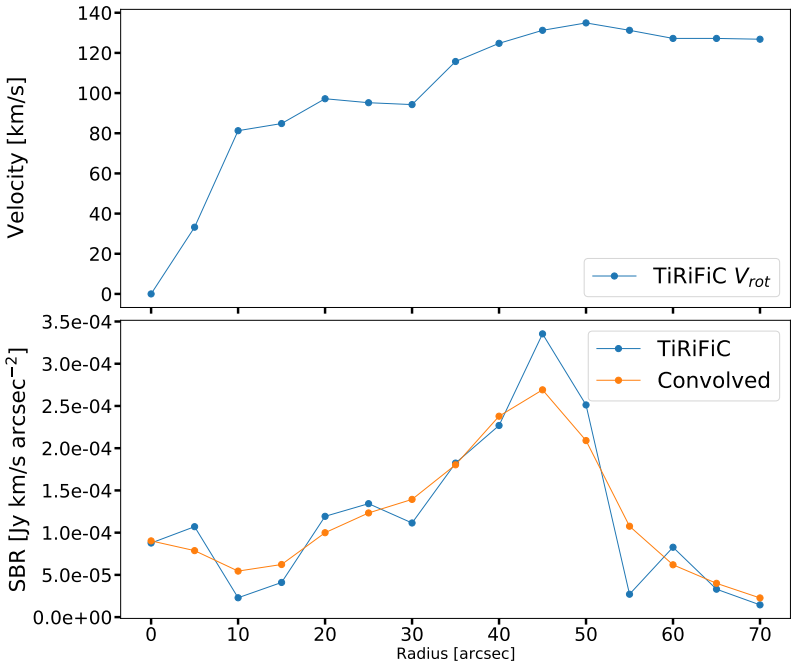

Figure 4.12: The figure shows some TiRiFiC outputs obtained by fitting the MeerKAT data. In the top panel we show the rotation curve. In the bottom panel, we show the TiRiFiC SBR (blue) and that obtained by convolving it with the MeerKAT beam (orange).

same contours at ~3×σ (where σ is the RMS of the re-binned cube), with subsequent contours increasing at each step by 2^n (with n=1,2,3 ..), both for the data and the model. In general, the model nicely follows the HI rotation in the data.

Fig. 4.12 shows the rotation curve of NGC 1436 obtained through our TiRiFiC fitting. As anticipated, the velocity increases with increasing distance from the center of the galaxy in the inner regions, and it reaches a plateu at ~50 arcsec. In the bottom panel, we show the derived surface brightness profile (SBR). The best-fitting model shows some up and down, which is unlikely to be real. If convolved with the MeerKAT beam, it shows a more regular trend. The HI SBR has a peak at a radius of 45 arcsec.

In general, by studying both the cold gas distribution and kinematics (both HI and H_2), we appreciate the high level of symmetry of NGC 1436. Both HI and H_2 are distributed within a settled ring where they are co-rotating, with no hints of any recent tidal or hydrodynamical disturbances. Given that the orbital time at the disc's edge is of ~300 Myr (rotational velocity ~130 km s^{-1}at a radius of ~ 6.7 kpc) we can rule out strong interactions in the last few orbital times, so for a period of the order of ~1 Gyr. Any conclusions on the processes shaping the properties of NGC 1436 must explain these results, too.

4.6 Star formation history

The second analysis we performed on NGC 1436 concerns the SFH of the quiescent and star-forming disc of the galaxy. To reach our goal, we used two software: the Penalised Pixel-Fitting code[5] (pPXF; Cappellari & Emsellem 2004; Cappellari 2017) and the Gas and Absorption Line Fitting code[6] (GandALF; Sarzi et al. 2006; Falcón-Barroso et al. 2006).

Here, we describe how we infer the distribution of stellar ages, and thus the SFH, in the inner star-forming disc and in the outer quiescent disc of NGC 1436. Both are defined by elliptical annuli whose position angle and ellipticity are those obtained in Sect. 4.5 with TiRiFiC. For the inner disc we avoid the galaxy centre (out to 9 arces) and, we cover the star forming disc (whose size is R_{SF} = 59 arcsec) out to 44 arcsec. The elliptical annulus used to study the quiescent disc starts just outside the truncated HI disc, which has a semi major axis of R_{HI} = 70 arcsec, slightly larger than the star-forming disc and reaches out to R_{25}. This conservative choice ensures that spectra extracted in this region of the disc are not contaminated by signal from the star-forming disc (see Fig. 4.13 for a comparison between R_{HI} and R_{SF}). To reconstruct the SFH in the star-forming disc and the quiescent regions outside it we extract and analyse a series of spectra from sectors of these elliptical annuli (hereafter called "apertures"). Since stellar populations within such regions should be rather similar beyond timescales corresponding to the orbital times between adjacent sectors, this approach allows to use the variance between the SFHs recovered in such apertures to estimate the uncertainty in our overall SFH for the star-forming disc and quiescent regions (more on this below). In order to have a similar signal to noise in each aperture, the apertures are defined to all have an identical area for the inner disc, and an identical area for the outer disc. Since the signal is stronger in the inner MUSE pointings, we could use a higher number of apertures there (18) with respect to the outer pointing (8 apertures). Fig. 4.14 shows the 8 and 18 apertures we used to extract spectra from the outer and inner MUSE pointings respectively. Both MUSE pointings include extra-galactic sources, some of which are within the elliptical annuli. Therefore, before extracting spectra, we masked these sources (white squares in Fig. 4.14).

In Fig. 4.15 and Fig. 4.16, we show examples of spectra extracted from an aperture in the quiescent disc and from an aperture in the star-forming disc, respectively. In general, all spectra extracted from apertures in the quiescent disc show contamination from the sky and no bright emission lines from the ionized gas, while spectra extracted from the star-forming disc have negligible sky contamination (relative to the bright stellar continuum) but bright ionised-gas emission lines. GandALF overcomes the problem of sky contamination by masking these lines.

With the aim of estimating the SFH, each aperture spectrum was fitted by pPXF and GandALF using spectral templates from the MILES single-age stellar population (SSP)

[5] a IDL and python version of pPXF are availeble at the following link `https://www-astro.physics.ox.ac.uk/~mxc/software/`

[6] GandALF is availeble at the following link `https://star.herts.ac.uk/~sarzi/`

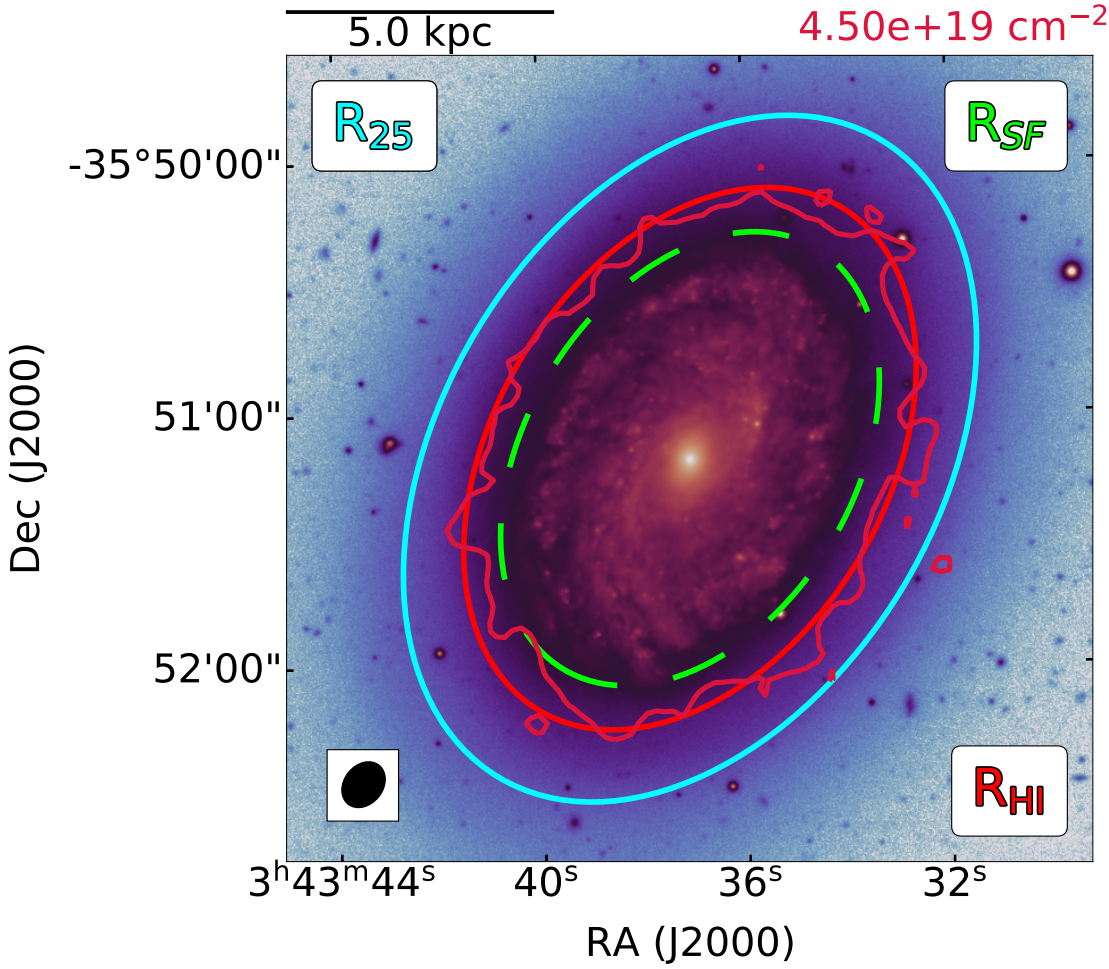

Figure 4.13: Comparison between the red ellipse – which follows the geometry of the lowest reliable HI contour, whose HI column density is shown on the top right of the figure (the same of Fig. 4.4, right panel) – and the lime dashed ellipse – which follows the star-forming disc of the galaxy. Red ellipse has a semi-major axis of $R_{\rm HI}$ = 70 arcsec, while the lime dashed ellipse has a semi-major axis of $R_{\rm SF}$ = 59 arcsec. We also show in the figure R_{25} = 88.5 arcsec (solid cyan line), which indicates the isophotal radius measured at 25 mag/arcsec^2 in B-band (de Vaucouleurs et al. 1991).

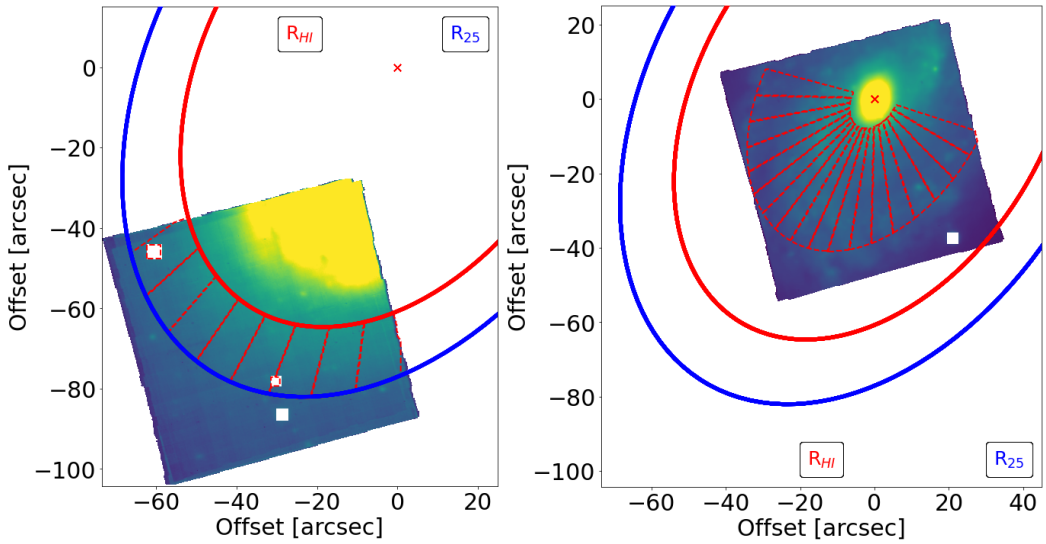

Figure 4.14: Left pannel shows sectors of the elliptical annulus overlaid to the MUSE image of the outer pointing from which we extracted MUSE spectra. Right pannel shows the same for the inner MUSE pointing. White squares are extra-galactic sources we masked. The red ellipse has the same size of the truncated HI disc (see also Fig. 4.13). R_{25} is the isophotal radius measured at 25 mag/arcsec^2 in B-band (de Vaucouleurs et al. 1991)

model library of Vazdekis et al. 2015[7]. We use the whole set of SSP templates with a Kroupa initial mass function (Kroupa 2001). This set covers a range in age between 30 Myr and 14 Gyr, with total metallicity $-2.27 \leq$[M/H]≤ 0.4 dex, and α-element overabundance [α/Fe] between 0 and 0.4 dex. These stellar templates are optimally combined by Gandalf to obtain the stellar spectrum model that - together with nebular emission when necessary - best matches the observed spectrum. This optimal combination of SSP models can then be used to construct a SFH through the sum of weighted single-age delta functions.

Similarly to Sarzi et al. 2018, we first fit the MUSE data with pPXF to measure the stellar kinematics by using the bluer part of the MUSE spectrum [4800-5850] Å and subsequently extend the fitting range to [6850] in the GandALF fit. During the pPXF we mask regions potentially affected by emission and allow for an additive correction for the shape of the continuum, A shorter range for the pPXF fit speeds up the fitting process and delivers robust results since most strong stellar absorption lines fall in the bluer end of the MUSE spectra. The GandALF fit then holds to the pPXF kinematics, but allows to change again the optimal combination of SSP templates in the stellar models in response to the additional use of emission lines in the fit and also in the use of reddening or of a multiplicative polynomial correction for the continuum shape.

[7]The MILES stellar-population model library can be found at the following link `http://miles.iac.es/`

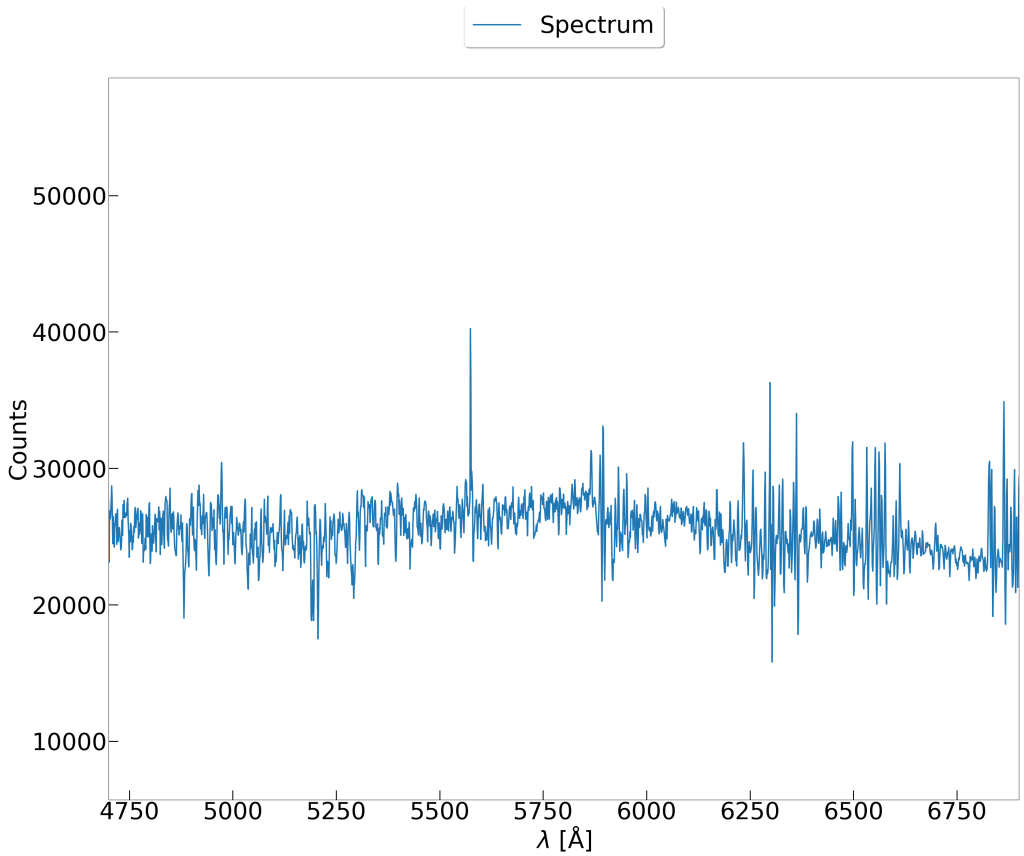

Figure 4.15: Example of a MUSE spectrum extracted from an aperture in the quiescent disc of NGC 1436. All spectra extracted from apertures in the quiescent disc, show contamination from the sky.

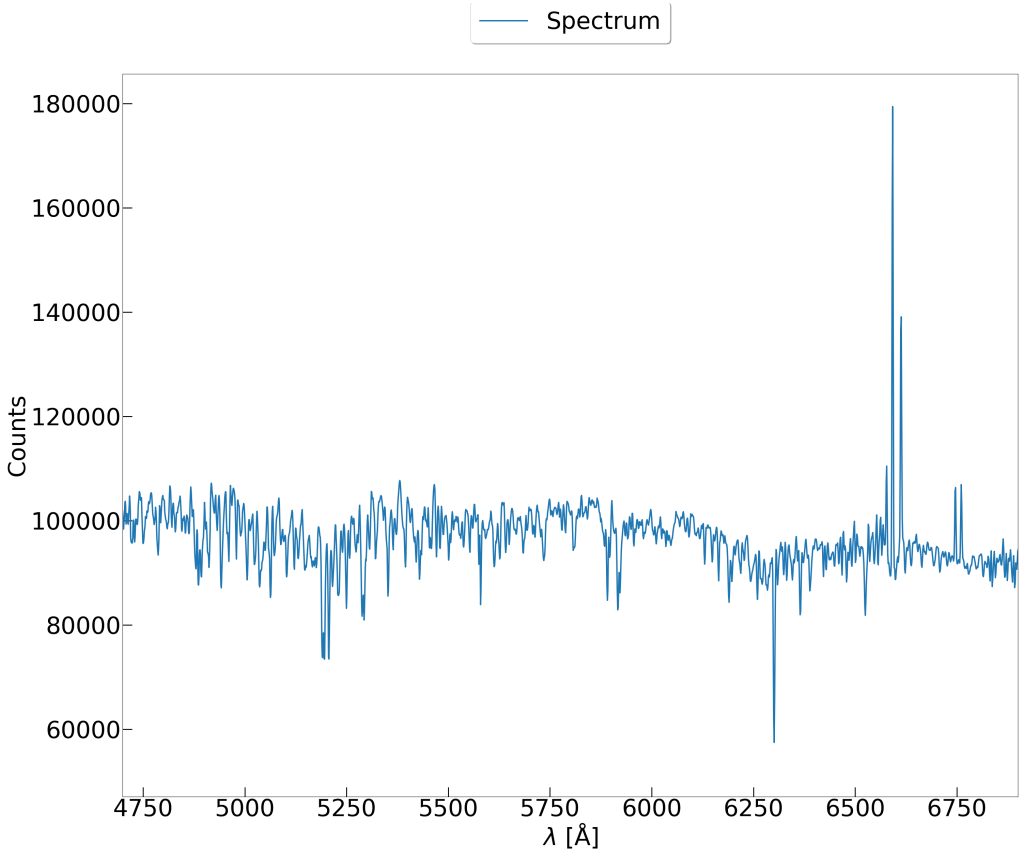

Figure 4.16: Example of a MUSE spectrum extracted from an aperture in the star-forming disc of NGC 1436.

We used two different GandALF emission line setup depending on whether the spectrum to be fitted was extracted from the inner or outer disc. This setup includes a list of emission lines which GandALF can fit or ignore. One of the reason why we used two different emission line setup for the star-forming and quiescent disc of NGC 1436, respectively, resides in the fact their ionised gas content is very different. The star-forming disc hosts a significant amount of ionised gas, which results in bright emission lines throughout the MUSE spectrum wavelength range. On the contrary, the quiescent disc shows only a few, very weak emission lines. As a result, while in the star-forming disc we can (and, in fact, we must) fit all known forbidden and recombination lines in order to minimise the error in the SFH determination, in the outer disc many weak lines are better ignored. A case in point is the Hβ line. If we fit it in the outer disc spectra, we find it to have extremely low signal-to-noise ratio and to be unphysically brighter than what would be expected based on the (also weak) Hα emission. The theoretical Hα/Hβ ratio is 2.86, and higher values can be observed in case of dust absorption, but in the outer disc we often find unphysical, lower values. An important difference in the GandALF setup is therefore that, in the outer disc, we ignore any weak Hβ emission.

Furthermore, although in theory GandALF can fit the data using two reddening components (Sarzi et al. 2018) which model (*i*) extinction of the entire spectrum due to diffuse dust and, (*ii*) extinction due to dust localised in the star forming regions to reproduce the observed Balmer decrement, we could not use this strategy due to flux calibration errors. In practice, with this strategy we would get bright and broad (in wavelength) residuals in the fit. Thus, we included instead a multiplicative polynomial in our fit in order to correct these errors. In general a polynomial order between 6 and 15 is required to have low residuals in both MUSE pointings.

In the fitting process, GandALF finds the best combination of MILES templates which better reproduces the data. In practice, the output of GandALF is a list of 1272 weights $M_i^{\rm SSP}$, which, once accounting for the distance to the object, give the stellar mass of the i-th SSP at the time of its birth., one for each SSP model included in the set of templates (see above). In Fig. 4.17 and Fig. 4.18 we show the comparison of the GandALF fits and the MUSE spectra extracted from an aperture of the outer and inner MUSE pointing, respectively. In Fig. 4.19 we show an example of the weights $M_i^{\rm SSP}$ assigned by GandALF to the MILES SSP templates to model some observed spectra (the figure ignores differences in [α/Fe], and in the rest of our analysis we focus on the distribution of weights in age). It is worth noting that the best fits typically include just a few SSP templates with a non-zero weight. For example, in the left panel of the figure, which shows the weights for an aperture in the outer disc, the youngest SSP with a weight different from zero is 5 Gyr old. In the right panel of the same figure, the youngest SSPs used to fit the spectrum extracted from the star-forming disc is just 30 Myr old. The exact distribution of weights along the time axis varies strongly from aperture to aperture in the inner disc, and from aperture to aperture in the outer disc. This variation reflects the uncertainty in our result, and indeed we use it to estimate error bars on the recovered SFHs (see below).

In order to estimate the SFH in each aperture, we bin the weights $M_{i,a}^{\rm SSP}$ in age bins (note the additional index a, which indicates the aperture). Since the sensitivity to discrim-

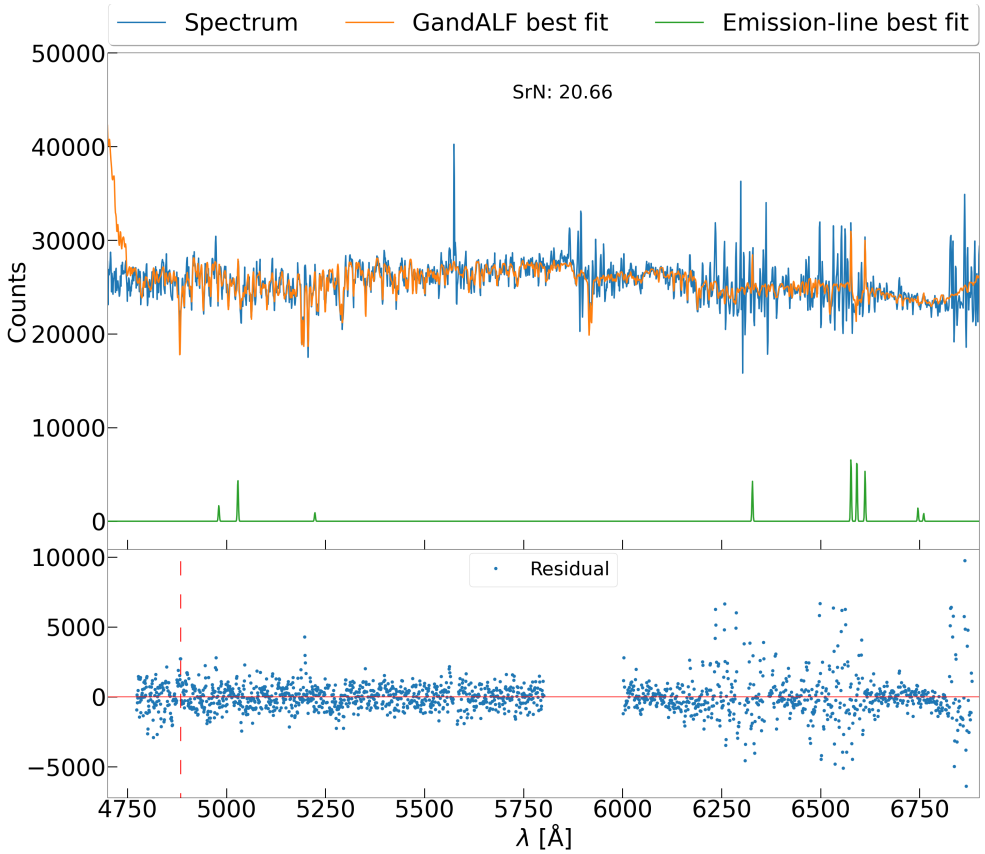

Figure 4.17: Top panel: best combination of SSP templates (GandALF fit) to model the MUSE data (spectrum - same as Fig. 4.15). The green line shows the emission line best fit. The bottom panel shows the residuals of the GandALF fit with the data. The lack of residuals indicates that GandALF did not fit that wavelenght range. The vertical dashed red line shows the Hβ wavelength. In this experiment we did not fit this line in emission.

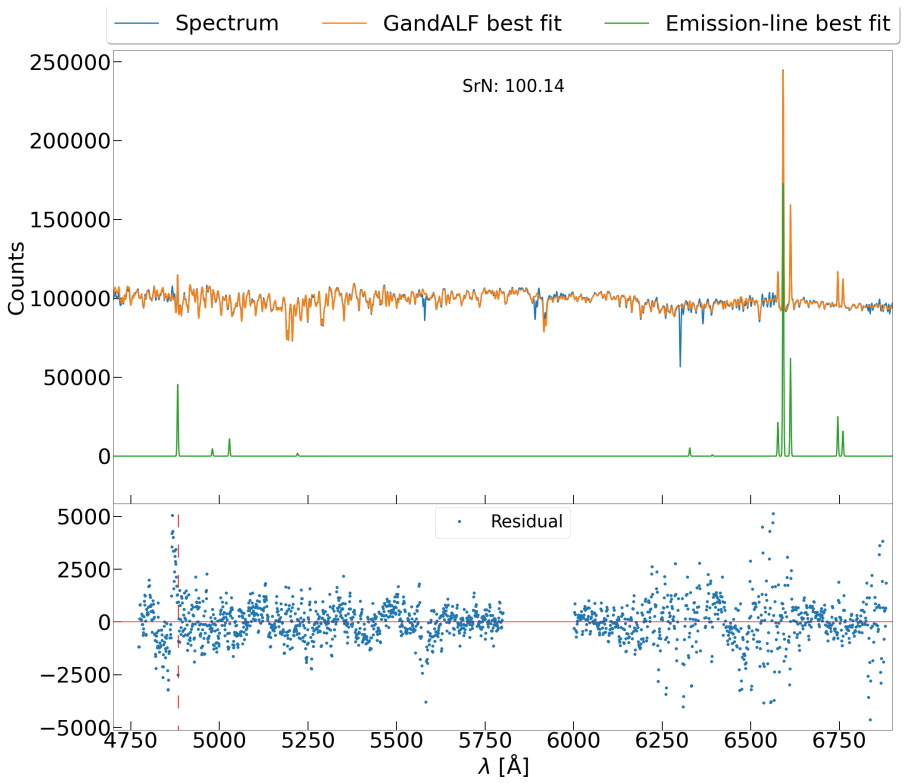

Figure 4.18: Top panel: best combination of SSP templates (GandALF fit) to model the MUSE data (spectrum - same as Fig. 4.16). The green line shows the emission line best fit. The bottom panel shows the residuals of the GandALF fit with the data. The lack of residuals indicates that GandALF did not fit that wavelenght range. The vertical dashed red line shows the position of Hβ, which makes clear that the large residuals are not centered in the line.

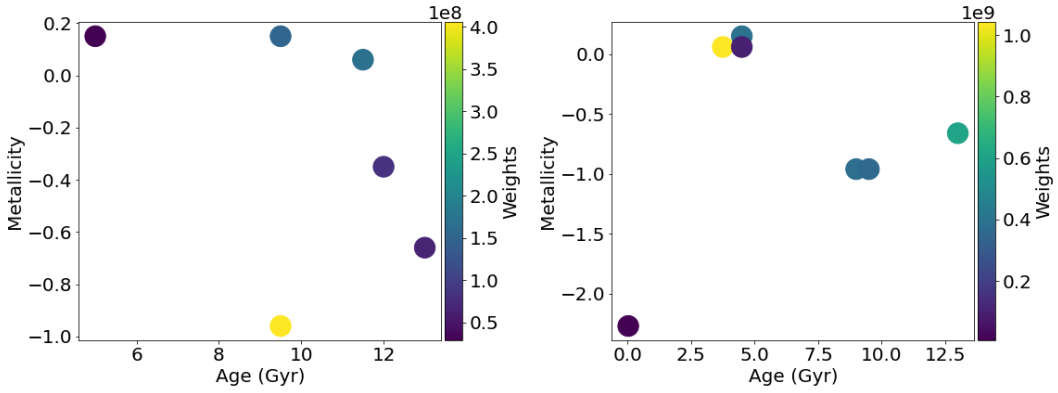

Figure 4.19: Left panel: MILES templates weights assigned by GandALF while fitting the the MUSE spectrum in Fig. 4.17. Right panel: MILES templates weights assigned by GandALF while fitting the the MUSE spectrum in Fig. 4.18.

inate between stellar populations decreases as the age of the stars increases, we decided to use a bin width of 1 Gyr between 0 and 6 Gyr, and to group older stars in bins 2 Gyr wide. We calculate the stellar mass $M_a(t_j)$ formed in the j-th time of the a-th aperture by adding all weights falling in that bin, i.e., $M_a(t_j) = \Sigma_i M_{i,a}^{\rm SSP}$ where the summation includes only the SSPs templates formed within the j-th time bin in the a-th aperture. Then, dividing the total stellar mass formed in the j-th time bin by the correpsonding binwidth Δt_j, we obtain the average SFR in that bin $SFR_a(t_j) = M_a(t_j)/\Delta t_j$. We have thus obtained the SFH (SFR as a function of time) of each aperture. In order to compare the SFH of apertures with a different total stellar mass we divide the SFH by the total stellar mass formed at all times $M_a = \Sigma_j M_a(t_j)$ (i.e., the sum of all weights for that aperture). Therefore, our final result for each aperture is a normalised star formation history $SFR_{a,\rm norm}(t_j) = SFR_a(t_j)/M_a$ showing the fractional stellar mass formed per unit time as a function of time.

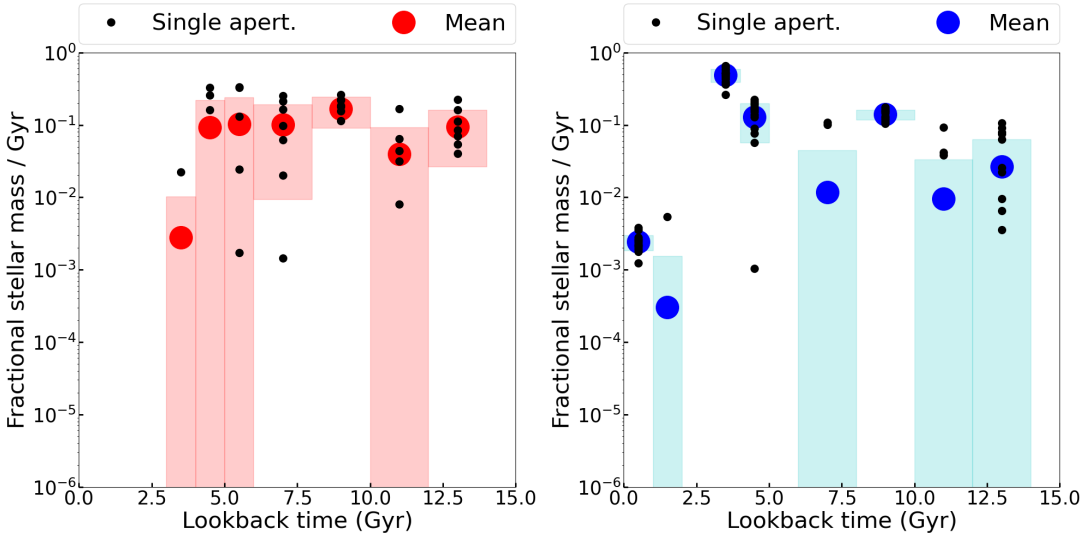

Figure 4.20: SFH of the quiescent (left) and the star-forming disc (right) obtained with 8 and 18 apertures, respectively. In both cases we used a polynomial of order 15 to correct flux calibration errors. In these experiments we used the whole set of SSP models to fit spectra of the star-forming disc, while we removed SSPs younger than 250 Myr in the case of the quiescent disc. In both panels: black dots represent the average fractional stellar mass formed within the bin edges measured in each aperture. While the larger colored dots are the mean of the average fractional SFR calculated including also the apertures where the SFR was zero. Colored shades show the uncertainties in the fractional stellar mass formed in each age bin. Please, refer to the text for details on how uncertainties were calculated.

The procedure just described delivers a first estimate of the SFHs of the quiescent and star-forming disc by, which we obtain averaging, for each time bin, the SFH measured in all apertures (as mentioned above, we have 18 apertures for the star-forming disc and 8

apertures for the quiescent disc). That is, we calculate $SFR_{\rm norm}(t_j) = \Sigma_a(SFR_{a,{\rm norm}}(t_j))/N_a$ where N_a is the number of apertures. Both for the quiescent and star-forming disc, we take the standard deviation $\delta SFR_{\rm norm}(t_j)$ of the $SFR_{a,{\rm norm}}(t_j))$ values in the j-th time bin as the uncertainty of our measurement in that bin.

We highlight that, unlike in other work in the literature, we include in the average and standard deviation calculation all apertures, also those where $SFR_{a,{\rm norm}}(t_j) = 0$ because GandALF returned no models with non-zero weight. As mentioned above, typically GandALF returns a relatively low number of SSP models with non-zero weight and, therefore, it is common for an aperture to have null $SFR_{a,{\rm norm}}(t_j)$ in some time bins. We believe that including these null values in the calculation of $SFR_{\rm norm}(t_j)$ and $\delta SFR_{\rm norm}(t_j)$ is the correct way of fully taking into account the uncertainties of our GandALF fits.

In Fig. 4.20 we show the normalised SFHs of the quiescent and star-forming disc, respectively. These SFHs were obtained using a multiplicative polynomial of order 15. Since the quiescent disc does not host any star formation activity, we used a subset of MILES templates which does not include SSP models younger than 250 Myr.

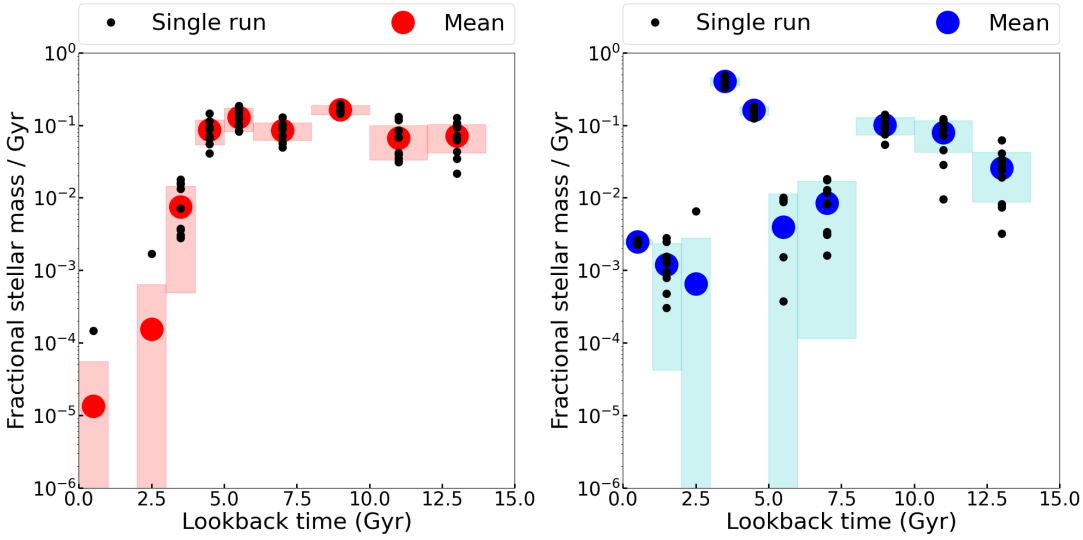

Figure 4.21: SFH of the quiescent (left) and the star-forming disc (right) obtained with set of pPXF and GandALF runs. In the case of the outer disc: (*i*) we always used a polynomial of order 15 to correct flux calibration errors and (*ii*) we progressively removed the youngest SSP models of previous run. In the case of the inner disc: (*i*) we used polynomial of different orders to correct flux calibration errors and (*ii*) we used the whole library of SSP models in all runs. In both panels: black dots represent the average fractional stellar mass formed within the bin edges measured in each run. While larger colored dots are the mean of the average fractional SFR including all runs where this value was zero. Colored shades show the uncertainties in the fractional stellar mass formed in each age bin. Please, refer to the text for details on how uncertainties were calculated.

When performing our GandALF fits we have had to make a number of choices. Some can be easily motivated based on our understanding of NGC 1436. E.g., the outer disc shows no sign of ionised gas emission, and therefore it is reasonable to not fit the extremely low-SNR Hβ line, which might otherwise systematically bias our SFH given its overlap with its stellar absorption line counterpart, which is a particularly sensitive to the stellar population age. Other choices are more arbitrary. For example, in the outer disc no star formation is ongoing. It is therefore reasonable to exclude MILES SSP templates younger than a certain age from the fit, but what should the actual age cut be? Likewise, we include in the fit a multiplicative polynomial of order 15, but we have verified that the quality of the fit does not change significantly for orders slightly below or above this value. Which polynomial order should we then adopt? All these arbitrary choices have some effect on the recovered SFH, and we thus attempt to include the resulting SFH variations in our uncertainties as follows.

We run pPXF/GandALF multiple times on the aperture spectra extracted from the outer pointing, setting a progressively higher lower-limit on the age of the SSPs included in the fit. The first run does not include SSPs younger than 50 Myr. In the last run, the younger stars are 600 Myr old. In all runs we used a multiplicative polynomial of order 15.

Similarly, we run pPXF/GandALF multiple times on the aperture spectra extracted from the inner pointing. In the star-forming disc, given the on-going star formation, we do not apply any lower limit to the age of the SSP templates. However, we have noticed that the SFH changes slightly depending on the order of the multiplicative polynomial included in the fit. We therefore repeated the fit for orders 6, 7, 8, 9, 10, 11, 12, 13, 14, 15. For all these values the residual of the fit is of small.

In both cases, we calculated the standard deviation of the SFHs obtained in the various GandALF runs. We compare this standard deviation to the uncertainty obtained by propagating the errors $\delta SFR_{\rm norm}(t_j)$ from each GandALF run (Fig. 4.20), and take as final uncertainty the largest value between the two. Also in this case, while calculating the mean and the standard deviation over the various GandALF runs, we included in the calculation all runs, also those where $SFR_{\rm norm}(t_j) = 0$.

We show in the left and right panels of Fig. 4.21 the SFHs of the quiescent and star-forming disc, respectively. From 14 to 4 Gyr the SFH of the outer disc stays constant, then it suddenly drops by about an order of magnitude and continues to decrease until it reaches a value consistent with no SFR in the youngest bin (fractional stellar mass/Gyr $\sim 10^{-5}$ between 0 and 1 Gyr ago). The SFH of the star-forming disc shows a first drop between 6-8 Gyr, followed by a burst in the average fractional SFR between 3-5 Gyr. Finally it shows an even more sharp drop between 2-3 Gyr (at about the same time when the SFH of the outer disc also drops.). However, instead of continuing to decrease, the fractional SFR stay constant in the last 3 Gyr.

Multiplying the fractional stellar mass formed in the most recent time bin of the inner disc by the total stellar mass formed at all times in the same region, which is $1.1{\times}10^{10}$ $M_\odot$, we obtain a SFR of roughly 2.8×10^{-2} $M_\odot$/yr. In order to check whether this value is consistent with other SFR measures, we converted the MUSE Hα map (Sarzi et al. 2018)

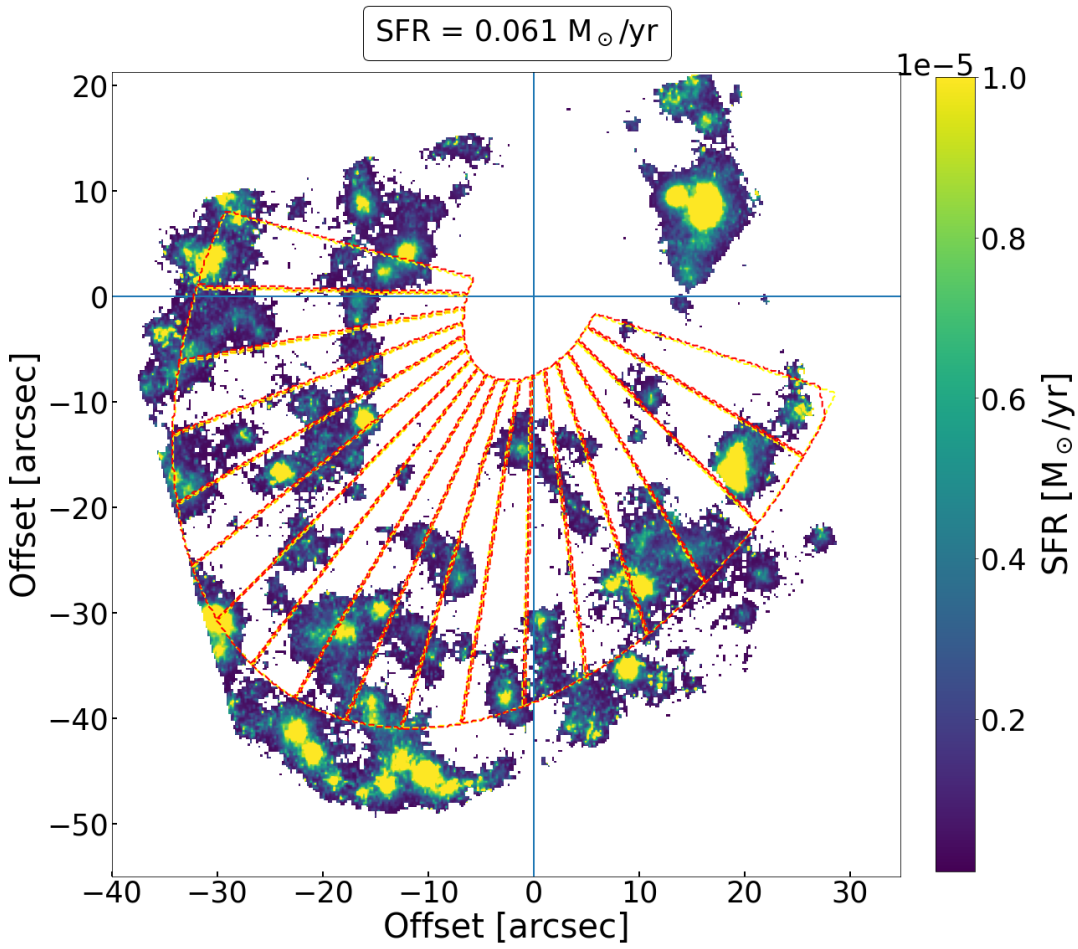

Figure 4.22: SFR map obtained from the Hα map using SFR($M_\odot$/yr) = $5.5\times10^{-42}L_{H\alpha}(erg/s)$ provided by (Calzetti et al. 2012). The Fig also shows the same 18 apertures in Fig. 4.14.

into a SFR map using the conversion SFR($M_\odot$/yr) = 5.5×10^{-42} $L_{H\alpha}(erg/s)$ provided by Calzetti et al. (2012) and assuming a distance of 20 Mpc (Blakeslee et al. 2009). We do this including only MUSE lines of sight where the standard BPT line ratios are those of HII regions, and we are thus confident that the Hα emission can be converted into a SFR. Then we measure the total SFR by summing the SFR of all 18 apertures used to derive the SFH of the star-forming disc (Fig. 4.22). The result is an Hα SFR of ~0.06 $M_\odot$/yr, within a factor of ~2 of the estimate based on our modelling of the MUSE spectra. Given the vastly different methods used, the agreement is remarkable and strengthens our SFH results.

In summary, we observed a rather flat SFH in both parts of the disc from 14 to 10 Gyr. Then, while the SFR of the outer disc stays constant until 5 Gyr ago, the inner disc experiences 2 main phases: first a drop, and then a rapid enhancement in the fractional SFR, which ends ~3 Gyr ago. Then both parts of the disc show a sharp drop in the fractional SFR (rougly an order of magnitude in the outer disc and even more in the inner disc). Finally, the fractional SFR in the outer disc keeps decreasing to zero while that of the inner disc stays constant to a value remarkably consistent with that of the SFR measured from the Hα emission. An interpretation of the differences in the SFHs of these two part of the disc are provided in the next section.

4.7 Discussion

Several properties of the multi-phase gas disc indicate that NGC 1436 has not experienced any significant tidal or hydrodynamical interaction in recent times: (*i*) the highly symmetric morphology and settled kinematics of the HI disc observed with MeerKAT at a resolution of $\sim$ 10 arcsec $\sim$ 1 kpc; (*ii*) the absence of HI disturbances, asymmetries or tails down to a column density of $\sim$ 10^{18} cm^{-2}; the perfect match between the regular morphology and kinematics of the various gas phases (atomic, molecular, ionised). The fact that the disc is settled now, does not imply that NGC 1436 has never experienced environmental interactions in the past. However, given the orbital time of 300 Myr at the edge of the HI disc (Sect. 4.5), we can rule out significant interactions in the last few orbits, say $\sim$ 1 Gyr. Thus we wonder "whether", "when" and "how" interactions with the Fornax cluster environment were relevant for the history of NGC 1436.

Significant insights come from the SFH of the inner and outer disc. The SFHs of the quiescent and star-forming disc that we see in Fig. 4.21 suggest that NGC 1436 was not a member of the cluster earlier than ~6 Gyr ago, and just 5 Gyr ago the Fornax environment became relevant for the evolution of NGC 1436. Indeed, between 14 and 5 Gyr the decrease of the SFR in the inner disc and the rather constant SFR in the outer disc are consistent with what we expect from spirals which do not live in dense environments. That is, up to $\sim$ 5 Gyr ago NGC 1436 seems to have formed its stars as a regular spiral, without being affected by strong tidal or hydrodynamical effects as those discussed in Chapt. 1. It was thus likely evolving in a relatively low-density environment, and its infall into Fornax must have happened after $z \sim 1$. Once infall into Fornax did start,

since the crossing time of the Fornax cluster is roughly 2 Gyr ($\tau_{\rm cross} \sim R_{\rm vir}/\sigma_{\rm cl}$; where $R_{\rm vir} = 700$ kpc $\sigma_{\rm cl} = 318$ km s^{-1}, Drinkwater et al. 2001a), it must have taken ~ 1 Gyr for NGC 1436 to reach its pericenter. This must have been the time of the most extreme interactions between the galaxy and the Fornax environment. At this point in time, indeed, the SFR of the galaxy changes both in the inner and in the outer disc.

In the outer disc we see a sharp drop of the SFR about 4 Gyr ago. After this sharp drop, the SFR continues to decrease to the current value of zero. We thus speculate that ~ 4 Gyr ago, at about pericenter, ram-pressure stripping was able to remove the majority of the HI content from the galaxy outer disc, causing the fast quenching of its star formation. NGC 1436 could only keep some HI within the inner star forming disc thanks to the stronger gravitational binding. However, by the time gas removal from the outer disc is complete, the accretion of cold gas onto the galaxy must have completely stopped. Therefore, the subsequent evolution (with NGC 1436 now moving away from pericentre) must have been characterised by a fully quenched outer disc and a starving inner disc. This would explain why the SFR of the inner disc has decreased in the last few Gyr, but not gone to zero. The main open question in this case is why, at the same time when the SFR of the outer disc suddenly drops to zero and just before the SFR of the inner disc starts decreasing to its current low (but non-zero) value, the SFR of the inner disc experienced a temporary increase. At the moment we do not have a robust answer to this, but we speculate that ram pressure itself may have temporarily enhanced the SFR, as might happen during a brief but significant phase in the life of many ram-pressure stripped galaxies (Poggianti et al. 2017; Vulcani et al. 2018; Ramatsoku et al. 2019). Alternatively, near pericenter the galaxy experienced a tidal interaction, which may have triggered a central SFR enhancement while, at the same time, moving some gas to large radius via tidal forces, from where it could more easily be stripped.

Following these events, NGC 1436 seems to have evolved more quietly, as demonstrated by the properties of the inner gas disc. The galaxy may now be past apocenter and on its way towards its second pericenter, where a new round of interactions may await it.

According to this interpretation, the galaxy has thus been severely affected but not completely quenched during its first passage through the centre of Fornax 4 Gyr ago, which might be reasonable for a high-mass galaxy ($M_\star \sim 1 \times 10^{10}$ M$_\odot$) moving within a low-mass cluster like Fornax.

Although we answered the questions about "whether", "when" and "how" the Fornax environment has become relevant for the evolution of NGC 1436, we still wonder "whether" the Fornax cluster environment has a favorite channel to transform spirals into lenticulars.

The SFH of the quiescent and star-forming disc of NGC 1436 shares some similarities with those of the three S0s, FCC 170, FCC 153 and FCC 177, whose SFHs was studied in Pinna et al. (2019a,b). Unfortunately, due to the different galaxy inclinations, the geometric definition we adopted is not the same as in Pinna et al. (2019a,b). Looking back in time, the disc of FCC 170, FCC 153 and FCC 177 formed their mass in long time scales and thus, their history before entering in Fornax is similar to NGC 1436 where they did not suffer of early quenching. Furthermore, all these three galaxies show episodes of SFR

enhancement in some regions of the disc at different time: FCC 170 between 13-14 and 10 Gyr ago; FCC 153 and FCC 177 between -10 Gyr ago and multiple episodes between 0-4 Gyr ago in their nuclear region.

However, according to our interpretation NGC 1436 should not have experienced any important episodes of pre-processing, while Pinna et al. (2019a,b) suggests that merger events might be the cause of the bursty SFH of S0s. They suggest that since FCC 153 and FCC 177 are not in the denset part of the cluster (see Fig 4.2), they were able to form stars for longer time.

In general the study of the SFHs of a sample of only four lenticulars is not exhaustive to see whether Fornax has a favourite way to transform spirals to S0s. Furthermore, HI has never been detected in FCC 170, FCC 153 and FCC 177. Thus although FCC 170 is within the part of the cluster where tidal interactions are expected to be relevant (Iodice et al. 2017a), it is very challenging to discriminate which was the most effective environmental interaction that removed their cold gas.

Chapter 5

Conclusion

In this thesis we studied the evolution of galaxies in the Fornax galaxy cluster. Being the closest (20 Mpc; Blakeslee et al. 2009) representative of the class of low-mass galaxy clusters ($\sim 5\times10^{13}$ $M_\odot$ within the virial radius, R_{vir} = 700 kpc; Drinkwater et al. 2001a), Fornax is an ideal target to study galaxy evolution in dense environment, which could highlight important differences with the evolution of galaxies observed in more massive clusters.

The Fornax cluster environment is expected to affect galaxy evolution differently from that of the closer (16 Mpc) and more massive ($\sim 8\times10^{14}$ $M_\odot$, Karachentsev et al. 2014) Virgo cluster. On the one hand, the density of the Fornax ICM and the velocity dispersion of Fornax galaxies are a factor of two lower that those in Virgo. On the other hand, the number density of galaxy is two times higher (Jordán et al. 2007). Therefore the impact of ram-pressure stripping in removing cold gas from galaxies should be smaller in Fornax than in Virgo. While tidal interactions that can affect both the cold gas and stellar distribution should be more effective in Fornax.

Differences between these two clusters also concern the population of bright massive galaxies. The fraction of ETGs with respect to the total number of galaxies is higher in Fornax, which suggests that bright massive galaxy accretion happened earlier than in Virgo, providing the Fornax environment enough time to quench them though environmental interactions. Another possible scenario involves pre-processing that these galaxies might have experienced while falling into Fornax. In both cases, this is not what is observed in the younger Virgo (Ferguson 1989a).

Although Fornax has a more dynamically evolved state than Virgo, there is evidence that its growth is not over yet. The Fornax region includes two main substructures: the main cluster centered on NGC 1399 and an infalling subgroup of galaxies dominated by NGC 1316, also known as Fornax A (Drinkwater et al. 2001a). In both substructures there is evidence of accretion of new HI-rich galaxies (e.g. Schröder et al. 2001; Waugh et al. 2002; Serra et al. 2019; Kleiner et al. 2021)

Due to its proximity, Fornax has been imaged and observed at a number of wavelengths by a range of telescopes and instruments, providing us with a good opportunity to study both the statistical properties of the cluster and individual Fornax members.

We performed two statistical studies based on the interferometric HI data collected with the ATCA telescope. HI is a key driver of galaxy evolution as it is the primary reservoir of fuel for star formation. In general, due to environmental interactions, cluster galaxies are HI deficient with respect to field and void galaxies and therefore their evolution proceeds faster. Previous blind HI surveys of Fornax were carried out with single dish data with a resolution of a factor of 15 worst than that of our ATCA data and a similar HI mass sensitivity, and thus they were not able to observed the resolved HI morphology of galaxies, which might reveal important information on on-going interactions.

Our ATCA observations covers a field of 15 deg^2 out to a distance of $\sim R_{\rm vir}$ from the cluster centre. Mosaicking these data as described in Sect. 2.2, we obtained a HI cube with spatial and velocity resolution of $67'' \times 95''$and 6.6 km s^{-1}, respectively, and with a 3σ $N_{\rm HI}$ and $M_{\rm HI}$ sensitivity of $\sim 2 \times 10^{19}$cm^{-2} and $\sim 2 \times 10^7$M$_\odot$, respectively.

With the aim of studying the evolution of galaxies in the Fornax cluster, we searched for HI emission within the ATCA footprint and detected 16 Fornax galaxies, whose HI morphology is often disturbed. The ATCA resolution was good enough to detect offsets between the optical and the HI centers, HI tidal tails and a possible case of truncated HI disc. Furthermore, the HI mass range of our ATCA HI detections covers about three orders of magnitude (from 8×10^6 to 1.5×10^{10} M$_\odot$).

We carried out a comparison between the projected 3D distribution of the HI detections and that of the general population of spectroscopically confirmed members of the Fornax cluster. For this purpose we made use of the spectroscopic catalogue of Maddox et al. (2019) from which we removed duplicates and compact stellar systems. The latter are not expected to host any HI and thus are not useful for our purpose of studying the removal of cold gas from galaxies in Fornax. This "cleaned" catalogue, compared with all the photometric catalogues published from the Fornax Deep Survey (FDS) collaboration (Iodice et al. (2019a), Raj et al. (2019) and Venhola et al. (2018) - whose data are at least $\sim 3\times$ deeper data than previous photometric surveys, e.g., Ferguson (1989b)), shows that our spectroscopic catalogue has a completeness higher than 50% in all magnitude bins brighter than m$_r$ = 16.5 mag, and $\sim$ 85% overall (please, see Sect. 1.5 for further details on how we obtain this catalogue). The final catalogue includes 79 galaxies brighter than m$_r$ = 16.5 mag, of which 15 are detected in HI with ATCA. One additional ATCA HI detection did not have previous optical redshift measurements. Thus, thanks to a newly spectroscopic ATCA detetion, we have knowledge on the velocity of a total of 80 Fornax galaxies brighter than m$_r$ = 16.5 mag.

The 2D distribution and the projected phase-space diagram of HI detections compared with that of the general population of spectroscopically confirmed Fornax members show that the sample of HI rich galaxies consist of recent arrivals into the cluster. Indeed, they reside outside the densest part of the cluster where old Fornax galaxies are more likely to be (see Fig. 2.12 and Fig. 2.13; see also Fig. 1.8 and Fig. 1.9 to see a detailed distribution of ETGs, LTGs and dwarfs galaxies in Fornax). This result implies that HI is lost down to the ATCA sensitivity within a crossing time ($\tau_{\rm HI,loss} \leq \tau_{\rm cross} \sim 2$ Gyr) and that HI detections are Fornax members since a time shorter than $\tau_{\rm cross}$.

Although only massive galaxies are expected to keep some HI after the first pericenter

passage, HI emission was detected in low-mass galaxies too (down to a stellar mass of $\sim \times 10^8 M_\odot$). This further confirms that we detected HI in recent Fornax arrivals. The 3D distribution of HI detections and the HI morphological inspection also revealed the existence of interacting sub-groups of galaxies. The most evident one is dominated by NGC 1365 which encloses 4 galaxies within a region of 250 kpc and a velocity range of 200 $\mathrm{km\,s^{-1}}$.

Thus, HI-rich Fornax galaxies which are currently falling into the cluster are both interacting with the cluster environment and possibly experiencing pre-processing. Consequences of these interactions are (*i*) an overall HI deficiency of Fornax galaxies with respect to the field – the field comparison sample included the HRS sample with Virgo excluded (Boselli et al. 2014a) and void galaxies (VGS - Kreckel et al. 2012) (Fig. 2.6) – and (*ii*) large H_2-to-HI ratio (Fig. 2.9).

A further comparison with the HI content of Virgo galaxies shows that, although the nature and the efficiency of physical mechanisms that removed HI in Virgo and Fornax galaxies might have been different, the level of HI deficiency in both clusters is similar. This suggests that both the time from the first infall of HI detected galaxies in Fornax and Virgo and pre-processing can play a role in the level of observed HI deficiency.

Finally, the HI-detected Fornax galaxies are also forming stars at a lower rate than non-cluster galaxies at fixed $M_\star$ (Fig. 2.10). This deficit of SFR is consistent with the deficit of HI when compared to non-cluster galaxies (Fig. 2.11). This implies that HI detections on their way to the Fornax cluster have used/lost gas on a time scale longer than the depletion time ($\tau_{\mathrm{H_2,depl}} \sim$ 1-2 Gyr Zabel et al. 2020), giving the SFR sufficient time to adjust itself to the slowly varying gas content – as in the field.

There is evidence that the HI removal in the central part of the cluster is likely to proceed faster ($\tau_{\mathrm{HI,loss}} < \tau_{\mathrm{H_2,depl}}$). Furthermore, HI non detected galaxies that in some cases are also slightly H_2 deficient (Zabel et al. 2019) can still form stars at a relatively unperturbed rate (Fig. 2.11).

The HI mass function (HIMF) provides further elements to statistically study the HI content of the whole Fornax cluster. Assuming that it is similar to that of the local Universe, it should follow a Schechter function, which is described by three main parameters: the slope α of the low-mass power-law part of the function, the characteristic HI mass M_* above which the number of HI objects decreases exponentially and a normalization factor ϕ_*. The HIMF is particularly important to study the impact of the cluster environment in shaping the HI content of cluster members. Indeed, due to active gas removal through environmental interactions, one would expect to measure a flat or even falling HIMF in clusters. This has been observed by several previous studies in a range of local overdensities but never before in Fornax. We therefore attempted to measure the slope of the low-mass end of the Fornax HIMF.

Unfortunately the low number of ATCA HI detections is not enough to constrain this parameter (Fig. 3.2). Thus, inspired by Pan et al. (2020), we explored a new Bayesian method to measure the HIMF in Fornax using both direct HI detections and the integrated HI flux at the position of HI non detected galaxies. The main goal is to estimate the slope α, while M_* derived from a small volume as that of a cluster is not well constrained due to

the small number of objects with a large HI mass (Jones et al. 2016), and ϕ_* is of marginal interest. The Bayesian method relies on two assumptions: *i*) the distribution of sources in the sky is Poissonian; (*ii*) the number of sources within a certain $M_{\rm HI}$ bin is convolved with the noise distribution (Eq. 3.3).

We firstly tested our Bayesian code with two sets of experiments. The former has the only requirement of having 50 galaxies above $M_*/2$, while the latter aims to simulate the case of the ATCA HI survey and thus, it includes only 15 galaxies above the ATCA detection limit ($M_{\rm HI} = 2{\times}10^7$ M$_\odot$). In both of them we simulated input Schecther HIMFs with different shapes: steep ($\alpha < -1$), falling ($\alpha > -1$) and flat ($\alpha = -1$). In each experiment we fixed the input parameters to generate a distribution of HI fluxes which we then perturbed with Gaussian noise. Finally we applied the Bayesian method to find the best-fitting parameter values. Results on recovering the input HIMF parameters are excellent in the case of 50 galaxies above $M_*/2$ (Sect. 3.5.1 and Appendix C). The second set of experiments with 15 galaxies above the ATCA detection limit also provided best-fitting parameter values in agreement with the input ones although they have larger uncertainties. For the reasons explained above, we are mainly interested in recovering α whose the average uncertainty on the best-fitting α is ±0.13 (Fig. 3.27; Sect. 3.5.2 and Appendix C).

Finally we applied this method to the real ATCA data. We measured the Schechter HIMF of the Fornax cluster using an *on* catalogue which includes integrated flux measured at the position of all spectroscopically confirmed Fornax members with a $m_r < 16.5$ mag (80 sources in total of which 16 are the ATCA HI detections whose flux was measured with SoFiA, see Sect. 2.2). The Bayesian code estimates a slope, $\alpha = -1.09^{+0.067}_{-0.097}$, which is flatter than those measured in larger volume of the local Universe by HIPASS ($\alpha = -1.37 \pm 0.03$, Zwaan et al. 2005) and ALFALFA ($\alpha = -1.25 \pm 0.02$, Jones et al. 2018b). This would seem to imply an agreement with the results reporting a flat HIMF in other local overdensities. However, we obtained an identical result by running our code on a control *off* catalogue, which includes 64 measurements of pure noise plus the integrated HI flux of our 16 ATCA detections. This strongly suggests that the HIMF of the Fornax cluster does not follow a Schechter function below the ATCA detection limit (like the *off* catalogue). Therefore, we find that the HIMF in Fornax, which seems to follow a Schechter function roughly down to the ATCA $M_{\rm HI}$ detection limit of $\sim 10^7$ M$_\odot$, drops rapidly to zero below this level. If so, a better formalism to study the distribution of HI masses in clusters including the HI non-detections would be one where the HIMF is described by a Schechter function down to a limiting HI mass, plus a delta function with much lower HI mass (possibly zero). It is worth noting that such a modified Schetchter plus delta HIMF is different from the case of a falling Schecther function with $\alpha < -1$, which would be truncated at $M_{\rm HI} \sim M_*$, thus above the typical HI detection limit.

The idea of a sudden drop of the HIMF below a limiting mass is supported by recent findings of no signal hidden in the noise by stacking about 470 spectra extracted at the position of HI non-detected galaxies in the Coma cluster (Healy et al. 2021). Therefore, we might be discovering that a general property of galaxy clusters is a truncation of the Schechter-like HIMF below a certain $M_{\rm HI}$ threshold, which so far we found to be of $\sim$

$10^7 M_\odot$ in the case of the low-mass Fornax cluster and $\sim 10^8 M_\odot$ in the case of more massive clusters like Coma. The exact value of this threshold will strongly depend on the selection function of the spectroscopic galaxy catalogue used, and for this reason we cannot at the moment draw any conclusions on the apparent difference between the values found in Fornax and Coma.

Thus, based on our ATCA survey, the comparison of HI detections with the general Fornax population, the comparison of Fornax with other, nearby, more massive clusters (Virgo and Coma) and the Bayesian study of the distribution of HI masses including the non-detections, we conclude that:: (*i*) whatever the nature of the environmental interactions in Fornax, the level of HI deficiency is similar to that observed in Virgo; (*ii*) evolution of Fornax galaxies can be affected both by interactions with the cluster environment and by pre-precessing (e.g. the NGC 1365 sub-group); (*iii*) the sample of HI detections consists of recent Fornax arrival whose gas has been used and removed over a long time scale, comparable to the H_2 depletion time; (*iv*) HI removal is faster than a cluster crossing time in galaxies which are reaching pericenter; (*v*) galaxies with no HI but H_2 can still form stars at a relatively unperturbed rate; (*vi*) probably as a consequence of point (*iv*) above, the HIMF of galaxies in the Fornax cluster most likely follow a Schechter function only down to $M_{\rm HI} \sim 10^7 M_\odot$, and drops rapidly below this limit, suggesting that Fornax is efficient at rapidly removing all HI from small galaxies.

The final part of this thesis consists in the study of the only possible truncated HI disc detected with ATCA: NGC 1436. Since the ATCA data at the position of this galaxy have a low signal-to-noise ratio, its HI morphology is not well constrained (Chapt 2). This is not the only reason why this galaxy attracted our attention. Indeed in the literature there are results showing that this is a lenticualr in the making (Raj et al. 2019; Iodice et al. 2019a).

It is known that in clusters, spiral galaxies can evolve into lenticulars (e.g. Dressler et al. 1997). We therefore asked ourselves whether the on-going transformation of NGC 1436 is caused by its interaction with the Fornax environment. To answer this question we analysed both the cold gas properties and the stellar populations of NGC 1436. The former analysis is based on MeerKAT HI observations collected as part of the on-going MeerKAT Fornax Survey (Serra et al. 2016). We obtained HI data with a resolution of 12×9.5 arcsec^2 ($\sim$ 1 kpc at the distance of Fornax) and a 3σ HI column density sensitivity of $N_{\rm HI} \sim 4.50 \times 10^{19}$ atoms/cm^{-2} assuming a linewidth of 25 km s^{-1}. Furthermore we carried out a comparison between HI and H_2. The latter data were presented in Zabel et al. (2021) and have a resolution of 2.68×2.06 arcsec with an average sensitivity of $\sim$2.046 mJy beam^{-1}.

Both HI and H_2 distributions show a high level of symmetry suggesting that this galaxy is not currently interacting with the Fornax environment (Fig. 4.4, Fig. 4.8). This idea is further supported by the consistency between the extremely regular kinematics of the two cold gas phases (Fig. 4.9 and Fig. 4.10). We can therefore rule out substantial interactions occurred within the last few orbital times ($\sim$1 Gyr), but any sign of more ancient interaction would have washed out by now. We must therefore find a different way to investigate further into the past history of NGC 1436.

This is where the analysis of the stellar populations becomes crucial. In general stellar populations depend on the distance from the center of the galaxy and this is particularly true for highly symmetric system such as NGC 1436. Thus, by deriving the SFHs of two different regions of the galaxies we inspected the evolutionary path of this galaxy. Specifically we measured the SFH of the quiescent disc and of the star-forming disc (Fig. 4.21). By looking at epochs between 14 and 6 Gyr ago we propose that this galaxy was not a Fornax member at that time. This is because we observe a situation very similar to that of field galaxies, with a faster evolution of the inner disc, which is characterized by shorter depletion time with respect to the outer disc. Thus, we imagine this galaxy as a typical field spiral galaxy: older in the center – and with a decreasing SFR – and bluer and still able to form new stars for a long time at its outskirts.

Then NGC 1436 entered in the cluster and spent roughly 1 Gyr (half of the Fornax crossing time) to reach its pericenter 5 Gyr ago. Here, the interaction with the Fornax environment proved fatal for the HI in the galaxy's outer disc, which was stripped away. While Fornax was removing HI from the outer disc of NGC 1436, it also promoted an enhancement in SFR in the inner disc. And thus, if the nature of environmental interaction was hydrodynamical, we imagine NGC 1436 as a typical ram-pressure stripped galaxy with a temporary increment of SFR. However we cannot really rule out the scenario of a tidal interaction, whose signatures would now be impossible to observe.

The impact of the interaction between NGC 1436 and the Fornax environment on the SFH of the now-quiescent outer of the galaxy disc are drammatic. Indeed, in the last 5 Gyr, the SFR has dropped to zero. In contrast, looking at the SFH in the same age window of the star-forming inner disc we find that it shows a significant drop (following that initial enhancement), but it does not drop to zero, reaching a SFR consistent within a factor 2 with the SFR measured from Hα data. This suggests that the inner gaseous disc, too strongly bound to the galaxy to be stripped, is slowly consuming whatever gas was left after the last burst of star formation, with no further gas accretion from the surrounding medium.

Thus the fate of the outer disc, which appeared on track to continue forming stars for a longer time than the inner star forming disc, suddenly changed 5 Gyr due to interactions with the Fornax cluster environment.

The evolutionary scenario of this lenticular in the making shares some similarities with those proposed for other three lenticulars in Fornax: FCC 170, FCC 153 and FCC 177 (Pinna et al. 2019a,b). Indeed in all of them there is an epoch where gas was quickly removed and since then, these galaxy has began to quench. However, not a merger (as proposed for FCC 170, FCC 153 and FCC 177) but ram-pressure might be responsible for the temporary enhancement of SFR we measured in the inner star forming disc of NGC 1436. However, we cannot firmly rule out that a merger and a subsequent reshuffling of the stellar populations in the last 5 Gyr is responsible for the observed SFH of these parts of NGC 1436.

Appendix A

From Loni et al. (2021)

In this section, we describe in detail each galaxy of our sample of HI detections from Loni et al. (2021), Chapt. 2. Whenever possible we compare the information estimated from our HI data with observations at other wavelengths. The galaxies are sorted according to increasing HI mass as in Fig. 2.2 and Fig. 2.3.

FCC 323

According to Ferguson (1989b), FCC 323 is a dE2/ImV. This is the faintest among our HI detections and, for the first time, we detected it in HI and thus measured its recessional velocity of $v_{\rm HI}$ = 1502 km s^{-1}. FCC 323 has a $M_{\rm HI}$ = (0.8±0.3)×10^7 M$_\odot$ and a $M_\star$ = (0.6±0.6)×10^8 M$_\odot$. The Fornax environment might have strongly affected the HI reservoir of FCC 323. It has the highest $M_{\rm HI}/M_\star$ offset from the (extrapolated) xGASS scaling relation in Fig. 2.6. Its closest galaxy both on the sky and velocity is NGC 1437B (120 kpc and 12 km s^{-1} away), leading us to think that FCC 323 and NGC 1437B might be part of a subgroup or a pair of galaxies.

FCC 120

FCC 120 is classified as ImIV by Ferguson (1989b). The HI emission associated with the galaxy seems to be quite regular. The ATCA spectrum in Fig. 2.3 shows one peak (within the uncertainties), which is different from the 100 - km s^{-1} - wide double horn spectrum detected by Schröder et al. (2001) based on Parkes data. Even if the latter data shows strong RFI at a velocity of 1250 km s^{-1}, this RFI does not affect the detection of the galaxy. However, $v_{\rm opt}$ from Maddox et al. (2019), agrees with our $v_{\rm HI}$. Deeper HI data (Serra et al. 2016) may confirm this. FCC 120 has a $M_{\rm HI}$ = (0.4±0.1)×10^8 M$_\odot$ and a $M_\star$ = (1.6±0.5)×10^8 M$_\odot$.

FCC 102

FCC 102 is an irregular ImIV classified by Ferguson (1989b). We detect HI emission associated with FCC 102 for the first time. Although the HI morphology is not resolved, the HI is offset towards the north with respect to the optical centre. The difference between $v_{\rm opt}$ from Maddox et al. (2019), and $v_{\rm HI}$ from ATCA data is almost 100 $\rm km\,s^{-1}$. However, those values are still consistent due to the large uncertainty on $v_{\rm opt}$, which was measured from absorption lines for this galaxy (Natasha Maddox, priv. comm.). Recently this galaxy was detected during MeerKAT test observations in preparation for the MeerKAT Fornax Survey Serra et al. (2016), confirming our ATCA HI results. FCC 102 has a $M_{\rm HI} = (0.5\pm0.1)\times10^8$ $\rm M_\odot$ and a $M_\star = (1.6\pm0.5)\times10^8$ $\rm M_\odot$. The comparison with HI belonging to non-cluster galaxies with similar $M_\star$ in Fig. 2.6 shows that FCC 102 is HI deficient.

We identify FCC 102 to be part of the NGC 1365 infalling subgroup. It lies between NGC 1365 and FCC 090 both on the sky and in velocity (see Fig. 2.12 and Fig. 2.13). Furthermore the HI elongation of FCC 102 is in the same direction as the HI elongation of NGC 1365.

NGC 1436

NGC 1436 is the closest HI detected spiral to the centre of the cluster (see Fig 2.12 and Fig. 2.13). Ferguson (1989b) classify this galaxy as ScII. The HI emission associated with NGC 1436 is confined well within the stellar body suggesting a truncated HI disc. However, Fig. 2.3 shows that the ATCA spectrum compared with that based on GBT data (Courtois et al. 2009) misses flux from the blushifted part of the disc. The reason of this discrepancy arises from a combination of low S/N and the presence, in at least some of the blue-shifted channels of the ATCA cube, of artefacts. The HI spectrum of NGC 1436 from Schröder et al. (2001) is more similar to that obtained with the GBT than to ours. The $M_{\rm HI}$ estimated by the ATCA flux is $(0.6\pm0.2)\times10^8$ $\rm M_\odot$, while the $M_\star$ of the galaxy is $(1.6\pm0.4)\times10^{10}$ $\rm M_\odot$. Whether adopting the ATCA or the GBT HI flux measurement, NGC 1436 would still be an HI deficient galaxy (see Sect.2.3.2). Similarly, it would still be the (HI and $\rm H_20pt$) detection with the largest $M_{\rm H_2}/M_{\rm HI}$ ratio in Fig. 2.9.

The high offset from the scaling relation in Fig. 2.9, the truncated HI disc in Fig. 2.2 and the molecular spiral structure detected by Zabel et al. (2019) show that NGC 1436 may have gone through a quick interaction with the cluster environment, which did not affect the inner spiral structure yet.

Furthermore, Raj et al. (2019) found that NGC 1436 appears to be transforming into a S0 in its morphological evolution. They found spiral arms only in the central region whereas its outer disc resembles the smooth structure typically found in the discs of S0 galaxies. The truncated HI disc agrees with the observation of a passively-evolving outer optical disc, which is being shaped by the Fornax environment.

FCC 090

FCC 090 is classified as a peculiar elliptical galaxy by Ferguson (1989b). We detected HI emission in FCC 090 for the first time. The HI morphology of FCC 090 is elongated towards the south. FCC 090 has a $M_{\rm HI} = (0.6\pm0.1)\times10^8$ M$_\odot$ and a $M_\star = (1.3\pm0.3)\times10^9$ M$_\odot$. Its $M_{\rm HI}/M_\star$ ratio makes it a HI deficient galaxy, which lies on the edge of comparison sample of non-cluster galaxies (Fig. 2.6).

FCC 090 is part of the NGC 1365 infalling subgroup. Within the subgroup, the HI morphology of FCC 090 is the only one which is extended towards the south; it is the farther galaxy from NGC 1365; it has the highest velocity in phase space. FCC 090 is also the westernmost galaxy in the triplet of the aligned HI disturbed galaxies. Besides FCC 090, this triplet includes FCC 102 and NGC 1365.

The HI and molecular distributions (Zabel et al. 2019) are difficult to compare due to the different resolutions between ATCA and ALMA. The molecular distribution extends beyond the stellar body showing a tail that points to the west in projection but it is still within our HI detection that does not show any peculiarity in that direction. Our knowledge on HI in FCC 090 as well as its belonging to the NGC 1365 subgroup, corroborates the idea of an infalling galaxy which is loosing the external gas envelope.

In the sample of dwarf galaxies studied by Hamraz et al. (2019) FCC 090 is one out of two outliers in the Fornax cluster with a very blue inner part. Recently, Zabel et al. (2020) showed that depletion time is shorter than usual (0.5 Gyr rather than 2 Gyr) which may be a consequence of the environmental interactions taking place in it.

ESO 358-G016

ESO 358-G016 is classified as Sdm (edge-on) by Ferguson (1989b). It has a $M_{\rm HI} = (0.7\pm0.2)\times10^8$ M$_\odot$ and a $M_\star = (1.2\pm0.2)\times10^8$ M$_\odot$. ESO 358-G016 is the only member of the NGC 1365 infalling subgroup with a regular HI morphology. Like all the low mass members of the subgroup, it is a HI deficient galaxy. It is also the second closest galaxy to NGC 1365 both on the sky and in phase space. Raj et al. 2019 suggested that ESO 358-G016 might have experienced disruptions of the outer disc due to the gravitational potential of the cluster. If that is the case, some HI survived in this process.

ESO 358-G015

ESO 358-G015 is classified as a peculiar Scd-III by Ferguson (1989b). It has a regular HI morphology, with a systemic velocity close to the recessional velocity of the cluster. It has a $M_{\rm HI} = (0.9\pm0.2)\times10^8$ M$_\odot$ and a $M_\star = (7.6\pm2.1)\times10^8$ M$_\odot$. Fig. 2.6 shows that ESO 358-G015 is a HI deficient galaxy. Furthermore, it is one of the four HI detected galaxies that are north of NGC 1399. Raj et al. (2019) identified a lopsided tail pointing to the centre of the cluster. They also suggested ESO 358-G015 to be a galaxy that is being pulled into the cluster centre, in the southern direction. The quite regular HI morphology does not provide clear support to this hypothesis.

ESO 358-G051

ESO 358-G051 is classified as SBcd-III by Ferguson (1989b). The HI distribution is regular and peaks on the optical centre. It is located north of NGC 1399 and it is the closest HI deficient galaxy from it (∼0.4 $R_{\rm vir}$). In general, among all our HI detections, only NGC 1427A is closer to NGC 1399. ESO 358-G051 has a $M_{\rm HI}$ = (1.0±0.2)×10^8 M$_\odot$ and a $M_\star$ = (2.1±0.5)×10^9 M$_\odot$. Fig. 2.6 shows that ESO 358-G051 is a HI deficient galaxy.

Raj et al. (2019) marked this galaxy as a recent infaller with strong central Hα emission powered by star formation. Iodice et al. (2019a) observed an ionised gas distribution extended towards the north. This is the opposite direction with respect to the H_20pt elongation detected by Zabel et al. (2019). However, the HI distribution does not seem to be disturbed, perhaps due to the ATCA resolution. Although ESO 358-G051 is a HI deficient galaxy, the unresolved HI morphology does not provide information about on going interaction with the Fornax environment.

ESO-LV 3580611

ESO-LV 3580611 is classified as SBm-III by Ferguson (1989b). The HI morphology shows a lopsided HI distribution in the northern part of the system. However, optical and HI distribution share the same centre. It has a $M_{\rm HI}$ = (1.1±0.2)×10^8 M$_\odot$ and a $M_\star$ = (1.0±0.4)×10^8 M$_\odot$. ESO-LV 3580611 is also one of the two HI deficient galaxies in our sample that is outside the caustic curves (Fig. 2.13). Schröder et al. (2001), based on the high deviation of ESO-LV 3580611 from the Tully-Fisher relation, suggested that this galaxy is falling into the cluster from the background.

According to Raj et al. (2019), ESO-LV 3580611 may have experienced disruptions in the outskirts of the disc due to gravitational potential well of the cluster. Thus, similarly to ESO 358-G016, HI has survived during the infall.

NGC 1437B

NGC 1437B is classified as Sd (edge-on) by Ferguson (1989b). The HI distribution shows an elongation to the south, while the HI peak corresponds to the optical centroid (Fig. 2.2).

This galaxy is located on the south east of the cluster, close to FCC 323 both on the sky and in velocity (see Fig. 2.12 and Fig. 2.13). Given the small separation of only 120 kpc with a difference of ∼10 km s^{-1} in velocity, they might be part of an interacting subgroup of galaxies. NGC 1437B has a $M_{\rm HI}$ = (2.4±0.5)×10^8 M$_\odot$ and a $M_\star$ = (5±1)×10^9 M$_\odot$ and it is a HI rich galaxy.

Fig. 2.9 shows that the Fornax environment has not strongly affected the $M_{\rm H_2}/M_{\rm HI}$ ratio yet. On the other hand, contrary to the case of NGC 1436, the two gas phases are probably experiencing the same environmental effect. Indeed, although the scales are different, we found consistency between the southern HI elongation of NGC 1437B and the elongation of the molecular morphology detected by Zabel et al. (2019). Thus, the

agreement between its M_{H_2}/M_{HI} ratio and the xGASS scaling relation might be due to a slower evolution with respect to that taking place in NGC 1436.

Raj et al. (2019) did not observed any hint of optical morphological transition from the late-type spiral structure, which supports the hypothesis of a recent infaller. However, they found an optical disturbance in form of tidal tail, which points to the south in projection and might be due to a recent fly-by of another galaxy in the cluster. The HI morphology agrees with the optical detected tail. If FCC 323 and NGC 1437B belong to the same subgroup, the former may be the fly-by galaxy that NGC 1437B has interacted with.

NGC 1351A

Classified as Sc (edge-on) by Ferguson (1989b). The HI distribution shows a projected elongation towards the south. It has a velocity similar to the recessional of the cluster (Fig. 2.13). NGC 1351A has a $M_{HI} = (5\pm1)\times10^8$ $M_\odot$ and a $M_\star = (3.5\pm0.8)\times10^9$ $M_\odot$. The HI reservoir is similar to that of non-cluster galaxies with the same $M_\star$ (Fig. 2.6). NGC 1351A is isolated both on the sky and in projected phase space (Fig. 2.12 and Fig. 2.13). Thus, the HI asymmetry might be due to the interaction with ICM. Zabel et al. (2019) detected a slightly more diffuse east side in the H_20pt distribution.

NGC 1437A

NGC 1437A is classified as SdIII by Ferguson (1989b). The HI morphology is quite regular and its HI content is comparable with that of non-cluster galaxies with the same $M_\star$ (see Fig.s 2.2 and 2.6). NGC 1437A has a $M_{HI} = (6\pm1)\times10^8$ $M_\odot$ and a $M_\star = (1.0\pm0.3)\times10^9$ $M_\odot$. Although the optical appearance of NGC 1437A is not regular and the location of its star forming regions suggests that the galaxy is travelling in a south-east direction (Raj et al. 2019), the HI distribution does not show any strong asymmetries. Thus, ram-pressure and tidal interaction might not be the cause of the asymmetric star forming regions. However, the poor resolution of the HI image may hide HI asymmetries in projection.

ESO 358-G060

ESO 358-G060 is a low mass galaxy classified as Sdm (edge-on) by Ferguson (1989b). The HI morphology is regular. ESO 358-G060 has a $M_{HI} = (1.1\pm0.2)\times10^9$ $M_\odot$ and a $M_\star = (1.0\pm0.6)\times10^8$ $M_\odot$. Fig. 2.6 shows that ESO 358-G060 has a HI reservoir comparable with that of non-cluster galaxies with the same $M_\star$. As discussed in Sect.2.3.2, we pointed out that the Fornax cluster environment is more effective in altering the gas content for galaxies with $M_\star < 3\times10^9$ $M_\odot$. This supports the idea that ESO 358-G060 is a likely new Fornax member which has not been affected by the cluster environment yet. Raj et al. (2019) observed irregular star-forming regions making the hypothesis of a disruptions due to the gravitational potential well of the cluster centre, during the fall.

However, since the HI distribution is not perturbed yet by environmental interactions, internal feedback might be the cause of the irregular star forming regions. Furthermore no $H_2$0pt was detected by Zabel et al. (2019) and it is a dust poor galaxy as discussed in Sect.2.4. Overall, this galaxy is forming star with lower rate than that predicted for galaxies with similar $M_{\rm HI}/M_\star$ (Fig. 2.11).

ESO 358-G063

Classified as Scd (edge-on) by Ferguson (1989b). The atomic hydrogen distribution is more extended to the south-east part of the system. On this side, HI contours are more spaced with respect to the opposite side of the disc where HI emission seems to be confined within the stellar body. ESO 358-G063 has a $M_{\rm HI}$ = (1.7±0.3)×10^9 M$_\odot$ and a $M_\star$ = (1.1±0.3)×10^{10} M$_\odot$. Despite the asymmetries in the HI distribution, ESO 358G-063 is not HI deficient, and the molecular gas detected by Zabel et al. (2019) has a regular morphology. Thus, the galaxy has just started to interact with the cluster environment. The idea is supported by its position in projected phase space (Fig. 2.13) where the galaxy is just outside the caustic curves. Raj et al. (2019) found irregular star-forming regions in the ill-defined spiral arms of ESO 358-G063, which may be signs of minor mergers.

NGC 1427A

NGC 1427A is classified as Im-III by Ferguson (1989b). The HI morphology shows a very long tail pointing to the south-east in projection (opposite direction to the centre of the cluster - we refer the reader to Lee-Waddell et al. (2018) for a detailed study about the origin of the tail). NGC 1427A has a $M_{\rm HI}$ = (2.1±0.4)×10^9 M$_\odot$ and a $M_\star$ = (2.3±0.5)×10^9 M$_\odot$. This is the second most massive HI galaxy of our sample, which has an HI content comparable to that of non-cluster (see Fig. 2.6). NGC 1427A is the closest HI detection to the centre of the cluster (0.2 $R_{\rm vir}$). Due to its high velocity (see Fig. 2.13) it is not clear whether NGC 1427A is already virialised in the cluster or not. If it is virialised, it may decrease its velocity while reaching its apocentre. It is the only $M_{\rm H_2}/M_{\rm HI}$ upper limit with $M_\star > 3\times10^9$ M$_\odot$ in Fig. 2.9. Despite the large HI reservoir no $H_2$0pt was detected by Zabel et al. (2019). This may be due to a recent merger which involved the NGC 1427A progenitors that might have lowered its metallicity. The HI-to-$H_2$0pt conversion might be inefficient to have a SFR consistent with its $M_{\rm HI}/M_\star$ ratio (Fig. 2.11).

NGC 1365

NGC 1365, the large barred spiral galaxy (SBbc(s)I by Ferguson 1989b), is the most massive galaxy in our sample. The optical morphology shows a well defined spiral structure, three northern arms and two more compressed southern ones. The HI morphology (Fig. 2.2) shows a very prominent extension to the north of the system and more dense contours corresponding to the two compressed optical arms. A very detailed study on the

structure of NGC 1365 is made by Jorsater & van Moorsel (1995). They also suggested that the motion of the galaxy through the ICM can account for its unwinding arms.

NGC 1365 has a $M_{\rm HI}$ = (1.5±0.3)×10^{10} $M_\odot$ and a $M_\star$ = (6.2±1.3)×10^{10} $M_\odot$. Fig. 2.6 shows that NGC 1365 is the only galaxy in our sample which is at the upper edge of the comparison sample of non-cluster galaxies due to its high $M_{\rm HI}/M_\star$. Besides evidence of environmental interactions from its morphology, the strong gravitational potential appears to have been able to hold a sufficient amount of HI to make it comparable with the general behaviour of local galaxies (see also Fig. 2.9).

NGC 1365 is the main member of the detected infalling subgroup of galaxies located to the south-west of the cluster. It is also the only galaxy in the subgroup with a normal HI content. The existence of the NGC 1365 subgroup is also supported by Drinkwater et al. (2001a) which found NGC 1365 to be part of a substructure.

There is a HI hole in the centre of the system where Zabel et al. (2019) detected warped $H_2$0pt emission due to the central bar. HI absorption was also investigated in Ondrechen & van der Hulst (1989).

Appendix B

From Loni et al. (2021)

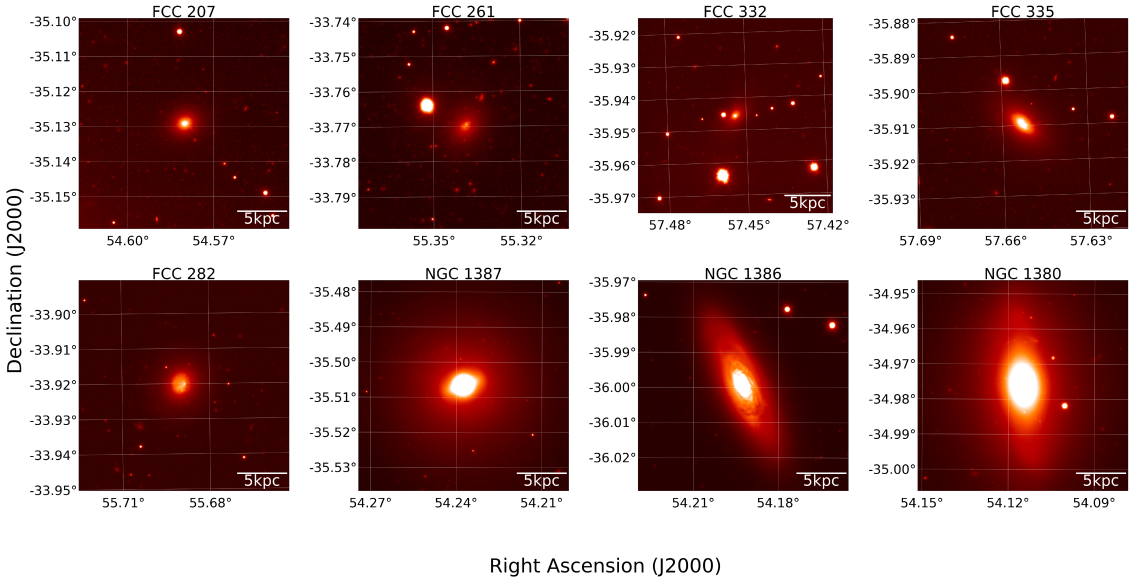

Figure B.1: Optical images of the eight H_2-rich HI-undetected galaxies (Zabel et al. 2019) for which we evaluated the M_{H_2}/M_{HI} ratio (Fig.2.9). They are sorted according to increasing M_{HI} upper limit. The *g*-band optical images come from the Fornax Deep Survey (Iodice et al. 2016; Venhola et al. 2018; Peletier et al. 2020b). We show a 5 kpc scale bar in the bottom-right corner.

Appendix C

Experiment Number	Number of galaxies	Input parameters			Best-fitting parameters		
		$\log_{10}\left(\frac{\phi_*}{\mathrm{Mpc}^3}\right)$	$\log_{10}\left(\frac{M_*}{\mathrm{M}_\odot}\right)$	α	$\log_{10}\left(\frac{\phi_*}{\mathrm{Mpc}^3}\right)$	$\log_{10}\left(\frac{M_*}{\mathrm{M}_\odot}\right)$	α
1	13527	1.96	9.4	-1.3	$1.947^{+0.065}_{-0.075}$	$9.414^{+0.098}_{-0.074}$	$-1.308^{+0.023}_{-0.026}$
2	3602	1.98	9.4	-1.15	$1.975^{+0.06}_{-0.059}$	$9.414^{+0.079}_{-0.069}$	$-1.152^{+0.031}_{-0.026}$
3	1164	1.98	9.4	-1.0	$2.009^{+0.054}_{-0.064}$	$9.38^{+0.078}_{-0.066}$	$-0.98^{+0.034}_{-0.037}$
4	497	1.98	9.4	-0.85	$1.989^{+0.046}_{-0.053}$	$9.387^{+0.07}_{-0.064}$	$-0.835^{+0.025}_{-0.036}$
5	273	1.97	9.4	-0.7	$1.961^{+0.046}_{-0.051}$	$9.427^{+0.072}_{-0.059}$	$-0.706^{+0.03}_{-0.035}$
6	16014	1.97	9.6	-1.3	$1.985^{+0.057}_{-0.065}$	$9.598^{+0.084}_{-0.078}$	$-1.294^{+0.021}_{-0.022}$
7	3742	1.96	9.6	-1.15	$1.944^{+0.06}_{-0.063}$	$9.622^{+0.086}_{-0.076}$	$-1.154^{+0.025}_{-0.028}$
8	1183	1.97	9.6	-1.0	$1.967^{+0.063}_{-0.064}$	$9.599^{+0.089}_{-0.078}$	$-0.999^{+0.036}_{-0.037}$
9	497	1.97	9.6	-0.85	$1.972^{+0.046}_{-0.053}$	$9.597^{+0.077}_{-0.07}$	$-0.844^{+0.026}_{-0.034}$
10	267	1.96	9.6	-0.7	$1.909^{+0.061}_{-0.062}$	$9.656^{+0.086}_{-0.073}$	$-0.759^{+0.052}_{-0.049}$
11	17678	1.95	9.8	-1.3	$1.967^{+0.053}_{-0.064}$	$9.792^{+0.082}_{-0.07}$	$-1.295^{+0.016}_{-0.02}$
12	4066	1.96	9.8	-1.15	$1.968^{+0.055}_{-0.058}$	$9.788^{+0.081}_{-0.069}$	$-1.146^{+0.023}_{-0.023}$
13	1192	1.96	9.8	-1.0	$1.942^{+0.058}_{-0.059}$	$9.816^{+0.08}_{-0.074}$	$-1.012^{+0.031}_{-0.029}$
14	478	1.95	9.8	-0.85	$1.948^{+0.053}_{-0.063}$	$9.797^{+0.082}_{-0.07}$	$-0.85^{+0.031}_{-0.042}$
15	268	1.96	9.8	-0.7	$1.937^{+0.048}_{-0.051}$	$9.834^{+0.09}_{-0.07}$	$-0.715^{+0.029}_{-0.036}$
16	19957	1.94	10.0	-1.3	$1.934^{+0.046}_{-0.055}$	$9.997^{+0.079}_{-0.066}$	$-1.306^{+0.015}_{-0.015}$
17	4313	1.95	10.0	-1.15	$2.002^{+0.049}_{-0.052}$	$9.943^{+0.07}_{-0.062}$	$-1.122^{+0.02}_{-0.021}$
18	1187	1.94	10.0	-1.0	$1.99^{+0.049}_{-0.047}$	$9.961^{+0.068}_{-0.073}$	$-0.97^{+0.03}_{-0.024}$
19	485	1.95	10.0	-0.85	$1.957^{+0.044}_{-0.051}$	$9.986^{+0.074}_{-0.066}$	$-0.844^{+0.023}_{-0.03}$
20	257	1.94	10.0	-0.7	$1.947^{+0.039}_{-0.035}$	$10.031^{+0.063}_{-0.061}$	$-0.695^{+0.024}_{-0.023}$
21	23050	1.94	10.2	-1.3	$1.972^{+0.043}_{-0.05}$	$10.166^{+0.067}_{-0.061}$	$-1.29^{+0.013}_{-0.014}$
22	4467	1.93	10.2	-1.15	$1.921^{+0.05}_{-0.053}$	$10.207^{+0.075}_{-0.07}$	$-1.156^{+0.019}_{-0.018}$
23	1228	1.94	10.2	-1.0	$1.934^{+0.054}_{-0.053}$	$10.199^{+0.077}_{-0.065}$	$-1.004^{+0.026}_{-0.025}$
24	474	1.94	10.2	-0.85	$1.935^{+0.04}_{-0.046}$	$10.218^{+0.068}_{-0.059}$	$-0.847^{+0.02}_{-0.022}$
25	256	1.94	10.2	-0.7	$1.905^{+0.049}_{-0.053}$	$10.247^{+0.088}_{-0.074}$	$-0.729^{+0.031}_{-0.037}$

Table C.1: The table refer to the set of 25 experiment described in Sect. 3.5.1. Input parameter columns correspond to the set of parameters shown in Fig. 3.3. Best-fitting parameters columns refer to the best-fitting parameters obtained with the method described in Chapt.3 using priors listed in Table 3.1.

Experiment Number	Number of galaxies	Input parameters			Best-fitting parameters		
		$\log_{10}\left(\frac{\phi_*}{\mathrm{Mpc}^3}\right)$	$\log_{10}\left(\frac{M_*}{\mathrm{M}_\odot}\right)$	α	$\log_{10}\left(\frac{\phi_*}{\mathrm{Mpc}^3}\right)$	$\log_{10}\left(\frac{M_*}{\mathrm{M}_\odot}\right)$	α
1	332	0.67	8.4	-1.3	$0.268^{+0.446}_{-0.74}$	$9.282^{+1.05}_{-0.9}$	$-1.33^{+0.173}_{-0.2}$
2	152	0.79	8.4	-1.15	$0.544^{+0.213}_{-0.29}$	$9.473^{+0.942}_{-0.84}$	$-1.109^{+0.057}_{-0.11}$
3	76	0.89	8.4	-1.0	$0.696^{+0.283}_{-0.567}$	$9.163^{+1.07}_{-0.836}$	$-1.089^{+0.142}_{-0.242}$
4	42	0.94	8.4	-0.85	$0.8^{+0.238}_{-0.449}$	$9.026^{+1.18}_{-0.645}$	$-0.956^{+0.133}_{-0.249}$
5	29	0.99	8.4	-0.7	$0.969^{+0.234}_{-0.29}$	$9.465^{+0.949}_{-0.937}$	$-0.799^{+0.119}_{-0.169}$
6	309	0.51	8.8	-1.3	$0.164^{+0.462}_{-0.631}$	$9.572^{+0.927}_{-0.907}$	$-1.336^{+0.16}_{-0.192}$
7	119	0.61	8.8	-1.15	$0.355^{+0.298}_{-0.375}$	$9.551^{+0.935}_{-0.825}$	$-1.143^{+0.081}_{-0.131}$
8	57	0.71	8.8	-1.0	$0.235^{+0.602}_{-0.604}$	$9.415^{+1.07}_{-0.876}$	$-1.296^{+0.268}_{-0.197}$
9	36	0.85	8.8	-0.85	$0.84^{+0.204}_{-0.259}$	$9.461^{+1.03}_{-0.806}$	$-0.882^{+0.093}_{-0.122}$
10	25	0.95	8.8	-0.7	$0.687^{+0.219}_{-0.24}$	$9.714^{+0.816}_{-0.777}$	$-0.884^{+0.088}_{-0.1}$
11	251	0.29	9.2	-1.3	$0.249^{+0.354}_{-0.471}$	$9.7^{+0.853}_{-0.809}$	$-1.23^{+0.1}_{-0.142}$
12	100	0.46	9.2	-1.15	$0.379^{+0.253}_{-0.328}$	$9.782^{+0.772}_{-0.781}$	$-1.109^{+0.069}_{-0.119}$
13	55	0.63	9.2	-1.0	$0.494^{+0.25}_{-0.369}$	$9.804^{+0.754}_{-0.839}$	$-1.043^{+0.09}_{-0.157}$
14	29	0.73	9.2	-0.85	$0.696^{+0.194}_{-0.245}$	$9.713^{+0.73}_{-0.606}$	$-0.893^{+0.088}_{-0.116}$
15	20	0.89	9.2	-0.7	$0.811^{+0.208}_{-0.258}$	$9.712^{+0.769}_{-0.568}$	$-0.773^{+0.143}_{-0.141}$
16	227	0.12	9.6	-1.3	$0.157^{+0.335}_{-0.442}$	$9.732^{+0.811}_{-0.811}$	$-1.236^{+0.098}_{-0.168}$
17	90	0.34	9.6	-1.15	$0.302^{+0.228}_{-0.281}$	$10.117^{+0.575}_{-0.696}$	$-1.098^{+0.058}_{-0.112}$
18	40	0.52	9.6	-1.0	$0.466^{+0.205}_{-0.251}$	$10.158^{+0.551}_{-0.628}$	$-0.994^{+0.061}_{-0.098}$
19	25	0.65	9.6	-0.85	$0.678^{+0.187}_{-0.207}$	$9.919^{+0.686}_{-0.518}$	$-0.865^{+0.073}_{-0.08}$
20	20	0.87	9.6	-0.7	$0.83^{+0.202}_{-0.22}$	$10.016^{+0.606}_{-0.53}$	$-0.754^{+0.14}_{-0.11}$
21	201	-0.06	10.0	-1.3	$0.168^{+0.349}_{-0.359}$	$9.8^{+0.789}_{-0.747}$	$-1.218^{+0.094}_{-0.101}$
22	70	0.16	10.0	-1.15	$0.276^{+0.255}_{-0.292}$	$10.04^{+0.639}_{-0.752}$	$-1.09^{+0.064}_{-0.103}$
23	38	0.4	10.0	-1.0	$0.441^{+0.189}_{-0.224}$	$10.346^{+0.409}_{-0.572}$	$-0.995^{+0.057}_{-0.081}$
24	24	0.64	10.0	-0.85	$0.656^{+0.193}_{-0.244}$	$10.156^{+0.558}_{-0.523}$	$-0.866^{+0.088}_{-0.106}$
25	18	0.84	10.0	-0.7	$0.699^{+0.242}_{-0.212}$	$10.357^{+0.427}_{-0.497}$	$-0.842^{+0.148}_{-0.105}$

Table C.2: The table refer to the set of 25 experiment described in Sect. 3.5.2. Input parameter columns correspond to the set of parameters shown in Fig. 3.15. Best-fitting parameters columns refer to the best-fitting parameters obtained with the method described in Chapt.3 using priors listed in Table 3.1.

Bibliography

2012, Society of Photo-Optical Instrumentation Engineers (SPIE) Conference Series, Vol. 8451, Software and Cyberinfrastructure for Astronomy II

Aarseth, S. J., Gott, J. R., I., & Turner, E. L. 1979, N-body simulations of galaxy clustering. I. Initial conditions and galaxy collapse times., ApJ, 228, 664

Aguerri, J. A. L. & González-García, A. C. 2009, On the origin of dwarf elliptical galaxies: the fundamental plane, A&A, 494, 891

Anderson, C. S., Heald, G. H., Eilek, J. A., et al. 2021, Early Science from POSSUM: Shocks, turbulence, and a massive new reservoir of ionised gas in the Fornax cluster, PASA, 38, e020

Bacon, R., Accardo, M., Adjali, L., et al. 2010, in Society of Photo-Optical Instrumentation Engineers (SPIE) Conference Series, Vol. 7735, Ground-based and Airborne Instrumentation for Astronomy III, ed. I. S. McLean, S. K. Ramsay, & H. Takami, 773508

Bahé, Y. M., McCarthy, I. G., Balogh, M. L., & Font, A. S. 2013, Why does the environmental influence on group and cluster galaxies extend beyond the virial radius?, MNRAS, 430, 3017

Balogh, M. L. & Morris, S. L. 2000, Hα photometry of Abell 2390, MNRAS, 318, 703

Barnes, D. G., Staveley-Smith, L., de Blok, W. J. G., et al. 2001, The HI Parkes All Sky Survey: southern observations, calibration and robust imaging, MNRAS, 322, 486

Barnes, D. G., Staveley-Smith, L., Webster, R. L., & Walsh, W. 1997, An HI survey for protogalaxies in the Centaurus and Fornax galaxy clusters, MNRAS, 288, 307

Bekki, K., Couch, W. J., & Shioya, Y. 2002, Passive Spiral Formation from Halo Gas Starvation: Gradual Transformation into S0s, ApJ, 577, 651

Bianconi, M., Smith, G. P., Haines, C. P., et al. 2018, LoCuSS: pre-processing in galaxy groups falling into massive galaxy clusters at z = 0.2, MNRAS, 473, L79

Bigiel, F., Leroy, A., Walter, F., et al. 2008, The Star Formation Law in Nearby Galaxies on Sub-Kpc Scales, AJ, 136, 2846

Binggeli, B., Sandage, A., & Tarenghi, M. 1984, Studies of the Virgo Cluster. I. Photometry of 109 galaxies near the cluster center to serve as standards., AJ, 89, 64

Binney, J. & Tremaine, S. 1987, Galactic dynamics

Blakeslee, J. P., Jordán, A., Mei, S., et al. 2009, The ACS Fornax Cluster Survey. V. Measurement and Recalibration of Surface Brightness Fluctuations and a Precise Value of the Fornax-Virgo Relative Distance, ApJ, 694, 556

Boquien, M., Kennicutt, R., Calzetti, D., et al. 2016, Towards universal hybrid star formation rate estimators, A&A, 591, A6

Boselli, A., Boissier, S., Cortese, L., et al. 2006, The Fate of Spiral Galaxies in Clusters: The Star Formation History of the Anemic Virgo Cluster Galaxy NGC 4569, ApJ, 651, 811

Boselli, A., Cortese, L., & Boquien, M. 2014a, Cold gas properties of the Herschel Reference Survey. I. ^{12}CO(1-0) and HI data, A&A, 564, A65

Boselli, A., Cortese, L., Boquien, M., et al. 2014b, Cold gas properties of the Herschel Reference Survey. II. Molecular and total gas scaling relations, A&A, 564, A66

Boselli, A., Fossati, M., & Sun, M. 2021, Ram Pressure Stripping in High-Density Environments, arXiv e-prints, arXiv:2109.13614

Boselli, A. & Gavazzi, G. 2006, Environmental Effects on Late-Type Galaxies in Nearby Clusters, PASP, 118, 517

Boselli, A. & Gavazzi, G. 2009, The HI properties of galaxies in the Coma I cloud revisited, A&A, 508, 201

Bournaud, F., Elmegreen, B. G., & Martig, M. 2009, The Thick Disks of Spiral Galaxies as Relics from Gas-rich, Turbulent, Clumpy Disks at High Redshift, ApJ, 707, L1

Briggs, D. S. 1995, in American Astronomical Society Meeting Abstracts, Vol. 187, American Astronomical Society Meeting Abstracts, 112.02

Briggs, F. H. 1990, The Space Density of Low-Profile Gas-Rich Galaxies at the Present Epoch, AJ, 100, 999

Buchner, J., Georgakakis, A., Nandra, K., et al. 2014, X-ray spectral modelling of the AGN obscuring region in the CDFS: Bayesian model selection and catalogue, A&A, 564, A125

Bureau, M., Mould, J. R., & Staveley-Smith, L. 1996, A New I-Band Tully-Fisher Relation for the Fornax Cluster: Implication for the Fornax Distance and Local Supercluster Velocity Field, ApJ, 463, 60

Bykov, A. M., Churazov, E. M., Ferrari, C., et al. 2015, Structures and Components in Galaxy Clusters: Observations and Models, Space Sci. Rev., 188, 141

Calzetti, D., Liu, G., & Koda, J. 2012, Star Formation Laws: The Effects of Gas Cloud Sampling, ApJ, 752, 98

Cantiello, M., D'Abrusco, R., Spavone, M., et al. 2018, VEGAS-SSS. II. Comparing the globular cluster systems in NGC 3115 and NGC 1399 using VEGAS and FDS survey data. The quest for a common genetic heritage of globular cluster systems, A&A, 611, A93

Cappellari, M. 2017, Improving the full spectrum fitting method: accurate convolution with Gauss-Hermite functions, MNRAS, 466, 798

Cappellari, M. & Emsellem, E. 2004, Parametric Recovery of Line-of-Sight Velocity Distributions from Absorption-Line Spectra of Galaxies via Penalized Likelihood, PASP, 116, 138

Cappellari, M., Emsellem, E., Krajnović, D., et al. 2011, The ATLAS^{3D} project - VII. A new look at the morphology of nearby galaxies: the kinematic morphology-density relation, MNRAS, 416, 1680

Catinella, B., Saintonge, A., Janowiecki, S., et al. 2018, xGASS: total cold gas scaling relations and molecular-to-atomic gas ratios of galaxies in the local Universe, MNRAS, 476, 875

Catinella, B., Schiminovich, D., Cortese, L., et al. 2013, The GALEX Arecibo SDSS Survey - VIII. Final data release. The effect of group environment on the gas content of massive galaxies, MNRAS, 436, 34

Cayatte, V., Kotanyi, C., Balkowski, C., & van Gorkom, J. H. 1994, A Very Large Array Survey of Neutral Hydrogen in Virgo Cluster Spirals. III. Surface Density Profiles of the Gas, AJ, 107, 1003

Chamaraux, P., Balkowski, C., & Gerard, E. 1980, The H I deficiency of the Virgo cluster spirals., A&A, 83, 38

Chung, A., van Gorkom, J. H., Kenney, J. D. P., Crowl, H., & Vollmer, B. 2009, VLA Imaging of Virgo Spirals in Atomic Gas (VIVA). I. The Atlas and the H I Properties, AJ, 138, 1741

Cluver, M. E., Jarrett, T. H., Dale, D. A., et al. 2017, Calibrating Star Formation in WISE Using Total Infrared Luminosity, ApJ, 850, 68

Cluver, M. E., Jarrett, T. H., Hopkins, A. M., et al. 2014, Galaxy and Mass Assembly (GAMA): Mid-infrared Properties and Empirical Relations from WISE, ApJ, 782, 90

Condon, J. J., Cotton, W. D., Greisen, E. W., et al. 1998, The NRAO VLA Sky Survey, AJ, 115, 1693

Cortese, L., Bekki, K., Boselli, A., et al. 2016, The selective effect of environment on the atomic and molecular gas-to-dust ratio of nearby galaxies in the Herschel Reference Survey, MNRAS, 459, 3574

Cortese, L., Boissier, S., Boselli, A., et al. 2012, The GALEX view of the Herschel Reference Survey. Ultraviolet structural properties of nearby galaxies, A&A, 544, A101

Cortese, L., Catinella, B., Boissier, S., Boselli, A., & Heinis, S. 2011, The effect of the environment on the H I scaling relations, MNRAS, 415, 1797

Cortese, L., Catinella, B., & Smith, R. 2021, The Dawes Review 9: The role of cold gas stripping on the star formation quenching of satellite galaxies, PASA, 38, e035

Cortese, L., Gavazzi, G., Boselli, A., et al. 2006, Witnessing galaxy preprocessing in the local Universe: the case of a star-bursting group falling into Abell 1367, A&A, 453, 847

Cortese, L. & Hughes, T. M. 2009, Evolutionary paths to and from the red sequence: star formation and HI properties of transition galaxies at z ~0, MNRAS, 400, 1225

Courtois, H. M., Tully, R. B., Fisher, J. R., et al. 2009, The Extragalactic Distance Database: All Digital H I Profile Catalog, AJ, 138, 1938

Crain, R. A., Schaye, J., Bower, R. G., et al. 2015, The EAGLE simulations of galaxy formation: calibration of subgrid physics and model variations, MNRAS, 450, 1937

Croton, D. J., Springel, V., White, S. D. M., et al. 2006, The many lives of active galactic nuclei: cooling flows, black holes and the luminosities and colours of galaxies, MNRAS, 365, 11

Davies, J., Minchin, R., Sabatini, S., et al. 2004, A multibeam HI survey of the Virgo cluster - two isolated HI clouds?, MNRAS, 349, 922

Davies, R. D. & Lewis, B. M. 1973, Neutral hydrogen in Virgo cluster galaxies., MNRAS, 165, 231

de Blok, W. J. G., McGaugh, S. S., & van der Hulst, J. M. 1996, HI observations of low surface brightness galaxies: probing low-density galaxies, MNRAS, 283, 18

de Blok, W. J. G., Walter, F., Ferguson, A. M. N., et al. 2018, A High-resolution Mosaic of the Neutral Hydrogen in the M81 Triplet, ApJ, 865, 26

De Lucia, G., Hirschmann, M., & Fontanot, F. 2019, Nature versus nurture: what regulates star formation in satellite galaxies?, MNRAS, 482, 5041

de Vaucouleurs, G., de Vaucouleurs, A., Corwin, Herold G., J., et al. 1991, Third Reference Catalogue of Bright Galaxies

Delhaize, J., Meyer, M. J., Staveley-Smith, L., & Boyle, B. J. 2013, Detection of H I in distant galaxies using spectral stacking, MNRAS, 433, 1398

Dey, A., Schlegel, D. J., Lang, D., et al. 2019, Overview of the DESI Legacy Imaging Surveys, AJ, 157, 168

Diaferio, A., Kauffmann, G., Balogh, M. L., et al. 2001, The spatial and kinematic distributions of cluster galaxies in a ΛCDM universe: comparison with observations, MNRAS, 323, 999

Domainko, W., Mair, M., Kapferer, W., et al. 2006, Enrichment of the ICM of galaxy clusters due to ram-pressure stripping, A&A, 452, 795

Dressler, A. 1980, Galaxy morphology in rich clusters: implications for the formation and evolution of galaxies., ApJ, 236, 351

Dressler, A. 1986, The Morphological Types and Orbits of H i Deficient Spirals in Clusters of Galaxies, ApJ, 301, 35

Dressler, A. & Gunn, J. E. 1983, Spectroscopy of galaxies in distant clusters. II. The population of the 3C 295 cluster., ApJ, 270, 7

Dressler, A., Oemler, Augustus, J., Couch, W. J., et al. 1997, Evolution since z = 0.5 of the Morphology-Density Relation for Clusters of Galaxies, ApJ, 490, 577

Dressler, A., Smail, I., Poggianti, B. M., et al. 1999, A Spectroscopic Catalog of 10 Distant Rich Clusters of Galaxies, ApJS, 122, 51

Drinkwater, M. J., Gregg, M. D., & Colless, M. 2001a, Substructure and Dynamics of the Fornax Cluster, ApJ, 548, L139

Drinkwater, M. J., Gregg, M. D., Holman, B. A., & Brown, M. J. I. 2001b, The evolution and star formation of dwarf galaxies in the Fornax Cluster, MNRAS, 326, 1076

Durbala, A., Finn, R. A., Crone Odekon, M., et al. 2020, The ALFALFA-SDSS Galaxy Catalog, AJ, 160, 271

Emsellem, E., Cappellari, M., Krajnović, D., et al. 2011, The ATLAS^{3D} project - III. A census of the stellar angular momentum within the effective radius of early-type galaxies: unveiling the distribution of fast and slow rotators, MNRAS, 414, 888

Fabello, S., Catinella, B., Giovanelli, R., et al. 2011, ALFALFA H I data stacking - I. Does the bulge quench ongoing star formation in early-type galaxies?, MNRAS, 411, 993

Falcón-Barroso, J., Bacon, R., Bureau, M., et al. 2006, The SAURON project - VII. Integral-field absorption and emission-line kinematics of 24 spiral galaxy bulges, MNRAS, 369, 529

Farouki, R. & Shapiro, S. L. 1981, Computer simulations of environmental influences on galaxy evolution in dense clusters. II - Rapid tidal encounters, ApJ, 243, 32

Fasano, G., Poggianti, B. M., Couch, W. J., et al. 2000, The Evolution of the Galactic Morphological Types in Clusters, ApJ, 542, 673

Ferguson, H. C. 1989a, Galaxy Populations in the Fornax and Virgo Clusters, Ap&SS, 157, 227

Ferguson, H. C. 1989b, Population Studies in Groups and Clusters of Galaxies. II. A Catalog of Galaxies in the Central 3.5 Degrees of the Fornax Cluster, AJ, 98, 367

Feroz, F., Hobson, M. P., & Bridges, M. 2009, MULTINEST: an efficient and robust Bayesian inference tool for cosmology and particle physics, MNRAS, 398, 1601

Fouqué, P., Solanes, J. M., Sanchis, T., & Balkowski, C. 2001, Structure, mass and distance of the Virgo cluster from a Tolman-Bondi model, A&A, 375, 770

Frank, K. A., Peterson, J. R., Andersson, K., Fabian, A. C., & Sanders, J. S. 2013, Characterization of Intracluster Medium Temperature Distributions of 62 Galaxy Clusters with XMM-Newton, ApJ, 764, 46

Freeland, E. & Wilcots, E. 2011, Intergalactic Gas in Groups of Galaxies: Implications for Dwarf Spheroidal Formation and the Missing Baryons Problem, ApJ, 738, 145

Freudling, W., Romaniello, M., Bramich, D. M., et al. 2013, Automated data reduction workflows for astronomy. The ESO Reflex environment, A&A, 559, A96

Furusho, T., Yamasaki, N. Y., Ohashi, T., Shibata, R., & Ezawa, H. 2001, Temperature Map of the Perseus Cluster of Galaxies Observed with ASCA, ApJ, 561, L165

Gavazzi, G., Boselli, A., Scodeggio, M., Pierini, D., & Belsole, E. 1999, The 3D structure of the Virgo cluster from H-band Fundamental Plane and Tully-Fisher distance determinations, MNRAS, 304, 595

Gavazzi, G., Boselli, A., van Driel, W., & O'Neil, K. 2005, Completing H I observations of galaxies in the Virgo cluster, A&A, 429, 439

Geréb, K., Catinella, B., Cortese, L., et al. 2016, GASS 3505: the prototype of H I-excess, passive galaxies, MNRAS, 462, 382

Geréb, K., Janowiecki, S., Catinella, B., Cortese, L., & Kilborn, V. 2018, A multiwavelength survey of H I-excess galaxies with surprisingly inefficient star formation, MNRAS, 476, 896

Giovanelli, R. & Haynes, M. P. 1983, The HI extent and deficiency of spiral galaxies in the Virgo cluster., AJ, 88, 881

Gottlöber, S., Klypin, A., & Kravtsov, A. V. 2001, Merging History as a Function of Halo Environment, ApJ, 546, 223

Grillmair, C. J., Freeman, K. C., Bicknell, G. V., et al. 1994, The Velocity Dispersion of Globular Clusters in NGC 1399, ApJ, 422, L9

Gunn, J. E. & Gott, J. Richard, I. 1972, On the Infall of Matter Into Clusters of Galaxies and Some Effects on Their Evolution, ApJ, 176, 1

Hamraz, E., Peletier, R. F., Khosroshahi, H. G., et al. 2019, Young stellar populations in early-type dwarf galaxies. Occurrence, radial extent, and scaling relations, A&A, 625, A94

Han, S., Smith, R., Choi, H., et al. 2018, YZiCS: Preprocessing of Dark Halos in the Hydrodynamic Zoom-in Simulation of Clusters, ApJ, 866, 78

Haynes, M. P. & Giovanelli, R. 1984, Neutral hydrogen in isolated galaxies. IV. Results for the Arecibo sample., AJ, 89, 758

Haynes, M. P. & Giovanelli, R. 1986, The Pattern of H i Deficiency in the Virgo Cluster, ApJ, 306, 466

Healy, J., Blyth, S. L., Verheijen, M. A. W., et al. 2021, H I content in Coma cluster substructure, A&A, 650, A76

Hess, K. M. & Wilcots, E. M. 2013, Evolution in the H I Gas Content of Galaxy Groups: Pre-processing and Mass Assembly in the Current Epoch, AJ, 146, 124

Hester, J. A. 2006, Ram Pressure Stripping in Clusters and Groups, ApJ, 647, 910

Hinz, J. L., Rieke, G. H., & Caldwell, N. 2003, The Tully-Fisher Relation in Coma and Virgo Cluster S0 Galaxies, AJ, 126, 2622

Högbom, J. A. 1974, Aperture Synthesis with a Non-Regular Distribution of Interferometer Baselines, A&AS, 15, 417

Horellou, C., Black, J. H., van Gorkom, J. H., et al. 2001, Atomic and molecular gas in the merger galaxy NGC 1316 (Fornax A) and its environment, A&A, 376, 837

Hubble, E. & Humason, M. L. 1931, The Velocity-Distance Relation among Extra-Galactic Nebulae, ApJ, 74, 43

Hughes, T. M. & Cortese, L. 2009, The migration of nearby spirals from the blue to red sequence: AGN feedback or environmental effects?, MNRAS, 396, L41

Iodice, E., Capaccioli, M., Grado, A., et al. 2016, The Fornax Deep Survey with VST. I. The Extended and Diffuse Stellar Halo of NGC 1399 out to 192 kpc, ApJ, 820, 42

Iodice, E., Sarzi, M., Bittner, A., et al. 2019a, The Fornax3D project: Tracing the assembly history of the cluster from the kinematic and line-strength maps, A&A, 627, A136

Iodice, E., Spavone, M., Cantiello, M., et al. 2017a, Intracluster Patches of Baryons in the Core of the Fornax Cluster, ApJ, 851, 75

Iodice, E., Spavone, M., Capaccioli, M., et al. 2017b, The Fornax Deep Survey with VST. II. Fornax A: A Two-phase Assembly Caught in the Act, ApJ, 839, 21

Iodice, E., Spavone, M., Capaccioli, M., et al. 2019b, The Fornax Deep Survey with the VST. V. Exploring the faintest regions of the bright early-type galaxies inside the virial radius, A&A, 623, A1

Jaffé, Y. L., Smith, R., Candlish, G. N., et al. 2015, BUDHIES II: a phase-space view of H I gas stripping and star formation quenching in cluster galaxies, MNRAS, 448, 1715

Jarrett, T. H., Cluver, M. E., Brown, M. J. I., et al. 2019, The WISE Extended Source Catalog (WXSC). I. The 100 Largest Galaxies, ApJS, 245, 25

Jarrett, T. H., Masci, F., Tsai, C. W., et al. 2013, Extending the Nearby Galaxy Heritage with WISE: First Results from the WISE Enhanced Resolution Galaxy Atlas, AJ, 145, 6

Jones, M. G., Espada, D., Verdes-Montenegro, L., et al. 2018a, The AMIGA sample of isolated galaxies. XIII. The HI content of an almost "nurture free" sample, A&A, 609, A17

Jones, M. G., Haynes, M. P., Giovanelli, R., & Moorman, C. 2018b, The ALFALFA H I mass function: a dichotomy in the low-mass slope and a locally suppressed 'knee' mass, MNRAS, 477, 2

Jones, M. G., Hess, K. M., Adams, E. A. K., & Verdes-Montenegro, L. 2020, The H I mass function of group galaxies in the ALFALFA survey, MNRAS, 494, 2090

Jones, M. G., Papastergis, E., Haynes, M. P., & Giovanelli, R. 2016, Environmental dependence of the H I mass function in the ALFALFA 70% catalogue, MNRAS, 457, 4393

Jones, M. G., Verdes-Montenegro, L., Damas-Segovia, A., et al. 2019, Evolution of compact groups from intermediate to final stages. A case study of the H I content of HCG 16, A&A, 632, A78

Jordán, A., Blakeslee, J. P., Côté, P., et al. 2007, The ACS Fornax Cluster Survey. I. Introduction to the Survey and Data Reduction Procedures, ApJS, 169, 213

Jorsater, S. & van Moorsel, G. A. 1995, High Resolution Neutral Hydrogen Observations of the Barred Spiral Galaxy NGC 1365, AJ, 110, 2037

Józsa, G. I. G., Kenn, F., Klein, U., & Oosterloo, T. A. 2007, Kinematic modelling of disk galaxies. I. A new method to fit tilted rings to data cubes, A&A, 468, 731

Józsa, G. I. G., Kenn, F., Oosterloo, T. A., & Klein, U. 2012, TiRiFiC: Tilted Ring Fitting Code

Karachentsev, I. D., Tully, R. B., Wu, P.-F., Shaya, E. J., & Dolphin, A. E. 2014, Infall of Nearby Galaxies into the Virgo Cluster as Traced with Hubble Space Telescope, ApJ, 782, 4

Kenney, J. D. P., van Gorkom, J. H., & Vollmer, B. 2004, VLA H I Observations of Gas Stripping in the Virgo Cluster Spiral NGC 4522, AJ, 127, 3361

Kennicutt, R. C. & Evans, N. J. 2012, Star Formation in the Milky Way and Nearby Galaxies, ARA&A, 50, 531

Kleiner, D., Serra, P., Maccagni, F. M., et al. 2021, A MeerKAT view of pre-processing in the Fornax A group, A&A, 648, A32

Koribalski, B. S., Staveley-Smith, L., Kilborn, V. A., et al. 2004, The 1000 Brightest HIPASS Galaxies: H I Properties, AJ, 128, 16

Kovac, K., Oosterloo, T. A., & van der Hulst, J. M. 2005, in IAU Colloq. 198: Near-fields cosmology with dwarf elliptical galaxies, ed. H. Jerjen & B. Binggeli, 351–354

Kreckel, K., Platen, E., Aragón-Calvo, M. A., et al. 2012, The Void Galaxy Survey: Optical Properties and H I Morphology and Kinematics, AJ, 144, 16

Kroupa, P. 2001, On the variation of the initial mass function, MNRAS, 322, 231

Larson, R. B., Tinsley, B. M., & Caldwell, C. N. 1980, The evolution of disk galaxies and the origin of S0 galaxies, ApJ, 237, 692

Lauberts, A. & Valentijn, E. A. 1989, The surface photometry catalogue of the ESO-Uppsala galaxies

Lee-Waddell, K., Serra, P., Koribalski, B., et al. 2018, Tidal origin of NGC 1427A in the Fornax cluster, MNRAS, 474, 1108

Leroy, A. K., Sandstrom, K. M., Lang, D., et al. 2019, A z = 0 Multiwavelength Galaxy Synthesis. I. A WISE and GALEX Atlas of Local Galaxies, ApJS, 244, 24

Loni, A., Serra, P., Kleiner, D., et al. 2021, A blind ATCA HI survey of the Fornax galaxy cluster. Properties of the HI detections, A&A, 648, A31

Lu, Y., Mo, H. J., Lu, Z., Katz, N., & Weinberg, M. D. 2014, Bayesian inferences of galaxy formation from the K-band luminosity and H I mass functions of galaxies: constraining star formation and feedback, MNRAS, 443, 1252

Lupton, P. 2005

Maddox, N., Hess, K. M., Obreschkow, D., Jarvis, M. J., & Blyth, S. L. 2015, Variation of galactic cold gas reservoirs with stellar mass, MNRAS, 447, 1610

Maddox, N., Serra, P., Venhola, A., et al. 2019, A spectroscopic census of the Fornax cluster and beyond: preparing for next generation surveys, MNRAS, 490, 1666

Maier, C., Kuchner, U., Ziegler, B. L., et al. 2016, CLASH-VLT: Strangulation of cluster galaxies in MACS J0416.1-2403 as seen from their chemical enrichment, A&A, 590, A108

Marasco, A., Crain, R. A., Schaye, J., et al. 2016, The environmental dependence of H I in galaxies in the EAGLE simulations, MNRAS, 461, 2630

Matthews, L. D., van Driel, W., & Gallagher, J. S., I. 1998, High-Resolution, High Signal-to-Noise, Global H i Spectra of Southern, Extreme Late-Type Spiral Galaxies, AJ, 116, 1169

McGee, S. L., Balogh, M. L., Bower, R. G., Font, A. S., & McCarthy, I. G. 2009, The accretion of galaxies into groups and clusters, MNRAS, 400, 937

McMullin, J. P., Waters, B., Schiebel, D., Young, W., & Golap, K. 2007, in Astronomical Society of the Pacific Conference Series, Vol. 376, Astronomical Data Analysis Software and Systems XVI, ed. R. A. Shaw, F. Hill, & D. J. Bell, 127

Meyer, M., Robotham, A., Obreschkow, D., et al. 2017, Tracing HI Beyond the Local Universe, PASA, 34, 52

Mitchell-Wynne, K., Santos, M. G., Afonso, J., & Jarvis, M. J. 2014, Beyond stacking: a maximum-likelihood method to constrain radio source counts below the detection threshold, MNRAS, 437, 2270

Moore, B., Katz, N., Lake, G., Dressler, A., & Oemler, A. 1996, Galaxy harassment and the evolution of clusters of galaxies, Nature, 379, 613

Moorman, C. M., Vogeley, M. S., Hoyle, F., et al. 2014, The H I mass function and velocity width function of void galaxies in the Arecibo Legacy Fast ALFA Survey, MNRAS, 444, 3559

Morokuma-Matsui, K., Serra, P., Maccagni, F. M., et al. 2019, Complex distribution and velocity field of molecular gas in NGC 1316 as revealed by the Morita Array of ALMA, PASJ, 71, 85

Mould, J. R., Hughes, S. M. G., Stetson, P. B., et al. 2000, The Hubble Space Telescope Key Project on the Extragalactic Distance Scale. XXI. The Cepheid Distance to NGC 1425, ApJ, 528, 655

Murakami, H., Komiyama, M., Matsushita, K., et al. 2011, Suzaku and XMM-Newton Observations of the Fornax Cluster: Temperature and Metallicity Distribution, PASJ, 63, S963

Nasonova, O. G., de Freitas Pacheco, J. A., & Karachentsev, I. D. 2011, Hubble flow around Fornax cluster of galaxies, A&A, 532, A104

Navarro, J. F., Frenk, C. S., & White, S. D. M. 1996, The Structure of Cold Dark Matter Halos, ApJ, 462, 563

Nulsen, P. E. J. 1982, Transport processes and the stripping of cluster galaxies., MNRAS, 198, 1007

Oemler, Augustus, J. 1974, The Systematic Properties of Clusters of Galaxies. Photometry of 15 Clusters, ApJ, 194, 1

Oh, S., Kim, K., Lee, J. H., et al. 2018, KYDISC: Galaxy Morphology, Quenching, and Mergers in the Cluster Environment, ApJS, 237, 14

Ondrechen, M. P. & van der Hulst, J. M. 1989, H I in Barred Spiral Galaxies. I. NGC 1365, ApJ, 342, 29

Pan, H., Jarvis, M. J., Allison, J. R., et al. 2020, Measuring the H I mass function below the detection threshold, MNRAS, 491, 1227

Paolillo, M., Fabbiano, G., Peres, G., & Kim, D. W. 2002, Deep ROSAT HRI Observations of the NGC 1399/NGC 1404 Region: Morphology and Structure of the X-Ray Halo, ApJ, 565, 883

Peletier, R., Iodice, E., Venhola, A., et al. 2020a, The Fornax Deep Survey data release 1, arXiv e-prints, arXiv:2008.12633

Peletier, R., Iodice, E., Venhola, A., et al. 2020b, The Fornax Deep Survey data release 1, arXiv e-prints, arXiv:2008.12633

Pinna, F., Falcón-Barroso, J., Martig, M., et al. 2019a, The Fornax 3D project: Thick disks in a cluster environment, A&A, 625, A95

Pinna, F., Falcón-Barroso, J., Martig, M., et al. 2019b, The Fornax 3D project: Unveiling the thick disk origin in FCC 170; possible signs of accretion, A&A, 623, A19

Pisano, D. J., Barnes, D. G., Staveley-Smith, L., et al. 2011, An H I Survey of Six Local Group Analogs. II. H I Properties of Group Galaxies, ApJS, 197, 28

Poggianti, B. M., Moretti, A., Gullieuszik, M., et al. 2017, GASP. I. Gas Stripping Phenomena in Galaxies with MUSE, ApJ, 844, 48

Poggianti, B. M., Smail, I., Dressler, A., et al. 1999, The Star Formation Histories of Galaxies in Distant Clusters, ApJ, 518, 576

Postman, M., Franx, M., Cross, N. J. G., et al. 2005, The Morphology-Density Relation in z ~1 Clusters, ApJ, 623, 721

Press, W. H. & Schechter, P. 1974, Formation of Galaxies and Clusters of Galaxies by Self-Similar Gravitational Condensation, ApJ, 187, 425

Quilis, V., Moore, B., & Bower, R. 2000, Gone with the Wind: The Origin of S0 Galaxies in Clusters, Science, 288, 1617

Raj, M. A., Iodice, E., Napolitano, N. R., et al. 2019, The Fornax Deep Survey with the VST. VII. Evolution and structure of late type galaxies inside the virial radius of the Fornax cluster, A&A, 628, A4

Ramatsoku, M., Serra, P., Poggianti, B. M., et al. 2019, GASP - XVII. H I imaging of the jellyfish galaxy JO206: gas stripping and enhanced star formation, MNRAS, 487, 4580

Rhee, J., Lah, P., Briggs, F. H., et al. 2018, Neutral hydrogen (H I) gas content of galaxies at z ≈ 0.32, MNRAS, 473, 1879

Rhee, J., Smith, R., Choi, H., et al. 2017, Phase-space Analysis in the Group and Cluster Environment: Time Since Infall and Tidal Mass Loss, ApJ, 843, 128

Roberts, I. D. & Parker, L. C. 2019, 'Observing' unrelaxed clusters in dark matter simulations, MNRAS, 490, 773

Rodríguez-Ardila, A., Prieto, M. A., Mazzalay, X., et al. 2017, Powerful outflows in the central parsecs of the low-luminosity active galactic nucleus NGC 1386, MNRAS, 470, 2845

Roediger, E. & Hensler, G. 2005, Ram pressure stripping of disk galaxies. From high to low density environments, A&A, 433, 875

Said, K., Kraan-Korteweg, R. C., & Staveley-Smith, L. 2019, The H I mass function in the Parkes H I Zone of Avoidance survey, MNRAS, 486, 1796

Sarzi, M., Falcón-Barroso, J., Davies, R. L., et al. 2006, The SAURON project - V. Integral-field emission-line kinematics of 48 elliptical and lenticular galaxies, MNRAS, 366, 1151

Sarzi, M., Iodice, E., Coccato, L., et al. 2018, Fornax3D project: Overall goals, galaxy sample, MUSE data analysis, and initial results, A&A, 616, A121

Sault, R. J., Teuben, P. J., & Wright, M. C. H. 1995, Astronomical Society of the Pacific Conference Series, Vol. 77, A Retrospective View of MIRIAD, ed. R. A. Shaw, H. E. Payne, & J. J. E. Hayes, 433

Scargle, J. D., Norris, J. P., Jackson, B., & Chiang, J. 2013, Studies in Astronomical Time Series Analysis. VI. Bayesian Block Representations, ApJ, 764, 167

Scharf, C. A., Zurek, D. R., & Bureau, M. 2005, The Chandra Fornax Survey. I. The Cluster Environment, ApJ, 633, 154

Schombert, J. M., Bothun, G. D., Schneider, S. E., & McGaugh, S. S. 1992, A Catalog of Low Surface Brightness Galaxies. List II, AJ, 103, 1107

Schröder, A., Drinkwater, M. J., & Richter, O. G. 2001, The neutral hydrogen content of ¡ASTROBJ¿Fornax cluster¡/ASTROBJ¿ galaxies, A&A, 376, 98

Schweizer, F. 1980, An optical study of the giant radio galaxy NGC 1316 (Fornax A)., ApJ, 237, 303

Serra, P., de Blok, W. J. G., Bryan, G. L., et al. 2016, in MeerKAT Science: On the Pathway to the SKA, 8

Serra, P., Jurek, R., & Flöer, L. 2012, Using Negative Detections to Estimate Source-Finder Reliability, PASA, 29, 296

Serra, P., Koribalski, B., Duc, P.-A., et al. 2013, Discovery of a giant HI tail in the galaxy group HCG 44, MNRAS, 428, 370

Serra, P., Maccagni, F. M., Kleiner, D., et al. 2019, Neutral hydrogen gas within and around NGC 1316, A&A, 628, A122

Serra, P., Trager, S. C., Oosterloo, T. A., & Morganti, R. 2008, Stellar populations, neutral hydrogen, and ionised gas in field early-type galaxies, A&A, 483, 57

Serra, P., Westmeier, T., Giese, N., et al. 2015, SOFIA: a flexible source finder for 3D spectral line data, MNRAS, 448, 1922

Sheardown, A., Roediger, E., Su, Y., et al. 2018, The Recent Growth History of the Fornax Cluster Derived from Simultaneous Sloshing and Gas Stripping: Simulating the Infall of NGC 1404, ApJ, 865, 118

Sheen, Y.-K., Yi, S. K., Ree, C. H., & Lee, J. 2012, Post-merger Signatures of Red-sequence Galaxies in Rich Abell Clusters at z ¡~0.1, ApJS, 202, 8

Shin, M.-S. & Ruszkowski, M. 2013, Ram pressure stripping in elliptical galaxies - I. The impact of the interstellar medium turbulence, MNRAS, 428, 804

Skilling, J. 2004, in American Institute of Physics Conference Series, Vol. 735, Bayesian Inference and Maximum Entropy Methods in Science and Engineering: 24th International Workshop on Bayesian Inference and Maximum Entropy Methods in Science and Engineering, ed. R. Fischer, R. Preuss, & U. V. Toussaint, 395–405

Solanes, J. M., Giovanelli, R., & Haynes, M. P. 1996, The H i Content of Spirals. I. Field Galaxy H i Mass Functions and H i Mass–Optical Size Regressions, ApJ, 461, 609

Solanes, J. M., Manrique, A., García-Gómez, C., et al. 2001, The H I Content of Spirals. II. Gas Deficiency in Cluster Galaxies, ApJ, 548, 97

Soto, K. T., Lilly, S. J., Bacon, R., Richard, J., & Conseil, S. 2016, ZAP - enhanced PCA sky subtraction for integral field spectroscopy, MNRAS, 458, 3210

Spavone, M., Iodice, E., van de Ven, G., et al. 2020, The Fornax Deep Survey with VST. VIII. Connecting the accretion history with the cluster density, A&A, 639, A14

Spiniello, C., Napolitano, N. R., Arnaboldi, M., et al. 2018, The Fornax Cluster VLT Spectroscopic Survey II - Planetary Nebulae kinematics within 200 kpc of the cluster core, MNRAS, 477, 1880

Springob, C. M., Haynes, M. P., & Giovanelli, R. 2005, Morphology, Environment, and the H I Mass Function, ApJ, 621, 215

Stevens, I. R., Acreman, D. M., & Ponman, T. J. 1999, Galaxies in clusters: the observational characteristics of bow shocks, wakes and tails, MNRAS, 310, 663

Su, A. H., Salo, H., Janz, J., et al. 2021, The Fornax Deep Survey (FDS) with the VST XI. The search for signs of preprocessing between the Fornax main cluster and Fornax A group, arXiv e-prints, arXiv:2101.05699

Su, Y., Nulsen, P. E. J., Kraft, R. P., et al. 2017, Gas Sloshing Regulates and Records the Evolution of the Fornax Cluster, ApJ, 851, 69

Takahashi, S. & Yamashita, K. 2003, XMM-Newton Observation of the Cluster of Galaxies Abell 1650, PASJ, 55, 1105

Theureau, G., Bottinelli, L., Coudreau-Durand, N., et al. 1998, Kinematics of the local universe. VII. New 21-cm line measurements of 2112 galaxies, A&AS, 130, 333

Thilker, D. A., Bianchi, L., Schiminovich, D., et al. 2010, NGC 404: A Rejuvenated Lenticular Galaxy on a Merger-induced, Blueward Excursion Into the Green Valley, ApJ, 714, L171

Toomre, A. & Toomre, J. 1972, Galactic Bridges and Tails, ApJ, 178, 623

Trager, S. C., Faber, S. M., Worthey, G., & González, J. J. 2000, The Stellar Population Histories of Early-Type Galaxies. II. Controlling Parameters of the Stellar Populations, AJ, 120, 165

van der Hulst, J. M., Ondrechen, M. P., van Gorkom, J. H., & Hummel, E. 1983, in IAU Symposium, Vol. 100, Internal Kinematics and Dynamics of Galaxies, ed. E. Athanassoula, 233–234

Vazdekis, A., Coelho, P., Cassisi, S., et al. 2015, Evolutionary stellar population synthesis with MILES - II. Scaled-solar and α-enhanced models, MNRAS, 449, 1177

Venhola, A., Peletier, R., Laurikainen, E., et al. 2018, The Fornax Deep Survey with the VST. IV. A size and magnitude limited catalog of dwarf galaxies in the area of the Fornax cluster, A&A, 620, A165

Venhola, A., Peletier, R., Laurikainen, E., et al. 2019, The Fornax Deep Survey (FDS) with VST. VI. Optical properties of the dwarf galaxies in the Fornax cluster, A&A, 625, A143

Vogelsberger, M., Genel, S., Springel, V., et al. 2014, Introducing the Illustris Project: simulating the coevolution of dark and visible matter in the Universe, MNRAS, 444, 1518

Vollmer, B., Cayatte, V., Balkowski, C., & Duschl, W. J. 2001, Ram Pressure Stripping and Galaxy Orbits: The Case of the Virgo Cluster, ApJ, 561, 708

Vulcani, B., Poggianti, B. M., Gullieuszik, M., et al. 2018, Enhanced Star Formation in Both Disks and Ram-pressure-stripped Tails of GASP Jellyfish Galaxies, ApJ, 866, L25

Wang, J., Koribalski, B. S., Serra, P., et al. 2016, New lessons from the H I size-mass relation of galaxies, MNRAS, 460, 2143

Waugh, M. 2005, PhD thesis, University of Melbourne.

Waugh, M., Drinkwater, M. J., Webster, R. L., et al. 2002, The large-scale distribution of neutral hydrogen in the Fornax region, MNRAS, 337, 641

Weilbacher, P. M., Streicher, O., & Palsa, R. 2016, MUSE-DRP: MUSE Data Reduction Pipeline

Westmeier, T., Kitaeff, S., Pallot, D., et al. 2021, SOFIA 2 - an automated, parallel H I source finding pipeline for the WALLABY survey, MNRAS, 506, 3962

Westmeier, T., Koribalski, B. S., & Braun, R. 2013, Gas and dark matter in the Sculptor group: NGC 55, MNRAS, 434, 3511

Whitaker, K. E., van Dokkum, P. G., Brammer, G., & Franx, M. 2012, The Star Formation Mass Sequence Out to z = 2.5, ApJ, 754, L29

Yi, S. K., Yoon, S. J., Kaviraj, S., et al. 2005, Galaxy Evolution Explorer Ultraviolet Color-Magnitude Relations and Evidence of Recent Star Formation in Early-Type Galaxies, ApJ, 619, L111

Zabel, N., Davis, T. A., Sarzi, M., et al. 2020, AlFoCS + Fornax3D: resolved star formation in the Fornax cluster with ALMA and MUSE, MNRAS

Zabel, N., Davis, T. A., Smith, M. W. L., et al. 2019, The ALMA Fornax Cluster Survey I: stirring and stripping of the molecular gas in cluster galaxies, MNRAS, 483, 2251

Zabel, N., Davis, T. A., Smith, M. W. L., et al. 2021, AlFoCS + F3D - II. Unexpectedly low gas-to-dust ratios in the Fornax galaxy cluster, MNRAS, 502, 4723

Zwaan, M. A., Meyer, M. J., Staveley-Smith, L., & Webster, R. L. 2005, The HIPASS catalogue: Ω_{HI} and environmental effects on the HI mass function of galaxies, MNRAS, 359, L30

Zwart, J. T. L., Santos, M., & Jarvis, M. J. 2015, Far beyond stacking: fully Bayesian constraints on sub-μJy radio source populations over the XMM-LSS-VIDEO field, MNRAS, 453, 1740